JOURNAL OF
MECHANICAL ENGINEERING
An International Journal

Vol 18 (1)	15 January 2021	ISSN 1823-5514	eISSN 2550-164X

A Method of the Lagrange Polynomial Interpolation with Weighting Factors for Reducing Computational Time

*Uthai Prasopchingchana**
Department of Mechanical Engineering, Faculty of Engineering,
Chulalongkorn University, Bangkok, 10330, Thailand.
**Uthai.P@Student.chula.ac.th*

ABSTRACT

This paper proposes a novel extrapolation method known as the Lagrange polynomial interpolation with weighting factors (LPI-WF) to determine initial guess values in each time step for solving equation systems of transient problems using iterative methods. The LPI-WF method is developed from the Lagrange polynomial interpolation to determine the direct extrapolation values and multiply them with the weighting factors. The weighting factors are calculated by considering the number of the previous time steps involved in the extrapolation and the duration between the present time step and the previous time steps. Thus, the LPI-WF method is proper for use with high-order temporal schemes. The key advantages of the LPI-WF method are that the computational time required to achieve the steady-state condition of the transient problems is reduced and the computation codes with the LPI-WF method is more stable than without the LPI-WF method at high time step values. A performance test of the LPI-WF method is carried out by comparing the computational time based on the "lid-driven cavity flow" problem for Reynolds numbers of 1000 and 5000. The test result shows that the computational time of the problem when the LPI-WF method is adopted can be reduced up to 10.46 % compared to the conventional method.

Keywords: *extrapolation, initial guess value, iterative method, Lagrange polynomial interpolation, weighting factors.*

ISSN 1823-5514, eISSN 2550-164X
Received for review: 2020-03-18
Accepted for publication: 2020-10-16
Published: 2021-01-15

Nomenclature

b	Width of the cavity, m.
EWF	Extrapolation weighting factor.
EWFN	Individual extrapolation weighting factor.
LIP	Lagrange interpolating polynomial.
LPI	Lagrange polynomial interpolation.
LPI-WF	Lagrange polynomial interpolation with weighting factors.
LTP	Temporal coefficient of the LPI method.
p	Pressure, Pa.
Re	Reynolds number.
SIMPLE	Semi-implicit method for pressure linked equations.
SUMEWFN	Summation of the individual extrapolation weighting factors.
SUMWD	Summation of the temporal individual weighting differences, s.
t	Time, s.
TT	Temporal difference value, s.
U	Velocity of the cavity lid, m/s.
u	Velocity component in the x direction, m/s.
v	Velocity component in the y direction, m/s.
WD	Temporal weighting difference, s.
WDN	Temporal individual weighting difference, s.
x	Cartesian coordinate in the horizontal direction of the cavity, m.
y	Cartesian coordinate in the vertical direction of the cavity, m.
ϕ*DEV*	Direct extrapolation value.
ϕ*EV*	Extrapolation value.
Greek symbol	
μ	Viscosity of fluid, kg/(s·m).
ρ	Density of fluid, kg/m^3.
ϕ	Solution in the previous time step.
ψ	Streamline.
ω	Vorticity.
Superscript	
**	Dimensionless.
Subscript	
ntmax	Maximum number of time steps.
max	Maximum.
min	Minimum.

Introduction

The iterative method is a popular method used to solve equation systems obtained from discrete methods, such as the finite difference method [1]-[3], the finite volume method [4, 5], the finite element method [6]-[9], the lattice Boltzmann method [1, 10], and the spectral element method [11, 12], due to the ease of code development and low computational time and memory. For solving transient problems, the use of an explicit iterative method has a limitation of time step values. Thus, properly imposing initial guess values in each time step is important to reduce computational time.

Extrapolation is a popular technique used to reduce the computational time of transient problems. It helps to determine the initial guess values of variables in the equations using the solutions of the previous time steps. In recent decades, several extrapolation methods have been proposed. The deformation gradient extrapolation method was proposed by Rashid [8]. This method was used to provide initial predictors for the next time step in the solutions of the large deformation finite element analysis. Three numerical examples showed that the use of the method to calculate the initial predictors could reduce the numbers of iterations required to achieve convergence. Also, the reliability and robustness of the equilibrium search of the solutions were improved. Markovinovic and Jansen [2] used the reduced-order models to determine initial guessed values for accelerating the solution convergence. They achieved 67 % maximum reduction in the computational time. Leemput et al. [10] employed the polynomial backward extrapolation to prescribe the initial guessed values for one-dimensional advection solved by using the lattice Boltzmann method. Liu et al. [13] proposed a methodology to improve the computational time of unsteady flow simulation called the dynamic mode extrapolation initial condition method. The method was applied by expressing the function in terms of time and space. The robustness of the method in reducing the computational time was confirmed by comparison test with the Lagrange extrapolation initial condition and the natural initial condition. The comparison results indicated that the method achieved a high computational time reduction for all cases. Moreover, extrapolation techniques proposed in [3]-[5], [7, 11, 12] were adopted for the purpose of reduction of computational time of many scientific, engineering, and economic problems. Some investigative studies [2, 3, 7, 8, 11] obtained positive results, whereas some [10, 12] could not verify any advantages of the extrapolation methods.

This article aims to present a new extrapolation method called LPI-WF, which helps to determine the initial guess values of each time step of the iterative methods for solving equation systems of transient problems approaching the steady-state condition. Furthermore, a performance test of the LPI-WF method is carried out with the well-known problem, “lid-driven cavity flow,” for *Re* of 1000 and 5000.

Details of the LPI-WF Method

The LPI-WF method is developed for solving equation systems of transient problems using iterative methods. The LPI-WF method accelerates solution convergence by applying initial guess values in each time step calculated from the solutions of the previous time steps. The LPI-WF method uses the LPI to extrapolate values directly from solutions of the previous time steps. The *EWF*s are calculated from time step values and numbers of time steps. The ϕEV of the LPI-WF method is the summation of the products of the *EWF* and the ϕDEV. Thus, ϕEV can be expressed as follows:

$$\phi EV = \sum_{n=1}^{ntmax-1} (EWF_n \phi DEV_n), \tag{1}$$

where *ntmax* is the maximum number of time steps required to solve the problems. A schematic diagram of the LPI-WF method is shown in Figure 1 when *ntmax* = 4. The *EWF* for each time step *n* can be obtained from

$$EWF_n = \frac{EWFN_n}{SUMEWFN}. \tag{2}$$

The *EWFN* for each time step *n* and the *SUMEWFN* are defined as follows:

$$SUMEWFN = \sum_{n=1}^{ntmax-1} (EWFN_n), \tag{3}$$

$$EWFN_n = \frac{WDN_n}{SUMWD}. \tag{4}$$

The *WDN* for each time step *n* and the *SUMWD* are defined as follows:

$$SUMWD = \sum_{n=1}^{ntmax-1} \left(\sum_{ntd=1}^{n} (WD_{n-ntd+1}) \right), \tag{5}$$

$$WDN_n = \sum_{ntd=1}^{n} (SUMWD - WD_{n-ntd+1}). \tag{6}$$

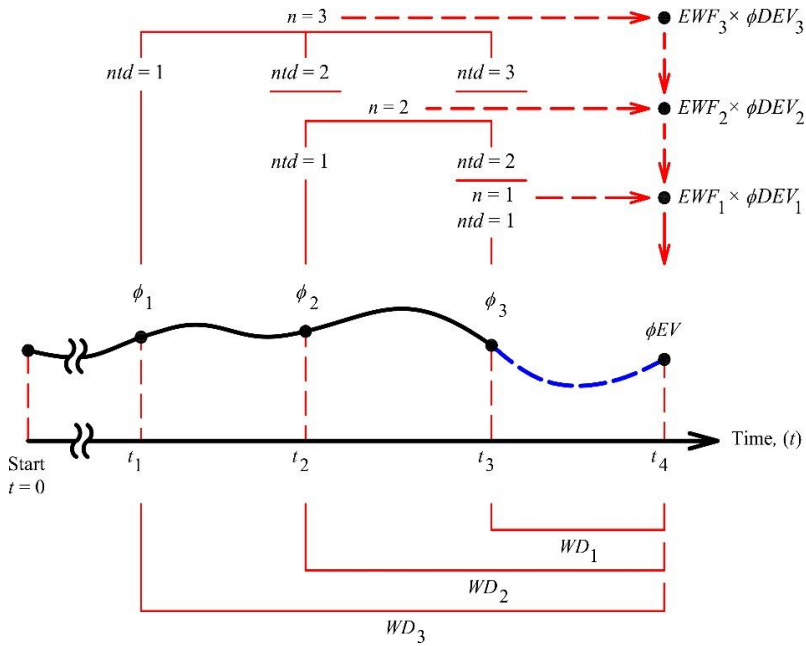

Figure 1: Schematic diagram of the LPI-WF method when *ntmax* = 4.

The *WD* is expressed as follows:

$$WD_{n-ntd+1} = t_{ntmax} - t_{ntmax-(n-ntd+1)}, \tag{7}$$

for $n = 1, 2, \ldots, ntmax - 1$ and $ntd = 1, 2, \ldots, n$

where *t* is the program time of each time step in transient problems. The ϕDEV can be obtained using the LPI method. Thus,

$$\phi DEV_n = \sum_{ntd=1}^{n} LTP_{n,ntd}\, \phi_{(ntmax-1)-n+ntd}. \tag{8}$$

The *LTP* is given as:

$$LTP_{1,1} = 1, \text{ for } n = 1,$$

$$LTP_{n,ntd} = \prod_{\substack{ntt=1 \\ ntt \neq ntd}}^{n} \frac{\left(-TT_{n,ntt}\right)}{\left(TT_{n,ntd} - TT_{n,ntt}\right)}, \quad \text{for } n = 2, 3, \ldots, ntmax - 1. \quad (9)$$

The *TT*s are computed from:

$$TT_{n,ntt} = t_{(ntmax-1)-n+ntt} - t_{ntmax}, \quad (10)$$

$$TT_{n,ntd} = t_{(ntmax-1)-n+ntd} - t_{ntmax}, \quad (11)$$

for $n = 1, 2, \ldots, ntmax - 1$, $ntd = 1, 2, \ldots, n$,
$ntt = 1, 2, \ldots, n, \quad and \ ntt \neq ntd.$

From the preceding texts, the procedures for determining the initial guess values from the solutions of the previous time steps using the LPI-WF method are as follows:

1. Calculate the *WD* from (7).
2. Determine the *WDN* from (6).
3. Find the *SUMWD* using (5).
4. Compute the *EWFN* from (4).
5. Calculate the *SUMEWFN* from (3).
6. Compute the *EWF* using (2).
7. Determine the *TT*s from (10) and (11).
8. Calculate the *LTP* of the LPI method from (9).
9. Find the ϕ*DEV*s from Equation (8).
10. Compute the ϕ*EV*s from (1). The calculated values of ϕ*EV*s are adopted as the initial guess values for iterative methods.

Code Validation

To prove the efficiency of the LPI-WF method in computational time reduction for calculating the initial guess values in each time step of the transient problems using iterative methods, a new code is developed for the performance test of the LPI-WF method. A well-known problem called "lid-driven cavity flow," for *Re* of 1000 and 5000 is selected for the performance test. This is because these numbers are the representatives of low and high laminar flows. Moreover, the numbers are used in the recognized solutions for code validation presented by Boltella and Peyret [14] and Bruneau and Saad [15]. The finite volume method with the LIP scheme [16] and the SIMPLE algorithm are employed to discretize the partial differential equations of the problem and to couple the continuity equation and the momentum equations, respectively. Code validation is carried out to ensure that the code delivers correct solutions.

The comparisons of solutions computed from the code with the benchmark and published numerical solutions of the problem reported in [14, 15] are used for the code validation. The code is based on a transient condition. However, the solutions reported in [14, 15] are the steady-state condition solutions. Therefore, a convergent criterion of the code for the final solutions is that the relative residuals of the present time step solutions and the previous time step solutions must be less than or equal to 10^{-5}, and must achieve the criterion consecutively at least ten times. Also, the criterion ensures that the solutions converged to the steady-state condition. A dimensionless time step value $\Delta t^{**} = 0.001$ (using $t^{**} = \Delta t\,|U|/b$,) and non-uniform mesh sizes of 150 × 150 and 200 × 200 are employed for computing the *Re* of 1000 and 5000, respectively. The performance test of the LPI-WF method is carried out on four categories as detailed in Table 1. Also, the code validation is performed on four categories simultaneously. The conventional method shown in Table 1 is a means whereby the initial guess values are equally imposed on the solutions in the latest previous time step.

"Lid-driven cavity flow" is a classical problem in Computational Fluid Dynamics, which is employed by numerous researchers [17]-[24] to verify or validate their methods or codes. Details of the problem are shown in Figure 2. Fluid flow in a square cavity is defined by the continuity equation and the momentum equations. Furthermore, the gravitational acceleration is neglected.

Table 1: Details of each category for the performance test of the LPI-WF method.

Category	*ntmax*	Extrapolation method
A	2	Conventional method
B	4	Conventional method
C	4	LPI method
D	4	LPI-WF method

For two-dimensional simulation, the equations can be written as:

$$\frac{\partial u}{\partial x} + \frac{\partial v}{\partial y} = 0, \tag{12}$$

$$\rho\left(\frac{\partial u}{\partial t} + u\frac{\partial u}{\partial x} + v\frac{\partial u}{\partial y}\right) = -\frac{\partial p}{\partial x} + \mu\left(\frac{\partial^2 u}{\partial x^2} + \frac{\partial^2 u}{\partial y^2}\right), \tag{13}$$

$$\rho\left(\frac{\partial v}{\partial t} + u\frac{\partial v}{\partial x} + v\frac{\partial v}{\partial y}\right) = -\frac{\partial p}{\partial y} + \mu\left(\frac{\partial^2 v}{\partial x^2} + \frac{\partial^2 v}{\partial y^2}\right), \tag{14}$$

where ρ, and μ are the density, and viscosity of the incompressible fluid in the square cavity, respectively.

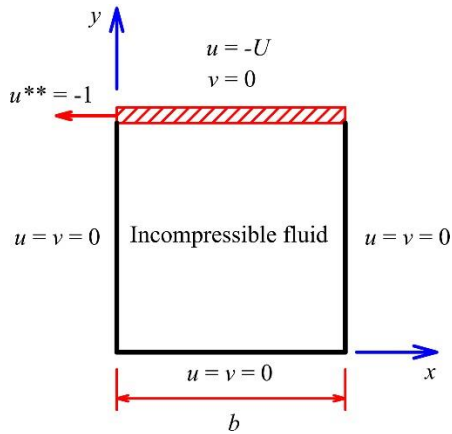

Figure 2: Details of the "lid-driven cavity flow" problem.

A summary of computational procedures is as follows:

1. Input the fluid properties into the code.
2. Specify *Re* and the velocity of the cavity lid.
3. Calculate the width of the cavity.
4. Input the initial values of the variables in the problem,
5. Compute the velocities and pressures of the fluid from (12), (13), and (14) by using the finite volume method with the LIP scheme and the SIMPLE algorithm to generate discrete equation systems. Then, solve the discrete equation systems using an iterative method.
6. Check the convergent criterion for each time step. If the solutions do not meet the convergent criterion, return to step 5. until the convergent criterion is achieved.
7. Determine the initial guessed values of the variables in the problem for computing in the next time step by using the extrapolation method (i.e., the conventional method, the LPI method, the LPI-WF method).
8. Repeat step 5. to 6.
9. Check the convergent criterion for termination of the code. If the solutions do not reach the convergent criterion, return to step 7. until the convergent criterion is achieved.

Figure 3 and Figure 4 display the contours of the ψ and ω computed from the code based on the "lid-driven cavity flow" problem for *Re* of 1000 and 5000. The patterns of the ψ and ω shown in Figure 3 and Figure 4 are similar to the patterns of the ψ and ω shown in [14, 15].

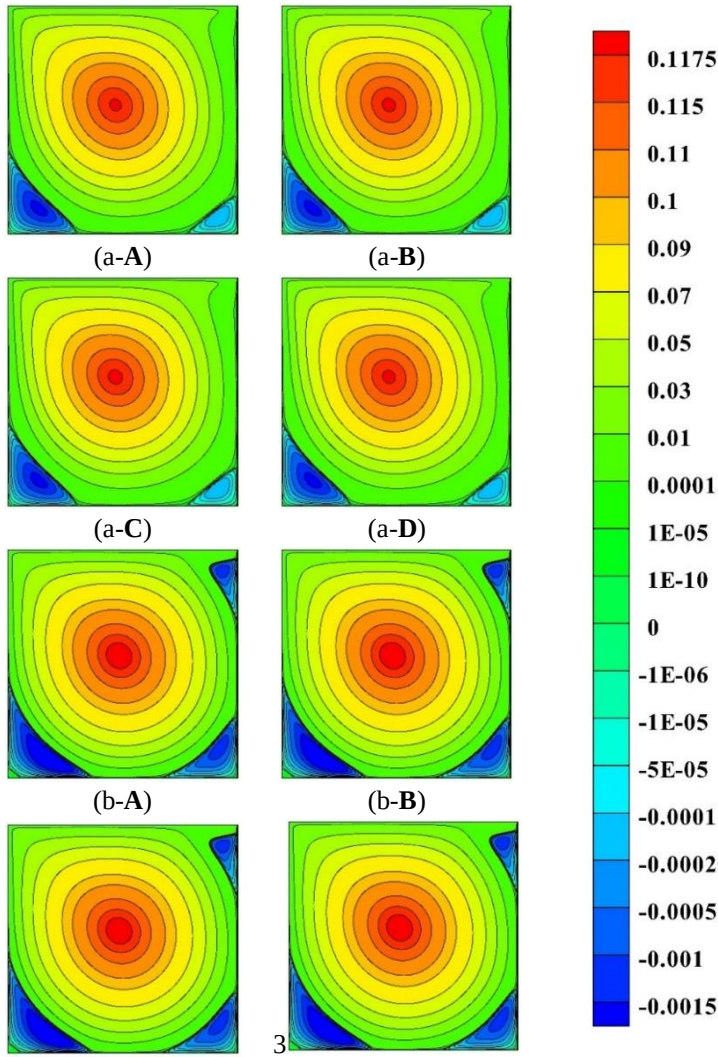

Figure 3: Contours of the ψ computed from the code based on the "lid-driven cavity flow" problem: (a-**A**) category **A** for *Re* = 1000, (a-**B**) category **B** for *Re* = 1000, (a-**C**) category **C** for *Re* = 1000, (a-**D**) category **D** for *Re* = 1000, (b-**A**) category **A** for *Re* = 5000, (b-**B**) category **B** for *Re* = 5000, (b-**C**) category **C** for *Re* = 5000 and (b-**D**) category **D** for *Re* = 5000.

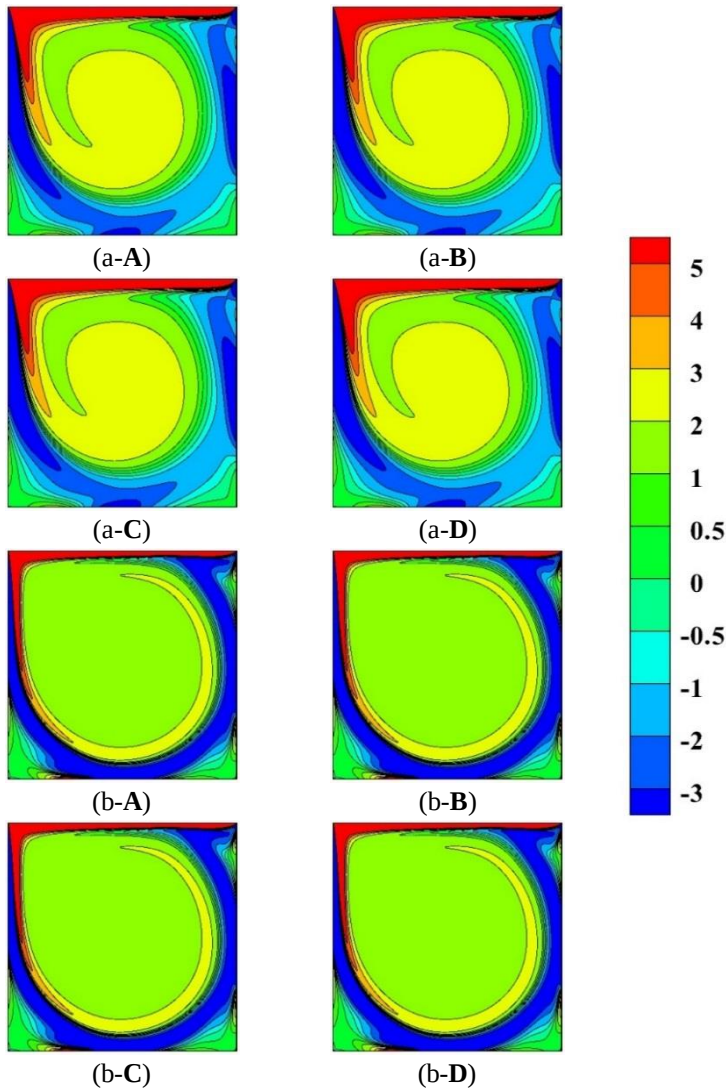

Figure 4: Contours of the ω computed from the code based on the "lid-driven cavity flow" problem: (a-**A**) category **A** for *Re* = 1000, (a-**B**) category **B** for *Re* = 1000, (a-**C**) category **C** for *Re* = 1000, (a-**D**) category **D** for *Re* = 1000, (b-**A**) category **A** for *Re* = 5000, (b-**B**) category **B** for *Re* = 5000, (b-**C**) category **C** for *Re* = 5000 and (b-**D**) category **D** for *Re* = 5000.

The dimensionless horizontal and vertical velocities (i.e., $u^{**} = u/|U|$ and $v^{**} = v/|U|$) on the dimensionless vertical and horizontal center lines (i.e., $y^{**} = y/b$ and $x^{**} = x/b$) of the cavity, respectively, are selected for comparison based on the "lid-driven cavity flow" problem for Re = 1000. The comparison between the dimensionless velocities computed from the code of this work and the dimensionless velocities reported in [14, 15] is shown in Table 2 and Table 3.

Table 2: Comparison between the dimensionless horizontal velocities computed from the code and the dimensionless horizontal velocities reported in [14, 15] based on the "lid-driven cavity flow" problem for Re = 1000.

y^{**}	u^{**}					
	Present work				[14]	[15]
	A	**B**	**C**	**D**		
1.0000	-1.0000000	-1.0000000	-1.0000000	-1.0000000	-1.0000000	-1.00000
0.9766	-0.6617013	-0.6620655	-0.6623109	-0.6619848	-0.6644227	
0.9688	-0.5776700	-0.5781232	-0.5784306	-0.5780242	-0.5808359	-0.58031
0.9609	-0.5133807	-0.5139125	-0.5142733	-0.5137946	-0.5169277	
0.9531	-0.4684216	-0.4690181	-0.4694226	-0.4688833	-0.4723329	-0.47239
0.8516	-0.3332189	-0.3336413	-0.3339621	-0.3335436	-0.3372212	
0.7344	-0.1867607	-0.1867906	-0.1868397	-0.1867802	-0.1886747	-0.18861
0.6172	-0.0563917	-0.0564056	-0.0564167	-0.0564001	-0.0570178	
0.5000	0.0619424	0.0617708	0.0616691	0.0618117	0.0620561	0.06205
0.4531	0.1076536	0.1074753	0.1073726	0.1075166	0.1081999	
0.2813	0.2779799	0.2781329	0.2782668	0.2780928	0.2803696	0.28040
0.1719	0.3849464	0.3854361	0.3857839	0.3853204	0.3885691	
0.1016	0.2964872	0.2972227	0.2977117	0.2970553	0.3004561	0.30029
0.0703	0.2198370	0.2204753	0.2208919	0.2203312	0.2228955	
0.0625	0.1995407	0.2001395	0.2005284	0.2000049	0.2023300	0.20227
0.0547	0.1787697	0.1793253	0.1796841	0.1792022	0.1812881	
0.0000	0.0000000	0.0000000	0.0000000	0.0000000	0.0000000	0.00000

The dimensionless horizontal and vertical velocities computed from the code with category **A** yield the highest maximum differences compared to the solutions reported in [14, 15]. The highest maximum differences of the dimensionless horizontal velocity are 1.39 % and 1.35 % compared to the solutions reported in [14, 15] on y^{**} = 0.0547 and y^{**} = 0.0625, respectively. Thus, the highest maximum differences of the dimensionless vertical velocity are 1.49 % and 1.45 % compared to the solutions reported in [14, 15] on x^{**} = 0.9375 and x^{**} = 0.9297, respectively. Besides, the maximum differences between the solutions, dimensionless horizontal velocity, computed from the code with category **D**, and the solutions reported in [14, 15] are 1.15 % and

1.12 % on $y^{**} = 0.0547$ and $y^{**} = 0.0625$, respectively. Also, the maximum differences between the solutions, dimensionless vertical velocity, computed from the code with category **D**, and the solutions reported in [14, 15] are 1.28 % and 1.24 % on $x^{**} = 0.9375$ and $x^{**} = 0.9297$, respectively.

Table 3: Comparison between the dimensionless vertical velocities computed from the code and the dimensionless vertical velocities reported in [14, 15] based on the "lid-driven cavity flow" problem for $Re = 1000$.

x^{**}	v^{**}					
	Present work				[14]	[15]
	A	**B**	**C**	**D**		
0.0000	0.0000000	0.0000000	0.0000000	0.0000000	0.0000000	0.00000
0.0312	-0.2251103	-0.2254315	-0.2256545	-0.2253564	-0.2279225	
0.0391	-0.2903928	-0.2907894	-0.2910641	-0.2906971	-0.2936869	-0.29330
0.0469	-0.3517003	-0.3521544	-0.3524685	-0.3520490	-0.3553213	
0.0547	-0.4065557	-0.4070475	-0.4073865	-0.4069337	-0.4103754	-0.41018
0.0937	-0.5229326	-0.5233599	-0.5236483	-0.5232631	-0.5264392	
0.1406	-0.4236065	-0.4239931	-0.4242531	-0.4239061	-0.4264545	-0.42634
0.1953	-0.3168067	-0.3172187	-0.3175008	-0.3171248	-0.3202137	
0.5000	0.0261299	0.0259989	0.0258801	0.0260336	0.0257995	0.02580
0.7656	0.3228789	0.3230505	0.3232078	0.3230060	0.3253592	
0.7734	0.3314039	0.3316044	0.3317819	0.3315510	0.3339924	0.33398
0.8437	0.3726714	0.3732945	0.3737411	0.3731495	0.3769189	
0.9062	0.3283593	0.3292032	0.3297821	0.3290087	0.3330442	0.33290
0.9219	0.3053948	0.3062299	0.3067999	0.3060400	0.3099097	
0.9297	0.2919080	0.2927229	0.2932790	0.2925360	0.2962703	0.29622
0.9375	0.2765008	0.2772919	0.2778314	0.2771112	0.2807056	
1.0000	0.0000000	0.0000000	0.0000000	0.0000000	0.0000000	0.00000

Table 4 shows the comparison between the maximum ψ, ω, and location on the primary vortex, and the minimum ψ, ω, and location on the lower-left secondary vortex computed from the code of this work and the results reported in [15] based on the "lid-driven cavity flow" problem for $Re = 5000$. The maximum ψ computed from the code with category **A** delivers the maximum difference of 2.45 % compared to the maximum ψ reported in [15]. Besides, the minimum ψ computed from the code with category **C** grants the maximum difference of 0.05 % compared to the minimum ψ reported in [15]. Moreover, the differences of the maximum and minimum ψ computed from the code with category **D** compared to the solutions reported in [15] are 2.42 % and 0.04 %, respectively.

Table 4: Comparison between the maximum ψ, ω, and location on the primary vortex, and the minimum ψ, ω, and location on the lower-left secondary vortex computed from the code and the results reported in [15] based on the "lid-driven cavity flow" problem for *Re* = 5000.

Vortex	Value	Present work				[15]
		A	**B**	**C**	**D**	
Primary vortex	ψ_{max}	0.11898	0.11901	0.11901	0.11901	0.12197
	ω	1.81501	1.81664	1.81683	1.81669	1.9327
	x^{**}	0.48818	0.48818	0.48818	0.48818	0.48535
	y^{**}	0.53493	0.53493	0.53493	0.53493	0.53516
Lower left secondary vortex	ψ_{min}	-0.0030704	-0.0030718	-0.0030721	-0.0030718	-0.0030706
	ω	-2.71265	-2.71275	-2.71269	-2.71273	-2.7244
	x^{**}	0.19452	0.19452	0.19452	0.19452	0.19434
	y^{**}	0.07477	0.07477	0.07477	0.07477	0.073242

Performance Test of the LPI-WF Method

The performance test of the proposed LPI-WF method is carried out by comparing the computational time for solving the "lid-driven cavity flow" problem in the four categories. The "lid-driven cavity flow" problem is simulated for *Re* of 1000 and 5000. The non-uniform mesh sizes used are 100 × 100 and 150 × 150 for *Re* of 1000, and 150 × 150 and 200 × 200 for *Re* of 5000. The computer CPU time is used as the computational time. The computational time reported in the following contents is rounded off to integer values. The processor of the computer employed for computing is Intel ® Core ™ i5-4460 CPU @ 3.20 GHz.

Figure 5, Figure 6 and Table 5 show the computational time comparison of the "lid-driven cavity flow" problem for *Re* of 1000 and 5000 in the different categories and on the dimensionless time step values from 0.001 to 0.004. All results show that the computational time of category **D** is less than the computational time of categories **A** and **B**. The maximum computational time reductions of category **D** are 10.46 % and 11.36 % of the computational time of category **A** for *Re* of 1000 at 100 × 100 mesh size and 0.004 dimensionless time step value, and category **B** for *Re* of 5000 at 150 × 150 mesh size and 0.004 dimensionless time step value, respectively. Also, the computational time of category **D** is less than the computational time of category **C** for *Re* of 1000 at 100 × 100 and 150 × 150 mesh sizes and 0.002, 0.003, and 0.004 dimensionless time step values, and for *Re* of 5000 at 200 × 200 mesh size and 0.003 and 0.004 dimensionless time step values. Thus, at high resolutions and large time step values, category **D** has higher performance than category **C** for reducing computational time. The maximum computational time reduction of category **D** is 3.3 % of the computational time of category **C** for *Re* of 5000 at

200 × 200 mesh size and 0.004 dimensionless time step value. As shown in Figure 6 (b), the result of category **A** at 0.004 dimensionless time step value, is divergent (i.e., the solution fails to converge). Thus, the computation of category **D** is more stable than the computation of category **A**.

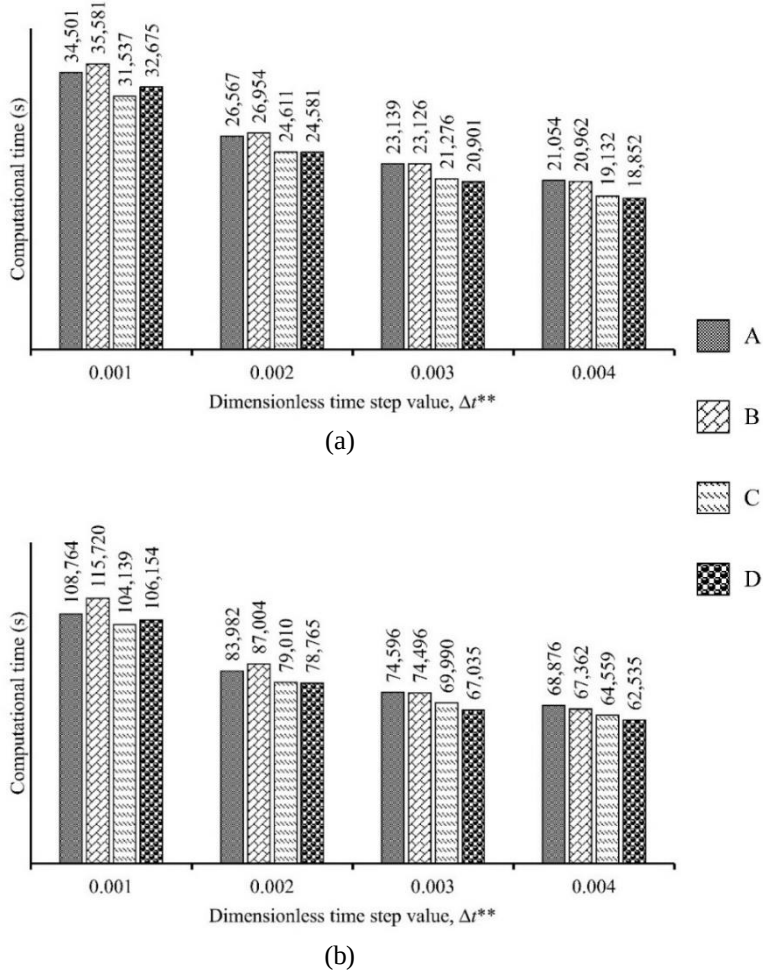

Figure 5: Comparisons of computational time based on the "lid-driven cavity flow" problem for *Re* = 1000 in the different categories: (a) 100 × 100 mesh size and (b) 150 × 150 mesh size.

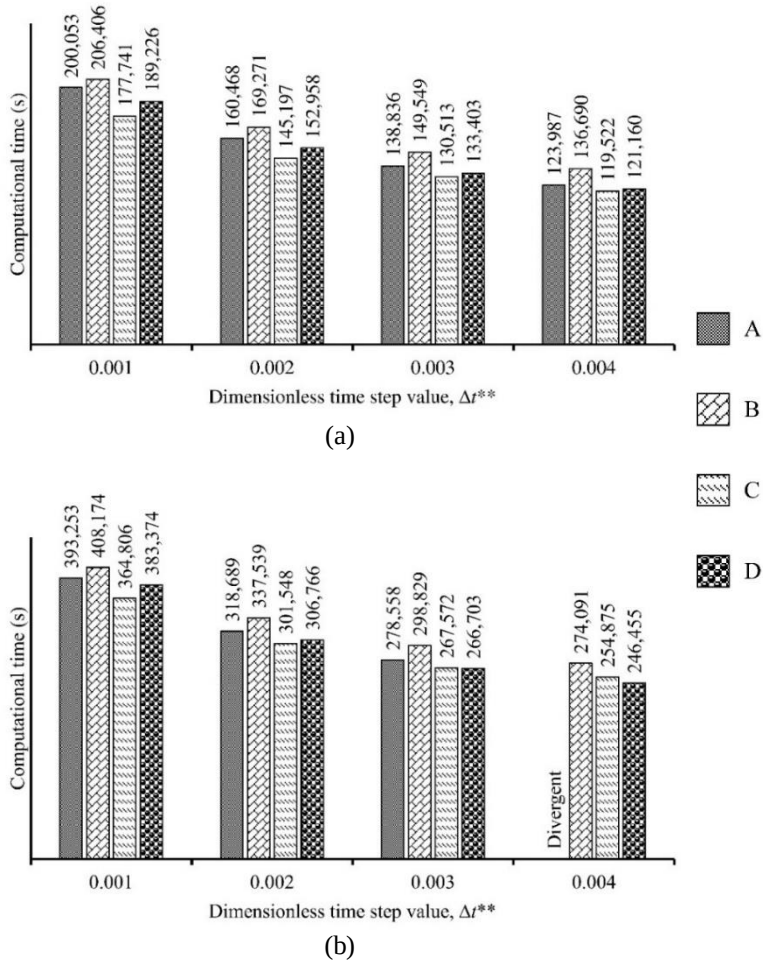

Figure 6: Comparisons of computational time based on the "lid-driven cavity flow" problem for *Re* = 5000 in the different categories: (a) 150 × 150 mesh size and (b) 200 × 200 mesh size.

Table 5: Number of iterations and computational time for the first ten time steps based on the "lid-driven cavity flow" problem for *Re* = 5000, 200×200 mesh size, and 0.003 dimensionless time step value.

Time step	Category	Number of iterations per time step	Improvement in the number of iterations (%) compared to category **A**	Computational time (s) per time step	Reduction of computational time (%) compared to category **A**
1	**A**	10	-	1778	-
	B	10	NA	1777	0.06
	C	10	NA	1780	NA
	D	10	NA	1778	NA
2	**A**	9	-	1032	-
	B	7	22.22	918	11.05
	C	7	22.22	901	12.69
	D	7	22.22	901	12.69
3	**A**	8	-	916	-
	B	7	12.50	753	17.79
	C	6	25.00	745	18.67
	D	6	25.00	745	18.67
4	**A**	9	-	795	-
	B	7	22.22	643	19.12
	C	6	33.33	635	20.13
	D	6	33.33	635	20.13
5	**A**	9	-	693	-
	B	7	22.22	544	21.50
	C	7	22.22	536	22.66
	D	7	22.22	535	22.80
6	**A**	9	-	626	-
	B	7	22.22	492	21.41
	C	7	22.22	484	22.68
	D	7	22.22	483	22.84
7	**A**	9	-	568	-
	B	8	11.11	448	21.13
	C	7	22.22	452	20.42
	D	7	22.22	441	22.36
8	**A**	8	-	520	-
	B	7	12.50	412	20.77
	C	7	12.50	442	15.00
	D	7	12.50	434	16.54
9	**A**	9	-	477	-
	B	7	22.22	380	20.34
	C	7	22.22	380	20.34
	D	7	22.22	380	20.34
10	**A**	8	-	439	-
	B	7	12.50	357	18.68
	C	7	12.50	357	18.68
	D	7	12.50	356	18.91

NA = Not available

Conclusions

The details of the LPI-WF method developed for determining the initial guess values of iterative methods to solve transient problems are demonstrated. The efficiency of the LPI-WF method are proven by the performance test carried out with the "lid-driven cavity flow" problem for *Re* of 1000 and 5000 at the different mesh sizes and various dimensionless time step values. The conclusion of this work is outlined in the following items:

1. The LPI-WF method is suitable for use with high-order temporal schemes such as the LIP scheme for extrapolation of initial guess values from solutions of previous time steps.
2 The procedures of the LPI-WF method are not complicated and are easy to add to the code of problem solvers for convergence acceleration to the steady-state condition of solutions.
3. From the results of the performance test, the computational time of the code with the LPI-WF method can be reduced up to 10.46 % of the computational time of the code with the conventional method for obtaining the steady-state condition of the solutions. Also, the computation of the code with the LPI-WF method at high dimensionless time step values is more stable than that of the conventional method.
4. Moreover, the performance of the LPI-WF method for reducing the computational time of the code is better than the performance of the LPI method at the high resolution of the mesh sizes and the large amounts of the dimensionless time step values.

Also, the LPI-WF method is implemented preliminarily as a performance test to verify the robust potential of the method for reducing the computational time of the flow solvers. For future work, to verify clearly that the LPI-WF method accelerates the convergence of solutions, the performance test of the method will be carried out extensively on both the "lid-driven cavity flow" problem at the various Reynolds numbers and other well-known problems.

References

[1] D. Arumuga Perumal, I. M. Gowhar, S. A. Ananthapuri and V. Jayakrishnan, "Computation of temperature distributions on uniform and non-uniform lattice sizes using mesoscopic lattice Boltzmann method," *Journal of Mechanical Engineering*, vol. 11, no. 2, pp 53-65, 2014.

[2] R. Markovinović and J. D. Jansen, "Accelerating iterative solution methods using reduced-order models as solution predictors," *International Journal for Numerical Methods in Engineering*, vol. 68, no. 5, pp 525-541, 2006.

[3] H. Hu, C. Chen and K. Pan, "Time-extrapolation algorithm (TEA) for linear parabolic problems," *Journal of Computational Mathematics*, vol.

32, no. 2, pp 183-194, 2014.
[4] P. Birken, T. Gleim, D. Kuhl and A. Meister, "Fast solvers for unsteady thermal fluid structure interaction," *International Journal for Numerical Methods in Fluids*, vol. 79, no. 1, pp 16-29, 2015.
[5] S. Sachs, M. Streitenberger, D. C. Sternel and M. Schäfer, "Extrapolation methods for accelerating unsteady partitioned fluid-structure interaction simulations," *International Journal of Multiphysics*, vol. 5, no. 4, pp 287-297, 2011.
[6] J. Huang, H. Wang and H. Yang, "Int-Deep: A deep learning initialized iterative method for nonlinear problems," *Journal of Computational Physics*, vol. 419, 2020.
[7] A. V. Malevsky and D. A. Yuen, "Large-scale numerical simulations of turbulent non-Newtonian thermal convection using method of characteristics," *Computer Physics Communications*, vol. 73, no. 1-3, pp 61-71, 1992.
[8] M. M. Rashid, "Deformation extrapolation and initial predictors in large-deformation finite element analysis," *Computational Mechanics*, vol. 16, no. 5, pp 281-289, 1995.
[9] Q. Zhang, S. Gui, H. Li and B. Lu, "Model reduction-based initialization methods for solving the Poisson-Nernst-Plank equations in three-dimensional ion channel simulations," *Journal of Computational Physics*, vol. 419, 2020.
[10] P. Van Leemput, M. Rheinländer and M. Junk, "Smooth initialization of lattice Boltzmann schemes," *Computers and Mathematics with Applications*, vol. 58, no. 5, pp 867-882, 2009.
[11] L. Grinberg and G. Em Karniadakis, "Extrapolation-based acceleration of iterative solvers: Application to simulation of 3D flows," *Communications in Computational Physics*, vol. 9, no. 3, pp 607-626, 2011.
[12] B. E. Merrill, Y. T. Peet, P. F. Fischer and J. W. Lottes, "A spectrally accurate method for overlapping grid solution of incompressible Navier-Stokes equations," *Journal of Computational Physics*, vol. 307, pp 60-93, 2016.
[13] Y. Liu, G. Wang and Z. Ye, "Dynamic mode extrapolation to improve the efficiency of dual time stepping method," *Journal of Computational Physics*, vol. 352, pp 190-212, 2018.
[14] O. Botella and R. Peyret, "Benchmark spectral results on the lid-driven cavity flow," *Computers and Fluids*, vol. 27, no. 4, pp 421-433, 1998.
[15] C. H. Bruneau and M. Saad, "The 2D lid-driven cavity problem revisited," *Computers and Fluids*, vol. 35, no. 3, pp 326-348, 2006.
[16] U. Prasopchingchana and T. Manewattana, "A new scheme for the finite volume method verified with two dimensional laminar natural convection in a square cavity," *Engineering Journal*, vol. 19, no. 4, pp 133-152, 2015.
[17] B. An, F. Mellibovsky, J. M. Bergadà and W. M. Sang, "Towards a better understanding of wall-driven square cavity flows using the lattice

Boltzmann method," *Applied Mathematical Modelling*, vol. 82, pp 469-486, 2020.

[18] N. B. Barik and T. V. S. Sekhar, "Mesh-free multilevel iterative algorithm for Navier–Stokes equations," *Numerical Heat Transfer, Part B: Fundamentals*, 2020.

[19] B. J. Gross, N. Trask, P. Kuberry and P. J. Atzberger, "Meshfree methods on manifolds for hydrodynamic flows on curved surfaces: A Generalized Moving Least-Squares (GMLS) approach, " *Journal of Computational Physics*, vol. 409, 2020.

[20] W. He, G. Qin, J. Lin and C. Jia, "A segregated spectral finite element method for the 2D transient incompressible Navier–Stokes equations," *Computers and Mathematics with Applications*, vol. 79, no. 2, pp 521-537, 2020.

[21] M. A. D. S. Lourenço and E. L. M. Padilla, "An octree structured finite volume based solver," *Applied Mathematics and Computation*, vol. 365, 2020.

[22] Q. Luo, "Discretized pressure Poisson algorithm for steady incompressible flow on two-dimensional triangular unstructured grids," *European Journal of Mechanics, B/Fluids*, vol. 80, pp 187-194, 2020.

[23] M. Ramos Ortega, A. Beaudoin and S. Huberson, "Optimized incompressible smoothed particle hydrodynamics methods and validations," *International Journal for Numerical Methods in Fluids*, vol. 92, no. 11, pp 1528-1550, 2020.

[24] Y. Vasyliv and A. Alexeev, "Development of General Finite Differences for complex geometries using a sharp interface formulation," *Computers and Fluids*, vol. 193, 2019.

Performance Optimization of Combined Cycle Power Plant Considering Various Operating Parameters

*Sachin Kumar**
Department of Mechanical Engineering, Jagannath University, 124103 Jhajjar, Haryana, India
**skmtech11@gmail.com*

ABSTRACT

Combined cycle power plants are popular in thermal engineering field for their higher efficiency as compared to normal cycles such as Rankine and Brayton Cycle. But main disadvantages of the cycle are waste heat rejection and low work output. To overcome these difficulties a heat recovery system is used in present work to recover waste heat of Brayton cycle as a steam generator for Rankine cycle in a combined Gas-Vapor cycle. In present work, effect of factors such as "compression ratio", "inlet air temperature" and "turbine inlet temperature" on cycle efficiency was calculated. It was found that cycle efficiency increases with increase in these factors. It was found that optimum value of compression ratio is 12-18 for maximum output of combined cycle. Whereas inlet air temperature has adverse effect on cycle efficiency so it should be kept lower while increase in turbine inlet temperature increases the cycle's work output and hence efficiency. Optimum values of turbine inlet temperature were found in range of 1600-1700 K

Keywords: *Combined cycle efficiency, Work Output, Compression Ratio (12-18), Inlet Air Temperature (IAT), Turbine Inlet Temperature (TIT).*

Nomenclature:-

AP = Approach Point
PP = Pitch Point
T = Temperature

ISSN 1823-5514, eISSN 2550-164X
Received for review: 2020-03-18
Accepted for publication: 2020-11-10
Published: 2021-01-15

WHRB = Waste Heat Recovery Boiler
$\dot{Q}$ = Heat Transfer Rate
w_C, w_T = specific work output of compressor and turbine
h = Enthalpy
C_P = Specific heat at constant pressure.
EO = Economizer Outlet.
FW = Water Flow Rate.
ST = Steam
G = Gas
W = Water
TIT = Turbine Inlet Temperature
T_{GEX} = Exit Gas Temperature
r = Compression Ratio
η = Efficiency
η_{CC} = Combined Cycle Efficiency.

Introduction

In electric power generation, a combined cycle is an assembly of heat engines that work in tandem off the same source of heat, converting it into mechanical energy, which in turn usually drives electrical generators. The principle is that the exhaust of one heat engine is used as the heat source for another, thus extracting more useful energy from the heat, increasing the system's overall efficiency. This works because heat engines are only able to use a portion of the energy their fuel generates (usually less than 50%). The remaining heat (e.g., hot exhaust fumes) from combustion is generally wasted. Combining two or more thermodynamic cycle results in improved overall efficiency and reduces fuel costs. In stationary power plants, a successful, common combination is the Brayton cycle (in the form of a turbine burning natural gas or synthesis gas from coal) and the Rankine cycle.

In combined cycle, a gas turbine generator generates electricity and heat in the exhaust is used to make steam, which in turn drives a steam turbine to generate additional electricity. This last step enhances the efficiency of electricity generation. Many new gas power plants in North America and Europe are of this type. Such an arrangement used for marine propulsion is called combined gas (turbine) and steam (turbine) (COGAS). Conversion of an existing steam power plant in a combined cycle power plant is cost effective as well as more efficient as compared to former [1]. Based on recent technology and future demand the main focus in study of CCGT is to focus on exergy optimization by reducing heat loss [2]. Moreover the power production of combined cycle can be increased by evaporator and absorption cooling up to 5-10% whereas as precooling of cycle reduce the

temperature range of combustion chamber [3, 4].

Various comparative studies on various kind of combined cycles and methods of improving efficiency of combined cycle and has been done by developing a genetic algorithm to study complex design of combined cycle for utilizing waste heat [5-8]. In 2004, exergy analysis of reheat combined cycle was done to design and optimization of cycle which in turns conclude that the efficiency and power output of the cycle can be increased by replacing reheat in expansion process [9, 10]. Cyclic efficiency of power plant can be increased by using air precooler connected to the evaporator of power plant [11]. Kakaras et al. [12-13] developed three method for air cooling viz; a) evaporative cooling b) refrigeration cooling c) evaporative cooling of pre-compressed air. It was concluded that the highest incremental electricity generation is realized by absorption intake air cooling. In terms of the economic performance of the investment, the evaporation cooler has the lowest cost of incremental electricity generation and lowest payback period. Concerning to the cooling method of pre-compressed air, the results shows a significant gain in capacity, but the total cost of incremental electricity generation in this case is the highest.

The cyclic performance of power plant can be increased by maximizing turbine rotor inlet temperature in the gas turbine; optimizing the gas turbine pressure ratio for gas turbine performance; optimizing steam turbine and boiler pressure; and maximizing steam injection in the gas turbine [14, 15]. Whereas pre-cooling of inlet air by absorption chiller can increase the cycle efficiency [16]. Butcher & Reddy [17] studied performance of a waste heat recovery power generation system based on second law analysis is investigated for various operating conditions. The temperature profiles across the heat recovery steam generator (HRSG), network output, second law efficiency and entropy generation number are simulated for various operating conditions.

Hawaj & Mutairi [18] investigated the effect of different parameters, such as steam to gas mass flow rate ratio, inlet steam turbine temperature, compressor pressure ratio, and gas turbine (GT) combustion efficiency on the performance of the combined cycle. In another aspect of the study, the relative advantage of using CCPP with absorption cooling over thermally equivalent mechanical vapor compression (MVC) cooling was also demonstrated. Whereas reheated cycle is best cycle as compared of single stage cycle and intercooled cycle [19]. Locopo et al. [20] did second law analysis of three different cycles viz., a cycle uses exhaust gases produced by the engine, another with the addition of cooling water with engine exhaust, and third, a regenerated cycle. The overall efficiency of the cycle was increased by 12% for the cycle without bottoming.

Godoya et al. [21] characterized combined cycle gas turbine power plants by minimum specific annual cost values and determined wide ranges of market conditions as given by the relative weights of capital investment

and operative costs, employing a non-linear mathematical programming model. Sipheng Zhu et al. [22] did a theoretical study of bottoming the Rankine cycle to recover engine waste heat by comparing five different working fluid on MATLAB software. Engine performance was mainly affected by working fluid properties and superheating temperature which causes slight changes in the overall efficiency of the cycle. Martinez et al. [23] reviewed micro heat and power system with renewable energy resources. Khan et al. [24] use bypass valves to optimize the performance and a 45% increase in network output was obtained with an increase in turbine inlet temperature from 1000K to 1400K simultaneously increasing the efficiency of the cycle from 15% to 31%. More ever the plant efficiency can be increased by providing sequential combustion and steam cooling [25]. Ahmadi et al. [26] reviewed solar power technologies used for electric power generation. Their work points out two ways of generating electricity by solar energy viz; converting solar irradiations into electricity using PV model, and, secondly, harnessing thermal energy by implementation of concentrated solar power (CRS) plants like Linear Fresnel collectors and parabolic trough collectors showing that PV modeled power plants are the better ones as compared to CRS.

A simulation model was proposed by Kumar et al. [27] for determining steam flow rate and overall efficiency of 250 MW coal based power plant. Effect of varying load on thermal efficiency of the plant was discussed and results shows that overall efficiency of the plant was slightly affected with increase in load. In 2019, Kumar et al. [28] proposed two ways of waste heat recovery system of a gas engine to generate electricity. In first approach a single heat recovery boiler was used in which all mixed gases are allowed to pass through before entering to pre-heater and grid cooler. Whereas, in second method, vapor mixture was allowed to pass through steam turbine. Comparing the both methods resulted that the first approach recovered 23931 KJ/s of waste heat with 23.5% power generating efficiency whereas in second approach 21253 KJ/s waste heat was recovered with 22.2% efficiency.

Since last few years various case studies and energy analysis as well as economical aspects of combined cycle power plant has been done [29-31]. In the present study effect of some design parameters such as gas turbine compression ratio, ambient air temperature, turbine inlet temperature, on factors such as fuel consumed (kg) per 100 kg of air, gas turbine outlet temperature, work obtained from the combined cycle, combined cycle efficiency will be calculated.

Design principle

An open circuit gas turbine cycle has a compressor, a combustor, and a turbine. In this type of cycle, the inlet turbine temperature and flue gas temperature are kept in ranges of 900-1400 °C, and, 450 to 650 °C

respectively. This range of temperature provides a lot of heat to be used in the Rankine cycle for the generation of steam. In the present work, the turbine's exhaust heat passed through a heat recovery steam generator (HRSG) with a live steam temperature between 420 and 580 °C to convert water into steam. The cooling process in the Rankine cycle is done by circulating water from outside sources like rivers of the cooling tower at low temperature, say, 15 °C.

Working Principle

A combined cycle power plant consists of a Brayton cycle at the first stage and a Rankine Cycle on a later stage is shown in Figure 1. In the first stage air as a fuel is compressed isentropically in an air compressor and then sent to the combustion chamber where compressed air is heated by fuel. The hot gas is then made to flow over turbine blades which in turn generate electricity and the exhaust is passed to the heat recovery steam generator. The output as steam from the steam generator is now used as working fluid for the second stage i.e. in the Rankine cycle, to generate electricity. At the second stage, the steam output from the steam generator is now passed to the steam turbine which in turns generates electricity and the exhaust of the steam turbine is passed to the condenser where it condensed in the form water and again fed to the steam generator with the help of water pump as shown in Figure 1.

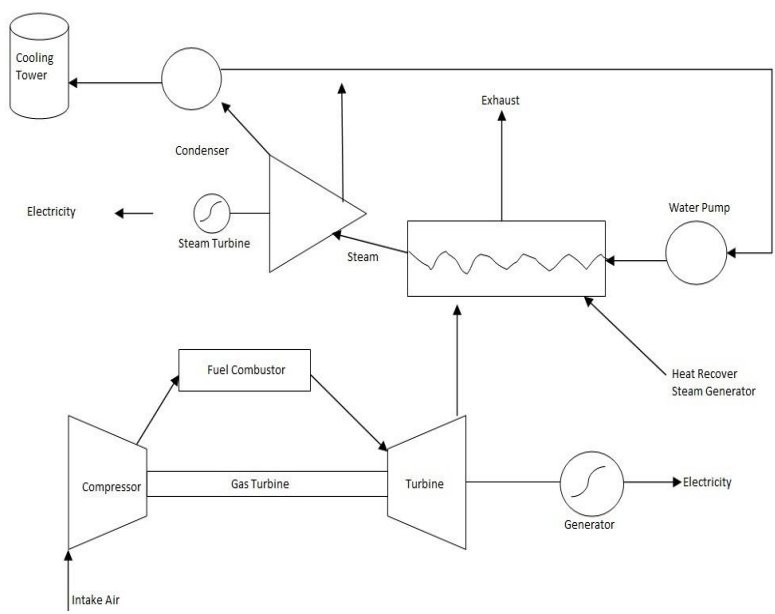

Figure 1: Working principle of single pressure CCPP.

The waste heat recovery process in a single pressure WHRB is illustrated on a temperature profile diagram in Figure 2. Water enters the boiler in the form of compressed liquid at condensate temperature (T_{FW}). As the water receives heat from the hot exhaust gases, it becomes saturated, starts boiling, and is superheated. On the hot side, the exhaust gases leaving the gas turbine enter the steam generator and get cooled finally to the stack temperature (T_{STACK}).

For maximum heat recovery, the stack temperature should approach the acid saturation point of the exhaust gases, while keeping the pressure drop as well as the size of the boiler within the desirable limits. The factors which affect the cost and effectiveness of any WHRB are the pinch point, approach point, allowable backpressure, stack temperature, steam pressure, and steam temperature. The minimum temperature difference for heat transfer, which is known as pinch point plays an important role in identifying the optimum heat recovery and size of heat exchangers. The approach point is the difference between the saturation temperature and the temperature of water leaving the economizer. Lowering the approach point will increase the probability of steaming in economizer which may cause hammering and blanketing.

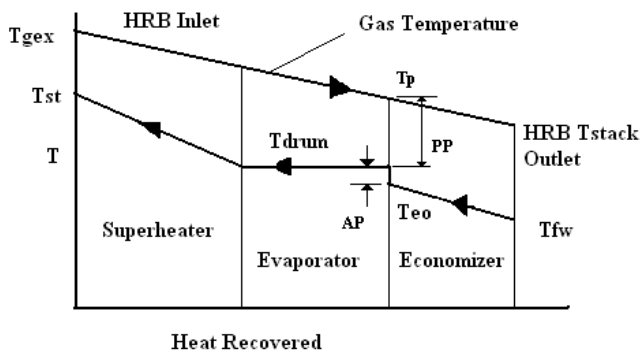

Figure 2: Temperature/Heat energy diagram for a single pressure WHRB.

The gas side pinch point temperature (T_P) and economizer exit temperature (T_{EO}) are calculated by assuming the drum saturation pressure (P_{Drum}).

$$T_P = T_{DRUM} + PP \quad (1)$$

$$T_{EO} = T_{DRUM} - AP \quad (2)$$

The steam generated for each kg/sec of exhaust gases can be determined by applying mass and energy conservation principles across the super-heater and evaporator.

$$\dot{m} = \dot{m}_{GEX} \times C_{PG} \frac{(T_{GEX} - T_P)}{(h_{ST} - h_{EO})} \quad (3)$$

The WHRB, being considered is a non-firing boiler. Therefore the heat transfer is predominantly by convection. It is customary to neglect the radiative heat transfer, particularly because the reduction in heat transfer due to soot deposition/ fouling etc. is also ignored and it is assumed that these two approximately compensate each other. The heat across each section of the boiler can be estimated as follow:

$$\dot{Q}_{ECON} = \dot{m}_w(h_{EO} - h_{FW}) \quad (4)$$

$$\dot{Q}_{EVAP} = \dot{m}_w(h_{FG} + C_{PW}(T_{DRUM} - T_o)) \quad (5)$$

$$\dot{Q}_{SUPR} = \dot{m}_w(h_{ST} - h_{FG}) \quad (6)$$

The flue gas temperature in the stack can also be estimated based on the heat balance across economizer.

$$T_{STACK} = T_P - \dot{m}_w \times \frac{(h_{LPEO} - h_{FW})}{(\dot{m}_{GEX} \times C_{PG})} \quad (7)$$

Low stack temperature is always desirable from the point of waste recovery. However, to avoid the corrosion from moisture formation in the economizer, the minimum temperature should always be kept higher than the acid dew point temperature. Also, the size of the economizer depends on the stack temperature which has, therefore, to be justified on the economic consideration.

Mathematical Modeling

The following Parameters are taken for the present study:

Compression ratio:	8-20
Inlet Air Temperature:	275-325 K
Turbine Inlet Temperature	1250-1700 K

The effect of all these parameters was studied to establish the combined cycle work output and efficiency. For a given compressor isentropic efficiency

η_c and pressure ratio r_c , other state variables for the incoming and outgoing streams can be calculated. The inlet and outlet humidity ratios will be the same. The energy balance yields the compressor work w_c and compressor outlet temperature.

$$w_{ai} = w_{ao} \tag{8}$$

$$\frac{T_{ao}}{T_{ai}} = [r_c]^{\frac{\gamma_c - 1}{\gamma_c \eta_c}} \tag{9}$$

The polytropic efficiency of the compressor and turbine can be calculated according to:

$$\eta_c = 1 - [0.04 + (r_c - 1)/150] \tag{10}$$

$$\eta_t = 1 - [0.03 + (r_t - 1)/180] \tag{11}$$

$$w_c = (h_{ao} - h_{ai}) \tag{12}$$

Specific heat ratio for the humidified air is being given by the following relation:

$$\gamma_c = \frac{C_{pc}}{C_{vc}} \tag{13}$$

where C_{pc} and C_{vc} can be determined from the following relations:

$$C_{pc} = C_{pa} + w_{ai} C_{pw} \tag{14}$$

$$C_{vc} = C_{va} + w_{ai} C_{vw} \tag{15}$$

Specific heat of air at constant pressure is given by the following relation:

$$C_{pa} = C_0 + C_1 T + C_2 T^2 + C_3 T^3 + C_4 T^4 \tag{16}$$

$$C_{va} = C_{pa} - R \tag{17}$$

$$C_p = C_{pa} + \frac{f}{f+1} \theta_{cp} \tag{18}$$

where,

$$\theta_{cp} = CP_0 + CP_1T + CP_2T^2 + CP_3T^3 + CP_4T^4 + CP_5T^5 \tag{19}$$

Enthalpy of air is being given by the following formula:

$$h_a = \int_0^T C_{pa}\,dt \tag{20}$$

$$h_a = C_0T + \frac{C_1}{2}T^2 + \frac{C_2}{3}T^3 + \frac{C_3}{4}T^4 + \frac{C_4}{5}T^5 + CH \tag{21}$$

For the expansion ratio of the gas turbine, "r_e" temperature at the exit of the turbine isentropic process can be calculated by:

$$T_{gos} = T_{gi}(r_e)^{\frac{(\gamma_g - 1)}{\gamma_g}} \tag{22}$$

The actual temperature T_{go} at the exit of the turbine can be calculated by:

$$\eta_T = \frac{T_{gi} - T_{go}}{T_{gi} - T_{gos}} \tag{23}$$

The energy balance yields the turbine work w_T given by the following relation:

$$w_T = (h_{gi} - h_{go}) \tag{24}$$

Change in enthalpy of air after adding fuel in the combustion chamber is:

$$\eta_{cc} m_f CV = h_{go} - h_{gi} = h_3 - h_2 \tag{25}$$

where h_{go} may be calculated as:

$$h_{go} = h_a + \frac{f}{1+f}\theta_h \tag{26}$$

$$\theta_h = H_0 + H_1T + H_2T^2 + H_3T^3 + H_4T^4 + H_5T^5 \tag{27}$$

Heat transfer and efficiency can be calculated by the following equations:

Pump work:

$$w_P = V_f (P_{DRUM} - P_{COND}) \tag{28}$$

If the efficiency of the pump is taken into consideration then:

$$h_{FW} = h_f + \frac{h_{FW} - h_f}{\eta_p} \tag{29}$$

Work done by the steam turbine is:

$$(W.D)_{ST} = h_{MST} - h_{EX} \tag{30}$$

Net work done will be:

$$(W.D)_{net} = (W.D)_{ST} - W_p \tag{31}$$

$$\dot{Q}_{SC} = (h_{MST} - h_{FW}) \tag{32}$$

Hence the associated bottoming cycle and plant efficiencies are:

$$\eta_{SC} = \frac{(W.D)_{net}}{Q_{SC}}$$

$$\eta_{CC} = \frac{P_{GT} + P_{SC}}{Q_{in}} = \frac{P_{CC}}{M_f LHV} \tag{33}$$

Result Analysis and Discussion

For the present study, the pressure ratio of gas turbines varied from 8 to 20 bar. With an increase in compression ratio, compressor exit temperature increases which result in the decrement of fuel consumption keeping the inlet temperature of the turbine constant (Figure 3). In the present work capacity of the blade material of the turbine for bearing thermal stress was kept on mind for deciding values of the inlet gas temperature of the turbine. The main purpose of the study is to focus on the recovery of waste heat of gas turbine

exit which can be utilized to generate steam in steam turbines and further generate electric power by implementing heat recovery steam generator.

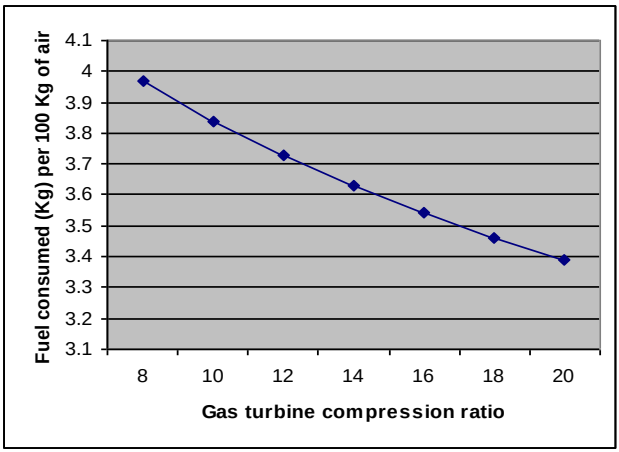

Figure 3: Effect of gas turbine compression ratio on fuel consumption

The cycle compression ratio has a direct effect on gas turbine outlet temperature. As the compression ratio increases, gas turbine outlet temperature decreases which makes lesser heat available for pressurized water in HRSG (Figure 4).

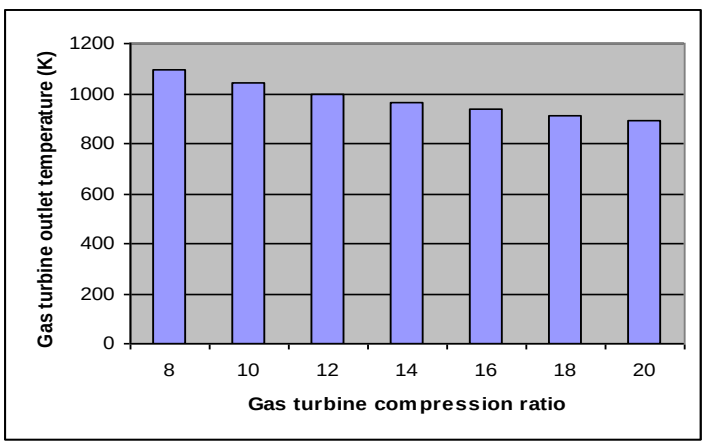

Figure 4: Effect of the compression ratio of the gas turbine on gas turbine outlet temperature.

For the lower cycle pressure ratio, sufficient heat is available to convert the pressurized water into steam. But after a pressure ratio of 18, flue gas temperatures becomes low enough to lower the heat supplied to pressurized water. Due to this steam turbine work output is decreased and after the pressure ratio of 18, a decreased work output from the cycle is obtained (Figure 5).

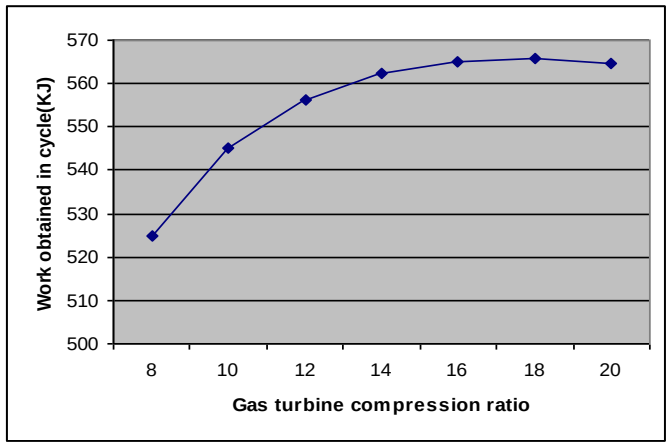

Figure 5: Change in work obtained from a combined cycle with a change in gas turbine compression ratio.

As it may be observed that there is not much gain in work output by changing the compression ratio but efficiency gain is reasonable (Figure 6). To calculate the cycle efficiency a ratio of work output and energy supplied is taken. As the increase in pressure ratio lower the fuel consumption so the energy supplied to the cycle decreases and efficiency increases.

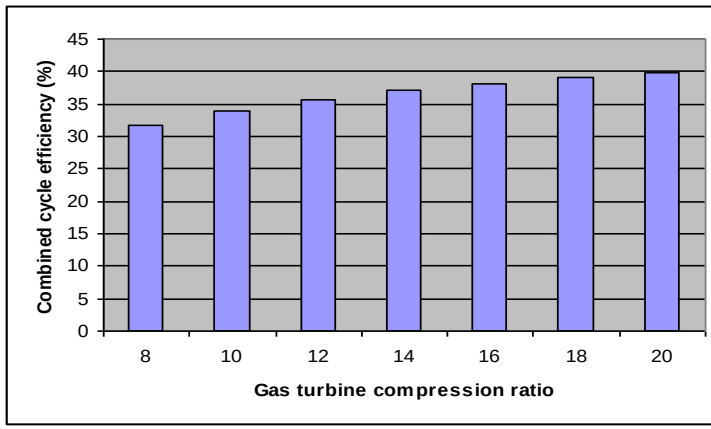

Figure 6: Change in combined cycle efficiency with a change in gas turbine compression ratio.

Ambient air temperature never remains constant. Now from the analysis, it is being found that as the IAT will increase fuel requirement will decrease. This is because TIT is fixed for this case and if the IAT increases then the combustion chamber inlet temperature will also increase. But the combustion chamber outlet temperature is fixed. So the fuel requirement decreases (Figure 7).

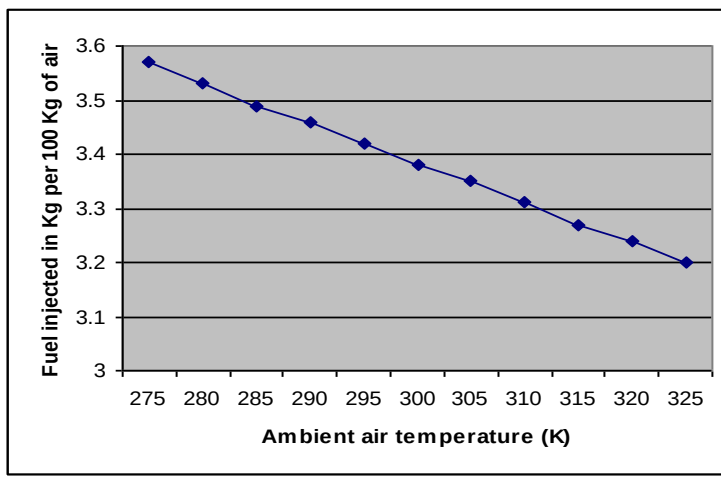

Figure 7: Change in fuel injected in the combustion chamber with a change in ambient air temperature.

For the design conditions if the TIT is fixed then, as the gas turbine inlet temperature will keep on increasing then the fuel requirement will decrease. But due to the increase in the ambient temperature the mass flow rate of the air to the compressor also decreases which leads to lesser work output and lesser efficiency (Figure 8). Inlet air cooling may bring the ambient air to the designed condition.

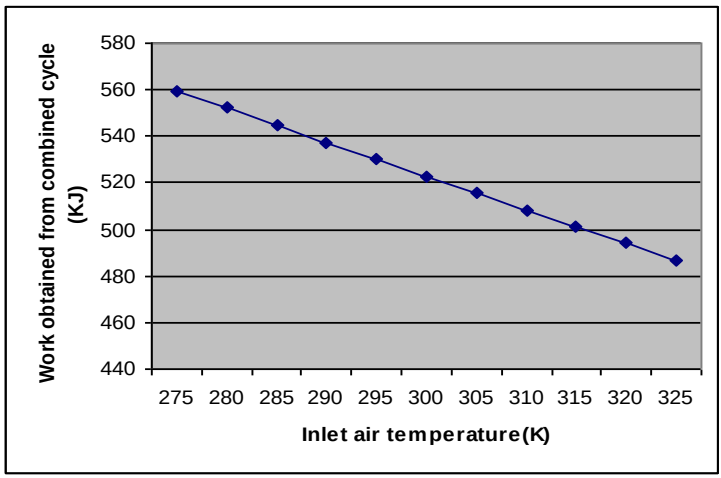

Figure 8: Change in work obtained from a combined cycle with a change in inlet air temperature.

An increase in ambient temperature reduced fuel consumption and simultaneously work output also decreased to a level that has a considerable impact on the performance of the combined cycle causing lower efficiency as shown in Figure 9. With the increase in the inlet or ambient air temperature, the fuel requirement of the combined cycle decreases by 11%, and similarly work output of the cycle also decreases by 14% which has more impact on cycle efficiency, thus, causing a reduction in combined cycle efficiency (Figure 9).

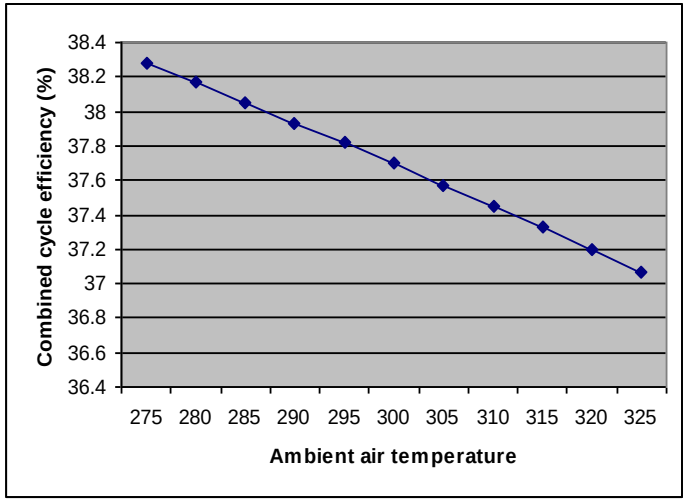

Figure 9: Change in combined cycle efficiency with a change in ambient air temperature.

Highest TIT is decided by the metallurgical stress-bearing capacity of turbine blade material. With the higher TIT larger is the fuel consumption and work obtained in the cycle and combined cycle efficiency also increases. For designing the gas turbine the compression ratio is kept between the maximum work and maximum efficiency. Increasing the TIT increases combined cycle efficiency. Benefit of increasing a lower temperature is more and it decreases with TIT. It is so due to increase in the consumption of fuel to attain higher TIT. After a turbine inlet temperature of 1700 K not much increase in efficiency is observed.

A significant increase in combined cyclic efficiency was noted with a varying inlet temperature of flue gases in the turbine. Higher flue gas temperature at turbine inlet results in larger work output and hence the performance increases as well. But as the inlet temperature of flue gases reaches a value 1700K no further significant change in combined cycle performance was achieved.

The energy analysis is not sufficient for accurate prediction of combined cycle power plant performance. Energy analysis gives only an idea about the efficiency and work obtained from the cycle. It does not tell us about the major sites of energy losses. For the complete analysis exergy analysis is also required. The present work makes a base for the exergy analysis.

Conclusion

In present work, waste heat of gas turbine was used to generate electricity by implementing heat recovery steam generator. Fuel consumption of power plant can be reduced by increasing compression ratio keeping inlet temperature of gas turbine constant, which in turn, decreases the gas turbine outlet temperature resulting less available heat for steam generator. With increase in compressor ratio, the cycle's work output and efficiency increases significantly and reaches to a maximum value at compression ratio 18 bar. It was observed that an increase in pressure ratio lower the fuel consumption and thus less energy consumption was occurred thus increased cyclic efficiency was obtained. Inlet ambient air temperature has adverse effect on cycle's efficiency and should be kept below 270 K. Turbine inlet temperature has remarkable effect on cycle's efficiency. It was observed that when turbine inlet temperature reaches to 1500 K then cycle's efficiency and work output increases effectively and from results it is clear that cycle reaches to maximum efficiency at 1700 K.

References

[1] Y. S. H. Najjar & M. Akyurt, "Combined cycle with gas turbine engine", *Heat Recovery Systems & CHP,* vol 14, no. 2, pp 93-103, 1994.

[2] J.H. Horlock, "Combined power plants present, and future", *Joumal of Engineering for Gas Turbines and Power, vol.* 117, pp 608-616,1995.

[3] M. De Lucia, C. Lanfranchi, & V. Boggio, "Benefits of compressor inlet air cooling for gas turbine cogeneration plants", *ASME Journal for Gas Turbine and Power,* vol. 118, pp 598-603, 1996.

[4] M. Mostafavi, A. Alaktiwi & B. Agnew, "Thermodynamic analysis of combined open-cycle-twin-shaft gas turbine (Brayton cycle) and exhaust gas operated absorption refrigeration unit", *Applied Thermal Engineering,* vol. 18, pp 847-856, 1998.

[5] T. Heppenstall, "Advanced gas turbine cycles for power generation: a critical review", *Applied Thermal Engineering,* vol. 18, pp 837-846, 1998.

[6] P.A. Pilavachi, "Power generation with gas turbine systems and combined heat and power", *Applied Thermal Engineering,* vol. 20, pp 1421-1429, 2000.

[7] Yousef S. H. Najjar, "Effcient use of energy by utilizing gas turbine combined systems," *Applied Thermal Engineering,* vol. 21, no. 4, pp 407-438, 2001.

[8] Manuel Valdés, M Dolores Durán nd Antonio Rovira, " Thermoeconomic optimization of combined cycle gas turbine power plants using genetic algorithms", *Applied Thermal Engineering,* vol. 23, no. 17, pp 2169-2182, 2003.

[9] A. Khaliq & S.C. Kaushik, "Second-law based thermodynamic analysis of Brayton/Rankine combined power cycle with reheat", *Applied Energy*, vol. 78, pp 79–197, 2004.

[10] A. Khaliq & S.C. Kaushik, "Thermodynamic performance evaluation of combustion gas turbine cogeneration system with reheat", *Applied Thermal Engineering*, vol. 24, pp 1785–1795, 2004.

[11] Y.S.Najjar, "Augmentation of gas turbine performance using air coolers", *Applied Thermal Engineering*, vol. 24, pp 415-429, 2004.

[12] E.Kakaras,"Compressor intake air cooling in gas turbine plants", *International Energy Journal*, vol. 29, pp 12-15, 2004.

[13] E.Kakaras, A. Doukelis, A. Prelipceanu, S. Karellas, "Inlet air cooling methods for gas turbine based power plants" - *ASME Journal for Gas Turbine and Power*, vol. 128, pp 312-317, 2006.

[14] T. Korakianitis, J. Grantstrom, P. Wassingho & Aristide F. Massardo, "Parametric performance of combined- cogeneration power plants with various power and efficiency enhancement", *Journal of Engineering for Gas Turbine and Power*, vol. 127, pp 65-72, 2005

[15] Kousuke Nishida, Toshimi Takagi & Shinichi Kinoshita, "Regenerative steam-injection gas-turbine systems", *Applied Energy*, vol. 81, pp 231–246, 2005.

[16] S. Boonnasa, P. Namprakai & T. Muangnapoh, "Performance improvement of the combined power cycle power plant by intake air cooling using an absorption chiller" – *Energy*, vol. *31*, pp 2036-2046, 2006.

[17] C.J. Butcher & B.V. Reddy, "Second law analysis of a waste heat recovery based power generation system", *International Journal of Heat and Mass Transfer*, vol. 50, pp 2355–2363, 2007.

[18] Osamah M. AL-Hawaja & Hamad AL-Mutairi, "A combined power cycle with absorption air conditioning", *Energy*, vol. 32, pp 971–982, 2007.

[19] A.L.Polyzakis, C.Koroneos & G.Xydis, "Optimum gas turbine cycle power plant", *Energy Conversion and Management*, vol. 49, pp 551-563, 2008.

[20] Iacopo Vaja, Agostino Gambarotta, "Internal Combustion Engine (ICE) bottoming with organic Rankine cycles (ORCs)," *Energy*, vol. 35, pp 1084-1093, 2010.

[21] E. Godoy, S.J. Benz and N.J. Scenna, "A strategy for the economic optimization of combined cycle gas turbine power plant by taking advantage of useful thermodynamic relationships", *Applied Thermal Engineering*, vol. 31, no. 5, pp 852-871, 2011,

[22] Sipeng Zhu, Kangyao Deng, Shuan Qu, "Energy and exergy analyses of a bottoming Rankine cycle for engine exhaust heat recovery," *Energy*, vol. 58, pp. 448-457, 2013.

[23] S.Martinez, G.Michaux, P. Salagnac, J.L. Bouvier, "Micro-combined

heat and power systems (micro-CHP) based on renewable energy sources", *Energy Convers. Manag*, vol. 154, pp 262-285, 2017.

[24] M.N. Khan , I.Tilili, " New advancement of high performance for a combined cycle power plant: Thermodynamic analysis", *Case Stusy in Thermal Engineering*, vol. 12, pp 166-175, 2018.

[25] J. Kotowicz, M. Brzeczek "Comprehensive multivariable analysis of the possibility of an increase in the electrical efficiency of a modern combined cycle power plant with and without a CO_2 capture and compression installations study", *Energy*, vol. 175, pp 1100–1120, 2019.

[26] Mohammad Hossein Ahmadi, Mahyar Ghazvini, Milad Sadeghzadeh, Mohammad Alhuyi Nazari, Ravinder Kumar, Abbas Naeimi, Tingzhen Ming, "*Solar power technology for electricity generation: A critical review*", Energy Sci Eng., vol. 6, pp 1–22, 2018.

[27] Ravinder Kumar, Ravindra Jilte, Mohammad H. Ahmadi, Rajneesh Kaushal, "A simulation model for thermal performance prediction of a coal-fired power plant", *International Journal of Low-Carbon Technologies*, vol. 14, pp 1–13, 2019.

[28] Abbas Naeimi, Mokhtar Bidi, Mohammad Hossein Ahmadi, Ravinder Kumar, Milad Sadeghzadeh, Mohammad Alhuyi Nazari, "Design and exergy analysis of waste heat recovery system and gas engine for power generation in Tehran cement factory", *Thermal Science and Engineering Progress*, vol. 9, pp 299–307, 2019.

[29] A. Boretti, S. Al-Zubaidy, "A case study on combined cycle power plant integrated with solar energy in Trinidad and Tobago", *Sustain. Energy Technol. Assess*, vol. 32, pp 100–110, 2019.

[30] A. Kumar, K.C. Nikam, A.K.Bahura, "An Exergy analysis of a 250MW Thermal Power Plant", *Renewable energy Research and Applications*, vol. 1 pp 197-204, 2020.

[31] D. Mugabe, L. Elbakidze, and G. Zaynutdinova, "Elasticity of substitution and technical efficiency: evidence from the US electricity generation," *Applied Economics*, vol. 52, pp. 1789–1805, 2020.

Electrospinning, Preparation and Characterization of Polyvinylidene Fluoride / Pectin Electrospun Loaded with Benzalkonium Chloride as a Drug Reservoirs

Mohd Syahir Anwar Hamzah, Celine Ng, Jumadi Abdul Sukor
Faculty on Engineering Technology, Universiti Tun Hussein Onn Malaysia, Pagoh Higher Education Hub, 84600 Pagoh, Johor, Malaysia.

Kamarul Syazwan Mohd Ali
Abdul Muaz Food Enterprise, 20-A, Pusat Perniagaan Benut, Jalan Pontian, 82100 Benut, Johor, Malaysia.

*Nadirul Hasraf Mat Nayan**
Oases Integrated Group (OIG), Universiti Tun Hussein Onn Malaysia, 86400 Parit Raja, Johor, Malaysia.
**nadirul@uthm.edu.my*

ABSTRACT

Porous nanofiber electrospun of polyvinylidene fluoride (PVDF)/pectin was successfully developed using electrospinning method containing benzalkonium chloride (BAC) as a drug model for the controlled drug delivery system assessment. The electrospun was tested for its mechanical, morphological, and wettability properties. Scanning electron microscope (SEM) micrograph demonstrated that the smooth surfaces of nanofibers morphology had achieved up to 2 wt% pectin inclusion with optimum fiber diameter, 143 ± 1.4 nm. The optimized scaffold PVDF/Pectin showed that the reduction of mechanical integrity and optimum value of tensile strength, modulus strength, and elongation at break were 5.98 ± 0.17 MPa, 16.82 ± 0.10 MPa, and 79.3 ± 1.3% MPa. Water contact angle analysis and degree of swelling suggested that inclusion of pectin had enhanced the wettability properties of hydrophobic PVDF electrospun with highest swelling capacity achieved of 78.9 ± 1.7%. The in vitro drug release tests using BAC, which was released from the hybrid electrospun nanofibers, achieved prolonged release profile due to elimination of the uncontrollable initial burst release.

ISSN 1823-5514, eISSN 2550-164X
Received for review: 2020-03-20
Accepted for publication: 2020-12-10
Published: 2021-01-15

Kinetic release study from Higuchi Model and Korsmeyer-Peppas further validates that the drug release mechanism is only influenced by the diffusion factor. The present study indicates the potential of PVDF/pectin electrospun nanofibers to be exploited as a tool for sustainable drug delivery system.

Keywords: *Electrospinning; drug delivery; polyvinylidene fluoride; pectin; benzalkonium chloride.*

Introduction

Sustained release of a drug delivery system (DDS) has gained great attention as an alternative solution to reduce uncontrollable initial burst release of conventional DDS. This system will improve oscillation of the systemic drug concentration and reduce the potential of under or overdosing cases. In this case, sustained release DDS provides high therapeutic efficiency with minimum side effects by prolonged release duration of loaded drug with constant systemic concentration [1]. Electrospun nanofibers membrane has great potential as drug carriers due to its unique characteristics such as a large surface area to volume ratio with control micro to nano-meter sizes of fiber. Besides, studies have shown that a wide range of polymer can be used in electrospinning process and drugs ranging from antibiotics and anticancer agents to proteins, aptamer, DNA, and RNA which have been incorporated into electrospun fibers [2]. These features provide a promising structure for high encapsulation of targeted drugs and potentially achieve controlled loading/release profile [3-4].

Polyvinylidene fluoride (PVDF) is a unique chemically inert thermoplastic fluoropolymer synthesized by the polymerization of vinylidene fluoride that exhibits strong piezoelectric properties, chemical resistance, biocompatibility, transparent, and widely used in biomedical applications as biosensor, smart DDS, and tissue engineering [5-6]. This material also is easily processed to generate well defined nanofibers which can then be used for DDS and tissue engineering studies. However, PVDF has poor reactive side-chain with hydrophobic characteristic which can cause inflammatory effect on host cell/tissue and less capable to act as drug carrier without the aid from bioactive, biomacromolecule, or drugs [7]. For that reason, some modifications and improvement of those particular properties are technically crucial.

Pectin is an underrated polysaccharide based which has been widely used in conjunction with certain polymers or other biomaterials in drug delivery system and tissue engineering. These polysaccharides contain –OH and –COOH chemicals groups at the polymer surface and subject to calcium induced gelation results in the formation of egg box like structures that can

help in modulating the fate of surface-attached bioactive components and cells as illustrated in Figure 1 [8-10]. The correlation between pectin in the polymer backbone has shown that to increase density of active site, surface free energy and water absorption content are more suitable for drug, biomolecule, and cell attachment [11-13].

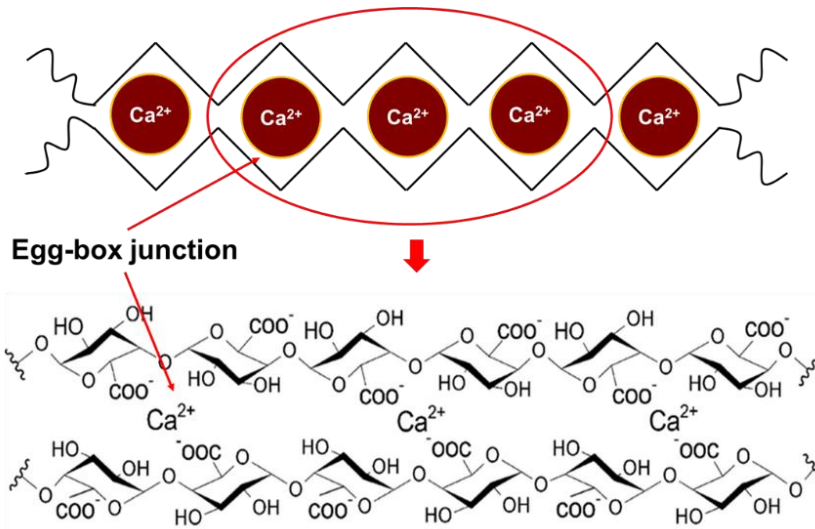

Figure 1: Illustration of 'egg-box' model of pectin.

Currently, no experimental works have utilized PVDF and pectin combination as nanodrug carrier for bioregenerative medicine applications. Few studies reported on the combination of polysaccharide materials into PVDF electrospun. Most existing researches have focused on combining of PVDF with other materials such as hydroxyapatite (HA), fibrin, chitosan, collagen, bio-glass, graphene oxide (GO), polycaprolactone (PCL), polyvinyl alcohol (PVA), and gold (Au) [5,7,14]. Therefore, this study utilizes the electrospinning method to fabricate a hybrid single layer polymeric nanofiber using PVDF-Pectin solution and benzalkonium chloride (BAC) as model drugs. This study aims to address the potential of pectin on improving the wettability and sustainable drug release properties of PVDF electrospun. The polymer blends were characterized via tensile test, morphological analysis, water contact angle (WCA), degree of swelling, and in vitro drug release profiles. This works will provide a new knowledge on the capability of the polymer blend materials application in drug delivery system.

Materials and Methods

Fabrication of PVDF-Pectin Electrospun

10% (w/v) PVDF polymer (Mw=89,000 g/mol, Sigma) solution was prepared in dimethylformamide (DMF) solution at 50 °C under magnetic stirring until a clear polymer solution was formed. Pectin (apple based, Sigma) solutions (1, 2, and 3 wt% diluted in acetic acid solution) was added slowly into the prepared PVDF solution forming homogenous PVDF/Pectin polymer solution. The copolymer solution was fed into a 5-mL disposable plastic syringe with a gauge needle size 0.7 mm. The syringe was loaded onto an electrospinning device with horizontal set up (eSpinner NF-COEN/II, Birooni Saintifik) that delivered the polymer to a collector panel at a flow rate of 1.5 mL/h with voltage 15 kV. The distance between the syringe tip and the collector was 10 cm. All spinning experiments were conducted at 23±2 °C as illustrated in Figure 2.

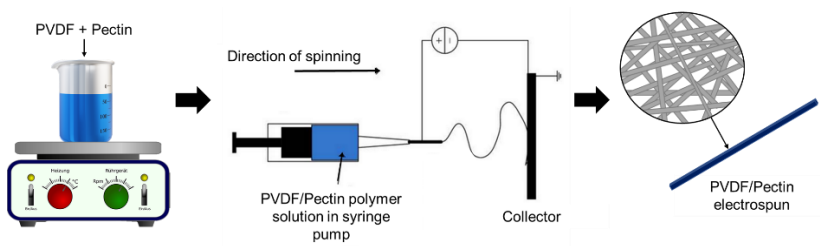

Figure 2: The schematic illustration of fabricating PVDF/Pectin electrospun membranes.

Scanning Electron Microscope

The electrospun produced was subjected to morphology analysis using Variable-Pressure Scanning Electron Microscope (VP-SEM, JEOL, USA) at an accelerating voltage of 10 kV. The SEM micrograph was used to determine the mean diameter of the electrospun nanofibers by using Image-J analysis

Mechanical Testing

The tensile test of the electrospun samples was assessed using a computer controlled Instron machine according to ASTM D882. The test was performed at a strain rate of 10 mm/min with load strength of 5kN at room temperature to determine tensile strength, modulus strength, and elongation at break properties of the samples. The measurement was performed triplicate and the average value was calculated.

Surface Wettability

Surface wettability was determined by measuring water contact angle using contact angle goniometer (VCA Optima system, AST Products USA) with droplets of each medium on the scaffolds. 5 µl of medium was gently dropped on the surface of scaffolds using a micro syringe and released from 1 cm above the surface to minimize the inconsistency between each measurement. The angle between scaffold surface and tangent line was measured. The measurement was performed five times at different locations of the membrane and the average value was calculated.

Degree of Swelling

The samples were dried in an oven at 70 °C for 24 h until constant weight to eliminate water before being placed in a phosphate buffered saline (PBS) for 24 h for degree of swelling studied [14]. The percentage of water adsorption (degree of swelling) was calculated using the formula below:

$$Degree\ of\ swelling = \frac{W_t - W_0}{W_t} x100\% \quad (1)$$

in which w_t represents the weight of swollen nanofiber at predetermined time and w^o is the initial weight of the nanofiber. The measurement was performed triplicate for each samples.

In-vitro Drug Loading and Release Profile

The electrospun samples were loaded with 0.14% benzalkonium chloride (BAC) for 24 h and dried at room temperature [15]. Then, the dried samples were immersed into phosphate buffer saline (PBS) at 37 °C for 24 h. The absorbance of the samples was observed at 272 nm using UV-vis (Thermo Scientific, Genesys 10S UV-VIS) to evaluate the drug release pattern. The mechanism was also studied with several kinetic models [16]:

Zero-Order Kinetics Model:

$$Q_t = Q_0 + K_0 t \quad (2)$$

Higuchi Model:

$$Q = K_H \times t^{1/2} \quad (3)$$

Korsmeyer-Pepas Model:

$$\frac{M_t}{M_o} = Kt^n \quad (4)$$

where Q_t represents the amount of drug dissolved in time (t), Q_o is the initial amount of drug in the solution, and K_o is the zero-order release constant. Meanwhile, Q indicates the amount of drug released in time, K_H is the Higuchi dissolution constant, and $t^{½}$ is the square root of time. Finally, M_t is the amount of drug dissolved as a function of time, M_o is the total amount of drugs being released, and t^n is an account for the log time measured as a result of the dissolution process. The measurement was performed triplicate for each sample.

Results and Discussion

Electrospinning Process

The incorporation of pectin into PVDF electrospinning solution directly influenced the nanofiber structure formation. Figure 3 exhibits the SEM micrographs of different electrospun nanofibers in this study. It was observed that the bead-free nanofibers were obtained for PVDF/pectin solution with slight increase in the average diameter of nanofibers up to 2 wt% pectin inclusion and reduces at 3 wt% as the excess of pectin has increased the viscosity of the polymer solution as shown in Table 1. However, due to ionic functionalities group from the polyanion of pectin, the blended polymer solutions had achieved minimal electrical conductivity for nanofibre formation although PVDF concentration was reduced. The average diameter of electrospun was ascertained to increase in correspondence to the polymer solution concentration [15, 17]. As previously mentioned, the incorporation of more than 3 wt% of pectin to PVDF solution further hindered the electrospinning process as the defective effect can be seen in Figure 3(d). The nanofiber morphology starts to lose its structure integrity and uniformity at higher inclusion of polysaccharides. A possible reason is that the increase of pectin has triggered more repulsive force among negative charge that disrupts the chain entanglement between pectin and PVDF in the polymer solution. The insufficient chain entanglements result in an unstable jet formation during the electrospinning process which causes beaded nanofiber electrospun [18].

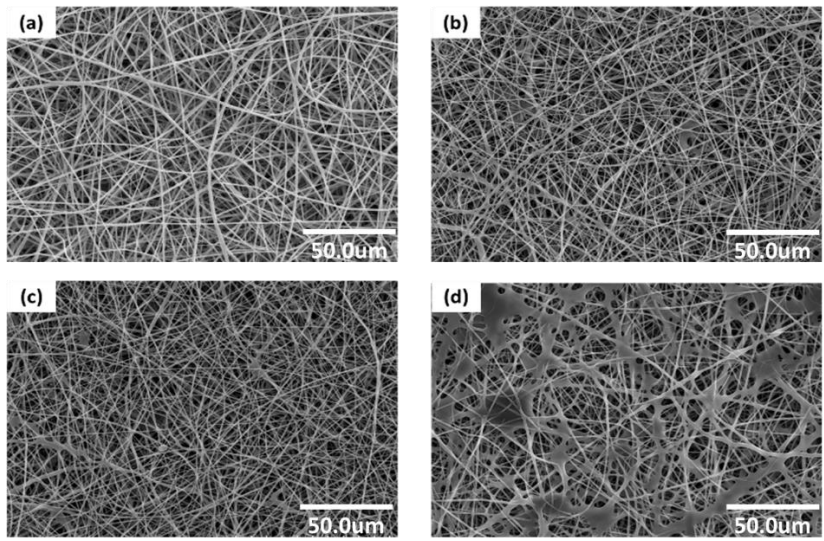

Figure 3: SEM micrograph of; (a) PVDF/0Pectin, (b) PVDF/1Pectin, (c) PVDF/2Pectin and (d) PVDF/3Pectin.

Mechanical Properties: Tensile Test

Table 1 shows the results from the tensile test done onto the PVDF/Pectin electrospun at different percentage. The results show that the incorporation of pectin into the PVDF polymer solution has slightly reduced the mechanical properties of the electrospun. As compared to the neat PVDF eletrospun, the tensile strength of PVDF/1Pectin is reduced by ~2.53% from 6.33 to 6.17 MPa, the modulus strength is reduced by ~7.14% from 19.05 to 17.69 MPa, while the elongation at break is increased by ~25.27% from 63.3% to 79.3%. The inclusion pectin has introduced an egg-box structure on the PVDF monomer which contributes to an increase of interfacial shear stress between both polymers. This likely has reduced the tensile properties [8,18]. On the other hand, introducing the amide side chain from pectin has contributed to stretchable enabled by the interchain hydrogen bond which maximized the tensile stress to 79.3±1.3% for PVDF/2Pectin [19]. Higher inclusion of pectin also has reduced the mechanical properties of PVDF/Pectin electrospun due to loss of structural integrity as shown in Figure 3(d). Overall, the PVDF/Pectin electrospun mechanical properties meets the requirement for soft collagenous tissues application for cartilage, skin, nerve, and cornea treatment at the scaffold tensile strength around 1 to 10 MPa [3,12,15].

Table 1: Mechanical properties and fibre diameter of electrospun

Sample	Tensile Strength (MPa)	Modulus Strength (MPa)	Elongation at break (%)	Diameter (nm)
PVDF/0Pec	6.33±0.12	19.05±0.33	63.3±1.2	133±1.9
PVDF/1Pec	6.17±0.25	17.69±0.19	76.9±1.7	138±2.2
PVDF/2Pec	5.98±0.17	15.82±0.10	79.3±1.3	143±1.4
PVDF/3Pec	4.16±0.19	8.45±0.21	58.9±1.1	129±0.7

Hydrophilicity Properties Analysis

The water contact angle analysis was used to investigate the wetting profile of electrospun surface chemistry on liquid contact. Table 2 demonstrates that the inclusion of pectin in the polymer solution reduces the water contact angle by altering the surface from hydrophobic to hydrophilic condition. Pectin consists of –OH and –COOH (ionized functional groups) transforms the polarity surface of electrospun which gives water interaction. Besides, previous studies also reported that as the size of the nanofibers decreased, the porosity increased as a result from air pocket effects that contribute to higher water contact angle of the electrospun surface [20]. Furthermore, the hydrophobic surfaces properties will greatly affect the swelling potential of electrospun by reducing the free surface energy for liquid interaction with electrospun fibers [21-22] as tabulated in Table 2. Swelling capacity is important in order to allow high loading capacity of drug molecules and migration of new cells during healing process. Swelling of the electrospun increased up to ~208.20% compared to that of neat PVDF electrospun when 2 wt% of pectin was added in the polymer solution. This owes to the hydrophilicity characteristic of pectin forming hydrogen bonds with water molecules spontaneously as the Gibbs free energy is a negative value [18,23].

Reduction of PVDF/3Pectin swelling percentage is subjected to the morphological defect on the nanofiber which probably enhances the surface roughness and leads to low water drop-material contact area. Considering that the purpose of adding pectin to improve the hydrophilicity properties of PVDF electrospun has successfully achieved up to 2 wt%, the PVDF/2Pectin was selected for further testing as it has balanced physical and mechanical properties.

Table 2: Water contact angle and swelling percentage of electrospun samples.

Sample	Water Contact Angle (°)	Degree of Swelling (%)
PVDF/0Pectin	103.9±2.6	25.6±1.9
PVDF/1Pectin	55.6±1.3	67.8±1.5
PVDF/2Pectin	43.2±2.1	78.9±1.7
PVDF/3Pectin	67.1±2.7	50.2±1.4

In-Vitro Controlled Drug Release

Figure 4 illustrates the cumulative drug release profile of PVDF/0Pectin and PVDF/2Pectin electrospun nanofibers. The early burst release pattern at early release for neat PVDF electrospun makes it inconvenient to be used as a delivery device for drugs or biomolecules. The initial bolus released leads to higher initial drug delivery which will reduce the lifetime effectiveness of the device. Besides, the burst release effects will cause systemic toxicity and wounded area, shorten drugs half-life in vivo, not economically friendly, and patient will require more frequent dosing [24-25]. This condition may due to the surface characteristic of the neat PVDF electrospun that does not fully support host-drug interactions. Inclusion of pectin in polymer solution reduces the burst release phenomenon as the charged density holds the target drugs and prolongs the release towards body system. The ability to form 'egg-box' like structure due to gelling effect has prevented direct hydrolytic degradation of host/drug interaction of PVDF/2Pectin [9-10]. Therefore, the carrier systems were significantly improved to maintain sustainable drug delivery system. Kinetic modeling of drug release was calculated using the concentration release of the hydrogel and recorded in Table 3. The PVDF/2Pectin electrospun treated is fitted mostly on the Higuchi Model as compared to Zero-Order. This shows that the release pattern is not at constant release as stated by the perfect theory of Zero-Order. However, referring to the Higuchi Model, the mechanism of drug release from the matrix follows the diffusion-controlled system. Based on the Korsmeyer-Peppas theory, n=0.248, it reveals that the release pattern is following the Fickian's diffusion theory. These theories explain that the drug release from the hybrid electrospun matrix is influenced by the diffusion factor only [16, 26].

Table 3: Kinetic drug release profile of PVDF/0Pectin and PVDF/2Pectin electrospuns

Sample	Zero-order		Higuchi		Koshmeyer-Peppas
	R^2	K_O	r^2	K_H	N
PVDF/0Pectin	0.454	1.303	0.627	8.285	0.319
PVDF/2Pectin	0.817	1.547	0.930	10.100	0.248

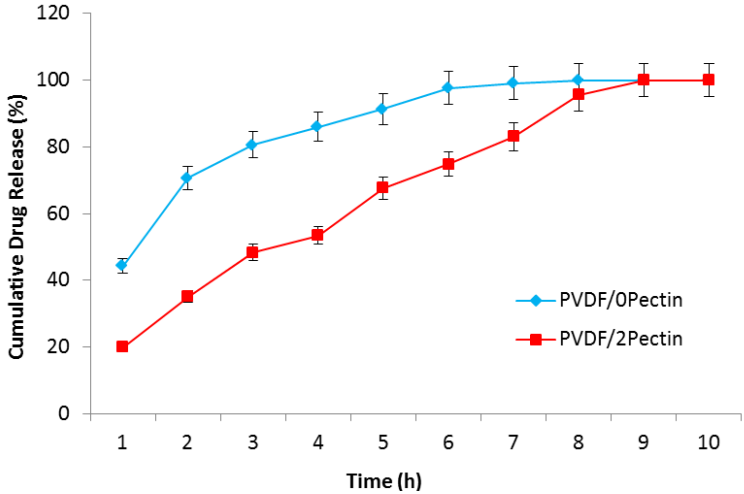

Figure 4: Cumulutative drug release for PVDF/0Pectin and PVDF/2Pectin electrospun samples.

Conclusion

This paper has studied the electrospinning of PVDF/Pectin solutions with different pectin concentration to see its effects on the morphology, mechanical, and wettability of electrospun samples. The PVDF/Pectin electrospun with up to 3 wt% pectin inclusion has successfully produced nanofibers as indicated from the SEM micrograph. However, the increase of pectin concentration of more than 2 wt% leads to bead formations due to the unstable jet formation resulting from viscous polymer solution. The mechanical integrity of the PVDF/Pectin electrospun was slightly reduced at an acceptable amount of tensile strength ranging from 6.17 to 4.16 MPa. Water contact angle and swelling percentage indicate that the inclusion of pectin has improved the hydrophilicity of the electrospun by introducing hydrophilic monomer on the polymer chain such as -OH and -COOH. Based on these findings, PVDF/2Pectin electrospun is suggested to be the best formulation. Further analysis shows that the incorporation of pectin has reduced the burst release effect and prolong drug release capabilities. Over and above, results from the Higuchi Model and Korsmeyer-Peppas Model prove that the factor for drug release is only influenced by the diffusion factor. This gives a decent sign for more upcoming analysis of this composite scaffold especially in vivo drug kinetic release study.

Acknowledgements

The authors would like to express the deepest appreciation to the Ministry of Education Malaysia (MOE) through the Fundamental Research Grant Scheme (FRGS/1/2019/TK10/UTHM/03/1, FRGS-Vote number K220) and the Malaysia Technical University Network Grant Scheme (MTUN-Vote number K124 and K243), as well as Universiti Tun Hussein Onn Malaysia (UTHM) through the Geran Penyelidikan Pascasiswazah (GPPS-Vote number H458) for funding this research.

References

[1] Xu, Y., Li, J.J., Yu, D.G., Williams, G.R., Yang, J.H. and Wang, X., "Influence of the drug distribution in electrospun gliadin fibers on drug-release behavior," *European Journal of Pharmaceutical Sciences*, vol. *106*, pp 422-430, 2017.

[2] Hu, X., Liu, S., Zhou, G., Huang, Y., Xie, Z. and Jing, X., "Electrospinning of polymeric nanofibers for drug delivery applications," *Journal of controlled release*, vol. *185*, pp 12-21, 2014.

[3] Xie, J., MacEwan, M.R., Schwartz, A.G. and Xia, Y., "Electrospun nanofibers for neural tissue engineering," *Nanoscale*, vol. *2*, no. 1, pp 35-44, 2010.

[4] Zhang, X., Tang, K. and Zheng, X., "Electrospinning and crosslinking of COL/PVA nanofiber-microsphere containing salicylic acid for drug delivery," *Journal of Bionic Engineering*, vol. *13*, no. 1, pp 143-149, 2016.

[5] Su, C., Li, Y., Dai, Y., Gao, F., Tang, K. and Cao, H., "Fabrication of three-dimensional superhydrophobic membranes with high porosity via simultaneous electrospraying and electrospinning," *Materials Letters*, vol. *170*, pp 67-71, 2016.

[6] Motamedi, A.S., Mirzadeh, H., Hajiesmaeilbaigi, F., Bagheri-Khoulenjani, S. and Shokrgozar, M.A., "Piezoelectric electrospun nanocomposite comprising Au NPs/PVDF for nerve tissue engineering," *Journal of Biomedical Materials Research Part A*, vol. *105*, no. 7, pp 1984-1993, 2017.

[7] Mouzakis, D.E., "Biomedical Polymer Composites and Applications," *Edited by Sabu Thomas, Kuruvilla Joseph, SK Malhotra*, 2014.

[8] Pacheco, D.P., Marcello, E., Bloise, N., Sacchetti, A., Brenna, E., Visai, L. and Petrini, P., "Design of Multifunctional Polysaccharides for Biomedical Applications: A Critical Review," *Current Organic Chemistry*, vol. *22*, no. 12, pp 1222-1236, 2018.

[9] Kaur, P., Garg, T., Rath, G. and Goyal, A.K., "In situ nasal gel drug delivery: A novel approach for brain targeting through the mucosal membrane," *Artificial cells, nanomedicine, and biotechnology*, vol. *44*. No. 4, pp 1167-1176, 2016.

[10] Giri, T.K., Ghosh, B. and Patra, F., "Chitosan-Based Nanoparticulate System for Pulmonary Drug Delivery," *Polysaccharide based Nano-Biocarrier in Drug Delivery*, CRC Press, 2018.

[11] Lin, H.Y. and Yeh, C.T., "Controlled release of pentoxifylline from porous chitosan-pectin scaffolds," *Drug delivery*, vol. *17*, no. 5, pp 313-321, 2010.

[12] Numata, K., Yamazaki, S., Katashima, T., Chuah, J.A., Naga, N. and Sakai, T., "Silk-pectin hydrogel with superior mechanical properties, biodegradability, and biocompatibility," *Macromolecular bioscience*, vol. *14*, no. 6, pp 799-806, 2014.

[13] Lin, H.Y., Chen, H.H., Chang, S.H. and Ni, T.S., "Pectin-chitosan-PVA nanofibrous scaffold made by electrospinning and its potential use as a skin tissue scaffold," *Journal of Biomaterials Science, Polymer Edition*, vol. *24*, no. 4, pp 470-484, 2013.

[14] Hamzah, M.S.A., Austad, A., Razak, S.I.A. and Nayan, N.H.M., "Tensile and wettability properties of electrospun polycaprolactone coated with pectin/polyaniline composite for drug delivery application," *International Journal of Structural Integrity*, vol. 10, no. 5, pp 704-713, 2019.

[15] Foong, C.Y., Hamzah, M.S.A., Razak, S.I.A., Saidin, S. and Nayan, N.H.M.," Influence of poly (lactic acid) layer on the physical and antibacterial properties of dry bacterial cellulose sheet for potential acute wound healing materials," *Fibers and Polymers*, vol. *19*, no. 2, pp 263-271, 2018.

[16] Singhvi, G. and Singh, M., "In-vitro drug release characterization models," *International Journal of Pharmaceutical Studies Research*, vol. *2*, no. 1, pp 77-84, 2011.

[17] Baji, A., Mai, Y. W., Wong, S. C., Abtahi, M., and Chen, P." Electrospinning of polymer nanofibers: effects on oriented morphology, structures and tensile properties," *Composites science and technology*, vol. 70, no. 5, pp 703-718, 2010.

[18] Akinalan Balik, B., and Argin, S., "Role of rheology on the formation of Nanofibers from pectin and polyethylene oxide blends," *Journal of Applied Polymer Science*, vol. 137, no. 3, pp 48294, 2020.

[19] Jeong, J. S., Moon, J. S., Jeon, S. Y., Park, J. H., Alegaonkar, P. S., and Yoo, J. B., "Mechanical properties of electrospun PVA/MWNTs composite nanofibers," *Thin Solid Films*, vol. 515, no. 12, pp 5136-5141, 2007.

[20] Hekmati, A.H., Khenoussi, N., Nouali, H., Patarin, J. and Drean, J.Y. "Effect of nanofiber diameter on water absorption properties and pore size of polyamide-6 electrospun nanoweb," *Textile Research Journal*, vol. *84*, no. 19, pp 2045-2055, 2014.

[21] Szewczyk, P., Ura, D., Metwally, S., Knapczyk-Korczak, J., Gajek, M., Marzec, M., Bernasik, A. and Stachewicz, U., "Roughness and fiber fraction dominated wetting of electrospun fiber-based porous meshes," *Polymers*, vol. 11, no. 1, pp 34, 2019.

[22] Haider, A., Haider, S. and Kang, I.K., "A comprehensive review summarizing the effect of electrospinning parameters and potential applications of nanofibers in biomedical and biotechnology," *Arabian Journal of Chemistry*, vol. 11, no. 8, pp 1165-1188, 2018.

[23] Okutan, N., Terzi, P., and Altay, F., "Affecting parameters on electrospinning process and characterization of electrospun gelatin nanofibers," *Food Hydrocolloids*, vol. 39, pp 19-26, 2014.

[24] Fenton, O.S., Olafson, K.N., Pillai, P.S., Mitchell, M.J. and Langer, R., "Advances in biomaterials for drug delivery," *Advanced Materials*, vol. *30*, no. 29, pp 1705328, 2018.

[25] Lee, E.J., Huh, B.K., Kim, S.N., Lee, J.Y., Park, C.G., Mikos, A.G. and Choy, Y.B., "Application of materials as medical devices with localized drug delivery capabilities for enhanced wound repair," *Progress in materials science*, vol. *89*, pp 392-410, 2017.

[26] Li, S., Jasim, A., Zhao, W., Fu, L., Ullah, M. W., Shi, Z., and Yang, G., "Fabrication of pH-electroactive bacterial cellulose/polyaniline hydrogel for the development of a controlled drug release system," *ES Materials & Manufacturing*, vol. *1*, no. 16, pp 41-49, 2018.

A Multi-Objective Optimization of Output Parameters of a Single Cylinder Diesel Engine Running Methyl Esters and Different Additives: Taguchi-Fuzzy Based Approach

Santhosh Kumar Gugulothu,[1] Jibitesh Kumar Panda[2], G.R.K. Sastry[1], Sruti Ranjan Mishra[3]*
[1]Department of Mechanical Engineering, NIT Andhra Pradesh, India
[2]Department of Mechanical Engineering, Anurag University, Hyderabad , India
[3]Department of Chemistry, GIET Bhubaneswar, India
** jibiteshpanda90@gmail.com*

ABSTRACT

The continuous dependency on fossil fuels for energy requirements, transportation and power generation sectors the research has increased considerably on alternative source of fuel. Recently, it can be seen that Madhuca Indica Methyl Ester is gaining popularity due to its economical nature, the similarity with diesel's properties. The primary aim of this research is to implement blends of Machuca Indica biodiesel using two different additives, 2-EHN and triacetin in different ratios for investigating single cylinder direct injection diesel engine output. In the current analysis, a Taguchi optimisation technique based on fuzzy logic is used to find the optimal combination of emission and performance parameters in order to make prediction of optimal input blends. It shows that the cylinder pressure of the blends is always higher than diesel. Among all blends, BL2 possesses the highest cylinder pressure under various load conditions. In terms of brake thermal efficiency, Among the blends, BL2 and BL3 possess BTE 12%, and 11% more than plain diesel in full load respectively. At maximum load, BSFC of Blend 2, 3 and 6 are (25, 22.5, 20)% less than plain diesel. BL5, BL6 and BL7 produced 3%, 1% and 0.3% less NOx than diesel. It is seen that BL2, BL3 and BL5 had lowermost UHC emission of 34%, 27% and 26%

ISSN 1823-5514, eISSN 2550-164X
Received for review: 2020-04-02
Accepted for publication: 2020-12-11
Published: 2021-01-15

than pure diesel at maximum load. This multi-objective optimization technique shows that the blend BL6 have optimal MPCI value of 0.75.

Keywords: *Madhuca Indica Methyl Ester, Multi-objective optimization, Diesel additive, Performance, Emission.*

Introduction

Fossil fuel depletion and environmental deterioration are two major problems that the world is facing nowadays. Oil contributes the largest share of the world economy. Almost 180 million barrels of oils are used every day around the world [1]. According to Peak oil concept, the demand for oil will beat supply, and this gap will advance to the rise of the deficiency that will result in growing energy crisis between 2010 and 2050 [2, 3]. Sustainability of energy is one of the most important issues that can affect the politics and economy of the world [4-7]. Even if for power and heat applications conventional energy source is considered as the main source of energy, increased awareness regarding environmental problems and continuously depleting conventional resource is creating a need for alternative fuels which are non-conventional and from renewable sources [7-10]. Non-conventional fuel can be derived from thermoelectric, thermo ionic or thermochemical conversion and renewable energy sources. Since biodiesel is available in large volume, biodegradable and non-toxic is best suitable as a renewable fuel. Biodiesel due to its miscibility with both diesel and alcohol have been as appropriate for combinations with ethanol or methanol as alternate fuels for achieving better performance and lesser emission [11-13]. Several biofuel varieties have been tried and tested by the researchers and the industry lately. However, Madhuca Indica oil due to its economical nature, the similarity with diesel's properties, and large scale availability have caught the limelight. Therefore, a fuel with high oxygen content, high cetane number and low amount of additives could play a significant role for better output. In this experimental study, 20% (by volume) two different biodiesel were combined with both plain diesel and additives in the required quantity to make seven different blends for further analysis.

Only experimentation does not guarantee the optimal blend. Therefore we need to move towards statistical analysis for finding the best combination of parameters for optimizing cost and time factors. fuzzy optimization focusses on solving of the fuzzy model optimally through optimization tools and techniques based on the formulation of fuzzy information in terms of the possibility distribution function, their membership functions etc. The methods used by Taguchi are statistical methods created by him to enhance the manufactured goods quality. It gives us the optimal operating conditions

to reduce the influence of the noise factor. As we cannot control the noise we modify the factors within our control to reduce what we cannot control. This helps to reduce random fluctuation caused by noise factors and achieving more consistent product. According to Taguchi, S/N ratio is an assessment of performance stability of an output characteristic which considers both averages as well as variation. However, directly implementing this method is not possible in a multi-objective optimization problem. So, previously, other theories like desirability function approach, grey relation theory and utility theory [9] were combined with the Taguchi method. Practically, assigning individual responses priority weights are based on assumptions and it won't lead to an optimum solution and may lead to uncertainty. To solve this problem the fuzzy-based Taguchi method is adopted. It is understood that many research works were carried out using different biodiesel and its blends with additives by adopting fuel and engine modifications. Most of them reported that higher NOx emission in diesel engines when the blends were used as fuels. It is observed that no research work was carried out on the utilization of 2-Ethylhexyl nitrate, triacetin with the Machuca Indica oil in diesel engines, to study the NOx reduction. The primary objective of the research of next-generation alternative fuels are:

- To prepare the different blends using surfactant and characterize them as fuels for the engine.
- To analyses the combustion, the heat released, performance and emission characteristics of unmodified diesel engine by using blends of two different additives and Madhuca indica methyl ester.
- To analyses the different input blends and predict the optimum among them using Taguchi fuzzy optimization technique.

Methodology

Fuel selection

Biodiesel is an alternative for fossil fuels from 100% renewable sources. An important class of organic reactions, where an ester is altered into another ester by interchanging alkyl groups is termed as Transesterification. Equation (Transesterification Reaction) (1) is shown below:

$$RCOOR' + R"OH \leftrightarrow RCOOR" \quad + R'OH \tag{1}$$

The oils used in this study were neat diesel, Madhuca Indica Methyl Ester (MIME) of 99.9% purity [13]. 2-Ethylhexyl nitrate (2-EHN) is usually used with a blend of diesel to rise its cetane number [14, 15]. Triacetin is a highly oxygenated additive to fuel which can be used in the combustion

process. After producing the required amount of the methyl ester from vegetable oil and collecting necessary diesel additives, their properties were established according to IS test methods in Figure 1.

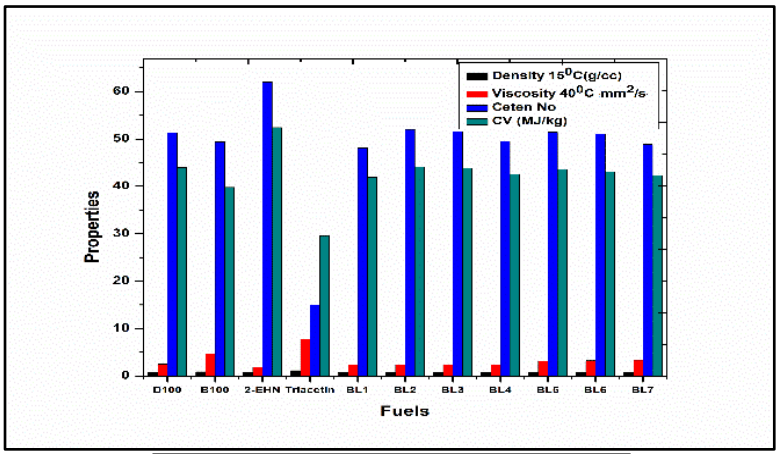

D100	100 % Diesel
BL1	(08+12) % Diesel, MIME
BL2	(04+08+16) % 2-EHN, Diesel, MIME
BL3	(06+08+14) % 2-EHN, Diesel, MIME
BL4	(08+08+12) % 2-EHN, Diesel, MIME
BL5	(04+08+16) % Triacetin, Diesel, MIME
BL6	(06+08+14) % Triacetin, Diesel, MIME
BL7	(08+08+12) % Triacetin, Diesel, MIME

Figure 1: Fuel properties.

Apparatus, Used (Performance and Emission)

The experimental setup uses water-cooled four-stroke, single-cylinder DI engine operating on diesel as shown in Figure 2 and the specification in Table 1. Different load conditions can be provided, i.e. (0, 3, 6, 9 and 12) kg on the engine, which leads the load range from no load to full load. The exhaust emission (CO, NOx, HC) for the experiment was analyzed (Testo-350). The instrument consists of the analyzer box and the control unit. The specifications of the gas analyzer are given below in Table 2. For the experiment, eddy current dynamometer was attached with the engine and allowed to run for 30 minutes using plain diesel for warming up.

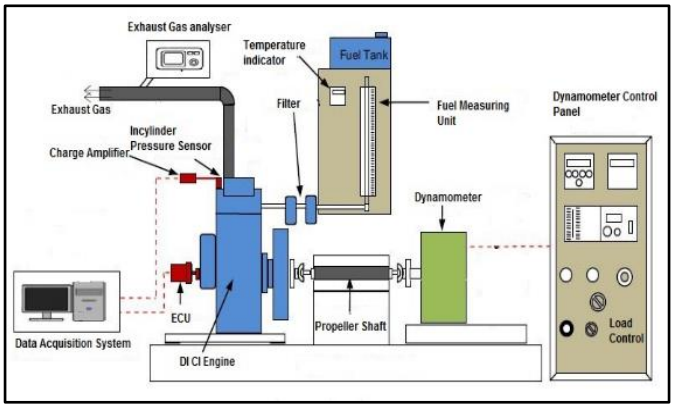

Figure 2: Experimental setup.

Table 1: Engine Specification

Make and type	Kirloskar, cylinder (One), Diesel (Four Stroke)
Engine type	CI Engine (Vertical Type)
Stroke length (mm)	110
Swept volume (CC)	661
C.R.(Compression ratio)	17.6
Power	3.5 kilowatts
Rated speed (RPM)	1500
Dynamometer	
Make	Power Mag
Type	Eddy current
Load measurement method	Strain Gauge
Maximum load	12-kilogram
Cooling	Water

Table 2: Precision for Testo 350

Apparatus Testo-350	Accuracy of instrument	Range
HC	< 400 ppm (100 to 4000 ppm) < ten % of mv (> 4000 ppm)	100 to 40,000 (ppm)
NOx	±5 ppm (0 to +99 ppm) ±5 % of mv (+100 to +1999.9 ppm) ± 10% of mv (+2000 to +3000 ppm)	0 to 4000 (ppm)

Results & Discussion

Cylinder pressure

In Figure 3, the deviations in the cylinder pressure (maximum) with biodiesel (MIME), D100, and additive (2- EHN, triacetin) blends are shown. It shows that the cylinder pressure of the blends is always higher than diesel. Among all blends, BL2 possesses the highest cylinder pressure under various load conditions. This could be due to the diesel additive's property (high cetane number & low auto-ignition temperature) [16-17].

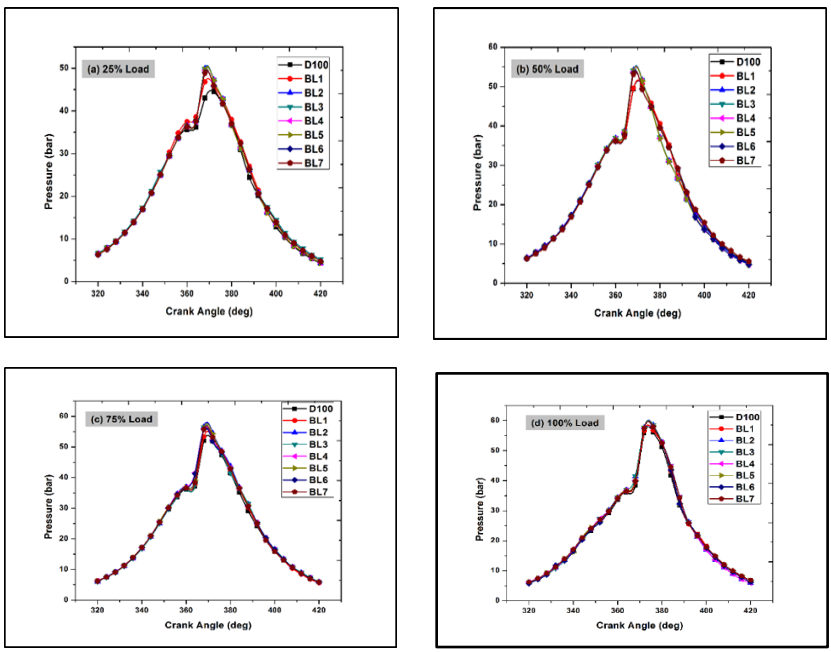

Figure 3: Cylinder pressure and load.

B.T.E. (Brake thermal efficiency)

Input chemical energy in the form of fuel converted to useful work is known as BTE [10]. Figure 4 shows that for every blend, BTE increases on increasing the load. Among the blends, BL2 and BL3 possess BTE 12%, and 11% more than plain diesel in full load respectively. This rise can also be due to better combustion of the fuel blend because of its higher cetane number, higher oxygen content, and higher flame velocity in the biodiesel and additive [18].

B.S.F.C. (Specific fuel consumption)

The quantity of fuel needed for producing 1- unit of energy by the engine is called BSFC. At maximum load (Figure 5), BSFC of Blend 2, 3 and 5 are (25, 22.5, 20)% less than plain diesel because of low density and heating value of biodiesel and diesel additives, which lead to lower consumption of fuel while producing same output power. The output parameters of the blend rely on the association between fuel injection system and properties of fuel (high viscosity of the biodiesel, low calorific value, oxygenation) [19- 20].

NOx (Oxides of nitrogen)

At 100% load (Figure 6), emission of NOx was found to be 4%, 2.1% and 3.6% more in BL1, BL3 and BL4 respectively. Due to high combustion temperature, oxygen and nitrogen molecules present in fuel ionize to form NO which is considered to be the key cause in the formation of NOx. But BL5, BL6 and BL7 produced 3.3%, 1% and 0.3% less NOx than diesel due to the fact that additive triacetin present in them possesses high latent heat of vaporization and low heating value that decreases the cylinder temperature. Thus due to triacetin, less heat will be generated (cooling effect) during combustion [21].

U.H.C. (Unburned hydrocarbon)

The increase in UHC Can be blamed for incomplete combustion of fuel which is directly related to the presence of oxygen in it. If there is less amount of oxygen in the fuel mixture, the hydrocarbons do not react completely that produces more unburned HC. It is seen from Figure 7, that BL2, BL3 and BL5 had lowermost UHC emission of 34%, 27% and 26% than pure diesel. The blends used in our experiment contain additives which increased its cetane number and improved combustion and reduce the emission of UHC considerably [22, 23].

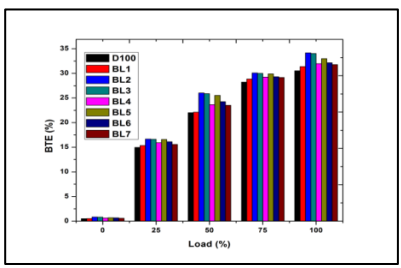

Figure 4: BTE with load.

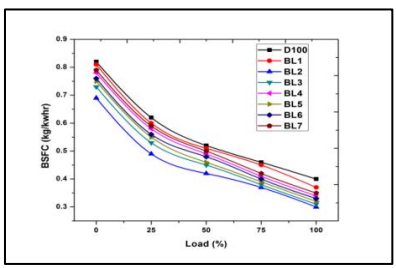

Figure 5: BSFC with load.

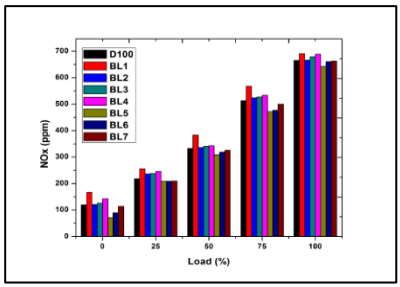

Figure 6: NOx with load.

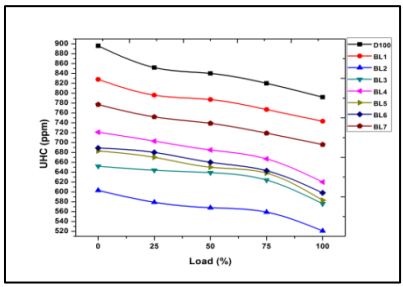

Figure 7: UHC with load.

Trade-off (BSFC- BTE- NOx)

In 25% load the parameters like BTE, BSFC and NOx are analyzed (Figure 8 (a)). As compared to diesel, BL1 and BL4 had slightly higher BTE. While in BL2, BTE and NOx are more which move the tradeoff area to top. Now in 50% load condition, Figure 8 (b) shows the same pattern of increase in NOX and BTE for some blends i.e. while raising the quantity of biodiesel and additive in it, the tradeoff region moves towards the top. Now considering a load of 75% we can visualize the pattern in which NOx, BSFC and BTE vary in different blends with different additives and Methyl esters (Figure 8 (c)). It is observed that in BL2 and BL3 having supplemented with 2- EHN and MIME, the NOx and BTE produced is higher while BSFC or fuel consumed is lesser. Though for BL5 and BL6, NOx and BSFC got reduced and BTE got intensified. Now, the result of varying the usage of MIME, 2-EHN and triacetin in various diesel blends are visualized in Figure 8 (d), in case of full load. It is seen that BSFC decreases but when BTE rises NOx also goes up. On the other hand, BL2 shows high emission of NOx and BTE but fairly low BSFC as portrayed in the top area of the graph. Interestingly BL6 shows the optimum tradeoff zone with higher BTE and lower BSFC and lowest NOx emission.

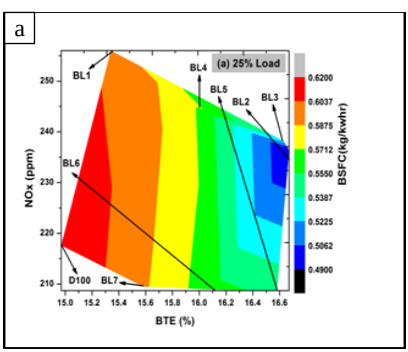

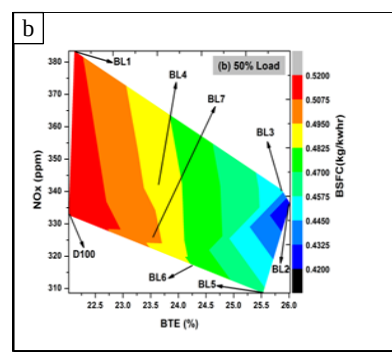

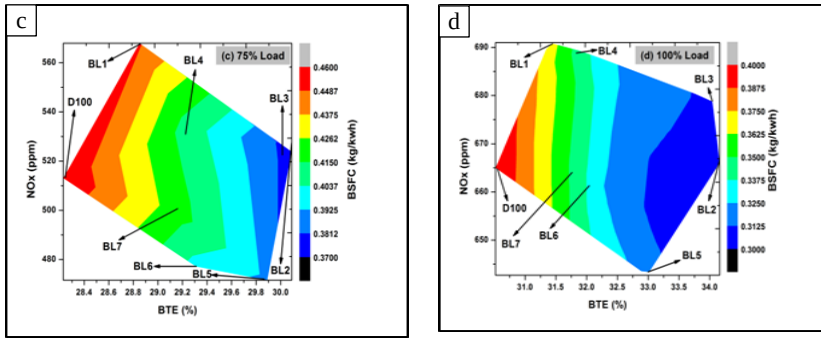

Figure 8: Trade-off study (BSFC- BTE- NOx).

Fuzzy based Taguchi optimization

The methods used by Taguchi are statistical methods created by him to enhance the manufactured goods quality. It gives us the optimal operating conditions to reduce the influence of the noise factor. According to Taguchi, S/N ratio is an assessment of performance stability of an output characteristic which considers both averages as well as variation. However, directly implementing this method is not possible in a multi-objective optimization problem. So, previously, other theories like desirability function approach, grey relation theory and utility theory [24-26] were combined with the Taguchi method. Practically, assigning individual responses priority weights are based on assumptions and it won't lead to an optimum solution and may lead to uncertainty [15]. To solve this problem the fuzzy-based Taguchi method is adopted. Also, there is a clear idea regarding the current workflow in Figure 9.

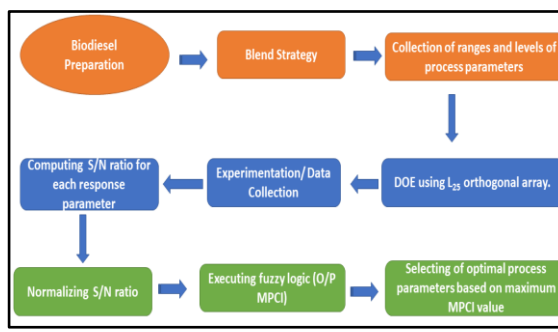

Figure 9: Flowchart for current workflow.

Optimum parameter selection of multi-objective optimization

For operating smoothly in the experimentation, forty permutations are provided in an L40 orthogonal array arrangement for a diesel engine between the different blends B and load A as explained in Table 3. This problem can be resolved in a direct manner which is implied by the fact that statistics was not in much focus; rather, S/N ratio was considered for handling the orthogonal array. The frequency of experiments conducted were observed to reduce and, optimal experimental arrangements were defined with the usage of Taguchi's technique for determining only a single characteristic. Larger the better and smaller the better are two methods through which the S/N ratio is found for analysing the factor effects numerically [9, 15, 21]. Thus from among all the quality characteristics (BSFC, BTE, UHC, and NOx), one of the quality characteristics can have its own set of process factor arrangement. Equation 2 is adopted to find the S/N ratio of 'larger-the-better' for BTE [16].

$$S/N = -10\,Log\frac{\sum_{i=1}^{n} y_i^2}{n} \tag{2}$$

Equation 3 S/N ratio of "smaller the better" for BSFC, UHC, and NOx [23].

$$S/N = -10\,Log\frac{\sum_{i=1}^{n} \frac{1}{y_i^2}}{n} \tag{3}$$

Here 'n' is the number, y measures i^{th} characteristic

Statistical analysis

Before the last step, i,e. normalisation process (Equation 4), various blends and loads were used for calculating the S/N ratio (average performance emission and emission) for the four parameters cited above using Taguchi techniques. The change of process parameter level with a change in BSFC, BTE, UHC and NOx (output properties) are depicted in signal-to-noise response graphs [9, 22-23] and the value range of signal-to-noise ratio shows a variation with output parameters of the engine.

$$X_{Normalized} = \frac{(X_i - X_{Min})}{(X_{Max} - X_{Min})} \tag{4}$$

Table 3: Taguchi's orthogonal array (L_{40})

Sl. No	A	B	BSFC (Kg/kwh)	BTHE (%)	NOx (PPM)	UHC(PPM)
1	0	D100	0.82	0.5	119.6	896
2	0	BL1	0.81	0.52	166.9	828
3	0	BL2	0.69	0.83	120.9	603
4	0	BL3	0.73	0.81	125.6	652
5	0	BL4	0.78	0.62	142.2	721
6	0	BL5	0.75	0.69	71.3	683
7	0	BL6	0.76	0.67	89.6	689
8	0	BL7	0.79	0.58	113.7	777
9	25	D100	0.62	14.97	217.6	852
10	25	BL1	0.6	15.34	256	796
11	25	BL2	0.49	16.67	236.3	579
12	25	BL3	0.53	16.63	238.2	644
13	25	BL4	0.58	15.9	245.8	703
14	25	BL5	0.55	16.58	208.7	670
15	25	BL6	0.56	16.12	208.9	680
16	25	BL7	0.59	15.58	209.5	752
17	50	D100	0.52	22.02	332.7	840
18	50	BL1	0.51	22.12	383.4	787
19	50	BL2	0.42	26.02	336.2	568
20	50	BL3	0.45	25.87	340.5	639
21	50	BL4	0.49	23.65	342.8	685
22	50	BL5	0.46	25.53	308.6	650
23	50	BL6	0.48	24.26	319	660
24	50	BL7	0.5	23.52	325.6	739
25	75	D100	0.46	28.23	513.1	820
26	75	BL1	0.45	28.85	567.9	767
27	75	BL2	0.37	30.09	523.8	559
28	75	BL3	0.38	29.99	527	624
29	75	BL4	0.41	29.24	533.6	667
30	75	BL5	0.39	29.89	471.6	638
31	75	BL6	0.4	29.31	477.2	643
32	75	BL7	0.42	29.16	500	719
33	100	D100	0.4	30.52	665	792
34	100	BL1	0.37	31.39	691	743
35	100	BL2	0.3	34.16	666	521
36	100	BL3	0.31	34.04	679	576
37	100	BL4	0.34	31.97	689	620
38	100	BL5	0.32	32.98	642.7	583
39	100	BL6	0.33	32.14	661	598
40	100	BL7	0.35	31.78	663	696

Considering Xi to be the S/N ratio and range of i starts from 0 ,1, 2….n. The maximum and minimum values of signal to noise ratio are denoted by Xmax and Xmin in the equation. Figure 10 represents the triangular member function which is used to obtain the optimum MPCI (max) by using an optimisation process (fuzzy) in output and input variables. The optimum value of MPCI has to be extracted next by using fuzzy techniques and Table 4 will give the optimum emission factor and performance for the study. Figure 11 (A, B, C, D) shows the combination of the different parameters and its effect on S/N ratio. Input combination [Load (0%), Fuel (D100)] for BSFC by projected amount of 2.974 (Least value among all S/N ratios), input [Load (100%), Fuel (BL2)] For BTE with a value of 30.629 (Highest value among all S/N ratios), input [Load (100%), Fuel (BL2)] in terms of NOx value stated -60.624 (lowest value among all S/N ratios) and input [Load (0%), Fuel (D100)] In terms of UHC, the projected value is -58.80 (lowest value among all S/N ratios). For both the input and output level, different fuzzy (eighty-one) rules are set out of which few are shown in and Table 5. After the response value is obtained, this method converts it to its equivalent S/N ratio. Taking input for load and fuel as 100 percent and BL2, the highest value obtained for MPCI is 0.75 displayed through simulation. Finally, after all the experimentations, the optimum blend is obtained as a combination of diesel, biodiesel and diesel additive in certain proportions at 100 Percent load called as Blend number 6 (BL6), details of which are presented in Table 4.

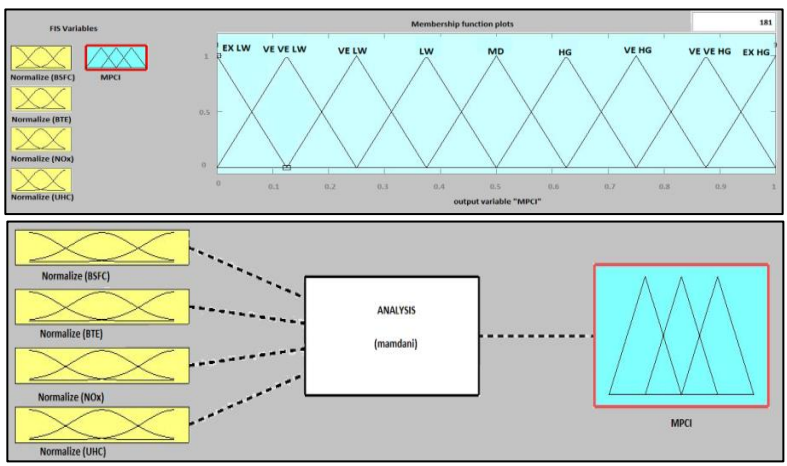

Figure 10: Membership functions (MPCI).

Table 4: Normalized value (Performance, emission and MPCI)

Sl. No	BSFC		BTE		NOx		UHC		MPCI
	SN Ratio	Normalize	SN Ratio	Normalize	SN Ratio	Normalize	SN Ratio	Normalize	
1	1.723	0	-6.020	0	-41.55	0.772	-58.80	0.000	0.17
2	1.830	0.012	-5.679	0.009	-44.44	0.625	-58.09	0.149	0.22
3	3.223	0.171	-1.618	0.119	-41.64	0.767	-55.95	0.204	0.41
4	2.733	0.115	-1.830	0.114	-41.97	0.750	-56.61	0.359	0.36
5	2.158	0.049	-4.152	0.050	-43.05	0.696	-57.52	0.894	0.26
6	2.498	0.088	-3.223	0.076	-37.06	1	-56.85	0.689	0.43
7	2.383	0.075	-3.478	0.069	-39.04	0.899	-57.00	0.515	0.36
8	2.047	0.037	-4.731	0.035	-41.11	0.794	-57.59	0.658	0.27
9	4.152	0.278	23.50	0.804	-46.75	0.508	-58.35	0.594	0.39
10	4.436	0.310	23.71	0.810	-48.16	0.437	-57.74	0.508	0.43
11	6.196	0.512	24.43	0.830	-47.46	0.472	-55.62	0.353	0.62
12	5.514	0.434	24.41	0.829	-47.53	0.468	-56.50	0.495	0.57
13	4.731	0.344	24.02	0.818	-47.81	0.455	-57.14	1.000	0.48
14	5.192	0.397	24.39	0.828	-46.39	0.527	56.62	0.898	0.57
15	5.036	0.379	24.14	0.822	-46.39	0.526	-56.83	0.651	0.52
16	4.582	0.327	23.85	0.814	-46.42	0.525	-57.23	0.852	0.47
17	5.679	0.452	26.85	0.896	-50.44	0.321	-58.22	0.785	0.44
18	5.848	0.472	26.89	0.897	-51.67	0.259	-57.63	0.607	0.47
19	7.535	0.665	28.30	0.935	-50.53	0.317	-55.46	0.000	0.68
20	6.935	0.596	28.25	0.934	-50.64	0.311	-56.39	0.149	0.60
21	6.196	0.512	27.47	0.912	-50.70	0.308	-57.04	0.204	0.51
22	6.744	0.574	28.14	0.931	-49.78	0.354	-56.44	0.359	0.62
23	6.375	0.532	27.69	0.918	-50.07	0.340	-56.58	0.894	0.57
24	6.020	0.491	27.42	0.911	-50.25	0.331	-57.07	0.689	0.52
25	6.744	0.574	29.01	0.954	-54.20	0.131	-58.00	0.515	0.47
26	6.935	0.596	29.20	0.960	-55.08	0.086	-57.40	0.658	0.49
27	8.635	0.791	29.56	0.969	-54.38	0.121	-55.32	0.594	0.71
28	8.404	0.764	29.53	0.969	-54.43	0.119	-56.12	0.508	0.64
29	7.744	0.689	29.31	0.963	-54.54	0.113	56.80	0.353	0.71
30	8.178	0.739	29.51	0.968	-53.47	0.168	-56.24	0.495	0.66
31	7.958	0.713	29.34	0.963	-53.57	0.162	-56.49	1.000	0.60
32	7.535	0.665	29.29	0.962	-53.97	0.142	-56.82	0.898	0.56
33	7.958	0.713	29.69	0.973	-56.45	0.016	-57.43	0.651	0.52
34	8.635	0.791	29.93	0.979	-56.78	0	-56.87	0.852	0.55
35	10.45	1	30.67	1	-56.46	0.016	-54.91	0.785	0.71
36	10.17	0.967	30.63	0.999	-56.63	0.007	-55.31	0.607	0.72
37	9.370	0.875	30.09	0.984	-56.76	0.001	-56.27	0.000	0.60
38	9.897	0.935	30.36	0.991	-56.16	0.031	-55.49	0.149	0.75
39	9.629	0.905	30.14	0.985	-56.40	0.019	-55.74	0.204	0.66
40	9.118	0.846	30.04	0.982	-56.43	0.018	-56.44	0.359	0.60

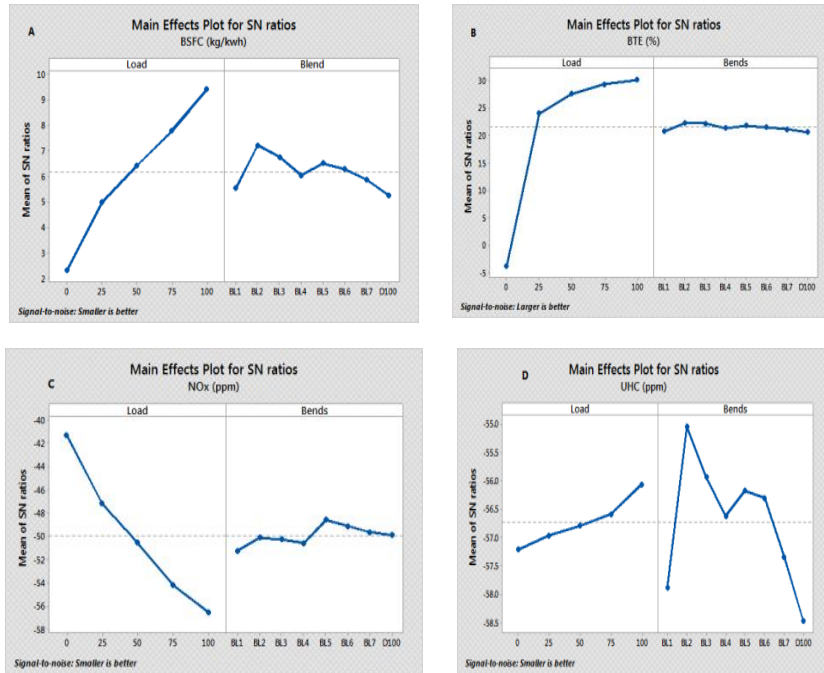

Figure 11: S/N response curve (A: BSFC, B: BTE, C: NOx, D: UHC).

Table 5: Fuzzy matrix (rule)

Sl.NO	BSFC	BTHE	UHC	NO_X	MPCI
1	LW	LW	LW	LW	EX LW
2	LW	LW	LW	MD	VE VE LW
3	LW	LW	MD	LW	VE VE LW
4	LW	LW	LW	HG	VE LW
5	LW	LW	HG	LW	VE LW
6	LW	LW	MD	MD	VE LW
7	LW	LW	MD	HG	LW
8	LW	LW	HG	MD	LW
9	LW	LW	HG	HG	MD
10	LW	MD	LW	LW	VE VE LW
11	LW	MD	MD	LW	VE LW
12	LW	MD	LW	MD	VE LW
13	LW	MD	MD	MD	LW
14	LW	MD	HG	LW	LW
15	LW	MD	LW	HG	LW
16	LW	MD	HG	MD	MD
17	LW	MD	MD	HG	MD
18	LW	MD	HG	HG	HG
19	LW	HG	LW	LW	VE LW
20	LW	HG	LW	MD	LW
21	LW	HG	MD	LW	LW
22	LW	HG	HG	LW	MD
23	LW	HG	LW	HG	MD
24	LW	HG	MD	MD	MD
25	LW	HG	MD	HG	HG
26	LW	HG	HG	MD	HG
27	LW	HG	HG	HG	VE HG
28	MD	LW	LW	LW	VE VE LW
29	MD	LW	LW	MD	VE LW
30	MD	LW	MD	LW	VE LW
31	MD	LW	LW	HG	LW
32	MD	LW	HG	LW	LW
33	MD	LW	MD	MD	LW
34	MD	LW	MD	HG	MD
35	MD	LW	HG	MD	MD
36	MD	LW	HG	HG	HG
37	MD	MD	LW	LW	VL
38	MD	MD	LW	MD	LW
39	MD	MD	MD	LW	LW
40	MD	MD	LW	HG	MD
41	MD	MD	HG	LW	MD
42	MD	MD	MD	MD	MD
43	MD	MD	MD	HG	HG

Sl.NO	BSFC	BTHE	UHC	NO_X	MPCI
44	MD	MD	HG	MD	HG
45	MD	MD	HG	HG	VE HG
46	MD	HG	LW	LW	LW
47	MD	HG	LW	MD	MD
48	MD	HG	MD	LW	MD
49	MD	HG	LW	HG	HG
50	MD	HG	HG	LW	HG
51	MD	HG	MD	MD	HG
52	MD	HG	MD	HG	VE HG
53	MD	HG	HG	MD	VE HG
54	MD	HG	HG	HG	VE VE HG
55	HG	LW	LW	LW	VE LW
56	HG	LW	LW	MD	LW
57	HG	LW	MD	LW	LW
58	HG	LW	LW	HG	MD
59	HG	LW	HG	LW	MD
60	HG	LW	MD	MD	MD
61	HG	LW	MD	HG	HG
62	HG	LW	HG	MD	HG
63	HG	LW	HG	HG	VH
64	HG	MD	LW	LW	LW
65	HG	MD	LW	MD	MD
66	HG	MD	MD	LW	MD
67	HG	MD	LW	HG	HG
68	HG	MD	HG	LW	HG
69	HG	MD	MD	MD	HG
70	HG	MD	MD	HG	VE HG
71	HG	MD	HG	MD	VE HG
72	HG	MD	HG	HG	VE VE HG
73	HG	HG	LW	LW	MD
74	HG	HG	LW	MD	HG
75	HG	HG	MD	LW	HG
76	HG	HG	LW	HG	VE HG
77	HG	HG	HG	LW	VE HG
78	HG	HG	MD	MD	VE HG
79	HG	HG	MD	HG	VE VE HG
80	HG	HG	HG	MD	VE VE HG
81	HG	HG	HG	HG	EX HG

Conclusions

Based on the experimental study to understand the potential of blended biofuels MIME and additives triacetin, 2-EHN on CI engine in terms of emission and performance and the same is validated using Taguchi –Fuzzy approach with the following conclusions:

- For every blend, BTE got increased with increasing the load. Among the blends, BL2 and BL3 possess BTE 12%, and 11% more than plain diesel in full load respectively.
- At maximum load, BSFC of blend 2, 3 and 5 are (25, 22.5, 20)% less than plain diesel.
- The NOx is observed to be (4, 2.1 and 3.6)% higher in case of the blend (2, 3, and 4) at higher load (100%) condition. But blend (5, 6 and 7) produced (3.3, 1 and 0.3) less NOx than D100.
- It is seen that BL2, BL3 and BL5 had lowermost UHC emission of 26%, 27% and 34% than pure diesel at 100% load.
- Afterwards, a model was designed using two input and one output parameters i.e fuel blend and load as output parameters and MPCI as output parameter using fuzzy rules. MPCI value of 0.75 is considered as the optimum value which is possessed by blend 5 resulting in higher emission control and performance.

References

[1] G. R. K Sastry, M. Deb, and J. K. Panda, "Effect of fuel injection pressure, isobutanol and ethanol addition on performance of diesel-biodiesel fuelled DI diesel engine," *Energy procedia*, vol. 66, pp 81-84, 2015.

[2] M. Deb, A. Paul, D. Debroy, G. R. K. Sastry, R. S. Panua, and P. K. Bose, "An experimental investigation of performance-emission trade off characteristics of a CI engine using hydrogen as dual fuel", *Energy*, vol. 85, pp 569-585, 2015.

[3] O. Armas, R. García-Contreras and Á. Ramos. "Pollutant emissions from engine starting with ethanol and butanol diesel blends," *Fuel Processing Technology*, vol. 100, pp 63-72, 2012.

[4] E. Khalife, M. Tabatabaei, A. Demirbas, and M. Aghbashlo, "Impacts of additives on performance and emission characteristics of diesel engines during steady state operation," *Progress in Energy and Combustion Science*, vol. 59, pp 32-78, 2017.

[5] F. Jaliliantabar, B. Ghobadian, A. P. Carlucci, G. Najafi, A. Ficarella, L. Strafella, A. Santino and S. De Domenico, "Comparative evaluation of physical and chemical properties, emission and combustion characteristics of brassica, cardoon and coffee based biodiesels as fuel in a compression-ignition engine," *Fuel*, vol. 222, pp 156-174, 2018.

[6] A. Atmanli, and N. Yilmaz, "A comparative analysis of n-butanol/diesel and 1-pentanol/diesel blends in a compression ignition engine," *Fuel*, vol. 234, pp 161-169, 2018.

[7] I. Örs, S. Sarıkoç, A. E. Atabani, S. Ünalan, and S. O. Akansu, "The effects on performance, combustion and emission characteristics of DICI engine fuelled with TiO2 nanoparticles addition in diesel/biodiesel/n-butanol blends," *Fuel*, vol. 234, pp 177-188, 2018.

[8] P. K. Bose, M. Deb, R. Banerjee and A. Majumder, "Multi objective optimization of performance parameters of a single cylinder diesel engine running with hydrogen using a Taguchi-fuzzy based approach," Energy, vol. 63, pp 375-386, 2013.

[9] J. K. Panda, G. R. K. Sastry and R. N. Rai, "A Taguchi-fuzzy-based multi-objective optimization of a direct injection diesel engine fueled with different blends of Leucas zeylanica methyl ester and 2-ethylhexyl nitrate diesel additive with diesel," *Journal of Energy Resources Technology*, Vol. 139, no. 4, pp 042209, 2017.

[10] S. Saravanan, G. Nagarajan and S. Sampath, "Multi response optimization of NOx emission of a stationary diesel engine," *Fuel*, vol. 89, no. 11, pp 3235-3240, 2010.

[11] M. Mubarak, A. Shaija, and T. V. Suchithra, "Experimental evaluation of Salvinia molesta oil biodiesel/diesel blends fuel on combustion, performance and emission analysis of diesel engine," *Fuel* 2119526, 2020.

[12] G. Dwivedi, and M. P. Sharma, "Investigation and improvement in cold flow properties of Pongamia biodiesel," Waste and Biomass Valorization vol. 6, no. 1, pp 73-79, 2015.

[13] G. R. K. Sastry, *Bio-Diesel: Bio-degradable Alternative Fuel for Diesel Engines*. Readworthy, 2008.

[14] H. Kuszewski, "Effect of adding 2-ethylhexyl nitrate cetane improver on the autoignition properties of ethanol–diesel fuel blend–Investigation at various ambient gas temperatures," *Fuel*, vol. 224, pp 57-67, 2018.

[15] J. K. Panda, G. R. K. Sastry and R. N. Rai, "Experimental analysis of performance and emission on DI diesel engine fueled with diesel-palm kernel methyl ester-triacetin blends: a Taguchi fuzzy-based

optimization," *Environmental Science and Pollution Research*, vol. 25, no. 22, pp 22035-22051, 2018.

[16] V. Ganesan, *Internal combustion engines*. McGraw Hill Education (India) Pvt Ltd, 2015.

[17] A. Paul, P. K. Bose, R. S. Panua, and D. Debroy,"Study of performance and emission characteristics of a single cylinder CI engine using diethyl ether and ethanol blends," *Journal of the energy institute*, vol. 88, no. 1, pp 1-10, 2015.

[18] G. R. K. Sastry and R. N. Rai, "A Comparative Investigation on DI Diesel by Using Different Blends of Diesel-Biodiesel-Additives: Performance and Emission Based Trade-off Analysis," *Journal of Physics: Conference Series*, IOP Publishing, vol. 1240, no. 1, pp 012163, 2019.

[19] G. R. K Sastry, J. K. Panda and P. Dutta, "A Study with Diesel Additives and Fish Methyl Ester on Diesel Engine at Full Load Condition," In *Applied Mechanics and Materials*, 789, pp. 179-183, 2015.

[20] M. Deb, A. Paul, D. Debroy, G. R. K. Sastry, R. S. Panua and P. K. Bose, "An experimental investigation of performance-emission trade off characteristics of a CI engine using hydrogen as dual fuel" *Energy*, vol. 85, pp 569-585, 2015.

[21] B. Mohan, W. Yang, V. Raman, V. Sivasankaralingam and S. K. Chou, "Optimization of biodiesel fueled engine to meet emission standards through varying nozzle opening pressure and static injection timing," *Applied energy*, vol. 130, pp 450-457, 2014.

[22] P. K. Bose, M. Deb, R. Banerjee and A. Majumder, "Multi objective optimization of performance parameters of a single cylinder diesel engine running with hydrogen using a Taguchi-fuzzy based approach," *Energy*, vol. 63, pp 375-386, 2013.

[23] S. Roy, A. K. Das and R. Banerjee, "Application of Grey–Taguchi based multi-objective optimization strategy to calibrate the PM–NHC–BSFC trade-off characteristics of a CRDI assisted CNG dual-fuel engine," *Journal of natural gas science and engineering*, vol. 21, pp 524-531, 2014.

[24] S. Erdoğan, M. K. Balki, S. Aydın and C. Sayin, "The best fuel selection with hybrid multiple-criteria decision making approaches in a CI engine fueled with their blends and pure biodiesels produced from different sources," *Renewable Energy*, vol. 134, pp 653-668, 2019.

[25] S. Salam, T. Choudhary, A. Pugazhendhi, T. N. Verma and A. Sharma, "A review on recent progress in computational and empirical studies of

compression ignition internal combustion engine," *Fuel*, vol. 279, pp 118469, 2020.

[26] M. H. E. Ahmadi, S. J. Royaee, S. Tayyebi and R. B. Boozarjomehry, "A new insight into implementing Mamdani fuzzy inference system for dynamic process modeling: Application on flash separator fuzzy dynamic modeling" *Engineering Applications of Artificial Intelligence*, vol. 90, pp 103485, 2020.

A Study of Air Velocity in a Cooling Tower that Affects the Diameter of the Droplet

Bambang Antoko[*]
Politeknik Perkapalan Negeri Surabaya
**bambangantoko@ppns.ac.id*

Dany Iman Santoso
Universitas Negeri Surabaya

Ary Bachtiar Krishna Putra, Sutardi
Institut Teknologi Sepuluh Nopember

ABSTRACT

The study of air velocity inside the cooling tower gives an overview of the process of heat or mass transfer. This study developed mathematical modelling based on the principle of continuity and statistical thermodynamics to track changes in radius, velocity, density, and temperature of droplets and air along with the droplet trajectory or tower height. Before that, the droplet radius range is predicted in advance to get the accuracy of the calculation. Also, water capacity and fan rotation are varied to determine their effect on cooling tower performance. The calculation results showed that 18 Lpm capacity gives efficiencies above 50%, while for 0.5 Lpm capacity, it produces efficiencies in between 25% to 40%. The highest efficiency indicates that the evaporation process occurs most efficiently. Mathematical modelling in calculations can also describe the increase in air temperature, which usually uses numerical simulations.

Keywords: *heat or mass transfer; mathematical modelling; statistical thermodynamics; droplet trajectory; tower height*.

Introduction

A cooling tower is a large heat exchanger that has high effectiveness, in between 40% to 70% [1–5]. Investigation about the phenomena of the water

ISSN 1823-5514, eISSN2550-164X
Received for review: 2020-05-04
Accepted for publication: 2020-12-24
Published: 2021-01-15

and air that work in it is an enticing thing to do, such as the droplet evaporation [1, 6]. Observations were made to the level of droplets to get a high level of accuracy [6–12]. It described fluid interactions in the form of mathematical modelling obtained from governing equations, for example, the droplet surface temperature, the average water temperature, change in velocity of the falling droplet, and so on [13–16].

Qi [17] reported that exergy from the water supply was not absorbed entirely by air, but much was destroyed in the rain zone by irreversibility. The highest heat transfer occurs in the spray zone, where water first contacts with air in the tower. Whereas Calderon [18] and Xia [19] conducted numerical investigations using different methods of cooling tower design to solve the heat transfer problem in the rain zone and produced a model that was close to the original. They figured out droplet temperature charts along the cooling tower heights.

Based on a review by Sun [20] that different nozzles provide different spray patterns. The characteristics of spray patterns are affected by the corresponding flow rate, pressure, mean droplet size, and quantified droplet size distribution. According to Li [21], the study needs to give a windbreak wall to the large size of the cooling tower so that airflow is not disturbed, which causes a decrease in its performance. Wind blowing from the outside of it causes this disturbance and affecting the airflow inside it.

In our two previous studies, this study has analysed the phenomenon of drifting and evaporation processes. This study based all on the movement of the droplet. Not only when it comes out of spray nozzles [22] but also when it moves along the height of the tower [23]. However, the movement of air that the fan sucked into it got less attention. Therefore, in this study, the analysis is focused on obtaining air velocity along the trajectory. Also, increasing or decreasing the temperature of working fluids due to the air movement.

Methods

This study derived the prediction of air velocity inside a cooling tower from the continuity equation [1, 4, 6, 9]. From this, this study obtained the maximum and average speeds of air used to calculate air velocity [7, 10, 16, 20] along with the height of the tower using the principle of orifice area because the bottom of the cooling tower has a different shape to the roof ($L^2 > A$), as shown in Figure 1.

Then, this study achieved droplet diameter prediction from air and water spray velocities [4, 9, 10]. From statistical thermodynamics, we made mathematical modelling to calculate the temperatures of the working fluids [2, 3, 5, 14].

Aerodynamics elements

Based on the movement of fluid, the fan sucked across the orifice, the velocity obtained is the average velocity [4, 10, 14]. When it enters, the speed is low, while when it exits, the rate is high [7, 8, 20]. Based on this phenomenon, the air velocity u (m/s) [3, 9] is as:

$$u = Q_a \big/ \left(\rho_a L^2 \right) \tag{1}$$

where Q_a (m^3/s) is the air capacity, ρ_a (kg/m^3) is the air density, and L (m) is the bottom diameter.

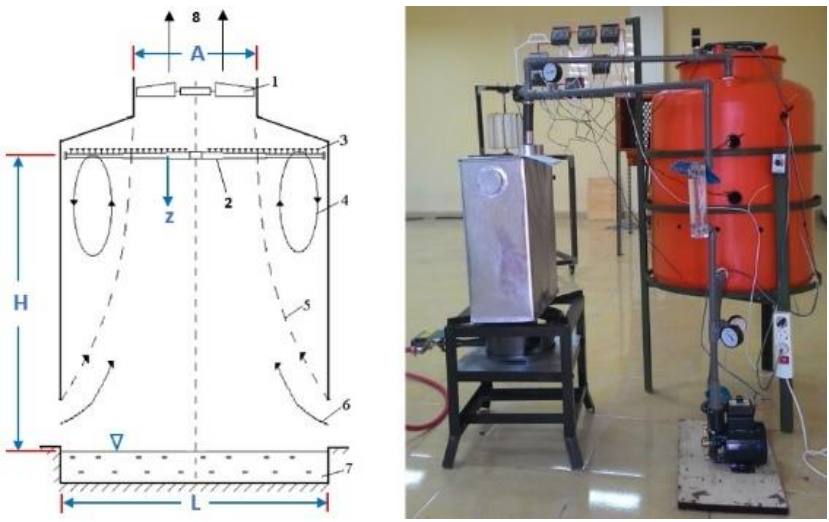

Figure 1: Scheme of the cooling tower: (1) Exhaust fan, (2) Delivery pipe, (3) Spraying nozzles, (4) Stagnation zone, (5) Line of stagnation zone, (6) Enter air, (7) Water basin, (8) Exit air.

Meanwhile, this study got the maximum velocity of air u_{max} (m/s) when it leaves the tower [6, 9] as:

$$u_{max} = Q_a \big/ \left(\rho_a A \right) \tag{2}$$

where A (m^2) is the roof cross-section area of the tower that is $A = \pi d_f^2 \big/ 4$ and d_f (m) is the suction fan diameter.

This study received the velocity of droplet v (m/s) from continuity at the nozzle [8, 15, 20] as:

$$v = \left(Q_w / A_n\right) - u \tag{3}$$

where Q_w (m^3/s) is the water capacity and A_n (m^2) is the nozzle cross-section area that is $A_n = \pi d_n^2 / 4$ where d_n (m) is the nozzle diameter.

Because the bottom part of the roof tower resembles an orifice, it forms non-uniform airflow inside the cooling tower. This study based the velocity of air $u(z)$ (m/s) along the vertical z-axis on the principle of simple geometry [1, 9] as:

$$u\left(z\right) \cong u_{\max} \frac{\pi\left(H-h\right)^2}{2\left[H-h+z\left(L\sqrt{\pi/2A}-1\right)\right]^2} \tag{4}$$

where H (m) is the height of the tower, h (m) is the height of the window, and z (m) is the position of observation.

Model of the interactions

The size of the droplet radius depends on the velocity that affects it. In the principle of continuity, the greater the rate, the smaller the radius. On the other hand, the temperature of the water that exits the nozzle also influences the droplet surface tension. Surface tension is directly proportional to the radius. From these two relationships, this study formulated the droplet radius R (m) [9, 10] as:

$$R \le 2.3 \frac{\sigma}{\rho_a u^2} \tag{5}$$

where σ (N/m) is the water surface tension.

From the relationship in Equation (5), this study gained a range of radius values. This study achieved the minimum radius when the air velocity that moves upward and holds the droplet falling is maximal [4]. Whereas the maximum radius received is based on the speed of the droplet falling relative to the average velocity of the air upwards [10].

In line with the principle of flow is a droplet with a large radius that has a large surface area as well, so that the drag force caused by the airflow is also getting larger. As a result, air will carry the droplet out of the tower in

the form of mass transfer because the droplet is still in the liquid phase. This study can see the range of droplet radius values, as shown in Figure 2.

Droplet velocity is much higher than air velocity, even when compared to the maximum speed [14, 15]. It is due to the effect of spraying on the nozzle, which causes high droplet velocity. Therefore, the possibility of droplet radius distribution is dominated by droplet velocity, as shown in Figure 3. From the distribution, the average value of the droplet radius is one-quarter [7] of its range, to make it easier.

The number of droplets N_d (dimensionless) that exit in the spraying process depends on the water capacity, velocity, and diameter [4, 10] as:

$$N_d(z) = \frac{3Q_w}{4\rho_w \pi R(z) v(z)} \tag{6}$$

where ρ_w (kg/m^3) is the liquid water density, $R(z)$ (m) is the droplet radius, and $v(z)$ (m/s) is velocity along the z-axis.

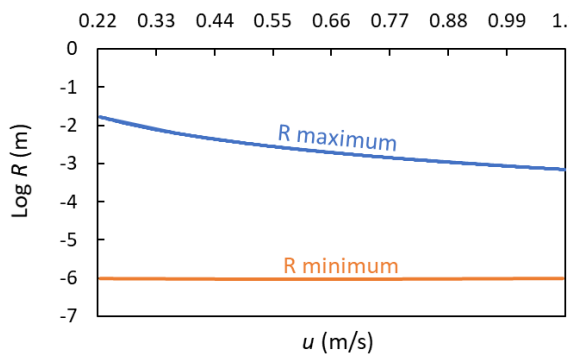

Figure 2: Droplet radius range values versus average air velocity.

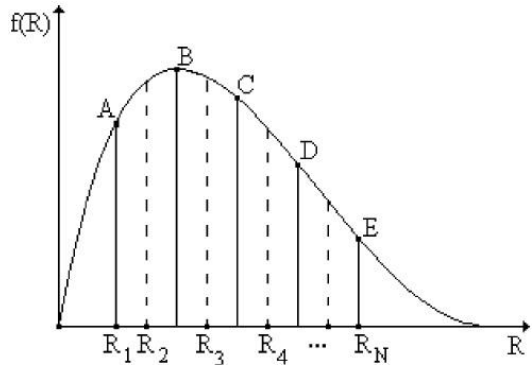

Figure 3: Probability distribution of droplet radius.

Some constants are related to fluid flow as follows: The Reynolds number Re (dimensionless), the heat exchange coefficient *Nu* (dimensionless), the mass exchange coefficient γ (m/s), and the drag coefficient C_d (dimensionless) as shown in Equation (7), Equation (8), Equation (9), and Equation (10), respectively [14, 15].

$$\mathrm{Re} = \frac{2\rho_a R(z)\left[v(z) - u(z)\right]}{\mu_a} \tag{7}$$

$$Nu = 2 + 0.5\,\mathrm{Re}^{0.5} \tag{8}$$

$$\gamma = \frac{D\left(2 + 0.5\,\mathrm{Re}^{0.5}\right)}{2R(z)} \tag{9}$$

$$C_d = \frac{24}{\mathrm{Re}}\left(1 + \frac{\mathrm{Re}^{2/3}}{6}\right) \tag{10}$$

where D (m^2/s) is the coefficient of diffusion for water vapor and μ_a (kg/m.s) is the air dynamic viscosity.

Then, the mathematical model that calculates interactions between water and airin the form of changes in droplet radius $R(z)$ (m), droplet fall velocity $v(z)$ (m/s), droplet temperature $T_w(z)$ (K), air temperature $T_a(z)$ (K), and droplet density $\rho(z)$ (kg/m^3) along the z-axis is presented by Equation

(11), Equation (12), Equation (13), Equation (14), and Equation (15), respectively [15, 16].

$$\frac{dR(z)}{dz} = -\frac{h_m\left[\rho_s\left(T_w(z)\right)-\rho(z)\right]}{\rho_w v(z)} \tag{11}$$

$$\frac{dv(z)}{dz} = \frac{g}{v(z)} - C_d\,\frac{\rho_a\left[v(z)-u(z)\right]^2}{2v(z)}\,\frac{\pi R(z)^2}{m} \tag{12}$$

$$\frac{dT_w(z)}{dz} = \frac{3\left\{h\left[T_a(z)-T_w(z)\right]-h_m\left[r-c_w T_w(z)\right]\left[\rho_s\left(T_w(z)\right)-\rho(z)\right]\right\}}{c_w\rho_w R(z)v(z)} \tag{13}$$

$$\frac{dT_a(z)}{dz} = \frac{4\pi}{\rho_a c_a}\,\frac{R(z)N_d(z)}{v(z)-u(z)}\,h\left[T_w(z)-T_a(z)\right] \tag{14}$$

$$\frac{d\rho(z)}{dz} = -4\pi\,\frac{R(z)^2 N_d(z)}{v(z)-u(z)}\,h_m\left[\rho_s\left(T_w(z)\right)-\rho(z)\right] \tag{15}$$

where ρ_s (kg/m^3) is the saturated water vapor density, c_w (J/kg.K) is the water specific heat, c_a (J/kg.K) is the air specific heat, and r (J/kg) is the latent heat of vaporization.

From Equation (7) to Equation (15), they are not independent but depend on each other. Therefore, to start the calculation needed boundary conditions in the form of initial values as also applied by researcher such as Fisenko and Brin [6] in their study in the simulation of a cross-flow cooling tower performance. The following are the initial values for each parameter but, keep in mind that the position $z = 0$ for water and air is different because this cooling tower is of counter flow type.

At $z = 0$ (the point of water exits the nozzles), the droplet radius:

$$R\big|_{z=0} = R_0 \tag{16}$$

the droplet velocity:

$$v\big|_{z=0} = v_0 \tag{17}$$

the droplet temperature:

$$T_w\big|_{z=0} = T_{w0} \tag{18}$$

At $z = H$ (the point of air enters the windows), the air temperature:

$$T_a\big|_{z=H} = T_{a0} \tag{19}$$

the water vapor density:

$$\rho\big|_{z=H} = \rho_0 \tag{20}$$

with these initial value definitions, this study formed a nonlinear boundary-value problem system fromordinary differential equations, which are Equation (11) to Equation (15).

The last thing to count is the performance of the cooling tower in the form of efficiency. As previously identified, the limitation of the system is the ambient air temperature entering it in the form of atmospheric temperature or temperature limit T_{lim}. The efficiency η as mentioned, around 40%, by Brin and Petruchik [2] such as:

$$\eta = \frac{T_{w0} - T_{wf}}{T_{w0} - T_{\text{lim}}} \tag{21}$$

where T_{wf} is the water average temperature in the water basin. This study also used the temperature limit to calculate air humidity in a cooling tower [2, 15] as:

$$\rho_s\left(T_a\right) \cdot \psi = \rho_s\left(T_{\text{lim}}\right) \tag{22}$$

where ψ is the air relative humidity.

Results and discussions

This study presented cooling tower dimensions in the experiment, as shown in Table 1. The water capacity and fan rotation are varied to obtain variations in droplet and air velocities. Also, this study have determined the load calculated based on previous studies: 0.5 Lpm (minimum), 6.0 Lpm (equilibrium), and 18 Lpm (maximum).

Table 1: The cooling tower dimensions

Dimensions	Value	Units
Tower height (H)	0.56	meter (m)
Bottom diameter (L)	0.65	meter (m)
Windows height (h)	0.20	meter (m)
Fan diameter (d_f)	8.0	inch (in)
Nozzle diameter (d_n)	0.001	meter (m)
Water capacity	0.5 – 18	Liter per minute (Lpm)
Fan rotation	300 – 1500	rotation per minute (rpm)

Changes in the droplet radius, as shown in Figure 4, undergo the highest decrease for the lowest capacity. Even though, from the count, the smallest load has the largest radius. This statement is in line with Fisenko and Brin [6]. The same thing is also presented by the graphs of the change in velocity droplet, as shown in Figure 5, where the lowest capacity also has the tallest velocity change, while the initial velocity is the lowest.

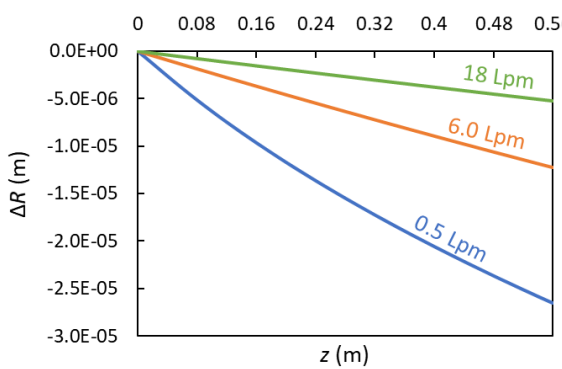

Figure 4: Droplet radius changes along its vertical trajectory.

Low water capacity has little momentum that airflow may carry some of the water in the form of a liquid phase because this is a counterflow. This

study observed this reduction through the graphs of changes in vapor density in Figure 6. It appears that the lowest capacity has the highest reduction in the mass of the droplet while crossing the airflow. Because low water capacity has a low water mass, reduction of airflow causes significant mass loss so that the density of low water capacity drops to a low value.

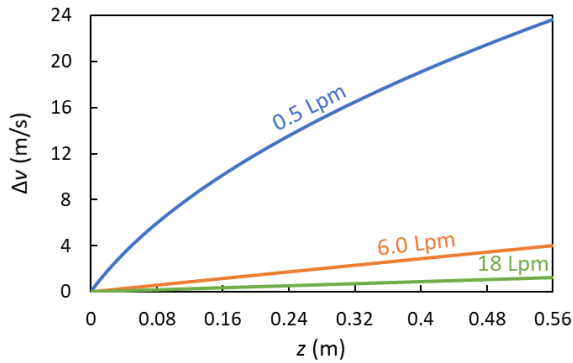

Figure 5: Changes in velocity of falling droplets along its trajectory.

Whereas for high capacity graphs, both 6.0 Lpm and 18 Lpm in Figure 6, the vapor density tends to remain. It indicates a mass reduction at high capacity relatively small. Since a high-water capacity has a high-water mass, the reduction in airflow has little effect on it so that the density graph remains high.

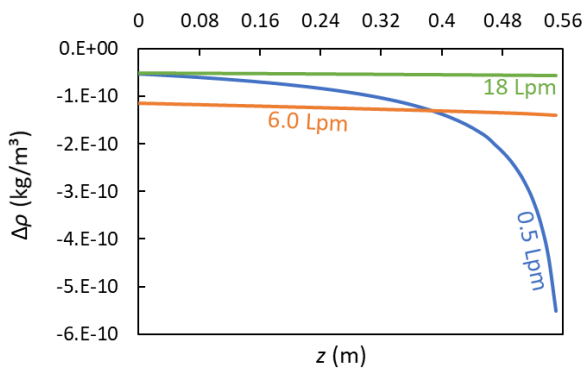

Figure 6: Reduction of vapor density along the droplet trajectory.

The highest droplet temperature reduction is achieved by the lowest capacity, as shown in Figure 7. Similarly, the highest increase in air temperature is also given by it, as illustrated in Figure 8. Both temperatures are the result of interactions within the tower.

High water capacity carries high mass water flow so that, with the same tower volume, it provides higher density, which causes lower temperature changes. With the same airflow capacity, it produces lower air temperature enhancements, as seen in Figure 8.

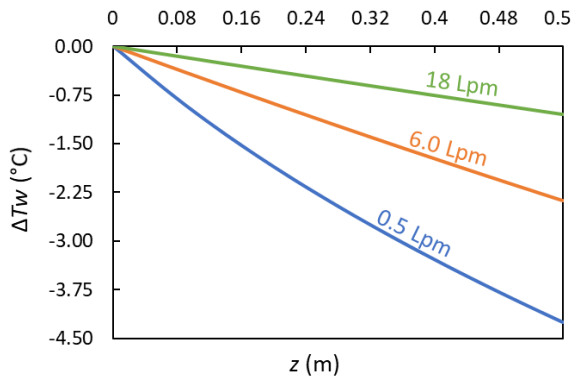

Figure 7: Decreased droplet temperature along its trajectory.

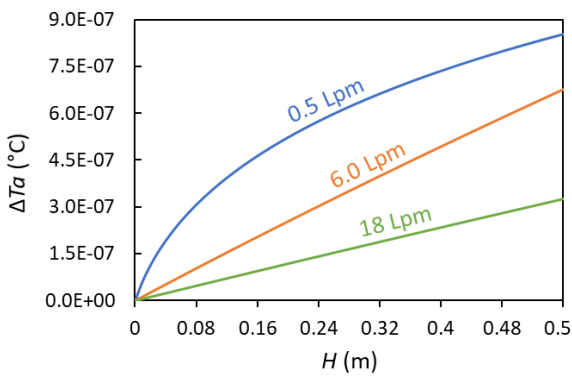

Figure 8: Increased air temperature along the tower height.

The same thing with air temperature is indicated by relative humidity, as shown in Figure 9. Humidity increases indicating that the water content in the air also increases. The lowest water capacity has the highest difference in

humidity. It is in line with the highest water mass reduction experienced by the low water capacity, which causes a difference in the highest humidity. Also, it is in line with Calderon et al. [5] and Fisenko et al. [9].

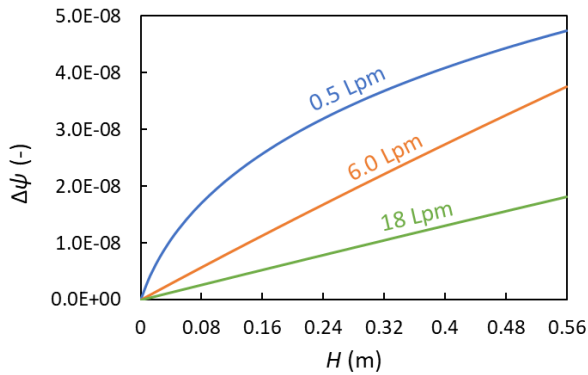

Figure 9: Increased relative humidity along the tower height.

Variations in fan rotation provide variations in the velocity of air across the tower. Figure 10 describes the variation in the form of it along with the tower height. When the fan sucked it in, the air has a horizontal velocity direction, then changes to a vertical direction when it reaches the tower roof so that the air velocity becomes very high when it exits the tower.

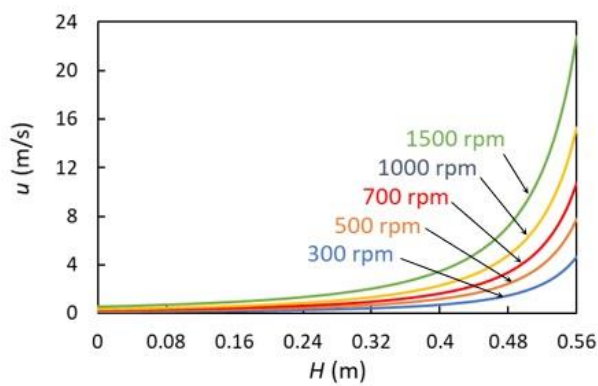

Figure 10: Air velocity along with tower height.

This study reflected the evaporation process in the performance graphs, as presented in Figure 11. From this graph, the highest capacity has

the highest efficiency, which means that the heat transfer process occurs most efficiently at it. A high mass flow rate of water accelerates the distribution of droplets to move heat into the air. Conversely, a low water mass flow rate causes a high-water mass loss. It inhibits the droplet evaporation process and reduces efficiency. This statement is in line with Brin and Petruchik [2].

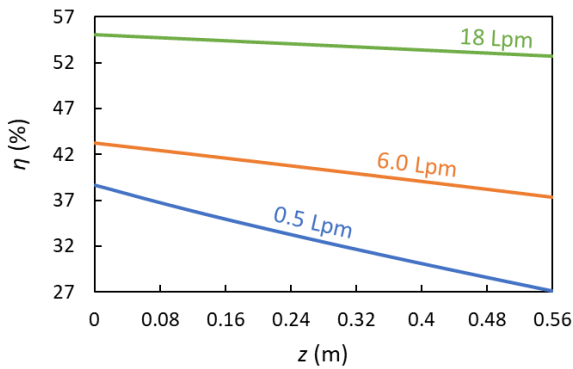

Figure 11: The cooling tower efficiency along the droplet trajectory depends on the water capacity.

Conclusions

The lowest water capacity produces the most substantial changes in droplet radius, velocity, density, and temperature, but it generates the smallest performance. It means the highest losses in the form of drifting for the droplet mass, which is still in a liquid phase. The air velocity reaches its maximum when it exits the tower, as well as its temperature and humidity.

References

[1] S.P. Fisenko, A.A. Brin, "Simulation of a cross-flow cooling tower performance," *International Journal of Heat and Mass Transfer*, vol. 50, pp 3216–3223, 2007.

[2] S. P. Fisenko, A. I. Petruchik, A. D. Solodukhin, "Evaporative cooling of water in a natural draft cooling tower," *International Journal of Heat and Mass Transfer*, vol. 45, no. 23, pp 4683–4694, 2002.

[3] A.I. Petruchik, A.D. Solodukhin, and S.P. Fisenko, "Evaporative cooling of water in complex-configuration film spray zones," *Journal of Engineering Physics and Thermophysics*, vol. 81, no. 1, pp 182–187, 2008.

[4] A.I. Petruchik, A.D. Solodukhin, and S.P. Fisenko, "Simulation of cooling of water droplet and film flows in large natural wet cooling towers," *Journal of Engineering Physics and Thermophysics*, vol. 74, no. 1, pp 62–68, 2001.
[5] A.V. Vlasov, G.V. Dashkov, A.D. Solodukhin, and S.P. Fisenko, "Investigation of the internal aerodynamics of the chimney-type evaporative cooling tower," *Journal of Engineering Physics and Thermophysics*, vol. 75, no. 5, pp 1086–1091, 2002.
[6] A.A. Brin, S.P. Fisenko, and Y.A. Khodyko, "Characteristic features of evaporative cooling of droplets in high-temperature flows," *Journal of Engineering Physics and Thermophysics*, vol. 84, no. 2, pp 292–297, 2011.
[7] A.A. Brin and S.P. Fisenko, "Heterogeneous condensation of a steam on nanoparticles in a laminar diffusion chamber," *Journal of Engineering Physics and Thermophysics*, vol. 79, no. 2, pp 212–216, 2006.
[8] S.P. Fisenko, A.A. Brin, "Heat and mass transfer and condensation interference in a laminar flow diffusion chamber," *International Journal of Heat and Mass Transfer*, vol. 49, pp 1004–1014, 2006.
[9] S.P. Fisenko, A.A. Brin, and A.I. Petruchik, "Evaporative cooling of water in a mechanical draft cooling tower," *International Journal of Heat and Mass Transfer*, vol. 47, pp 165–177, 2004.
[10] D. O. Glushkov, G. V. Kuznetsov, and P. A. Strizhak," Influence on Radiative Heat and Mass Transfer Mechanism in System Water Droplet – High Temperature Gases on Integral Characteristics of Liquid Evaporation," *Thermal Science*, vol. 19, no. 5, pp 1541–1552, 2015.
[11] G. Miliauskas, A.Adomavičius, M.Maziukienė, "Modelling of water droplets heat and mass transfer in the course of phase transitions. I: Phase transitions cycle peculiarities and iterative scheme of numerical research control and optimization," *Nonlinear Analysis: Modelling and Control*, vol. 21, no. 1, pp 135-151, 2016.
[12] V. Ramanauskas, M.Maziukienė,and G.Miliauskas, "The combined heat and mass transit processes of water droplets in biofuel technologies," *Energetika*, vol. 63, no. 2, pp 75-81, 2017.
[13] A.A. Brin and A.I. Petruchik, "Thermal calculation of the ejection cooling tower and method of improving its efficiency," *Journal of Engineering Physics and Thermophysics*, vol. 84, no. 2, pp 287-291, 2011.
[14] A. A. Brin, A. I. Petruchik, and S.P. Fisenko, "Mathematical modelling of evaporative cooling of water in a mechanical-draft tower," *Journal of Engineering Physics and Thermophysics*, vol. 75, no. 6, pp 1332–1338, 2002.
[15] S.P. Fisenko, A.I. Petruchik, "Toward to the control system of mechanical draft cooling tower of film type," *International Journal of*

Heat and Mass Transfer, vol. 48, pp 31–35, 2005.

[16] A. I. Petruchik and S. P. Fisenko, "Two-dimensional calculation of the parameters of a steam-air mixture in a film-type heat and mass exchanger," *Journal of Engineering Physics and Thermophysics*, vol. 76, no. 5, pp 1048–1054, 2003.

[17] X. Qi, Y. Liu, and Z. Liu, "Exergy based performance analysis of a shower cooling tower," *Journal of Mechanical Engineering*, vol. 59, no. 4, pp 251-259, 2013.

[18] O. M. Hernández-Calderón, E. Rubio-Castro, and E. Y. Rios-Iribe, "Solving the heat and mass transfer equations for an evaporative cooling tower through an orthogonal collocation method," *Computers and Chemical Engineering*, vol. 71, pp 24-38, Dec. 2014.

[19] Z. Z. Xia, C. J. Chen, and R. Z. Wang, "Numerical simulation of a closed wet cooling tower with novel design," *International Journal of Heat and Mass Transfer*, vol. 54, pp 2367-2374, 2011.

[20] Y. Sun, Z. Guan, and K. Hooman, "A review on the performance evaluation of natural draft dry cooling towers and possible improvements via inlet air spray cooling," *Renewable and Sustainable Energy Reviews*, vol. 79, pp 618-637, 2017.

[21] X. Li, H. Gurgenci, Z. Guan, X. Wang, and L. Xia, "A review of the crosswind effect on the natural draft cooling towers," *Applied Thermal Engineering*, vol. 150, pp 250-270, 2019.

[22] D. I. Santoso, B. Antoko, Prabowo, D. Ichsani, "Study of the evaporation process in the spray on a mechanical draft wet cooling tower," *Journal of Engineering and Technological Sciences*, 2020. (accepted article).

[23] D. I. Santoso, B. Antoko, H. Sasongko, T. Yuwono, "Study of the phenomenon of droplet movement along with the height of the cooling tower," *IIUM Engineering Journal*, 2020. (accepted article).

Development and Characterization of Oil Palm Empty Fruit Bunch Fibre Reinforced Polylactic Acid Filaments for Fused Deposition Modeling

Vignesh Sekar, Mazin Zarrouq, Satesh Narayana Namasivayam*
School of Computer Science and Engineering, Taylor's University, No. 1 Jalan Taylor's, 47500 Subang Jaya, Selangor, Malaysia
**svikiviki94@gmail.com*

ABSTRACT

In recent years, Natural Fibre-Reinforced Composites (NFRC) making its impact in all applications, and they have reached their way into the field of Additive Manufacturing (AM) as well. This increases the demand for natural fibre based filaments in the field of AM. Hence, this research aims to develop filaments made of Polylactic acid (PLA) reinforced with Oil Palm Empty Fruit Bunch Fibre (OPEFBF) and to investigate its physical, thermal and mechanical properties. PLA with 10, 20, 30, and 40 wt.% of OPEFBF were melt blended, hot-pressed, and successfully extruded as filaments. Later, its physical, thermal, water absorption, biodegradation, and mechanical properties are investigated. OPEFBF reinforced filaments show lesser values of densities, increased Tensile Modulus (TM), better bio and thermal degradation compared to the pure PLA. However, its rate of water absorption is high with reduced Tensile Strength (TS) than the pure PLA. Later these filaments reinforced with different OPEFBF contents are 3D printed using Fused Deposition Modeling (FDM) technology. Filaments with lesser fibre content were easy to print. Filaments with 10 wt.% OPEFBF was continuously printed whereas, filaments with higher fibre content clogged in the nozzle. Overall, PLA reinforced with OPEFBF has been developed and successfully applied to the field of additive manufacturing by FDM.

Keywords: *Additive Manufacturing, Fused deposition modeling, Natural fibre-reinforced composite, Bio-degradable filament, Oil palm empty fruit bunch fibre.*

ISSN 1823-5514, eISSN 2550-164X

Received for review: 2020-07-06
Accepted for publication: 2020-12-17
Published: 2021-01-15

Introduction

In this present era, Additive Manufacturing (AM) is one of the recognized technologies in all applications because AM helps in developing products with complex shapes and geometry [1]. There are varieties of techniques under AM. Fused Deposition Modelling (FDM) is one of that which is simple and economical. There are only selected thermoplastic polymers which are used in FDM because of its melting and printing temperature [2]. Later, natural fibre/filler reinforced composite (NFRC) filaments come into the business because they are cost-effective and exhibit lower environmental impacts [3]. Out of all the NFRC filaments, PLA-based NFRC receives much attention because of its biodegradability [4]. Table 1 shows the available PLA based NFRC filaments for additive manufacturing.

Table 1: List of PLA based NFRC filaments for AM

Matrix	Filler/Fibre	Filler Content (%)	Properties Tested*	References
PLA	Paulownia Wood	25	T.S	[5]
PLA	Orange Wood	25	T.S	
PLA	Poplar Wood	10, 30	T.S, F.S, I.S	
PLA	Wood powder	0 – 50	F.T, F.S	
PLA	Aspen Sawdust	5	T.S	
PLA	Bamboo	15, 20	F.T	
PLA	Pine Lignin	5	T.S	
PLA	Cork powder	5	T.S	
PLA	TMP	10 – 20	F.T, T.S	
PLA	Sugarcane	3 – 15	T.S, F.S	
PLA	Flax	15	F.T	
PLA	Harekeke	0 – 30	T.S	
PLA	Hemp	0 – 30	T.S	
PLA	Oil Palm Fibre	0 – 40	F.T	This Study

* F.T: Filament Testing, T.S: Tensile Strength, F.S: Flexural Strength, I.S: Impact Strength.

It can be seen from Table 1 that natural fibres/fillers from wood, bamboo, sugarcane, pine, flax, hemp, harakeke are used as reinforcement for PLA. Fibres from oil palm can also be used as reinforcement in producing filaments for additive manufacturing. To demonstrate this, Marwah et al., reinforced fibres from oil palm fronds with high-density polyethylene and produced filaments which were suitable for AM [6]. Ahmad et al., reinforced oil palm fibres with acrylonitrile butadiene styrene and produced filaments which were suitable for AM [7]. Similarly, fibres from Oil Palm Empty Fruit Bunch (OPEFB) can be reinforced with PLA to produce filaments for AM. Oil palm is one of the essential crops, especially in countries like Malaysia and

Indonesia. These two countries are being active contenders for oil palm cultivation and palm oil production [8]. During the production of palm oil, numerous biomasses like fronds, empty fruit bunches, trunks, and shells are produced. Out of all, OPEFB is the second abundant biomass produced after fronds, and it covers 70% of the fibrous portion produced from the tree itself [9]. Almost 65% of OPEFB are being wasted, and therefore researchers are finding a way to use it effectively. These OPEFBF are used in producing low-value products like papers and fibreboards [10]. However, developing high-value products remains a challenge. Hence, this research takes up the challenge of developing filaments for additive manufacturing using OPEFBF, which can be a significant turning point in the field of 3D printing. Only a few pieces of research have been recorded for investigating the mechanical strength of the filament made of natural fibre composite. Kariz et al., produced filaments made of PLA reinforced with wood fibres and studied its morphological, rheological, and mechanical properties. Filgueira et al., fabricated filaments made of PLA reinforced with thermomechanical pulp fibres and analyzed its water uptake and mechanical properties of it. They all have concluded there wasn't a satisfactory mechanical strength obtained from the filaments and they have stated voids and porosity formation in the filament due to the addition of fibres as the main reason [11], [12]. To further investigate the reason for the decrease in mechanical properties of the PLA based natural fibre reinforced filaments, this research has been performed. There are PLA based filaments reinforced with fibres or fillers of wood, dried distilled grains, kraft lignin, hemp, and harakeke, which are in research stages [13]. Additionally, there are also PLA based filaments reinforced with pine wood, bamboo fill, straw, lay wood, and cherrywood fibres, which are commercially available under various trade names [14]. Table 2 shows some of the commercially available PLA based natural fibre reinforced filaments along with the trading companies.

Table 2: List of PLA based NFRC filaments available commercially [14]

Matrix	Natural Fibre/Filler	Company
PLA	Bamboo/bamboo fill	ColorFabb, NL
PLA	Pine/wood fill	ColorFabb, NL
PLA	Laywood/cherrywood	CC products, DE
PLA	Straw plastic/dried crop residues	Jinghe co., CN

As shown, there are a lot of PLA based NFRC filaments that are in the research stage as well as in the commercialization stage. This research was performed to initiate the PLA based filaments reinforced with oil palm fibres into the field of additive manufacturing by FDM technology. There have been many kinds of analysis available on studying the thermal, biodegradation, and

water absorption properties of the composite. They all have concluded that reinforcement of natural fibres into the polymer matrix improves the thermal degradation, increases the water absorption rate, and become easily degradable. However, filaments made of a natural fibre-reinforced composite is a recent trend and hence needs further investigation. Therefore, PLA reinforced OPEFBF filaments, which are produced by extrusion, are studied for its thermal, biodegradation, water absorption properties and are tested for 3D printing by FDM technology.

Materials

PLA pellets were supplied by NatureWorks Corporation. The grade provided was Ingeo™ Biopolymer 2003D with a specific gravity of 1.24 and a melt flow index of 6 g/10 min. Oil Palm Empty Fruit Bunch Fibres (OPEFBF) were outsourced from the nearest palm oil mill. The diameter of the fibres was ranging from 0.2 mm to 0.5 mm, with the length ranging from 20 mm to 40 mm.

Methods

Preparation of the Composite

Fibres are soaked, rinsed, and cleaned to get rid of impurities. The cleaned fibres are sun-dried, followed by oven drying at 60℃ for 24 hours to reduce the moisture content. Later, the dried fibres are grinded and sieved to less than 0.5 mm. PLA pellets are placed in an oven at 60℃ for 24 hours. Once PLA pellets are dried, they are placed in a crucible along with 10, 20, 30, and 40wt.% of dried OPEFBF at different batches and heated at around 210℃ inside an oven. The temperature considered was slightly higher than the average melting temperature of PLA because of the convection inside an oven. Melted PLA, along with fibres, are manually mixed and kept inside an oven. This mixing and heating process was repeated until the materials all well blended to form a composite lump. Further, the composite lumps are pre-heated at 180℃ for 5 minutes in GT-7014-H hydraulic moulding press, and they are hot-pressed with the pressure of 2 tons for 15 minutes, followed by cold pressing for 5 minutes. Improper dispersion of fibres was noted at few places, and it doesn't count much since the composite will undergo further extrusion (melting and winding).

Filament Formation

PLA-OPEFBF composite lumps which are produced by hot-press are crushed into smaller pieces using a mechanical hammer. The crushed composites are then placed into an extruder to produce filaments with different fibre contents.

This pre-process (melt blending and hot-press) reduces the sedimentation of OPEFBF when directly placed into an extruder along with PLA pellets. Table 3 shows the formulation of PLA-OPEFBF composites and filaments.

Table 3: Formulation of PLA-OPEFBF composites and filaments

Code	PLA (wt.%)	OPEFBF (wt.%)
0	100	0
10	90	10
20	80	20
30	70	30
40	60	40

The extruder used was the Wellzoom Desktop Single Screw Extruder. Barrel temperature was kept at 180℃, and the temperature of the die was maintained at 185℃, considering the melting temperature of pure PLA. The screw speed of 20 rpm was maintained. Figure 1 shows the overall methodology used in this research.

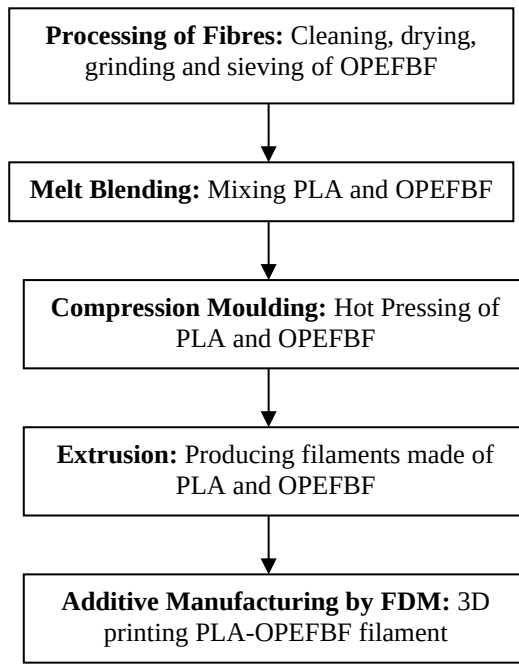

Figure 1: Overall methodology of this research.

Density Calculation

Composites as per type V specimen of ASTM D638 standard and filaments portion with a diameter of approximately 1.75 ± 0.5 mm, length of 90 mm were cut, and their densities (ρ) were calculated using the Equation (1),

$$Density\ (\rho) = \frac{Mass\ of\ the\ composite/filament\ (grams)}{Volume\ of\ the\ composite/filament\ (cu.cm)} \quad (1)$$

Morphological Observation

PLA-OPEFBF filaments were observed under the SWIFT M5 Multi Phase 100 microscope that has 6 volts, a 20-watt halogen bulb for illumination. Filaments were observed under a magnification factor of 4x.

Thermo Gravimetric Analysis

Thermal analysis was carried out using a Pyris Diamond TGA 8000 from PerkinElmer. Samples weighing around (5±1 mg) underwent thermal scanning with the nitrogen atmosphere at a rate of 20 ml/min from 25℃ to 600°C. The heating rate of 10°C/min was considered for the composites and filaments. Composite reinforced with 10wt.% OPEFBF was used to compare with the filament since it has fewer voids compared to the other fibre compositions.

Water Uptake Test

PLA and OPEFBF reinforced filaments with different fibre contents approximately with the length of 60 ± 1 mm, and a diameter of 1.75 ± 0.5 mm were immersed in 100 mL of distilled water for 30 days (720 hours). The filaments were initially dried at 30℃ for 24 hours, and the initial dried weight was measured using Shimadzu TX423L top loading balance with a repeatability of 0.001 g. The samples were taken out after 30 days, and the weight change was measured. This change in weight over time helps in understanding the water absorption properties of the filaments. Water uptake of the filaments was calculated by the following Equation (2) [15],

$$Water\ Uptake\ (\%) = \frac{W_i - W_0}{W_0} \times 100 \quad (2)$$

where, W_0 (g) is the dry weight of the filaments, and W_i (g) is the weight of the filaments after immersion.

Soil Burial Test

Soil burial test was conducted to explain the degradation properties of the filaments. Filaments with a diameter of 1.75 ± 0.5 mm and a length of 60 mm (both pure PLA and OPEFBF reinforced) were buried under the soil for 4 weeks. Organic soil outsourced from Kim Wei Nursery, Malaysia, was used. It contains coco peat, red burnt soil, fine sand, charcoal, and microbes as

constituents. The average atmospheric temperature was around 30°C, with 80% humidity. The buried filaments were taken out after 4 weeks, washed cleanly, and are placed in an oven at 50°C for 12 hours before weighed. Loss of weight over the buried time helps in understanding the degradation properties of the filaments. The loss of weight of the filaments was measured by using the following Equation (3) [16],

$$W_{Loss}\,(\%) = \frac{W_i - W_0}{W_i} \times 100 \qquad (3)$$

where, W_{loss} is weight loss (%), W_i (g) is the initial weight of unburied filaments, and W_0 (g) is the weight of the buried filaments.

Mechanical Testing

Filaments with a diameter of approximately 1.75 ± 0.5 mm and 90 mm length were considered for testing. Tensile testing was performed in an Instron Universal Testing Machine (load cell of 50 kN) at the speed of 20 mm/min as per ASTM D638. Three samples of filaments were considered for each of the formulations. Figure 2 shows the tensile testing setup of PLA-OPEFBF filament.

Figure 2: Tensile testing setup of PLA-OPEFBF filament.

Results and Discussions

Properties of PLA-OPEFBF Filaments

PLA-OPEFBF filaments were successfully produced by extrusion. Figure 3 shows the successfully extruded PLA-OPEFBF filaments with different fibre contents. At higher loadings of fibre content, the processing might be complicated since the fibres will agglomerate in the matrix, which in turn might affect the properties of the filaments [17]. Hence OPEFBF content for filaments considered was less than 40wt.%.

Figure 3: Successfully extruded filaments (Code: 0, 10, 20, 30, and 40).

Filaments produced with 10wt.% OPEFBF content was easy to produce, and as the fibre content tends to increase, OPEFBF starts to agglomerate in the matrix. Filaments with higher fibre contents were hard to process since they did not flow evenly through the nozzle of the extruder. Their diameter was a bit inconsistent, ranging from 1.7 mm to 1.8 mm. Filaments with different fibre content exhibit distinct colour shades and tend to become darker as the content of the fibre increases. Pure PLA filament was consistent in diameter with no voids in it. An increase in fibre content to the filament made them porous, causing shape irregularity and necking by exhibiting crests and troughs around the fibre area. Figure 4 shows the microscopic image of the successfully extruded filaments.

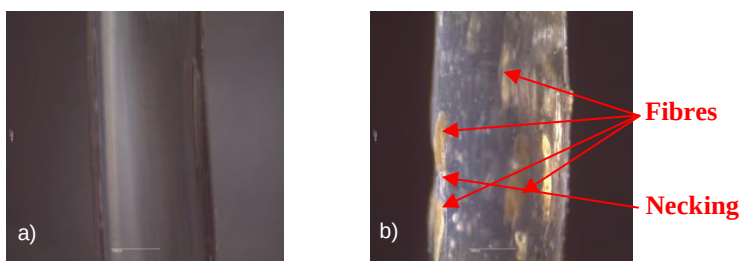

Figure 4: Microscopic image of the successfully extruded filaments (4x) a) PLA filament and b) Sample code 10 filament.

On an overall basis, it was seen that fibre content over a confined region in the composite was higher than the filament. Table 4 shows the densities of PLA-OPEFBF composite and filaments. There was an unusual trend in densities of the filaments can be seen. It might be due to the inconsistency in the diameter of the filaments upon addition of OPEFBF. However, the densities of the filaments reinforced with OPEFBF was found to be lower than the pure PLA filaments. This is because; addition of natural fibres to the polymer filaments makes them porous. This porous nature helps in producing filaments with lower density. This is in accordance with the other research, where they have produced filaments made of PLA reinforced with wood fibres [11].

Table 4: Densities of PLA-OPEFBF composite and filament

Code	Density of the composite (g/cm^3)*	Density of the filament (g/cm^3)*
0	1.17	1.34
10	1.05	0.97
20	1.03	0.87
30	1.03	1.10
40	1.10	1.20

*Average value of three specimens

Thermal Properties of PLA-OPEFBF Composites and Filaments

Figure 5 shows the effect of fibre content on the thermal degradation of the composite. It can be seen from Figure 5 that the first step of a decrease in mass happens between 100℃ to 150℃. This might be due to the loss of moisture content present in the composites. The second and third loss curve occurs between 250℃ to 450℃ might be due to the loss of constituents like lignin, cellulose, and hemicellulose [18]. The second degradation curve of the PLA starts at around 280℃ to 300℃, and the third degradation curve occurs at around 360℃ to 380℃. This is the typical PLA curve which confirms the PLA and has been reported by the previous paper [19]. PLA with 10wt.% OPEFBF reinforcement shows better thermal degradation with the second loss curve at around 350℃ to 400℃ and third loss curve at around 420℃ to 450℃.

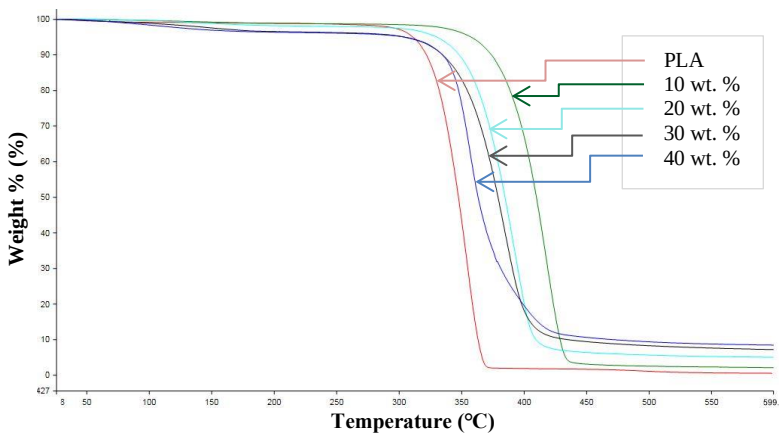

Figure 5: Effect of fibre content on thermal degradation of the composites.

Further increase in fibre content beyond 10wt.% reduces the thermal degradation temperature both at the second and third loss curve. However, all the composites reinforced with OPEFBF exhibit increased thermal degradation

compared to pure PLA. It is evident from the above discussion that all the composites possess better thermal stability nearer to 210℃ and ensures the composites will not degrade at the 3D printing temperature (210℃). Table 5 shows the char residue values at 600℃. PLA with 10wt.% OPEFBF has a lower mass residual at 600℃ and PLA reinforced with 40wt.% OPEFBF has the highest mass residual at 600℃.

Table 5: Char residue values at 600℃

Code	Char Residue at 600℃
40	0.424
30	0.356
20	0.255
10	0.122
10 (Filament)	0.057
0	0.028

Figure 6 shows the comparison of the thermal degradation of PLA-OPEFBF composite and filament.

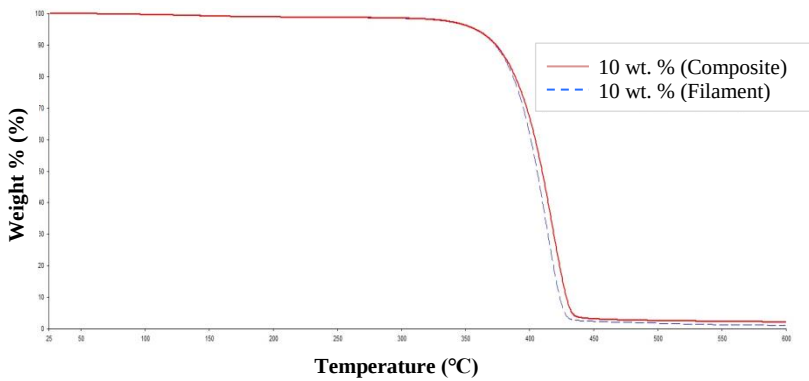

Figure 6: Thermal degradation of PLA-OPEFBF composites and filaments.

It can be seen from Figure 6 that the thermal degradation temperature of the composite is slightly higher than the filaments. It is due to the increased fibre content in the case of the composite, which exhibits higher restricted molecular mobility than the filaments. It can also be seen that the mass residual at 600℃ for the composite is slightly higher than the filament. Hence, the result says the filaments might have a slightly lesser fibre content compared to the composites. This reduction of fibre content is due to the sedimentation effect that happened in the extruder. Again, the OPEFBF reinforced

composites get melted in the heating compartment and guided to the spool winder during extrusion. At this stage, few portions of OPEFBF are deposited in the extruder itself, which was visible during flushing the extruder at each batch.

Water Absorption Properties of PLA-OPEFBF Filaments

Figure 7 shows the effect of fibre content on the water absorption properties of the filaments.

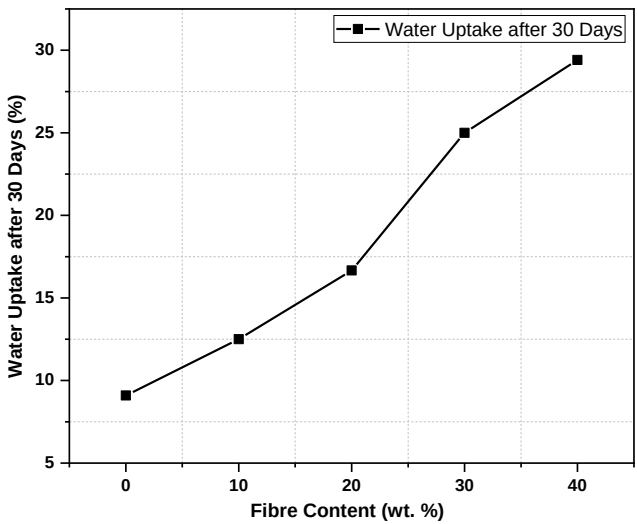

Figure 7: Effect of fibre content on water absorption of the filaments.

It was found that the water uptake content of the OPEFBF reinforced filaments was higher than the pure PLA filaments. The number of OH group increases when OPEFBF are used as reinforcement. These free OH groups tend to form hydrogen bonding when it comes in contact with the water, which leads to the increased weight of the filaments [20]. It can also be seen in Figure 7 that the water absorption of the filaments increases with an increase in fibre content. This is due to increased porosity and hydrophilic sites in the filament, which allows penetration of water molecules, thereby causing an increase in the mass of the filaments. The initial weight of the PLA to 40wt.% OPEFBF reinforced filaments were in the range between 0.11 gms to 0.17 gms respectively, and after 30 days, they were in the range between 0.12 gms to 0.22 gms. Water absorption of the filament reinforced with 40wt.% OPEFBF was 29%, which is 20% higher than the pure PLA filament.

Bio-Degradation Properties of PLA-OPEFBF Filaments

Figure 8 shows the effect of fibre content on the degradation properties of the filaments. It can be noticed from Figure 8 that the weight loss percentage for the OPEFBF reinforced filaments was higher compared to the pure PLA. PLA shows a weight loss of 9% and PLA reinforced filament with 10wt.% to 40 wt.% OPEFBF shows a weight loss of 14% to 21%. This is because OPEFBF is easily degradable in the soil. It can also be noted that the addition of OPEFBF increases the degradation rate. The addition of OPEFBF to filaments caused increased porosity due to poor adhesion between the matrix and the reinforcement.

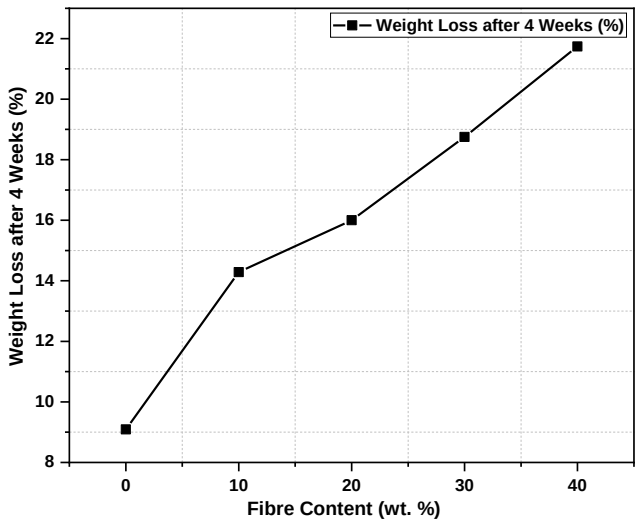

Figure 8: Effect of fibre content on the bio-degradation of the filaments.

This porosity in the filaments allows constituents of the soil and atmospheric moisture and makes the filaments swell in the first stage. In the second stage, fibres would start to aggregate, and wearing might happen, and at the last stage, the polymer chains start to degrade into carbon dioxide and water [16]. This whole mechanism would guarantee the produced PLA-OPEFBBF will be bio-degradable. PLA reinforced with 40wt.% OPEFBF shows 21% weight loss after 4 weeks, 12% higher than pure PLA.

Mechanical Properties of PLA-OPEFBF Filaments

Figure 9 shows the variation of Tensile Modulus (TM) of the PLA-OPEFBF filaments with varied fibre content, respectively. It can be seen from Figure 9

that the TM of the filaments increases upon the addition of OPEFBF. It is due to the stiffness of each OPEFBF involved in the reinforcement [17]. An 18% increase in TM than pure PLA for the 40 wt.% filaments has been recorded.

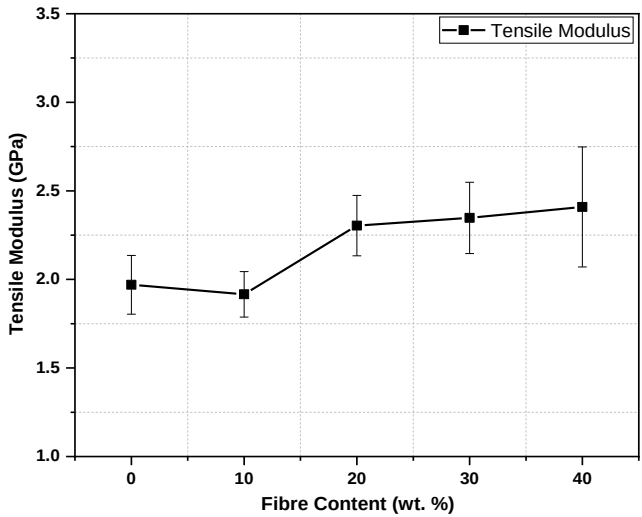

Figure 9: Tensile modulus of the filaments with varied fibre content.

Table 6 shows the tensile modulus and tensile strength of the PLA-OPEFBF with varied fibre content.

Table 6: Tensile modulus and tensile strength of the PLA-OPEFBF filament with varied fibre content.

Code	Tensile Modulus (GPa)	Tensile Strength (MPa)
0	1.97 ± 0.17	35.90 ± 1.36
10	1.92 ± 0.13	22.79 ± 2.38
20	2.30 ± 0.17	13.85 ± 2.04
30	2.35 ± 0.20	12.53 ± 2.22
40	2.41 ± 0.34	12.84 ± 1.84

Figure 10 shows the Tensile Strength (TS) of the PLA-OPEFBF filaments with the varied fibre content. It can be seen from Figure 10 that the TS of the OPEFBF reinforced filaments decrease upon the addition of fibres. This reduction in TS is due to the increased void content upon the addition of fibres. This is in accordance with the researches when NFRC based filaments

are produced with PLA as a matrix [11], [12]. The reduction of fibre content during the conversion of PLA-OPEFBF composite to the filament has happened could also be the reason for the reduction in the mechanical properties of the filaments.

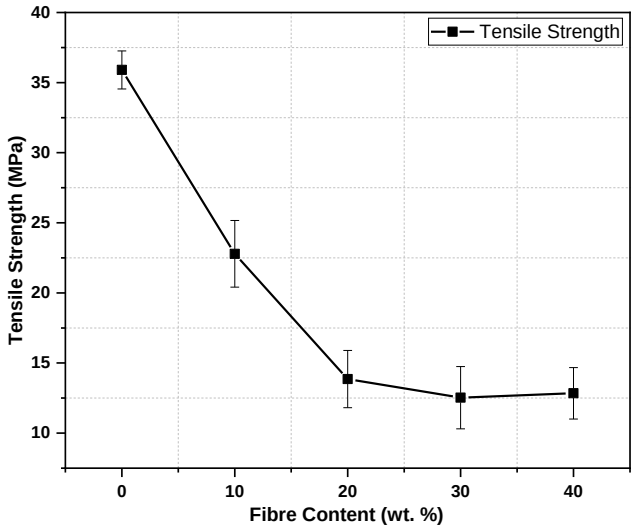

Figure 10: Tensile strength of the filaments with varied fibre content.

The reduction of fibre content in the filament is due to the sedimentation effect during the extrusion. It means that the extrusion hasn't happened effectively in producing filaments with enough reinforcement. Pre-treating the natural fibres could be considered an option to increase the interference between the polymer and reinforcement, which increases the mechanical properties of the filament [12]. We have not considered treating the fibres because we felt the usage of chemicals used during the pre-treatment might affect the 3D printers. However, in recent times, many researchers used different chemicals for treatments, compatibilizers, toughening agents, and plasticizers to improve the adhesion between the polymer and reinforcement and have successfully 3D printed the filaments [5]. Hence, further studies will be performed to increase the mechanical properties of the PLA-OPEFBF filament by adopting those techniques, as mentioned above.

3D Printing of PLA-OPEFBF Filaments

PLA-OPEFBF filaments produced by extrusion are 3D printed using FDM technology with the help of Raise 3D N2 Plus printer. The diameter of the

nozzle was 0.4 mm, and the printing temperature considered was 210℃ at a rate of 70 mm/s. It was harder to print the filaments with higher fibre content because of the increased inconsistent diameter regions. Also, increased fibre content increases the probability of nozzle clogging during the process. Filaments with 10wt.% OPEFBF was more accessible to 3D print since it has lower regions of inconsistent diameter. Table 7 shows the results of 3D printing the PLA-OPEFBF filament with different fibre content.

Table 7: Results of 3D printing the PLA-OPEFBF filaments with different fibre content

Code	Meting Temperature	Results of 3D Printing
10	210℃	Successful and Continous
20	210℃	Successful and Non-Continous
30	210℃	Unsuccessful
40	210℃	Unsuccessful

Filament with lower fibre content flows evenly and smoothly through the nozzle, and as the fibre content increases, the process becomes complicated. We know the fact that FDM is a melt extrusion method, and it works in the way that OPEFBF reinforced filament enters into a heating compartment, gets heated up, and the melted portions are passed out through the nozzle of the 3D printer. During this process, a few portions of OPEFBF get sedimented, which inturn clogged the nozzle, and as the fibre content increases, the higher the chance of getting clogged. Figure 11 shows the results of 3D printing the PLA-OPEFBF filament with different fibre content. Also, the temperature of the 3D printing process was kept constantly at 210℃ for the filaments with different fibre contents. This temperature may not be ideal for the filaments with different fibre contents since increasing the percentage of OPEFBF would change the melting temperature of the resulting mixture. As a result, 3D printing the filament with a higher fibre content of OPEFBF turns to be tedious. Hence, further investigation is needed to identify the exact process temperature for the filaments with different fibre contents. 3D printed structures were found to be hollow with inconsistent filament flow, and cavities have been noticed at fewer places. This was due to the slip-stick extrusion defect during the printing process, which causes poor surface finish and poor adhesion amongst the layers. Similar justification has been addressed by Stoof et al., when they initiated the 3D printing of natural fibre-reinforced composites [21].

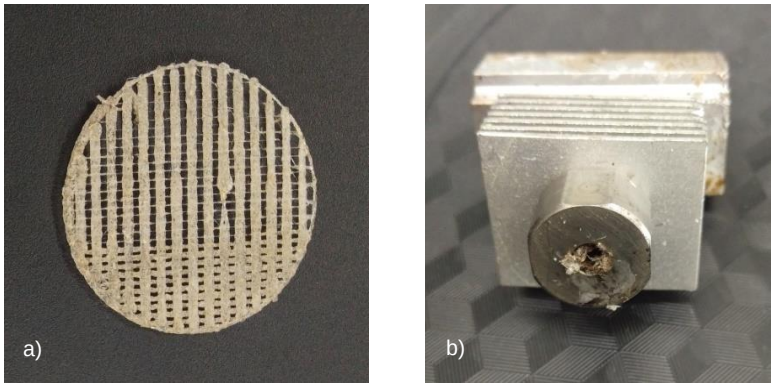

Figure 11: Results of 3D printing the PLA-OPEFBF filaments with different fibre content. a) Successfully 3D printed code 10 filament b) Clogged nozzle during 3D printing of code 30 filament.

Conclusion

PLA reinforced with varying contents of OPEFBF filaments have been produced and investigated for its physical, thermal, water absorption, biodegradation, and mechanical properties. TGA results infer that the OPEFBF reinforced filaments offer better thermal degradation than the pure PLA, and it also proves that the filament can withstand the process temperature (210°C) of 3D printing without degradation. 40 wt.% OPEFBF reinforced filament shows an increase in 18% of tensile modulus over pure PLA. The mechanism involved in bio-degradation reveals the filaments are environment friendly. However, these OPEFBF reinforced filaments with increased water absorption and reduced tensile strength, hinder it from being applied for real-time applications. Increased porosity due to the addition of fibres and decreased amount of reinforcement in the filaments due to sedimentation effect inside the extruder has been provided as reasons for the reduced tensile strength. Later, these filaments are tested for 3D printing. Filaments reinforced with 30 and 40 wt.% of OPEFBF gets clogged in the 3D printer. Clogging in the nozzle is due to inconsistency in the diameter of the filaments as the fibre content increases. Also, few portions of OPEFBF gets sedimented in the heating compartment of the 3D printer gets carried away and clogged the nozzle of the printer. However, filaments reinforced with lesser contents of OPEFBF gets successfully printed. By doing so, this research shows the importance of producing filaments from the agricultural and industrial waste of oil palm, which can contribute to the community of additive manufacturing for

commercialization. Further studies will be performed to make the filaments more effective and to be applied for real-time applications.

Acknowledgement

This work was partially sponsored by Taylor's University Flagship Research Grant TUFR/2017/001/05. The author is thankful to Taylor's University for funding scholarship during this research work.

References

[1] S. N. H. Mazlan, M. R. Alkahari, F. R. Ramli, and M. N. Sudin, N. A. Maidin, O. K. Sun, "Manufacturability of Mechanical Structure Fabricated using Entry Level 3D Printer," *Journal of Mechanical Engineering*, vol. 5, no. 3, pp 98-122, 2018.

[2] N. A. Sukindar, M. K. A. M. Ariffin, B. T. H. T. Baharudin, C. N. A. Jaafar and M. I. S. Ismail "Optimization of the Parameters for Surface Quality of the Open-source 3D Printing," *Journal of Mechanical Engineering*, vol. 3, no. 1, pp 33-43, 2017.

[3] S. Yunus, A. H. Abdullah, N. H. A. Halim, Z. Salleh and Y. Md. Taib, "Low Energy Impact on the Short Kenaf Fibre Reinforced Epoxy Composites : Effect to the Residual Strength and Modulus." *Journal of Mechanical Engineering*, vol. 12, no. 2, pp 72-3, 2015.

[4] M. N. Hafsa, N. Kassim, S. Ismail, S. A. Kamaruddin, T. M. Hafeez, M. Ibrahim and Z. H. Samsudin, "Study on Surface Roughness Quality of FDM and MJM Additive Manufacturing Model for Implementation as Investment Casting Sacrificial Pattern," *Journal of Mechanical Engineering*, vol. 5, no. 6, pp 25-34, 2018.

[5] V. Mazzanti, L. Malagutti, and F. Mollica, "FDM 3D printing of polymers containing natural Fillers: a review of their mechanical properties," *Polymers*, vol. 11, no. 7, pp 1094, 2019.

[6] O. M. F. Marwah, N. F. A. Halim, M. S. Shukri, E. J. Mohamad, and M. Ibrahim, "A study on palm fiber reinforces as a filament in portable FDM," *ARPN Journal of Engineering and Applied Sciences*, vol. 11, no. 12, pp 7828– 7834, 2016.

[7] M. N. Ahmad, M. K. Wahid, and N. A. Maidin, M. H. Ab Rahman, M. H. Osman, I. F. A. Elias, "Mechanical characteristics of oil palm fiber reinforced thermoplastics as filament for fused deposition modeling (FDM)," *Advances in Manufacturing*, vol. 8, pp 72-81, 2020.

[8] H. J. W. Mutsaers, "The challenge of the oil palm : Using degraded land for its cultivation," *Outlook on Agriculture*, vol. 48, no. 3, pp 190-197 2019.

[9] K. H. Or, A. Putra and M. Z. Selamat, "Oil palm empty fruit bunch fibres

as sustainable acoustic absorber," *Applied Acoustics,* vol. 119 (2017), pp 9-16, 2017.

[10] E. O. Momoh and A. I. Osofero, "Recent developments in the application of oil palm fibers in cement composites," *Frontiers of Structural and Civil Engineering*, vol. 14 , no. 1, pp 94-108, 2020.

[11] M. Kariz, M. Sernek, M. Obućina, and M. K. Kuzman, "Effect of wood content in FDM filament on properties of 3D printed parts," *Materialstoday communications*, vol. 14 (2018), pp 135–140, 2018.

[12] D. Filgueira, S. Holmen, J. K. Melbø, D. Moldes, A. T. Echtermeyer, and G. Chinga-Carrasco, "Enzymatic- assisted modification of thermomechanical pulp fibers to improve the interfacial adhesion with poly(lactic acid) for 3D Printing," *ACS Sustainable Chemistry and Engineering*, vol. 5, no. 10, pp. 9338–9346, 2017.

[13] V. Sekar, M. H. Fouladi, S. N. Namasivayam, and S. Sivanesan, "Additive Manufacturing : A Novel Method for Developing an Acoustic Panel Made of Natural Fiber-Reinforced Composites with Enhanced Mechanical and Acoustical Properties," *Journal of Engineering,* 19 pages, 2019.

[14] B. Tisserat, Z. Liu, V. Finkenstadt, B. Lewandowski, S. Ott, and L. Reifschneider, "3D printing biocomposites," *Journal of Plastics Research Online 2015 (Society of Plastics Engineers),* pp 1–3, 2015.

[15] N. V. David and M. Azlan, "Moisture Absorption Properties and Shock Cushioning Characteristics of Bio-Based Polyurethane Foam Composites," *Journal of Mechanical Engineering*, vol. 5, no. 2, pp 157-168, 2018.

[16] A. K. M. M. Alam, M. D. H. Beg, M. F. Mina, A. A. Mamun, and A. K Bledzki "Degradation and stability of green composites fabricated from oil palm empty fruit bunch fiber and polylactic acid : Effect of fiber length," *Journal of Composite Materials*, vol. 49, no. 25, pp 3103-3114, 2014.

[17] M. D. H. Beg, J. O. Akindoyo, S. Ghazali, and A. A. Mamun, "Impact modified oil palm empty fruit bunch fiber/poly (lactic) acid composite," *International Journal of Chemical, Nuclear, Materials and Metallurgical Engineering*, vol. 9. no. 1, 2015.

[18] T. Ohkita and S. H. Lee, "Thermal degradation and biodegradability of poly (lactic acid)/corn starch biocomposites," *Journal of Applied Polymer Science*, vol. 100, no. 4, pp 3009-3017, 2006.

[19] M. H. Fouladi, S. N. Namasivayam, V. Sekar, P. Marappan, H. L. Choo, T. K. Ong, R. Walvekar and C. Baniotopoulos "Pretreatment Studies and Characterization of Bio-Degradable and 3d- Printable Filaments from Coconut Waste," *International Journal of Nanoelectronics and Materials*, vol. 13(Special Issue), pp 137–148, 2020.

[20] N. I. Ismail and Z. A. M. Ishak, "Effect of fiber loading on mechanical and water absorption capacity of Polylactic acid / Polyhydroxybutyrate-co- hydroxyhexanoate / Kenaf composite," *IOP Conf. Series: Materials*

Science and Engineering, vol. 368 (2018), pp 012-014, 2018.
[21] D. Stoof and K. Pickering and Y. Zhang "Fused deposition modelling of natural fibre/polylactic acid composites," *Journal of Composites Science*, vol. 1, no. 1, pp 8, 2017.

A Regression Analysis: Ergonomic Comfort vs. Air Quality, Noise, Lighting and Temperature in the Composite Trimming Process Working Room

A. Shukur, N.I.S Hussein, S.R. Kamat*
Faculty of Manufacturing Engineering,
Universiti Teknikal Malaysia Melaka, Hang Tuah Jaya,
76100 Durian Tunggal, Melaka, Malaysia.
**azurin@mara.gov.my*

D.Yuniawan
Faculty of Technic, University of Merdeka Malang, East Java, Indonesia

ABSTRACT

This study was set to identify how working environment affected workers' comfort and to determine the maximum level of air quality, noise, lighting and temperature allowed for each working environment. Workers seemed uncomfortable with the working environment in the working room. To validate the situation, a survey was conducted in the present study on all workers who were involved in the cutting process to determine their feelings in certain setting environment conditions. Next, the environment values were obtained by using specific and certain measurement tools. All the data taken from these two conditions were analyzed using the Minitab software. The study found that most of the working environment parameters in the trimming room exceeded the maximum allowable level of ISO standards. For air quality an average of 30% RH was obtained, which was below the allowable value of 40 – 60% RH. For noise, the obtained value was about 150 dB, which exceeded the maximum level of 85 dB. For in-room lighting, the obtained value was about 200 lux; far below the ISO standard of 750 lux and finally, for temperature the obtained value was about 31.7^{0}C, which was higher than ISO standard of 26^{0}C. It can be concluded that all the working environments do not contribute to good feeling to the workers while doing their job in that room. This means that measures need to be taken to

ISSN 1823-5514, eISSN2550-164X
Received for review: 2020-08-12
Accepted for publication: 2020-12-10
Published: 2021-01-15

overcome the situation in order to improve the workers' feelings and provide them with comfort while doing their job.

Keywords: *Working Environment; Workers' Comfort*

Introduction

This study was conducted at ABC company at Batu Berendam, Melaka. The company produces ceramic panels for airplanes. This study focuses on the effect of working environment on the workers' comfort. It is generally known that physical working environment at workplace is the top requirement that employers need to provide for the workers for their pleasure, comfort and satisfaction. Workers' performance will be affected by this environment and it has been proven to have a significant impact on job satisfaction. There are several factors that contribute to job satisfaction such as lighting, noise, air quality and working room temperature. In this study, discussing human ergonomic in working environment such as air quality (air ventilation in working room), noise and lighting is inevitable [1].

Today, ergonomic concepts in the working environment of work are increasingly relevant in the field work since development encompasses human life for fun. Several studies conducted by previous researchers have proven to be relevant ergonomic factors in the workplace that influence the level of job satisfaction [1, 2, 3, 4] that carried out their research in circles respondents and the scope of employment. Workers will feel dissatisfied if the light condition is not good [5]. Several environmental factors also contribute to body fatigue and job dissatisfaction with heat and noise at work as the main factor [6].

The main purpose of this paper is to analyze the working environment factors that contribute to the workers' comfort, especially in a manufacturing plant. This is based on previous studies done by Nur Asilah that proved the existence of significant correlation between ergonomic factors and level of job satisfaction among employees due to its existence of sudden take-rest problems caused by fatigue among most local production workers [7]. The study was done by conducting an initial interview with a human resource officer in the study organization, which proved that there was a problem of job dissatisfaction among the workers expenditure in the research organization. This problem contributed to decreased motivation for performing tasks, increasing the rate of termination and consequently decreasing factory productivity [7]. Interviews were also conducted with some workers which found that fatigue and discomfort problems occurred in carrying out the task due to the environmental conditions in their organization [7].

Physical conditions of the workplace in terms of environmental ergonomics, occupational health, and work psychology includes lighting, noise, temperature, relative humidity, and air flow rate [8-10]. Exposure to noise because of work is in connection with negative effects on human health, and its connection with being deaf has been substantiated. In industrial environment, exposure to the noise is in connection with a vast range of physical effects on health. In this regard, we can mention heart disease and absence due to work illness and tiredness [11]. The direct and indirect influences of lighting intensity on human productivity and capacity as another environmental factor have been examined in various studies, such as improvement of lighting condition which will decrease vision disturbance and neck and shoulder pains [12]. Given the above, levels of noise and light by directly and indirectly affecting physical and mental aspects, impact human productivity and performance [15].

The objective of the study is to find out whether the current working environment condition in the working room affect the comfort of workers. This can be achieved through the collection of environmental data and also a survey on workers, which is then analyzed using Minitab software to prove the environmental conditions faced indeed affect the comfort of workers, either in a good way or vice-versa, and to determine the extent to which the reading value of the environment complies with set standards.

Thus, keeping work environment safe and healthy, along with providing human health and comfort, and increasing their productivity and performance will increase an organization's productivity and will also increase quality and quantity of its products and services.

Methodology

The data of all the environment factors were taken at the workplace of the workers to get the real data in a real working room environment during the composite panel cutting process. Firstly, the data for all of these parameters (working environment conditions) were obtained while the workers were doing trimming composite panel in a closed workroom by using specific measurement tools. For air quality and temperature data, a measurement tool called Temperature and Humidity Data Logger was used, a Dosimeter was used for noise data, and a Lux meter for lighting data. All the measurement tools are brought in the cutting room to get the actual value in the room. All the data were taken inside the cutting room in the morning. Using different timings of the day, however, will not affect the data value.

The data were then processed using the Minitab software and at this stage, the system asked for a response value. To get the response value, a survey needed to be done on the 10 workers to get the feedback for every

type of working room environment condition. The survey form employed a scale from 1 to 5 where 1 indicated most uncomfortable, 2 for not comfortable, 3 for less comfortable, 4 for comfortable and 5 for most comfortable. There were 19 sets of working environment conditions that were asked in the survey form. For example, for condition set no. 1, the condition: air quality was 30%RH, working room temperature was 29.8^0C, noise was 120dB and lighting was 150 lux. The workers were required to indicate their own feelings in every condition. Finally, the data were compiled, analyzed descriptively and presented in a graphical form by using Minitab software. The data collected is recorded in the Table 1. Figure 1 shows the flow process of the study. The data in Table 1 were subsequently entered and processed using Minitab application software. Then, the software generated a result in the form of graphs for further analysis to obtain relevant conclusions.

Table 1: The working environment data during the cutting process on 13/3/2017

No	Working Environment	Inside cutting room (min)	Inside cutting room (max)
1	Air Quality	30%RH	58.7%RH
2	Temperature	29.8^0C	31.7^0C
3	Noise	120dB	130dB(3mm), 150dB(5mm)
4	Lighting	150-200 lux	150-200 lux

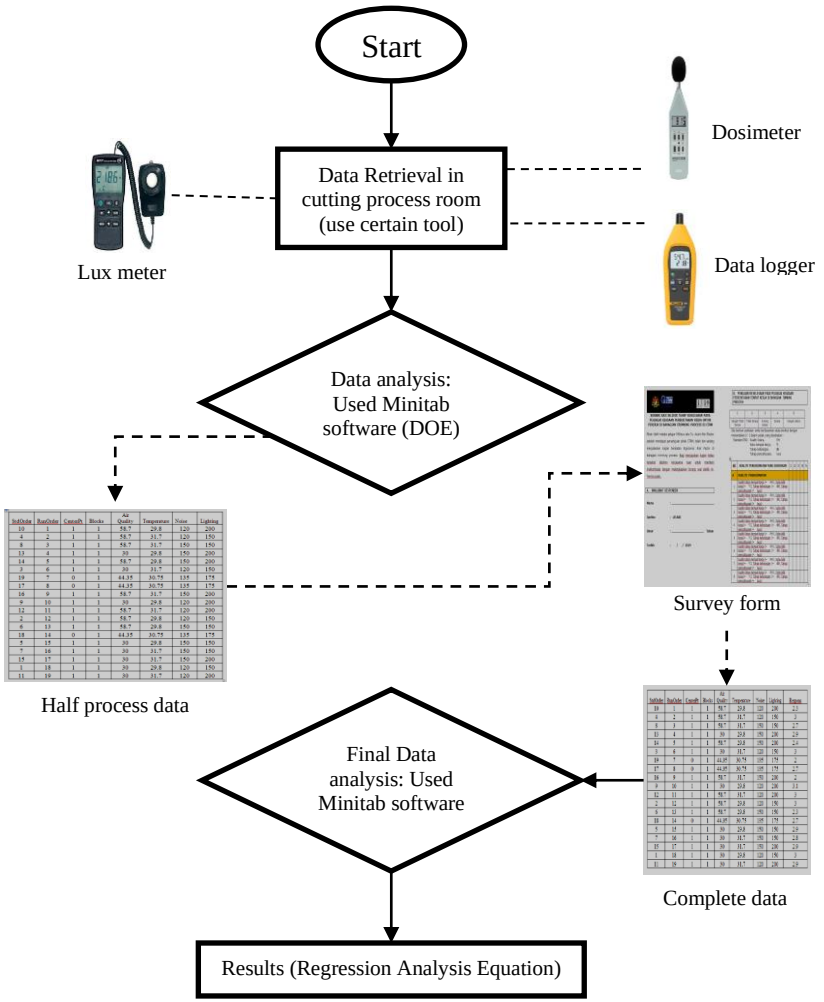

Figure 1: The flow process of study.

Results and Discussion

The present study employed a Regression analysis method because it is a reliable method of identifying which variables have an impact on a topic of interest. The process of performing a regression allows you to confidently determine which factor matters most, which factor can be ignored, and how these factors influence each other. The result below are generated using raw

data from Table 1 and the data from the survey are processed using Minitab software (DOE - Full Factorial design). The result is shown in Table 2.

Table 2: Regression Analysis: Ergonomic Comfort versus Air Quality, Noise, Lighting: Analysis of DOE

	DF	Adj SS	Adj MS	F-Value	P-Value
Regression	4	0.95000	0.23750	2.74	0.071
Air Quality	1	0.49000	0.49000	5.64	0.032
Temperature	1	0.01000	0.01000	0.12	0.739
Noise	1	0.36000	0.36000	4.15	0.061
Lighting	1	0.09000	0.09000	1.04	0.326
Error	14	1.21526	0.08680		
Lack-of-Fit	12	0.88860	0.07405	0.45	0.847
Pure Error	2	0.32667	0.16333		
Total	18	2.16526			

The smaller the P-Value obtained, the greater the impact of the performance properties which total employee comfort. Table 2 shows the results of analysis of DOE. Through this analysis, the factor of air quality is the most impactful factor followed by noise. Thus, this finding has proven that in the actual condition, air quality and noise are very bad to the workers' feelings. The other factors such as lighting and temperature, although give an impact to the worker comfort, are not as bad as air quality and noise. Among air quality, noise, temperature and lighting, there is no correlation between them and they are independent factors. However, the analysis shows that all of them give an impact to the workers' comfort. In this case, it clearly shows that the air quality factor greatly influences the rate of workers' comfort. For controlling dust method, although an effort has been taken by using the dust collector, it still contributes to poor air quality due to poor air ventilation in the working room. The ideal relative humidity is 40% – 60% RH [14].

In this study, the working room is not well-ventilated, causing the working room temperature to be a little bit higher than the normal room temperature. This is followed by the noise produced from the cutting tool while cutting the composite panel which is quite high i.e. exceeding 85 db.

Table 3: Model Summary

S	R-sq	R-sq(adj)	R-sq(pred)
0.294626	43.87%	27.84%	6.91%

From Table 3, it can be seen that the R-sq (pred) percentage is 6.91% and this value is much smaller and it should be approaching 100%. This means the data obtained for the ergonomic risk response exceeds the max allowable limit. This is because in this study, the feedback provided by the respondents almost entirely mentioned uncomfortable, in which 80% mentioned not satisfied with the set of environment conditions in the survey practices.

Table 4: Coefficients

	Coef	SE Coef	T-Value	P-Value	VIF
Constant	4.32	2.54	1.70	0.111	
Air Quality	0.01220	0.00513	-2.38	0.032	1.00
Temperature	0.0263	0.0775	0.34	0.739	1.00
Noise	0.01000	0.00491	-2.04	0.061	1.00
Lighting	0.00300	0.00295	-1.02	0.326	1.00

From Table 4 that is automatically generated from the analysis, every coefficient value for every single parameter can be extracted from the coefficient column to automatically generate the regression formula or equation for ergonomic comfort as shown below:

Regression Equation (Ergonomic Comfort, EC):

$$EC = 4.32 - 0.01220\ Air\ Quality + 0.0263\ Temperature - 0.01000\ Noise - 0.00300\ Lighting \quad (1)$$

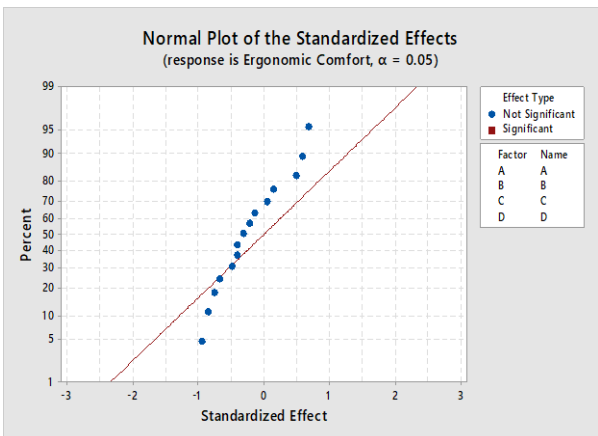

Figure 2: The normal plot of the standardized effects for Ergonomic Comfort.

In Figure 2, Figure 3 and Figure 4, A refer to Air Quality, B refer to Temperature, C refer to Noise and D refer to Lighting. In the Figure 1, there is no significant point indicating all the abnormal factors and in Figure 2, all factors are located far behind the red line 4.303 indicating that all factors are not suitable for the working environment, which is always at an unbalanced level.

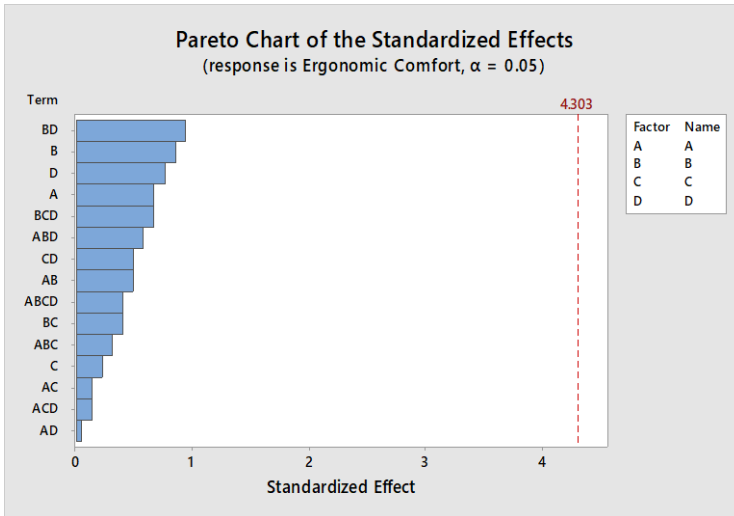

Figure 3: The Pareto chart of the standardized effects.

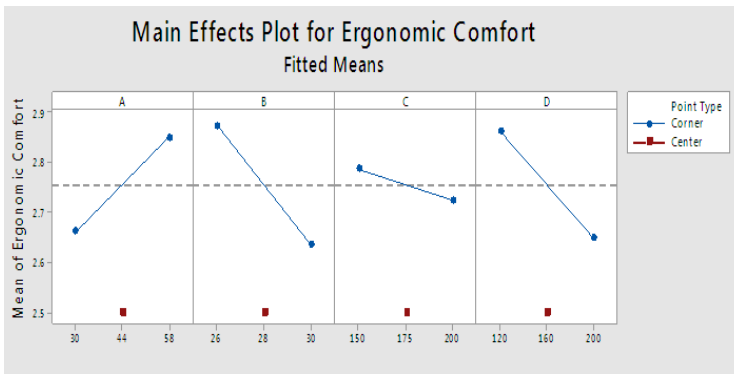

Figure 4: The main effects for Ergonomic Comfort.

In Figure 3, the largest value for each factor is taken (A: Air quality = 58, B: Temperature = 26, C: Noise = 150, D: Lighting = 120) and is included in the generated formula (1) for validation calculation purpose as below.

$$EC = 4.32 - 0.01220\,(58) + 0.0263\,(26) - 0.01000\,(150) - 0.00300\,(120)$$
$$= 4.32 - 0.71 + 0.684 - 1.5 - 0.36$$
$$= 2.434$$

$$\text{Ergonomic Comfort Actual value} = 2.72$$

$$\text{Validation} = (2.434 - 2.72)/(2.434) \; x \; 100\% = \mathbf{11.75}\%$$

Validation for Ergonomic Comfort (EC) was found to be more than 10% as all respondents stated that they were uncomfortable, as a result of the surveys conducted on them for various combinations of factors, namely sound, air quality, lighting and temperature. Workers are uncomfortable in most of the factors associated with composite cutting work, especially sound and lighting factors.

With reference to the ISO 45001:2018, this standard mentioned the importance of identifying the cause of certain problems that can affect the mood or morale of the workers. This study found that discomfort resulting from an unconducive work environment during the cutting process and also the need to do an assessment of this matter as the cause. It is revealed that the management of the company does not take such things seriously to comply with the above-mentioned standard. The results of this study show that the working environment is not very good, and this indicates that the management does not do as recommended in the ISO standard with regard to increasing workers' productivity and morale. Apparently in this study the management needs to improve the working environment.

Several studies done by other researchers were given certain result regarding to the working environment and workers comfort. From Thach [23] study found that noise gave the most effect to the workers stress followed by thermal comfort and air quality and lighting.

This finding is in line with the opinions of Shikdar and Sawaqed [6] who agree that layout factors and comfortable workspace in an organization can maximize productivity, improve performance and job satisfaction. Therefore, it is the employer's responsibility to provide a workplace with good layout and ergonomic features in an organization to ensure the optimum level of comfort among the workers is capable of improving efficiency and job satisfaction.

The findings are consistent with Haiying Wong's who found in his study that 70% of workers had voted comfortable when the temperature was

under 28.9 ^{0}C and most of them were slightly uncomfortable when the temperature increased to 32 ^{0}C and higher [15]. However, workers had low expectation on their working environment and were more easily to be satisfied owing to a limited choice [15].

In a study by Modesta Kameni Nematchoua, a significant effect of the similar indoor environment (air quality, temperature and lighting) on workers performance by using formula that had been generated using INOVA was found [16]. It also found that air temperature has a significant effect in the workers' productivity [16]. Lan et. Al reported that by increasing the indoor temperature to above 28 ^{0}C, the concentration rate of workers reduced by 0.5% [17].

Taffrere said that occupational exposure to heat and noise were found to exceed occupational exposure limits [18]. Any sound environment will be subjected to a substantial number of sound sources that affect ordinary human activities, people's concentration and mood [19]. Most people today spend a great deal of time at work, so it would be desirable that their work environment is acoustically pleasant in order to ensure effective work and satisfaction of the workers. Results from Sun study has illustrate that when exposed to high ILL, U-ILL and CCT environment, participants reported highest satisfaction on productivity and attention, while lowest score on stress, difficulty of conducting work and fatigue [20].

The other result from Sidek shows that the level of satisfaction on the three dimensions of workplace ambient is more than 4.5 out of 7 Likert scale, which implied that the workers are somehow satisfied with their workplace ambient denying the claim of extreme workplace ambient and forced labour practice in the Malaysia Government related palm oil mills [21]. The analysis revealed 6 factors with 18 related elements. From a multi linear regression analysis, we develop a job satisfaction model built on factors of human resource policies, safety, ergonomics, air quality, thermal comfort and disturbing equipment. The results reveal that ergonomics plays the most important role in workers' satisfaction for the respondent Turkish automotive workers [22].

Conclusion

The results of the study revealed that the workers felt that their working environment was stressful. It was also found that the workers had been working under bad working environments with most of the working environment factors exceeding the limit of the ISO standards value. This has contributed to an unbalanced result on regression analysis in Minitab. From the ISO Safety Management System (ISO 45001:2018) [13], the working environment in that working area does not comply with ISO 45001, which

sets the minimum standard of practice to protect workers worldwide such as opportunity to introduce other health, and safety aspects such as worker wellness/wellbeing, and improving worker protection. It is hoped that the results of this study will be used as a guide by other researchers in the future by using the formula generated from this regression analysis and subsequently become a reference or main reason to make improvements to the work process or environment.

Acknowledgments

The author would like to thank the Faculty of Manufacturing Engineering, Universiti Teknikal Malaysia Melaka for the facilities support. The author is also grateful to the Majlis Amanah Rakyat (MARA) and Institut Kemahiran MARA Jasin for their support during the author's postgraduate studies.

References

[1] Zafir Mohamed Makhbul & Fazilah Mohd Hasun. "Ergonomik dan tekanan di Malaysia Implikasi Terhadap Teori, Metodologi dan Pengurusan." *Jurnal Pengurusan*, vol. 26, pp 99-130, 2007.

[2] Siti Zawiah Md Dawal & Zahari Taha, "The effect of job and Environmental factors on job satisfaction in automotive industries", *International Journal of Occupational Safety and Ergonomics*, vol. 12, no.3, pp 267-280, 2006.

[3] Zafir Mohamed Makhbul, Durrishah Idrus & Mat Rebi Abdul Rani. "Ergonomics design on the work stress outcomes." *Jurnal Kemanusiaan*, vol. 9, pp 50-61, 2007.

[4] Zafirah Ab Muin & Maimunah Sapri, "Level of organization on the Importance of ergonomics to health and safety at the workplace." *4th International Conference on Business and Economic Research Proceeding*, Bandung, Indonesia, 2013.

[5] Sarimah Ismail & Faridatul Akmar Talip, "Kepuasan Bekerja Staf Akademik Jabatan Pendidikan Teknikal Dan Kejuruteraan Fakulti Pendidikan, Universiti Teknologi Malaysia, Skudai." *The 2nd International Conference on Business Management 2nd ICBM 2016*. Universiti Teknologi Malaysia, Skudai, Johor, 2010.

[6] Shikdar, A. A. & Sawaqed, N. M. "Worker productivity and occupational Health and safety issues - in selected industries." *Computers and Industrial Engineering*, vol. 45, no.4, pp 563-572, 2003.

[7] Nur Asilah Mohd. Taib, "Kepuasan kerja dalam kalangan operator Pengeluaran", Universiti Utara Malaysia, Sintok, 2015.

[8] K. C. Parsons, "Environmental ergonomics: a review of principles, methods and models." *Applied Ergonomics*, vol. 31, no. 6, pp 581–594, 2000.
[9] Minyoung Kwon, Hilde Remoy, Maartje Van den Bogaard "Influential design factors on occupant saqtisfaction with indoor environment in workplaces." *Building and Environment*, vol. 157, pp 356-365, 2019.
[10] E. Sundstrom and M. G. Sundstrom, "Workplaces: The Psychology of Physical Environment in Offices and Factories." *Cambridge University Press*, United Kingdom, 1986.
[11] P. Leather, D. Beale, and L. Sullivan. "Noise, psychosocial stress and their interaction in the workplace." *Journal of Environmental Psychology*, vol. 23, no. 2, pp 213–222, 2003.
[12] A. Aarås, G. Horgen, H.-H. Bjørset, O. Ro, and H. Walsøe. "Musculoskeletal, Visual and psychosocial stress in VDU operators before and after multidisciplinary ergonomic interventions. A 6 years prospective study —part II." *Applied Ergonomics*, vol. 32, no. 6, pp 559 - 571, 2001.
[13] Brad Kelechava. (2018). The Benefits of ISO 45001. [Online]. Available: https://blog.ansi.org/
[14] Sterling EM et al. (1985). Criteria for human esposure to humidity in occupied building. [Online]. Available: www.codair.com-
[15] Haiying Wong, "Thermal Environment Investigation and Analysis on Thermal Adaptation of Workers in Rubber Factory." *Energy and Building*, vol. 158, pp 1625-1631, 2018.
[16] Modesta Kameni Nematchoua. "Influence of Indoor Environment Quality on The Self Estimated Performance of Office Workers in The Tropical Wet And Hot Climate of Cameroon." *Journal of Building Engineering*, vol. 21, pp 141-148, 2019.
[17] P. Lan, Z Lian, "Use of Neurobehavioral Tests to Evaluate the Effect Indoor Environment Quality on Productivity." *Building Environment*, vol. 44, pp 2208 - 2217, 2009.
[18] Taffere G.R. "Magnitude of occupational exposure to noise, heat and associated factors among sugarcane factory workers in Ethiopia." *Journal of Public Health (Germany)*, vol. 28, issue 5, pp 517-523, 2020.
[19] Suhanek. M, "A case study of different sound environments – a way to a more pleasant and more efficient work." *Sigurnost*, vol. 61, Issue 4, pp 345-356, 2019.
[20] Sun. "Work performance in relation to lighting environment in office buildings." *Indoor and Built Environment*, vol. 28, Issue 8, pp 1064-1082, 2019.
[21] Sidek. "People sustainability in palm oil production: The influence of production technology on workplace ambient." *IEEE Region 10 Humanitarian Technology Conference, R10-HTC 2015-co-located with*

8th International Conference on Humanoid, Nanotecnology, Information Technology, Communication and Control, Environment and Management, HNICEM 201525 January 2016, Articul number 7391849.

[22] Ozturkoglu. "A manufacturing-oriented model for evaluating the satisfaction of workers-Evidence from Turkey." *Industrial Journal of Industrial Ergonomic*, vol. 54, pp 73-82, 2016.

[23] Thach, "Associations of perceived indoor environment of quality with stress in the workplace." *Indoor Air*, vol. 30, pp 1166-1177, 2020.

Design of an Environmental Stress Cracking (ESC) Tester using Fracture Mechanics Approach

*Muhamad Syafiq Mohamad Nor Azli, Muhammad Faris Mohd Radzi, Muhammad Naguib Ahmad Nazri, Mohd Shahneel Saharudin**
Universiti Kuala Lumpur Malaysia Italy Design Institute (UniKL MIDI), Taman Shamelin Perkasa, Cheras Kuala Lumpur, 56100, MALAYSIA
**mshahneel@unikl.edu.my*

Fawad Inam
Department of Engineering and Computing, University of East London, London E16 2RD, United Kingdom

ABSTRACT

In this research, an ESC tester machine was built by utilising a fracture mechanics approach. The machine consists of critical components such as an aluminium frame, 3D printed pulley and bracket, DC motor, Arduino microcontroller, and fasteners. The test was performed by securing an acrylic sample using a hook fixed to bracket on the base of the frame and integrated load cell with Arduino microcontroller board. Digital camera was used to capture images with Image J processing software to measure the transient damage area and macro-crack length development at each test condition. The results suggested that the applied load can influence the fracture toughness values. At 55N, the fracture toughness for the acrylic was 1.9 MPa.m$^{1/2}$. Increasing the load to 65N, the fracture toughness dropped by 60% to 0.7 MPa.m$^{1/2}$. The minimum fracture toughness was observed at 85N load; a 91% reduction was recorded. Maximum damage area of 89 mm^2 was recorded for sample tested at 55N while minimum damage area was at 85N load, where only 31.81 mm^2 area was calculated. It can be concluded that this newly built machine can be used to perform fracture toughness test on polymeric materials under environmental stress cracking (ESC) condition.

Keywords: *Fracture mechanics, stress cracking, design, image processing, polymer.*

ISSN 1823-5514, eISSN2550-164X
Received for review: 2020-08-14
Accepted for publication: 2020-11-18
Published: 2021-01-15

Introduction

Environmental stress cracking (ESC) is an unexpected brittle failure and has been one of the most common problems for thermoplastic based materials, with an enormous industrial and economic implications [1]. In general, the ESC phenomenon occurs on plastics when polymer-based products are subjected to both mechanical stress and aggressive liquid exposure [2]. However, in certain scenarios, even if amorphous polymers are in contact with non-aggressive liquid like water, the stress failure is also slightly lower than their estimated limit due to plasticization and softening effects. In the past 70 years, the mechanisms of ESC failure in polymeric materials have been widely studied [3, 4]. The development of ESC in plastics was observed to be more of a physical than a chemical process [5, 6]. The aggressive liquid media does not cause a chemical degradation of the polymer, but gradually dispersed into the polymer matrices under tension and causes hydrostatic pressure [7], which expedites the cracking movement and consequently produces unexpected brittle catastrophe of the plastic based components [8]. It has been determined that ESC is accountable for 25% of plastic component failures in service [9, 10] as ESC was observed as one of the most common reasons for the unexpected brittle failure of thermoplastic polymers [11, 12].

The history of ESC test on thermoplastic polymers using fracture mechanics approach can be traced back to 1998 from a publication by Moskala [13]. In this particular publication, a plaque produced from injection moulding technique was machined according to compact tension sample to study creep crack growth rate as a function of K_{1C}. Apart from that, this research also determined polymer molecular weight and studied the effects of caustic concentration on creep crack growth behaviour.

Scanning Electron Microscopy analysis of the fracture surfaces revealed that crack growth proceeded by the formation of novel discontinuous growth bands. In most recent studies by Lin and Schlarb [8] and Nomai et al. [9], these authors also used similar method, however their main contributions were towards the experimental system. They reported on the temporal development of damage area and recorded their results using a Canon CCD-camera. In addition, a constant load of 300 N was applied on all compact tension specimens and all recorded images were saved and analysed for image processing analysis. Damage area and crack length were calculated from the pixel numbers. In order to calculate the pixel numbers, a reference line was drawn on specimens before any experimental work was carried out.

Unexpected brittle failure caused by ESC can be a two-step process; initiation of a crack followed by propagation of the crack until failure. Flaws such as contaminants, impurities, shrinkage voids and machining marks often causes crack initiation. Therefore, crack initiation is more of an erratic process and is hard to measure by means of experimental approach.

Nevertheless, crack propagation can be studied through fracture mechanics approach, in which the crack is located, (da/dt) or known as the rate of crack propagation is recorded as a function of the applied loading and the geometry of the structure. In case of a crack growing is gradual and in stable manner, the relationship between da/dt and K is stated by;

$$da/dt=AK^m \quad (1)$$

where A and m are constants which depend on material properties and test conditions.

The objective of this research is to design and fabricate ESC tester using the fracture mechanics approach. Even though ESC behaviour has been widely discussed in literature, there is no single study which report on the design of ESC tester using fracture mechanics approach. The design and fabrication of inexpensive ESC tester is shown and the manufacturing method of important components were also presented in this report.

Methods

Figure 1 shows the flowchart of the design process. Normally in design process, a flowchart is used to show the steps involved in product development. In this research, the first step was to define the problem with respect to existing design from literature. It is worth to mention that previous studies have not dealt with the design of ESC tester. Most studies only produce 2D drawing of experimental setup and the load applied to their materials. The following step was to determine the design specifications based on requirement needed in the experimental work.

The main components involved were load, motor type, pulley, wire rope, clamping device with an aluminum frame making up as the machine structure. Then, based on these requirements, the conceptual design was presented and designed using CAD software (Solidworks). Prior to that, a simulation of electronics circuit and the coding was performed using Tinkercad software.

Next, complete assembly of all mechanical parts was done in Solidworks to achieve precision and efficiency. Design improvement and optimization of materials were also carried out at this stage. After careful considerations, actual fabrication and assembly were then executed. EDM wire cut was used to cut the aluminum stand for clamping purpose whilst 3D printer was used to manufacture the customized pulley and bracket.

Various fixtures like bolts and nuts, aluminum frame, bearing and pins were acquired from Asia Bolts and Nuts Sdn. Bhd., Kuala Lumpur, Malaysia.

Final testing was carried out to ensure all components were appropriately assembled so that the machine can function as intended.

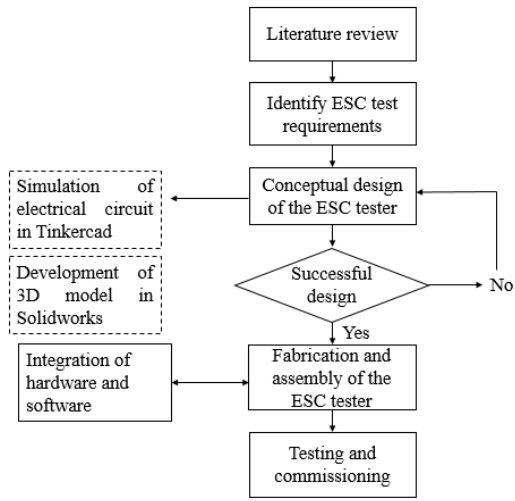

Figure 1: Flowchart of the ESC tester design process.

The schematic of experimental setup in Figure 2 was obtained from the design process and used as guidelines for the conceptual design. Acrylic sheet 3 mm in thickness acquired from Acrylic Signs Material, Off Jalan Pasar, Kuala Lumpur, Malaysia was used as polymer sample.

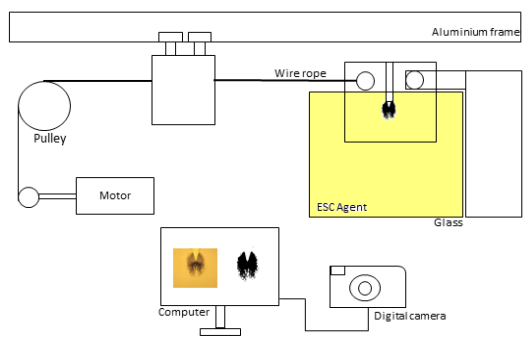

Figure 2: Schematic of experimental setup (not drawn to scale).

Compact tension specimens were cut using laser cutter machine as shown in Figure 3, and the dimensions referred from previous publication is shown in Figure 4 [8, 13, 14].

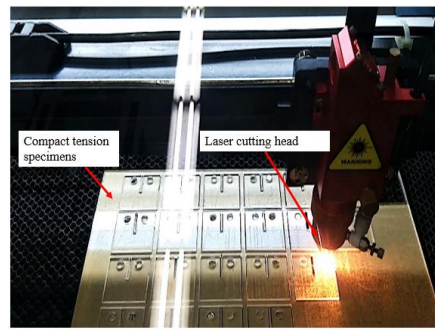

Figure 3: Preparation of compact tension specimens using laser cutter machine.

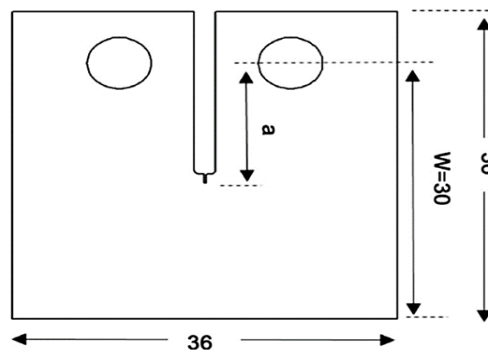

Figure 4: Compact tension sample.

A sharp pre-crack was made by tapping a razor blade into the bottom of the sample slots. The pre-crack length should be between 0.45 to 0.55 mm. The pre-crack device is shown in Figure 5. The sample is then placed at the bottom and razor blade is fitted onto the load container. At pre-determined height, the load is released to produce a pre-crack on compact tension sample. Since this research paper focuses on the design of ESC tester, the design of pre-crack device is not discussed here.

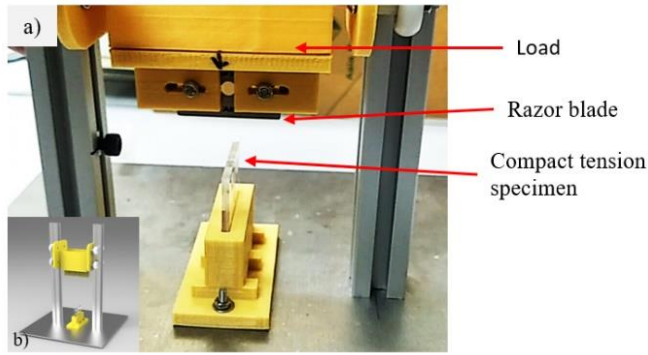

Figure 5: (a) Actual pre-crack station and, (b) a 3D rendering image in Solidworks.

The K_1c was obtained from the following equation.

$$K_{1c} = f\left(\frac{a_0}{W}\right).\left(\frac{F_{max}}{BW^{1/2}}\right) \quad (2)$$

A schematic of the rig used for the crack growth test is shown below. A customized 3D printed pulley is pulled by steel rope 1mm in diameter and attached to an aluminium T-slot to allow for uniaxial translation. The 3D printed pulley and a bracket are shown in Figure 6.

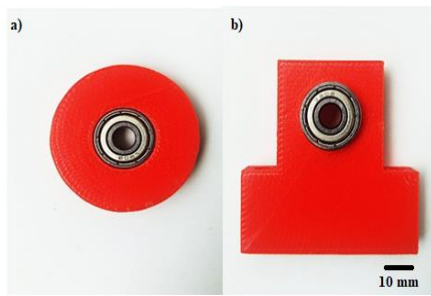

Figure 6: Customized 3D printed parts; pulley (a) and bracket (b) fitted with bearings.

In order to determine the mechanical properties of a sample, applied load and extension were recorded. A micro load cell from luggage scale was used to measure any changes in applied load. The change of crack length was also measured using ultrasonic sensor. Both the load cell and ultrasonic

sensor were connected to Arduino microcontroller. Table 1 shows the list of main components and their prices. The total cost to build this portable machine was RM 1,638.45 and the cost breakdown of each component is as presented.

Table 1: List of main components and prices

No.	List of main component	Purpose	Specifications	Cost (RM)
1	Aluminium T-slot	Frame	45mmx45mm	45.40
2	Pulley with bearing	Support movement and change of direction	Bearing diameter 17 mmx 12 mm	26.00
3	DC Motor	Converts energy from electrical to mechanical	12V	18.00
4	Motor speed controller	Control motor speed	3A, 4-16V	35.00
5	Steel rope/wire	Connects pulley and motor	1 meter length	26.96
6	Load cell	Converts a force into an electrical signal	Maximum load 45kg	24.95
7	Arduino Uno microcontroller	Control operations	Supply voltage 12V Analog input pins 6 SRAM 2kB	40.00
8	Glass container	Contain aggressive liquid	100mmx100mmx100mm	21.00
9	Bolts and nuts	Fastener	M4x50mm M6x50mm	25.00
10	Acrylic	Cover	500x300mmx3mm	60.28
11	Camera	Image capture	EOS 4000D	1250
12	Software	Post processing	ImageJ	0
Total cost				RM 1638.45

Characterization of ESC

The specimens for ESC-testing were prepared as mentioned earlier. The compact tension sample was immersed in the stress cracking agent, methanol. Mechanical properties of a sample were determined based on two parameters; load applied and also the extension. Further crack at the damaged area will completely be surrounded by the methanol during testing period. The time-based development of the crack length and damage area was monitored and recorded using a Canon CCD-camera. A load of 55N, 65N, 75N and 85N were applied to all the test samples. Wire rope was pulled by a motor governed by the speed controller. Load cell was connected to the hook attached to sample. The load can be measured using load cell from luggage scale placed in series with the compact tension sample. Changes in length of sample or simply known as extension was then measured by ultrasonic sensor. The sensor takes all the measurement from the frame to central loading [15]. The measured crack length gave an input to the calculation of K_{1C}. Post processing analysis was then carried out using ImageJ software [16] to determine the transient damage area as well as crack growth size by analysing all the captured surface images that were saved into the computer. The images were initially transformed to a binary image and then the pixels with certain grey level were selected by a defined threshold. Then the damage area was calculated based on the pixel numbers. The wiring configuration from digital Vernier calliper to Arduino microcontroller is shown in Figure 7. Rendered image of the ESC tester is shown in Figure 8(a) and (b). Load cell and ultrasonic sensor that were linked to Arduino Uno microcontroller is also presented in Figure 8(b). The measurement of surface roughness was performed using Mitutoyo surface roughness tester. Five readings were taken and computed at 0.25 mm cut off.

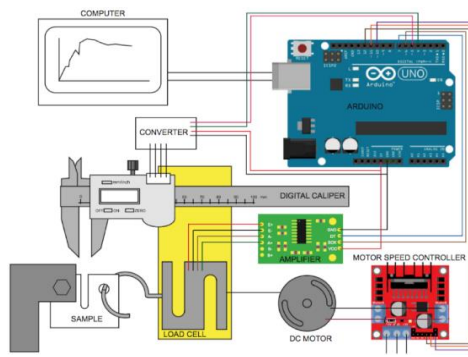

Figure 7: Wiring configuration from digital Vernier calliper to Arduino microcontroller.

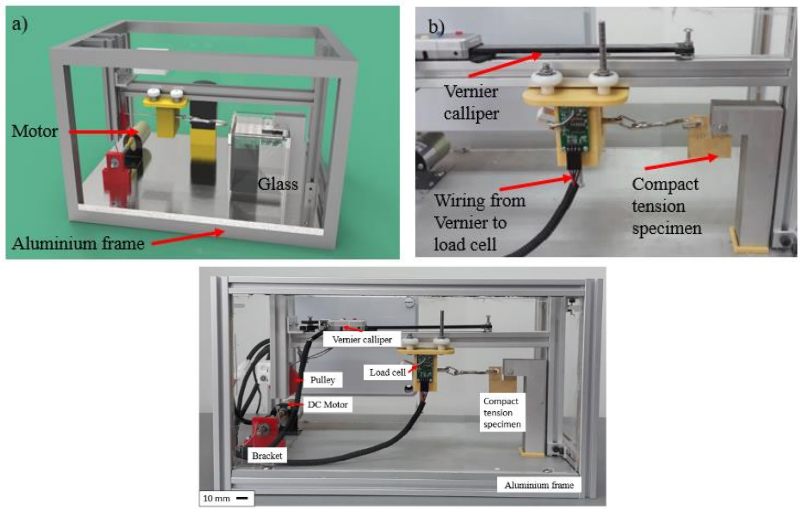

Figure 8: (a) Rendering image of an ESC tester in Solidworks, (b) wiring from Vernier calliper to load cell and front view of actual ESC tester

Results and discussion

Figure 9 shows initial sample setup in Smart Shooter remote capture and advanced camera control mode. The images were captured in video format with frame rate of 40 fps. FPS is also known as the frequency at which consecutive images called frames appearing on a display. Figure 10 shows the development of crack as a function of time. It can be observed that the crack developed really quick when aggressive liquid like methanol is in contact with polymeric material subjected to stress. We have tested four different loads on the acrylic samples to determine the differences among them and validate the machine. Figure 11 shows how the damage area was determined. First, the image was converted to grayscale by converting each pixel's colour information into a brightness measurement. In the ImageJ toolbar, a rectangle was used to specify the area of interest. Then, based on known reference line, the area was calculated. The result shows that the fracture toughness of acrylic samples depends on the applied load. The higher the load, the lower the fracture toughness. Figure 12 (a) shows at 55N load, the fracture toughness for acrylic sample was 1.9 $MPa.m^{1/2}$. When the load was increased to 65N, the fracture toughness dropped 60% to 0.7 $MPa.m^{1/2}$. Likewise, the minimum fracture toughness was observed at 85N load, where a 91% reduction was recorded. It was also noted that the results

presented here were in line with existing publication by Lin and Schlarb where a critical fracture toughness K_{1C} for neat polycarbonate was approximately 5 MPa.m$^{1/2}$ [8]. The difference in K_{1C} is due to the different material types. We believe that this mechanical tester is an ideal tool for ESC test. The damage areas calculated from grey scale images were presented in Figure 12 (b). Sample tested at 55N load obtained the highest damage area (89 mm^2), and this can be associated with the high fracture toughness. The higher the fracture toughness, the longer will be the immersion time and damage area. The minimum damage area was observed for sample tested with 85N load, where 32 mm^2 in damage area was recorded. Low fracture toughness means the sample failed rapidly and the immersion time is shorter than sample with higher fracture toughness. The effect of ESC agent on the surface roughness is presented in Figure 12(c). The measurement was carried out using portable Mitutoyo surface roughness tester on immersed samples. The results indicate that the highest surface roughness was observed for sample tested with 55N, where the roughness was 4.7 µm. Sample tested with 85N load recorded only 0.4 µm roughness value.

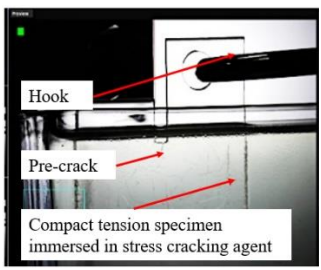

Figure 9: Initial sample setup in remote capture and advanced camera control.

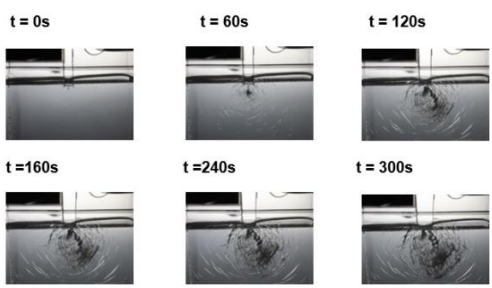

Figure 10: Development of crack as a function of time.

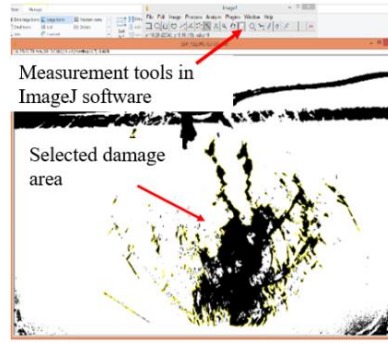

Figure 11: Selected damage area calculation in ImageJ software.

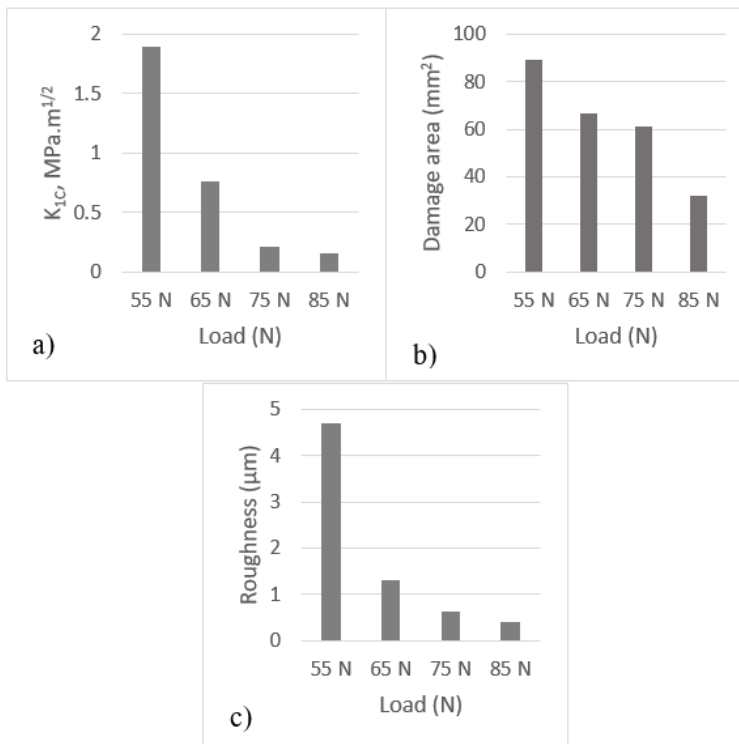

Figure 12: (a) K_{1C} of acrylic at different loads, (b) damage area of acrylic at different loads, and (c) effect of ESC agent on acrylic surface roughness.

Conclusion

In this project an ESC tester using fracture mechanics approach was successfully designed and fabricated. The total cost of this project is RM 1,638. The results show that at 55N load, the fracture toughness for acrylic sample was 1.9 MPa.$m^{1/2}$. In the case of 65N load, the fracture toughness dropped 60% to 0.7 MPa.$m^{1/2}$. Likewise, the minimum fracture toughness was observed at 85N load, where a 91% reduction was recorded. The damage area calculated from grey scale images also indicated similar trend. Sample tested at 55N load resulted in the highest damage area (89 mm^2), this can be associated with the high fracture toughness. The higher the fracture toughness, the longer is the immersion time and damage area. The minimum damage area was observed for sample tested with 85N load, where 32 mm^2indamage area was recorded. Low fracture toughness means that the sample failed rapidly and the immersion time is shorter than sample with higher fracture toughness. The effect of ESC agent on the surface roughness was also studied. The results show that the highest surface roughness was observed in sample tested with 55N load, where the roughness was 4.7 µm. Sample tested with 85N load recorded only 0.4 µm roughness value. The surface roughness values were aligned with fracture toughness results presented earlier. It can be concluded that this machine can be used to measure fracture toughness of polymeric based materials. However, a contact between the liquid used in this experimental work and load cell could damage the component. Thus, this can be the limitation of the developed ESC tester. A customised lid can be fabricated and placed on top of glass to reduce risk of spillage. For future recommendation, the ESC tester can be improved by replacing wire rope and pulley with an electrical powered screw mechanism. In this way, the load can be equally distributed and the deformation of wire rope can be avoided.

Acknowledgement

The authors would like to thank the Centre for Research & Innovation (CORI) Universiti Kuala Lumpur for the financial support, without which the analysis of relevant data will not be possible.

References

[1] C. Hopmann, N. Borchmann, S. Koch, and D. Alperstein, “Influencing the environmental stress cracking resistance of amorphous thermoplastic parts by the example of polycarbonate and water,” *Polym. Eng. Sci.*, vol. 59, no. S1, pp E361-E366, 2019.

[2] L. F. Al-Saidi, K. Mortensen, and K. Almdal, “Environmental stress

cracking resistance. Behaviour of polycarbonate in different chemicals by determination of the time-dependence of stress at constant strains," *Polym. Degrad. Stab.*, vol. 82, no. 3, pp 451–461, 2003.

[3] A. K. Saad, H. A. Abdulhussain, F. P. C. Gomes, J. Vlachopoulos, and M. R. Thompson, "Studying the mechanism of biodiesel acting as an environmental stress cracking agent with polyethylenes," *Polymer (Guildf).*, vol. 191, pp 122278, 2020.

[4] P. R. Lewis, "Environmental stress cracking of polycarbonate catheter connectors," *Eng. Fail. Anal.*, vol. 16, no. 6, pp 1816–1824, 2009.

[5] R. F. Farias, E. L. Canedo, R. M. R. Wellen, and M. S. Rabello, "Environmental Stress Cracking of Poly (3-hydroxibutyrate) Under Contact with Sodium Hydroxide 3," *Mater. Res.*, vol. 18, no. 2, pp 258–266, 2015.

[6] M. Khodabandelou, M. K. Razavi Aghjeh, and M. Rezaei, "Fracture behavior and environmental stress cracking resistance (ESCR) of HIPS/PE blends and the effect of compatibilization on their properties," *Eng. Fract. Mech.*, vol. 76, no. 18, pp 2856–2867, 2009.

[7] M. S. Saharudin, A. Rasheed, I. Shyha, and F. Inam, "The degradation of mechanical properties in halloysite nanoclay – polyester nanocomposites exposed to diluted methanol," *Journal of Composite Materials*, vol. 51, no. 11, pp 1653-1664, 2017.

[8] L. Lin and A. Schlarb, "A study on environmental stress cracking in nano-SiO2-filled polycarbonate," *J. Mater. Sci.*, vol. 47, no. 18, pp 6614–6620, 2012.

[9] J. Nomai and A. K. Schlarb, "Environmental stress cracking (ESC) resistance of polycarbonate/SiO_2 nanocomposites in different media," *Journal of Applied Polymer Science*, vol. 134, no. 43, pp 45451, 2017.

[10] L. M. Robeson, "Environmental stress cracking: A review," *Polym. Eng. Sci.*, vol. 53, no. 3, pp 453–467, 2013.

[11] M. S. Saharudin, R. Atif, I. Shyha, and F. Inam, "The degradation of mechanical properties in polymer nano-composites exposed to liquid media – a review," *RSC Adv.*, vol. 6, no. 2, pp 1076–1089, 2016.

[12] L. Andena, L. Castellani, A. Castiglioni, A. Mendogni, M. Rink, and F. Sacchetti, "Determination of environmental stress cracking resistance of polymers: Effects of loading history and testing configuration," *Eng. Fract. Mech.*, vol. 101, pp 33–46, 2013.

[13] E. J. Moskala, "A fracture mechanics approach to environmental stress cracking in poly(ethyleneterephthalate)," *Polymer (Guildf).*, vol. 39, no. 3, pp 675–680, 1998.

[14] M. S. Saharudin, J. Wei, I. Shyha, and F. Inam, "Environmental Stress Cracking Resistance of Halloysite Nanoclay-Polyester Nanocomposites," *World J. Eng. Technol.*, vol. 5, no. 3, pp 389–403, 2017.

[15] J. H. Arrizabalaga, A. D. Simmons, and M. U. Nollert, “Fabrication of an Economical Arduino-Based Uniaxial Tensile Tester,” *J. Chem. Educ.*, vol. 94, no. 4, pp 530–533, 2017.
[16] E. Moghbelli, R. Banyay, and H.-J. Sue, “Effect of moisture exposure on scratch resistance of PMMA,” *Tribol. Int.*, vol. 69, pp 46–51, 2014.

Numerical Simulations and Experimental Studies on the Formability of Drawing Quality Steel in Single Point Incremental Forming

Zeradam Yeshiwas, A. Krishniah*
Department of Mechanical Engineering, College of Engineering, Osmania University, Hyderabad, India
**zeruhulu@gmail.com*

ABSTRACT

Based on numerical simulation and experimental studies the process parameter optimization on the formability using a 1 mm thickness Drawing Quality Steel(CR2) in Single Point Incremental Forming (SPIF)was studied. The sample shape chosen was the hayperbolic cone and fabricated using different parameter leveles. A model of numeric simulation was developed in ABAQUS explicit and then experimentally verified using a CNC milling machine. The influence of three significant control factors, namely tool radius, feeding rate, and step depth on the formability was studied. Optimization of process parameters was conducted using the L9 Taguchi orthogonal array. For optimal formability, to assess the optimum combination of process parameters, a signal noise (S/N) ratio was used. The percentage contribution of the method parameters to formability was determined by the Study of Variance (ANOVA). The findings of the study indicated that the depth of the step followed by feed rate and tool radius, was the dominant factor influencing formability. Furthermore, a good agreement (<8% error) between the numerical simulation and experimental study was seen. The study based on the Taguchi configuration of the study shows that at a feed rate (A2) 1000 mm/min, with tool radius (B1) 8 mm, and with step depth (C2) 0.8 mm, the optimal conditions for maximum formability were achieved.

Keywords: *Drawing Quality Steel, Formability, Incremental forming, Numerical simulation, Thickness distribution*

ISSN 1823-5514, eISSN2550-164X
Received for review: 2020-09-11
Accepted for publication: 2020-12-21
Published: 2021-01-15

Nomenclature

ϵ_T: True strain	αp: Maximum Forming angle
Δt: Time increment	Δd: Error
ΔZ: Step depth	d_e: Depth at fracture
α_e: Wall angle at fracture	DF: Degrees of freedom
ds: Depth at minimum thinning	F: Variance
α_s: Wall angle at maximum thinning	MS: Mean square
C_d: Dilatational wave speed	P: Test static
Le: Element length	SS: Sum of squares

Introduction

Formability in SPIF can be measured using one of the three different methods, i.e. measuring the maximum wall-angle, taking into account the maximum formability depth achieved, or examining the maximum reduction in thickness achieved without failure. Various studies have assessed the impact of process parameters on SPIF formability, i.e., step depth, the radius of the forming tool, and feed rate. This section has attempted to summarize the literature concerning the impact of process parameters in SPIF.

Many scholars have found the impact of step depth on formability and some of the researchers concluded that the higher value of the Step-depth increases formability [1]-[5]. Another group of researchers [6]-[8] labeled the effect of step depth on formability and reported that the lower step depth value improves formability.

There have been several reports on the impact of the forming-tool radius on formability. Recent work covers [4], [5], [9]-[11], and the researchers concluded that formability increases when the radius of the tool increases. Several authors including [7], [8], [12]-[14] have used experimental studies to test the impact of tool radius on formability. The researchers concluded that formability increases as the radius of the forming tool decreases. For another study, Malwad [13] explored the effect on the formability of the tool radius. In the study, 3 mm and 6 mm radius tools were used for performing the fabrication. The work has been an experimental inquiry into an aluminum alloy. The study concluded that formability improves to some degree, as tool radius decreases.

A considerable amount of research on the effect of feed rate on formability has been published including [5], [7], [12], [14] and found that the formability increases as the feed rate decreases. Bagudanch [4] also assessed the impact of feed rate on formability in SPIF. The study was carried out using the experimental process, and the material being tested was a polymer. The researchers conclude with a high feed rate, that formability increases. Besides, Golabi [9] and Uheida [15] assessed the impact of feed

rate on formability in SPIF. These experiments were carried out using numerical simulation and experimental methods, and the research materials included steel and titanium. The researchers conclude that there is no significant effect of feed rate on formability.

Hussain [22] and Al-Ghamdi [23] suggested that the tool diameter could be optimized to achieve the maximum improvement in formability. Obikawa [24], Hussain [25] and Davarpanah [2] are some of the researchers who conclude that step depth should be optimized to achieve the greatest improvement in formability. Ambrogio [26], suggested that the feed rate should be optimized to achieve the maximum improvement in formability.

It was observed that much of the previous research in formability studies focused on aluminium alloys and had less concern for other material classes. Therefore in this study, cold-rolled drawing grade steel material was used. Furthermore, the literature review reveals contradictory findings about the effect on the formability of tool diameter, feed rate, and step depth. Therefore process parameter optimization was achieved in this study using Taguchi experimental design.

Material and Methods

This study aimed to investigate the effect of process parameters on the formability and optimization of process parameters using drawing quality (CR2) steel sheets in single point incremental forming (SPIF), which is one of the widely used materials in the automotive industry. Tables 1 and Table 2 respectively describe the composition and mechanical properties of the CR2 steel sheet.

Table 1: Composition of drawing quality steel

Quality		Constituent, Percent, *Max*			
Designation	Name	Carbon	Manganese	Sulfur	Phosphorus
CR2	Drawing	0.12	0.50	0.035	0.040

Table 2: Mechanical properties of drawing quality steel

Quality	Yield Stress *R*e, MPa	Tensile Strength *R*m, MPa	Elongation Percent, *A*, *Min*
Designation			*L*o = 80 mm
CR2	240 *Max*	370 *Max*	30

To obtain the true stress-strain curve of Drawing Quality (CR2) steel, the uniaxial Tension test was conducted with a sheet thickness of 1 mm. The specifications of the specimens are obtained according to the ISO 6892-1:2009 standard. Stress and strain are computed from measurements in a tension test of the tensile force, F, and the elongation, ΔL (load-displacement data). The true stress-strain data from the tensile test is approximated using power low as given in Equation (1).

$$\sigma_T = 568\varepsilon_T^{\,0.23} \tag{1}$$

Figure 1 depicted the procedure that was used for the experimental and numerical studies.

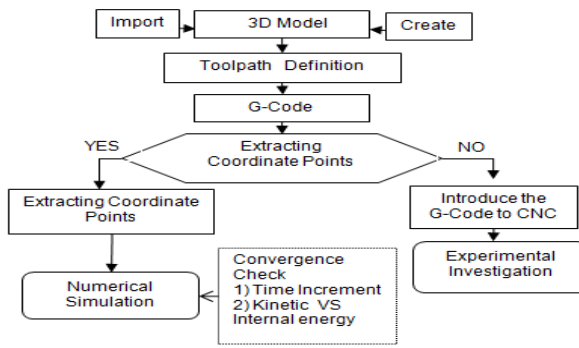

Figure 1: Method for the FEM simulation and experimental study.

A hyperbolic-cone component with a top opening diameter of 140 mm and a wall angle varying from 32 ° to 85 ° (Figure 2) was the sample shape chosen for the conduct of numerical simulation and experimental investigation.

The two most common methods to define the tool path in SPIF [20] are the contour and the spiral toolpath strategies. In this analysis, using CAM software, the contour toolpath was developed and the coordinate points were extracted using the Microsoft Excel formula [16], [17]. The coordinate points were then introduced to define displacement in the numerical simulation, whereas the G-code was directly introduced to the three-axis CNC Mill for the fabrication of the sample parts. Forming time was estimated using the relationship between feed rate and the total forming distance.

Taguchi Design of experiment and NOVA analysis has been done using MINITAB 19 software. The model of the finite element was validated by finding the maximum depth at minimum thinning and comparing with the

depth at the crack with the physical experiment. Error assessment was then made between the finite element model and the physical experiment.

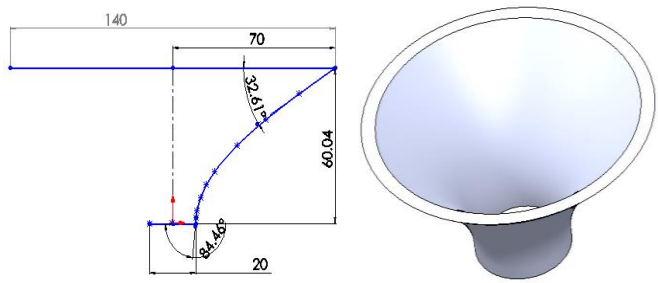

a) b)

Figure 2: Hyperbolic-cone chosen as a sample shape to study the formability a) two-dimensional view, and b) three-dimensional view.

Finite Element Model

In ABAQUS software, the finite element model was developed. The explicit approach of ABAQUS was selected to minimise the long computational time. The blank is modelled as a square measuring 290 mm X 290 mm X 1 mm and fixed at the four edges of the square (Figure 3). Blank is defined as a deformable body and meshed with shell elements (S4R). For mesh generation the approximate element size was 2 mm. A friction coefficient of 0.15 was applied between tool and forming surface. Hemisphere forming tools with a radius of 4 mm, 5 mm, and 6 mm have been chosen and defined as rigid analytical parts. The material properties introduced and position vs time data was defined as the displacement of the tool.

Mass scaling was introduced to reduce the time needed for simulations. A convergence check was done to find a bounded solution. Convergence check was done using two approaches firstly by checking the time increment, i.e., a convergent solution is obtained if the time increment (Δt) is less than the stable time increment (Δt_{min}). The stability limit is the ratio between the characteristic length of the element and the wave speed.

$$\Delta t = \frac{L_e}{Cd} \tag{2}$$

where element length, Le, and the dilatational wave speed of the material, Cd.

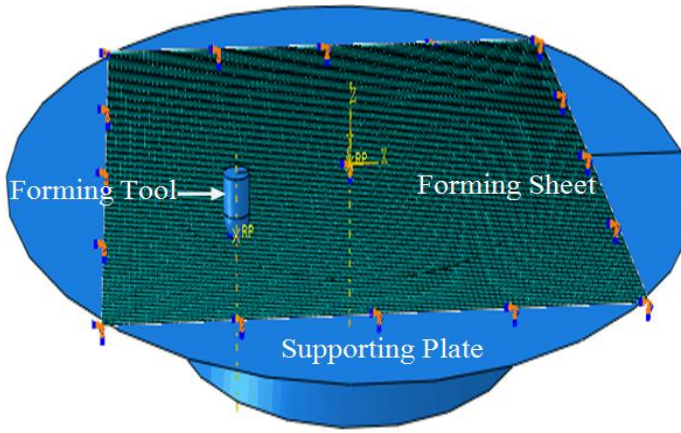

Figure 3: Single point incremental forming model.

The second approach is by checking the ratio of kinetic energy to internal energy. The ratio of kinetic energy to internal energy does not get too large, typically less than 10% [17, 21]. Figure 4 shows the kinetic energy to internal energy ratio in forming the hyperbolic-cone. Both time increment and the ratio of internal energy to kinetic energy have been satisfied in all numerical simulations.

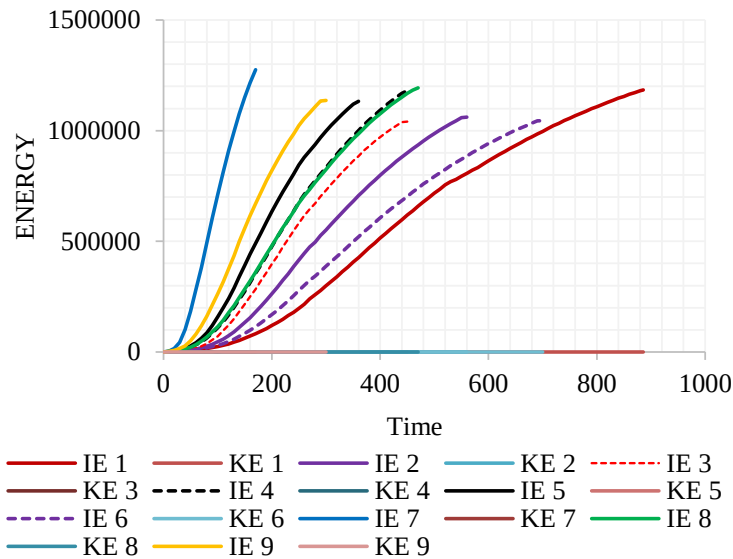

Figure 4: Internal energy combined with kinetic energy history.

Experimental setup

For the forming process, hemispheric tipped forming tools of a different radius of 4mm, 5 mm, and 6 mm were selected as shown in Figure 5. The forming tool moved along the path created from the CAM package until a crack was observed. The fixture for the work holding was mounted on a machine table with three axes CNC Mill, as shown in Figure 6. The material used in the present study was Cold rolled steel sheet (CR2/Drawing quality) 290 mm*290 mm*1 mm in dimension. In the forming process, drawing quality sheets of metal were fastened along their edges in a specially built fixture that was placed on the CNC machine table. Oil was applied to minimize friction between the forming tool and the blank surface.

Figure 5: Forming tools with Φ8, Φ10 and Φ12 diameter spherical end.

Figure 6: Experimental setup for single point incremental forming.

Taguchi Design of Experiment

The study aims to find the formability of drawing quality steel sheets (CR2) in the SPIF process through numerical simulations and experiments. The study also aims to find the optimum combination of factors that influence the formability. Several factors affect formability. However, in this study, the tool diameter, feed rate, and step depth were considered as most prominent once and included as an input factor.

As the number of factors is 3 with each at three levels, the standard orthogonal array L9 (33) was selected (Table 3) for the study using the array selection table [19]. Therefore, nine experiments to be conducted with factor combination as stipulated in the L9 (33) array, as indicated in Table 4.

Table 3: Factors and levels chosen for experimental design

			Factor Levels		
Factors	Symbol	Units	1	2	3
Feed	A	mm/min	800	1000	1500
Tool diameter	B	mm	8	10	12
Step	C	mm	0.5	0.8	1

Table 4: Experimental layout L9 (33) orthogonal array

Experiment No.	A	B	C
1	800	8	0.5
2	800	10	0.8
3	800	12	1
4	1000	8	0.8
5	1000	10	1
6	1000	12	0.5
7	1500	8	1
8	1500	10	0.5
9	1500	12	0.8

The highest value of formability angle or forming depth is significant for formability improvement. For this reason, the ‘‘larger-the-better’’ equation was used for the calculation of the S/N ratio. For this objective S/N ratio is defined by Equation 3 according to the Taguchi method.

$$S/N = -10\log\left[\frac{1}{n}\sum_{1}^{n} y_i^{\,2}\right] \tag{3}$$

Result and discussion

Numerical Simulation Result

Based on the Taguchi designs of the experiment, hyperbolic-cone samples were formed. Following the successful execution of the numerical simulation for the sample part, the post-processing was done to find the maximum depth at a minimum thinning. For all combinations of factors, the shell thickness contour plot for the formed parts is plotted as shown in Figure 7.

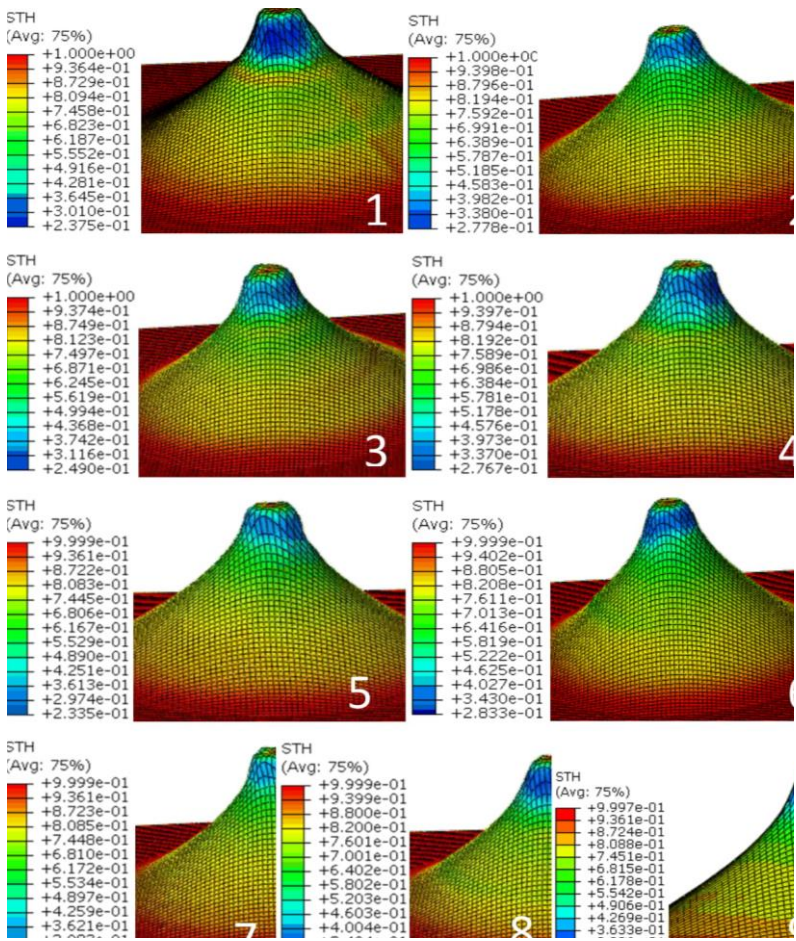

Figure 7: Thickness distribution contour plot under the condition of different combinations of process parameters for trial 1 to 9.

Using the contour of the SHT (Shell thickness) and the path option, the distance "Z" along the path (depth) was found at the maximum thinning. Figure 8 shows the depth measurement method. The measurement starts from the undeformed area, and ends with the maximum thinning at the nodal level. To validate the proposed FE model; the simulated forming depth was executed from the contour plot as shown in Figure 9, Figure 10 and Figure 11, and compared with experimental data.

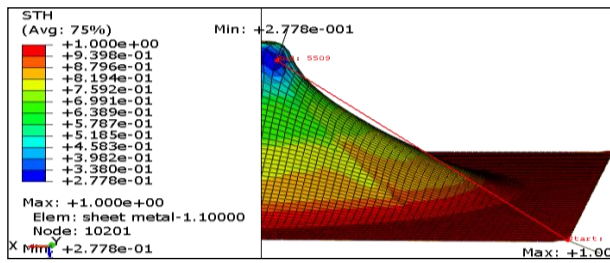

Figure 8: Depth measurement method at a maximum thinning.

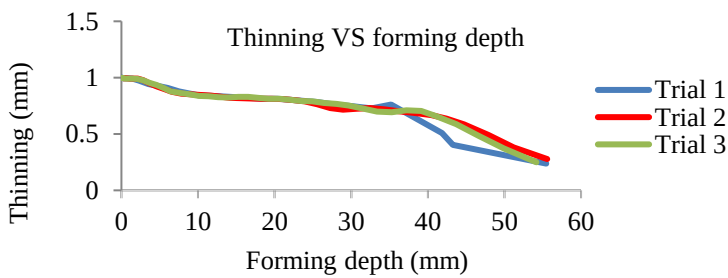

Figure 9: Distribution of thickness with depth for trial 1 trial 2 and trial 3.

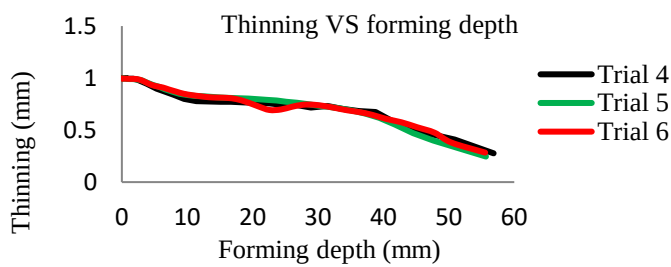

Figure 10: Distribution of thickness with depth for trial 4 trial 5 and trial 6.

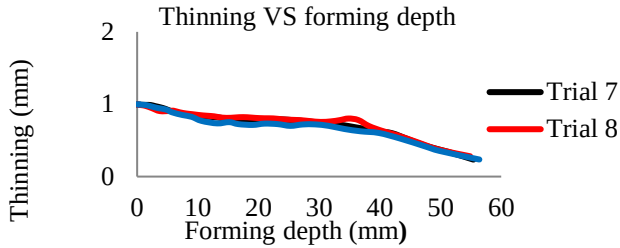

Figure 11: Distribution of thickness with depth for trial 7 trial 8 and trial 9.

Experimental Result

As shown in Figure 12, fabrication was performed for all the experimental combinations according to Taguchi L9 (3^3) orthogonal array to confirm the formablity predicted in the numerical simulation. The fabrication was stopped when the crack is begun. After the fabrication of the sample parts, the component depth up to the fracture was measured using Vernier Height Gauge as shown in Figure 13.

Figure 12: Parts formed based of L9 (3^3) design of experiment.

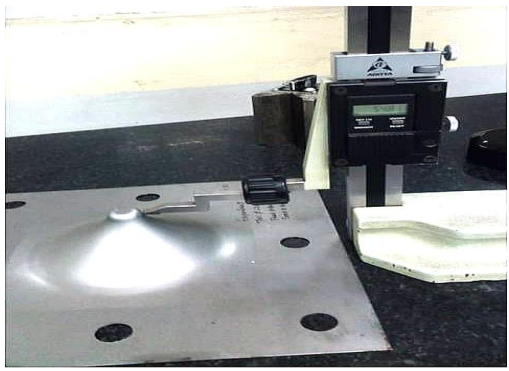

Figure 13: Depth measurement method using Vernier Height Gauge.

Figure 14 shows the Parabolic-cone with an initial opening radius of 70 mm was formed on the CNC milling machine until the crack is formed to measure the depth at the crack.

Figure 14: Magnified view of the crack formed in experiment 1.

In SPIF, One of the widely used ways of finding the maximum formability at which the material can be formed before failure occurs is the maximum wall angle (φmax) [1, 5]. The forming sheet material failure occurs during the SPIF process, as the forming depth of the parts increases. Forming depth can therefore be used as a formality measure [9, 11]. In this paper, Both the maximum angle of the wall at a crack and the maximum forming depth achieved at failure or maximum thinning were used to evaluate the formability.

The angle corresponding to the depth at a crack is called the maximum formability angle and computed using Equation 4 [7, 18].

$$\alpha_p = \tan^{-1}\left(\frac{\Delta Z}{\Delta X}\right) \tag{4}$$

In the above equation, ΔZ/ΔX gives the slope at any point p on the toolpath and represents the wall angle at p. Table 5 describes the findings obtained from the measurement of the maximum forming angle and depth at the crack.

Error Evaluation

When the fracture occurs in the experimental trials, the depth at fracture (de) were measured and compared with the depth at minimum thinning (ds) achieved from the numerical simulation. Figure 12 shows the fabricated parts after experiments, and the corresponding simulations depicted in Figure 7. To verify the accuracy of the proposed prediction of formability, the relative error between the simulation and physical experiment forming depth was calculated as shown in Table 5 using Equation (5).

$$\Delta d(\%) = \frac{|d_e - d_s|}{d_e} * 100\% \tag{5}$$

$$\Delta \alpha(\%) = \frac{|\alpha_e - \alpha_s|}{\alpha_e} * 100\% \tag{6}$$

Table 5: Formability depth, maximum formability angle and error

Trial No.	Simulation ds (mm)	Fabricated de (mm)	Error Δd (%)	Simulation α_s(°)	Fabricated α_e(°)	Error Δα%
1	55.45	53.79	3.09	79.11	75.74	4.45
2	55.58	54.17	2.61	79.69	76.5	4.17
3	54.68	53.93	1.39	76.93	75.93	1.32
4	56.84	55.65	2.13	82.733	79.89	3.56
5	55.67	54.55	2.05	79.38	77.81	2.02
6	55.55	53.99	2.88	78.58	75.96	3.45
7	55.42	53.79	3.03	79.41	75.74	4.85
8	53.13	52.44	1.32	73.07	72.77	0.41
9	56.39	54.81	2.89	81.94	77.6	5.59

αe, wall angle at fracture; αs, wall angle at maximum thinning

Optimum combination of process parameters

Depth at the crack and maximum formability angle were measured via the experimental design for each combination of the control factors by using Taguchi techniques, optimization of the measured control factors were provided by signal-to-noise (S/N) ratios. Table 6 shows the values of the S/N ratios for observations of depth at the crack and at the minimum thinning.

Table 6: the experiment response for the formability

Experimental Results		Numerical Simulation	
1/(S^2)	S/N	1/(S^2)	S/N
0.000346	34.61	0.000325	34.88
0.000341	34.68	0.000324	34.9
0.000344	34.64	0.000334	34.76
0.000323	34.91	0.00031	35.09
0.000336	34.74	0.000323	34.91
0.000343	34.65	0.000324	34.89
0.000346	34.61	0.000326	34.87
0.000364	34.39	0.000354	34.51
0.000333	34.78	0.000314	35.03

The level values of control factors for the maximum forming depth or forming angle given in Table 7 and 8 are shown in graph forms in Figures 15(a) and Figure 15(b). Optimal forming parameters of the control factors for maximizing the forming depth can be easily determined from these graphs. The best level for each control factor was found according to the highest S/N ratio in the levels of that control factor.

Table 7: shows the optimal levels of control factors (fabricated)

	Mean S/N ratio(dB)			
Parameter	Level 1	Level 2	Level 3	Max-min
Feed Rate	34.64	34.76	34.59	0.17
Tool Radius	34.71	34.60	34.68	0.11
Step Depth	34.55	34.78	34.66	0.23

Table 8: shows the optimal levels of control factors (simulation)

Parameter	Mean S/N ratio(dB			
	Level 1	Level 2	Level 3	Max-min
Feed Rate	34.84	34.97	34.80	0.17
Tool Radius	34.95	34.77	34.89	0.18
Step Depth	34.76	35.01	34.85	0.25

In the numerical simulation, the levels and S/N ratios for the factors giving the best formability depth and angle value were specified as factor A (Level 2, S/N = 34.97), factor B (Level 1, S/N = 34.95), and factor C (Level 2, S/N = 35.01). In the experimental study, the levels and S/N ratios for the factors giving the best formability depth and angle value were specified as factor A (Level 2, S/N = 34.76), factor B (Level 1, S/N = 34.71), and factor C (Level 2, S/N = 34.78). In other words, optimum formability was obtained at a feed rate (A2) 1000 mm/min, with tool radius (B1) 8 mm and with step depth (C2) 0.8 mm (Figure 15(b)). From this, it can be concluded that the best setting factor to achieve maximum formability is A2B1C2.

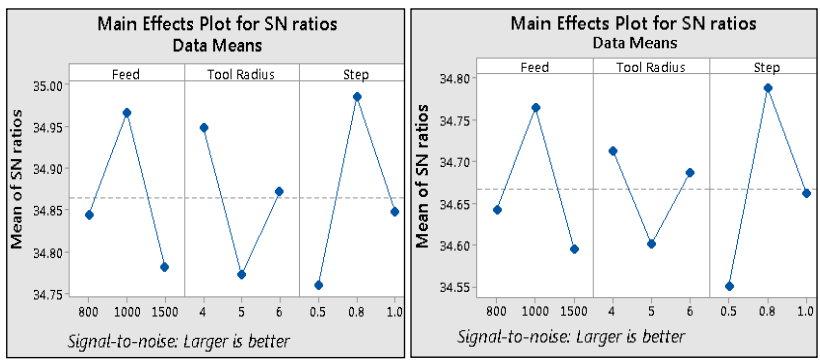

(a) (b)

Figure 15: Optimum combinations of factors for the maximum forming depth (a) Numerical Simulation and (b)Fabricated part.

Confirmation experiment

After the optimal levels of forming parameters are identified, a confirmation test is necessary to check the accuracy of the analysis. However, the optimal setting of process parameters is found among the experiments. The confirmation experiment presents the maximum value of depth at the crack in experiment 4 with a combination setting of A2B1C2. The maximum wall angle achieved is 79.89°, and the depth at a crack is 55.65. This value is higher than the value achieved for all combinations of parameters during experimentation.

In the numerical simulation, the confirmation experiment presents the maximum value of depth at the minimum thinning is achieved in experiment 4 with a combination setting of A2B1C2. The maximum wall angle achieved is 82.73°, and the depth at a crack is 56.84. This value is higher than the value achieved for all combinations of parameters during simulation.

Kurra [7] reported the same results, using Extra Deep Drawing (EDD) steel in the SPIF process to investigate the impact of process parameters on maximum wall angle. The optimum process parameters for maximum formality to be tool diameter at level 1 (6 mm) and step depth at level 2 (1.1 mm). Gulti [12] and Oleksik [8] also stated that the formability is increased by decreasing the tool diameter.

Analysis of variance (ANOVA)

Table 9 and Figure 10 show the ANOVA for formability. In the experimental study, the percentage of the confidence level of feed rate is 29.04%, with a tool radius of 12.7% and a step depth of 53.25% on formability. In the numerical simulation study, the percentage of the confidence level of feed rate is 25.92%, with a tool radius of 22.56% and a step depth of 37.97% on formability. The values clearly show the step-depth is the main factor influencing the formability in both the numerical simulation (37.97% contribution) and the physical experiment (53.25% contribution).

Table 9: Analysis of variance for the maximum forming depth (Experimental)

Source	DF	SS	MS	F	P	P(%)
Feed Rate	2	1.77	0.88	5.85	0.14	29.04
Tool Radius	2	0.77	0.38	2.57	0.28	12.76
Step Depth	2	3.24	1.62	10.74	0.08	53.25
Error	2	0..30	0.15			
Total	8	6.09				

DF, degrees of freedom; F, variance; MS, mean square, P, test static, SS, sum of squares.

Table 10: Analysis of variance for the maximum forming depth (simulation)

Source	DF	SS	MS	F	P	P(%)
Feed Rate	2	2.13	1.07	1.91	0.34	25.92
Tool Radius	2	1.86	0.93	1.66	0.38	22.56
Step Depth	2	3.12	1.56	2.80	0.26	37.97
Error	2	1.12	0.56			
Total	8	8.227				

DF, degrees of freedom; F, variance; MS, mean square, P, test static, SS, sum of squares.

Interaction plot

The interaction plot for formability is shown in Figure 16 for the experimental study and numerical simulation respectively.

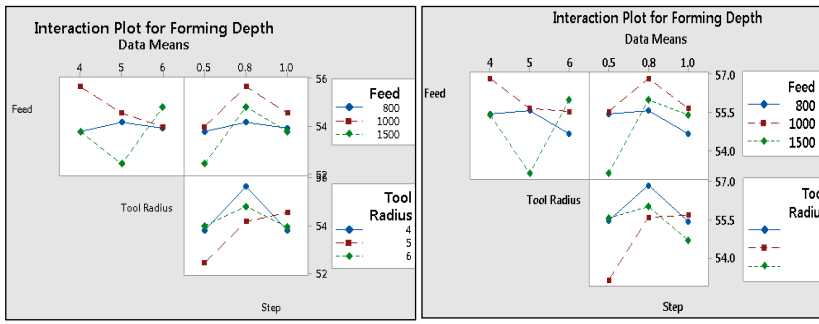

(a) (b)

Figure 16: Interaction plot (a) pysical experimental (b) numerical simulation

In both numerical simulation and experimental studies from the interaction of step depth with feed rate, the maximum formability was observed for the 0.8 step depth with a 1000 mm/min feed rate than other combinations. From the interaction of step depth with tool radius, the maximum formability was observed for the 0.8 step depth with a 4 mm tool radius than other combinations. From the interaction of feed rate with tool radius, the maximum formability was observed for the 1000 mm/min feed rate with a 4 mm tool radius than other tool radius and feed rate combination.

Conclusions

The present study appears to be the first study to investigate the effect of feed rate, forming tool radius, and step depth on the formability of drawing quality steel (CR2) based on IS 513: 2008 in SPIF. Using numerical simulation and physical experiment, the formability has been further optimized by a systematic experimental plan using Taguchi experiment design. From the results of the study, the following conclusion are made.

Bosetti and Bruschi [11] reported the fracture depth for a truncated cone with the wall angle formed using a 1.2 mm thick sheet of AA5182 aluminium alloy. The fracture depth was greater than 132 mm at the feed rate of 1000 mm/s and step depth of 0.8 mm and greater than 137 mm at a feed rate of 100 mm/s and step depth of 0.3 mm. Ziran et al. [36] evaluated the maximum wall angle for a U-shaped part using an AA-3003O aluminium sheet with a thickness of 1 mm. the maximum formability angle achieved using different tool diameter values was greater than 80°. Gulati et al. [34] conducted an optimization study using Taguchi design of experiment to found that optimum parameters for the maximum forming angle using

hyperbolic cone fabricated from an aluminium 6063 sheet the predicted optimal values for the wall angle found to be 88.29°. All the results reported by Bosetti and Bruschi [11], Ziran et al. [36], and Gulati et al. [34] shown that aluminium alloys are more formable than drawing quality steel in single point incremental forming.

- Results showed that the numerical simulation could predict the formability with a maximum error of below 6% when compared with the experimental values.
- The error between the experimental study and numerical simulation can be caused by fabrication error or mass scaling.
- The maximum formability is much associated with step depth. Its contribution is 53.25% in the experimental study and 55.4% in the numerical simulation.
- The average formability based on forming depth is 55.60 in the simulation and 54.12 in the fabrication and the error is 2.73%.
- The average formability based on the forming angle associate with this depth is 79.54 in the simulation and 76.43 in the fabrication and the error is 2.73%.

Reference

[1] R. Conte, G. Ambrogio, D. Pulice, F. Gagliardi and L. Filice, "Incremental Sheet Forming of a Composite Made of Thermoplastic Matrix and Glass-Fiber Reinforcement," *Procedia Engineering*, vol. 207, pp 819-824, 2017.

[2] M. A. Davarpanah, A. Mirkouei, X. Yu, R. Malhotra and S. Pilla, "Effects of incremental depth and tool rotation on failure modes and microstructural properties in Single Point Incremental Forming of polymers," *J. Mater. Process. Technol*., vol. 222, pp 287–300, 2015.

[3] C. Pandivelan and A. K. Jeevanantham, "Formability evaluation of AA 6061 alloy sheets on single point incremental forming using CNC vertical milling machine," *J. Mater. Environ. Sci.*, vol. 6, no. 5, pp 1343–1353, 2015.

[4] I. Bagudanch, M. L. Garcia-Romeu, G. Centeno, A. Elías-Zúñiga and J. Ciurana, "Forming force and temperature effects on single point incremental forming of polyvinylchloride," *J. Mater. Process. Technol.*, vol. 219, pp 221–229, 2015.

[5] X. Zhang, J. Wang and S. Zhang, "Study on Process Parameters on Single Point Incremental Forming of PVC," *Mater. Sci. Forum*, vol. 878, pp 74–80, 2017.

[6] X. Song, J. Zhang, W. Zhai, M. Taureza, S. Castagne and A. Danno, "Numerical and Experimental Study of Micro Single Point Incremental Forming Process," *Procedia Eng.*, vol. 207, pp 825–830, 2017.

[7] S. Kurra, N. Swetha, C. V. Reddy and S. P. Regalla, "Experimental and finite element studies of single stage incremental forming process : effect of process parameters on maximum wall angle and thickness distribution," *Adv. Mater. Process. Technol.*, vol. 0698, no. December, pp 1–13, 2017.

[8] V. Oleksik, A. Pascu and E. Avrigean, "Theoretical and Experimental Studies on the Influence of Process Parameters on Strains and Forces of Single Point Incremental Forming," *Adv. Mater. Res.*, vol. 939, pp 367–372, 2014.

[9] S. Golabi and H. Khazaali, "Determining frustum depth of 304 stainless steel plates with various diameters and thicknesses by incremental forming," *J. Mech. Sci. Technol.*, vol. 28, no. 8, pp 3273–3278, 2014.

[10] S. D. Majagi, G. Chandramohan and M. S. Kumar, "Effect Of Incremental Forming Process Parameters On Aluminum Alloy using Experimental Studies," *Adv. Mater. Res.*, vol. 1119, pp 633–639, 2015.

[11] Y. Li, Z. Liu, W. J. T, Bill. Daniel and P. A. Meehan, "Simulation and Experimental Observations of Effect of Different Contact Interfaces on the Incremental Sheet Forming Process," *Mater. Manuf. Process.*, vol. 29, no. 2, pp 121–128, 2014.

[12] V. Gulati, A. Aryal, P. Katyal and A. Goswami, "Process Parameters Optimization in Single Point Incremental Forming," *J. Inst. Eng. Ser. C*, vol. 97, no. 2, pp 185–193, 2015.

[13] D. S. Malwad and V. M. Nandedkar, "Deformation Mechanism Analysis of Single Point Incremental Sheet Metal Forming," *Procedia Mater. Sci.*, vol. 6, no. Icmpc, pp. 1505–1510, 2014.

[14] D. G. M. V. Naga chaitanya, Sunder singh sivam S.P and M. Gopal, "An Experimental Investigation on the Single Point Incremental Forming Of Aluminium," *Int. J. Eng. Res.*, vol. 3, no. Special 1, pp 155-159, 2014.

[15] E. H. Uheida, G. A. Oosthuizen and D. Dimitrov, "Investigating the Impact of Tool Velocity on the Process Conditions in Incremental Forming of Titanium Sheets," *Procedia Manuf.*, vol. 7, pp 345–350, 2017.

[16] Y. Zeradam and A. Krishnaiah, "Extraction of Coordinate Points for the Numerical Simulation of Single Point Incremental Forming Using Microsoft Excel," *International Conference on Emerging Trends in Engineering (ICETE): Learning and Analytics in Intelligent Systems*, vol. 2, pp 577-586, 2020.

[17] Y. Zeradam and A. Krishnaiah, "Numerical Simulation and Experimental Validation of Thickness Distribution in Single Point Incremental Forming for Drawing Quality Steel," *Int. J. Appl. Eng. Res.*, vol. 15, no. 1, pp 101–107, 2020.

[18] K Suresh, SD Bagade and SP Regalla, "Deformation behavior of extra deep drawing steel in single-point incremental forming," *Mater Manuf Process*, vol. 30, no. 10, pp 1202–1209, 2015.
[19] R. Ganesan, Research methodology for engineers. MJB Publishers, 2011.
[20] Y.Zeradam and A. Krishnaiah, "Spiral Toolpath Definition and G-code Generation for Single Point Incremental Forming," *J Mech Eng*, vol. 17, no. 1, pp 91-102, 2020.
[21] J. Jeswiet and D. Young, "Forming limit diagrams for single-point incremental forming of aluminium sheet," *Journal of Engineering Manufacture*, vol. 219, no. 4, pp 359–364, 2005.
[22] G Hussain, HR Khan, L Gao and N Hayat, "Guidelines for Tool-size Selection for Single-point Incremental Forming of an Aerospace Alloy," *Materials and Manufacturing Processes*, vol. 28, no. 3, pp 324–329, 2013.
[23] KA Ghamdi and G Hussain, "Threshold Tool-radius Condition Maximizing the Formability in SPIF Considering a Variety of Materials: Experimental and Fe Investigations," *International Journal of Machine Tools and Manufacture*, vol. 88, pp 82–94, 2014.
[24] T Obikawa, S Satou and T Hakutani, "Dieless Incremental Micro-forming of Miniature Shell Objects of Aluminum Foils," *International Journal of Machine Tools and Manufacture*, vol. 49, no.12–13, pp 906–915, 2009.
[25] G Hussain, L Gao, N Hayat and NU Dar ,"The Formability of Annealed and Pre-aged AA-2024 Sheets in Single-point Incremental Forming," *International Journal of Advanced Manufacturing Technology*, vol. 46, no. 5–8, pp 543–549, 2010.
[26] G Ambrogio and F Gagliardi, "Temperature Variation During High Speed Incremental Forming on Different Lightweight Alloys," *International Journal of Advanced Manufacturing Technology*, vol. 76, no.9–12, pp 1819–1825, 2015.

Large-Eddy Simulation of Unsteady Pitching Aerofoil using a One-equation Subgrid Scale (SGS) Model based on Dynamic Procedure

Firdaus Mohamad
Faculty of Mechanical Engineering, Universiti Teknologi MARA (UiTM), 40450 Shah Alam, Selangor, MALAYSIA
firdausmohamad@uitm.edu.my

*Takeo Kajishima**
Department of Mechanical Engineering, Osaka University 2-1 Yamadaoka, Suita, Osaka 565-0871, JAPAN
**kajisima@mech.eng.osaka-u.ac.jp*

ABSTRACT

Large-Eddy Simulations (LES) for an oscillating NACA0012 aerofoil at Reynolds number 1.35 × 10^5 have been performed to investigate the capability of a new approach of a One-equation SGS model. The phenomena of the oscillating aerofoil at higher amplitude angle (α_{amp}) is believed to produce deep dynamic stall in which strong non-equilibrium turbulence could also visible. Hence, a new approach of a one-equation SGS model is proposed where the coefficient of production term in the k_{SGS} transport equation is defined dynamically. From the simulations, the leading-edge vortex (LEV), dynamic stall vortex (DSV), shedding mechanism and trailing edge vortex (TEV) are captured in this study.

Keywords: *LES, Dynamic Stall, One-equation SGS Model, Dynamic Procedure*

Introduction

Predictions of complex flow fields involving both static and dynamic stall are important in a broad range of industrial applications such as turbomachinery, wind turbine aerodynamics, helicopter blade rotors and manoeuvrable wings.

ISSN 1823-5514, eISSN 2550-164X
Received for review: 2020-10-12
Accepted for publication: 2020-11-16
Published: 2021-01-15

Dynamic stall is defined as the phenomenon of exceeding the normal static stall angle. These phenomena are associated with various complex fluid flows such as separations, reattachments and vortex developments which contribute to the unusual aerodynamic characteristics. In terms of turbulence interactions, the dynamic stall produces strong non-equilibrium turbulence in which the turbulence kinetic energy production is imbalanced with the dissipation [1]. Therefore, common subgrid scales (SGS) turbulence models are thought to be insufficient to correctly capture the drastic changes of aerodynamic loads at high angles of attack and moderately high Reynolds numbers.

Experimental works are required to understand and visualize the phenomena of oscillating airfoils. McCroskey et al. [2] conducted an experiment based on oscillating NACA0012 airfoil by using a 7 × 10 ft wind tunnel to investigate the boundary layer separation and vortex shedding mechanism. They concluded that the unsteady separation of the turbulent boundary layer was the primary cause of the vortex shedding mechanism. Lee and Gerontakos [3] executed several experiments to understand the overall flow phenomena of the dynamics stall around an oscillating airfoil. They revealed a clear mechanism of dynamic stall at different stages, such as light-stall oscillating and attached-flow oscillating cases.

Additionally, computational simulations are crucial for any fluid flows analysis. For the dynamic stall simulations, the unsteadiness of boundary layer interaction induced by oscillation can be captured and visualized by means of numerical simulations. Generally, very fine grid density is required to capture all the vortices for the entire dynamic stall process, including unsteady boundary layer separation, transition, shear layer instabilities, laminar separation bubble (LSB) bursting and vortex surface interactions [4], [5]. Thereby, Direct Numerical Simulation (DNS) is a meaningful solution if the computational resources are not a problematical issue. However, as the Re number increases especially for industrial engineering applications such as helicopter blade rotors, wind turbines blades and maneuverable wings [4], [6], the DNS demands tremendous computational capability and memory allocations. Hence the Reynolds-averaged Navier-Stokes (RANS) also can be considered as an option. However, as far as dynamic stall simulation is concerned, the leading-edge transitional flows play an important role in the development of separated flow downstream. Hence, RANS requires an alternative approach to identify the laminar-transition flows by setting the production term to zero prior to available data from experiment. On top of that, the solution of RANS also requires an additional transitional model to predict the transitional flows [4], [7].

Large-eddy simulation (LES) is gaining more attention in studying the complexity of dynamic stall phenomena. A series of comprehensive dynamic stall simulations using LES can be reviewed in Visbal and Garmann [8], Benton and Visbal [9], Visbal and Benton [4] and Visbal [10]. However, none

of these studies were focused on the effect of non-equilibrium of turbulence models. Dindart and Kaynak [11] revealed the importance of a non-equilibrium SGS model to determine the separation and vortex shedding mechanism of the dynamic stall compared to an equilibrium SGS model. A study by Mukai et al. [12] showed that the LES of the Smagorinsky model (SM) with coarse grid spacing in the spanwise direction successfully captured some aspects of the unsteady phenomenon.[12], [13]. Gulillaud et al. [14] also used SM to study the effect of the leading edge vortex (LEV) on the lift coefficient unsteadiness on a pitching NACA0012 at a Reynolds number of 20000. Meanwhile, a Mixed-Time-Scale (MTS) SGS model was used by Almutairi et al. [15] to observe the laminar separation bubbles near the stall of NACA0012 at a Reynolds number of 5×10^4. Their finding shows that an increase of the spanwise domain contributed to intermittent bursting of the laminar separation bubble. Besides, Kim and Xie [16] have also investigated the dynamic stall of NACA0012 using the MTS model to have a better understanding of several factors such as spanwise extension and the effect of freestream turbulence.

To this end, this paper deals with simulations of oscillation airfoils using a new approach of non-equilibrium SGS turbulence model known as a one-equation dynamic (OD) model. NACA0012 airfoil at Reynolds number of 1.35×10^5 was used as a case study to evaluate the turbulence model. Besides, the results of 2 different numbers of grids in a spanwise direction have also been presented.

Governing Equations

In LES, the large-scale flow structures are explicitly solved while the small eddies are numerically modeled. Spatial filtering is commonly used to differentiate between large and small eddies. The spatial filtering or grid filtering is denoted by the overbar ($\bar{f}$) and is described as:

$$\bar{f}(x) = \int_{-\infty}^{\infty} G(y) f(x-y)dy, \tag{1}$$

where the function G is a filter function. The filtered Navier-Stokes equations are defined in non-inertial frame of reference:

$$\frac{\partial \bar{u}_i}{\partial x'_i} = 0, \tag{2}$$

$$\frac{\partial \bar{u}_i}{\partial t} + \frac{\partial (\bar{u}_i + 2\epsilon_{imn}\Omega'_m x'_n)\bar{u}_j}{\partial x'_j} = -\frac{\partial}{\partial x'_i}(\bar{P}) + \nu \frac{\partial^2 \bar{u}_i}{\partial x'_j x'_j} - \frac{\partial \tau_{ij}}{\partial x'_j} - \epsilon_{ijk}\frac{\partial \Omega'_j}{\partial t}x'_k - \epsilon_{ijk}\epsilon_{mnk}\Omega'_j\Omega'_m x'_n \tag{3}$$

where $\bar{P}$ is the effective pressure, ν is the kinematic viscosity, ϵ_{ijk} is Levi-Civita's alternating tensor, $\bar{u}_i$ is the filtered velocity and the Ω'_i is defined as the angular velocity component of the non-inertial system. For the coordinate system, x'_i is derived based on the transformation in non-inertial frame of reference. For this simulation, the axis of rotation is in x_3 direction. The effect of system rotation appears as Coriolis term, centrifugal term and angular acceleration component of the non-inertial system as a result of coordinate transformation for time derivative term and non-linear convective term.

The subgrid-scale (SGS) stress, $\tau_{ij} = \overline{u_i u_j} - \bar{u}_i \bar{u}_j$, appears as a result of filtering in Equation (3) is parameterized by an eddy viscosity model:

$$\tau_{ij} - \frac{\delta_{ij}}{3}\tau_{kk} = -2\upsilon_t \bar{D}_{ij}. \tag{4}$$

Here, δ_{ij} is the Kronecker delta and τ_{kk} is the trace of the SGS stress (added to the pressure term). The υ_t is called the SGS eddy viscosity while the $\bar{D}_{ij}$ is the grid-scale (GS) rate-of-strain tensor:

$$\bar{D}_{ij} = \frac{1}{2}\left(\frac{\partial \bar{u}_i}{\partial x'_j} + \frac{\partial \bar{u}_j}{\partial x'_i}\right). \tag{5}$$

The SGS eddy viscosity is calculated based on:

$$\nu_t = C_\nu \Delta_\nu \sqrt{k_{sgs}} \tag{6}$$

where k_{sgs} is the SGS kinetic energy. The characteristic length in above relation is calculated based on:

$$\Delta_\nu = \frac{\bar{\Delta}}{1 + \frac{C_k \bar{\Delta}^2 \bar{D}^2}{k_{sgs}}} \tag{7}$$

where the grid filter length $\bar{\Delta} = \sqrt[3]{\Delta_1 \Delta_2 \Delta_3}$ is calculated based on the cell volume. The k_{sgs} in Equation (6) is solved by solving the transport equation:

$$\frac{\partial k_{sgs}}{\partial t} + \frac{\partial}{\partial x'_j}\left(\bar{u}_j k_{sgs}\right) = P_{k_{sgs}} - C_\varepsilon \frac{k_{sgs}^{\frac{3}{2}}}{\bar{\Delta}} - \varepsilon_\omega \tag{8}$$

$$+\frac{\partial}{\partial x'_j}\left[\left(\nu + C_d \Delta_v \sqrt{k_{sgs}}\right)\frac{\partial k_{sgs}}{\partial x'_j}\right].$$

This transport equation is also presented in a non-inertial frame of reference. In most studies, the SGS models such as Smagorinsky Model, Dynamic Smagorinsky Model and One-equation SGS kinetic energy are fundamentally based on the assumption that the small scale turbulence is nearly homogeneous and isotropic; hence the rotation effects (Coriolis and Centrifugal) are not counted in the equation [17]. In addition, the impact of system rotation on SGS is less dominant than the local rotation rate of the GS [18], [19]; therefore we made no modification to the model.

In the transport equation of Equation (8), there are 4 terms in the right-hand side that respectively represent the production, the dissipation, the additional dissipation and the diffusion terms. For the production term, $P_{k_{sgs}} = -\tau_{ij}\overline{D}_{ij}$, is responsible for the energy transfer from GS to SGS in the context of the one-equation model. For τ_{ij}, any SGS stress model can be applied. In the case of the eddy viscosity model of Smagorinsky type:

$$P_{k_{sgs}} = 2(c\bar{\Delta}^2|\overline{D}|)\overline{D}_{ij}\overline{D}_{ij} = c\bar{\Delta}^2|\overline{D}|^3. \tag{9}$$

In this study, the dynamic procedure is used to obtain the coefficient, c in Equation (9) in which any smoothing or averaging is not necessary, and thus a negative value of c by Equation (9) is allowed. The negative value indicates the reverse transfer of energy or from SGS to GS portion and it is important for inhomogeneous cases. It is important to note that the negative value of production term will only decrease the k_{SGS}. The backscatter of energy is not represented in the filtered equation of motion because the eddy viscosity ν_t is always positive. For this model, we denoted the model as One-Equation Dynamic Model (OD).

The coefficients for the OD model are $C_\nu = 0.05$, $C_k = 0.08$, $C_\varepsilon = 0.835$ and $C_d = 0.10$. For the detail elaboration for the dynamic procedure such as the test filter that has been used, reader is advice to refer [19], [20].

Computational Setup

This study is focused on dynamic stall simulation around NACA0012 at a Reynolds number of 1.35×10^5 based on chord length and freestream velocity. This range of Reynolds number is believed to still be able to provide a well resolved large-eddy simulation and would be within the range of developed turbulent boundary layer before the dynamic stall takes place [4], [9]. This

setup corresponded to the setup of the wind tunnel experiment conducted by Lee and Gerontakos [3]. Their experiment was conducted based on a 0.15 *m* chord length (*c*) and 2.5*c* span. The freestream velocity was 14 *m/s* and the turbulence intensity of 0.08% was measured at freestream velocity.

In this study, the airfoil performs the pitching motion based on the sinusoidal mode where:

$$\alpha(t) = \alpha_{mean} + \alpha_{amp}\sin\left(\frac{2kU_\infty}{c}t\right). \quad (10)$$

The α_{mean} and α_{amp} represent mean angle of attack and amplitude respectively. The pitching axis is located at quarter chord from the leading edge. The $k = \pi fc/U_\infty$ is reduced frequency. The α_{mean} and α_{amp} were set to 10° and 15° respectively. These prescribed kinematic parameters would result in $\alpha_{min} = -5°$ and $\alpha_{max} = 25°$ where the importance of dynamic stall phenomenon such as LEV, shedding of LEV, trailing-edge vortex (TEV) and the interaction with boundary layer could be evaluated. For the same kinematic parameters, researchers were varied the reduced frequency, *k (0.01-0.4)* [16], [21]–[23], the effect of unsteady freestream velocity [16], grid resolution and domain size effect [16].

Computational Domain and Grid

A typical *C*-type grid is used in this study where ξ coordinate goes around the airfoil and η is in the outward direction from the solid wall and cut-line after the trailing edge. Meanwhile ζ is in the spanwise direction. The domain is extended 0.1*c* in a spanwise direction and had a uniform spacing. A study by Visbal and Garmann [5] showed that the spanwise extension of 0.1*c* was sufficient to capture the LEV and DSV. The domain size for X and Y direction was extended to the 20*c* as shown in Figure 1. This domain extension was found sufficient to hinder the boundary reflections [22].

The grid was designed to have more concentrated nodes near the airfoil to ensure the $y^+ \leq 1$ to capture the boundary layer separation and reattachment. Hence, the height of the first node adjacent to the airfoil wall was set to 1×10^{-4} and 3×10^{-4} around the leading and trailing edge respectively. The finished *C*-mesh around the airfoil, leading and trailing edge is shown in Figure 2. The details of the grid parameter are listed in Table 1.

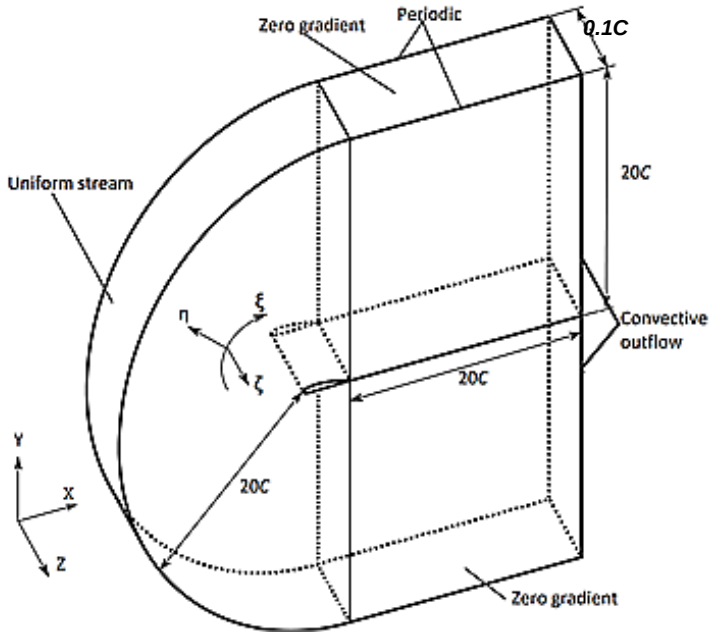

Figure 1: Computational domain and boundary conditions.

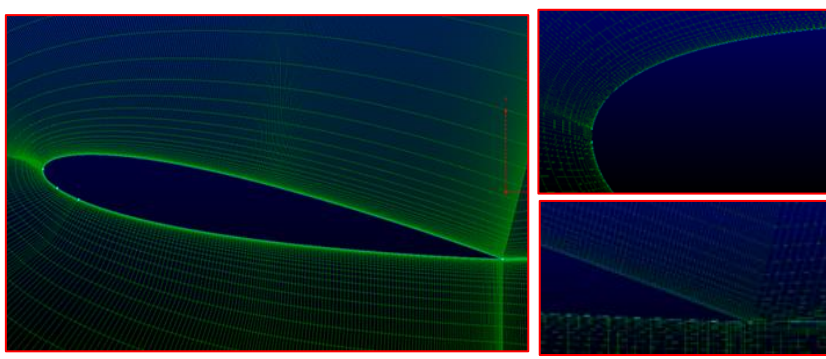

Figure 2: Close up of C-type mesh around NACA0012 (trailing edge and leading edge).

Table 1: Grid Parameters

Grid Type	*C*-grid
# of points along the wake	65
# of points on the pressure side	193
# of points on the suction side	386
# of points on wall normal	50
# of points spanwise	33, 66
L_z/c	0.1

Boundary Conditions

No-slip boundary condition was imposed at the solid wall around the airfoil. The convective outlet boundary condition was used at the velocity outlet. For the inlet, freestream velocity without disturbance was set around the *c*-curve. Periodic boundary condition was applied to the spanwise direction. The computational domain and their respective boundary conditions are shown in Figure 1.

Numerical Procedure

The spatially filtered Navier-Stokes Equations (NSE) were solved using in-house finite difference method code. The influence of rotational effect was added in the momentum equation as shown in Equation (3). The non-linear term was discretized based on Quadratic Upstream Interpolation for Convective Kinematics (QUICK) upwinding scheme. In our calculation, the kinetic energy of SGS transport equation also needed to be solved. For the non-linear term, the donor cell method was adopted. For the diffusion term, 2nd order central finite difference method was applied. In order to solve the temporal discretization, explicit time stepping procedure based on Adams-Bashforth method of the 2nd order accuracy was used. For this calculation, non-dimensional time step was set to $\frac{\Delta t U_\infty}{c} = 3 \times 10^{-5}$ to provide enough temporal resolution of SGS features. The Poisson equation was solved with the SOR (successive over relaxation) method.

Validation Studies

Validation studies have been carried out to confirm the numerical scheme, mesh and solver used in this study. Experimental results by Lee and Gerontakos [3] were used for validation purpose. Pitching motion and Reynolds number were set to $10 + 15\sin(\omega t)$ and $Re = 1.35 \times 10^5$ respectively. Drag coefficient hysteresis is shown in Figure 3. A good satisfactory result between experimental and simulation is observed in the region of attached flows. However, a less satisfactory agreement is further

observed, particularly at higher angle-of-attack. In this region, various flow phenomena are expected such as separation, reattachment and vortex development where the turbulence models used to predict those phenomena play an essential role. This observation is also stressed by Geng et al. [21]. They concluded that the drag coefficient hysteresis results were less satisfactory agreement with experimental results even though a better mesh resolution, turbulence models and time step size were used. Therefore, solver, mesh resolution and the numerical scheme that have been used in this study are within the accepted range.

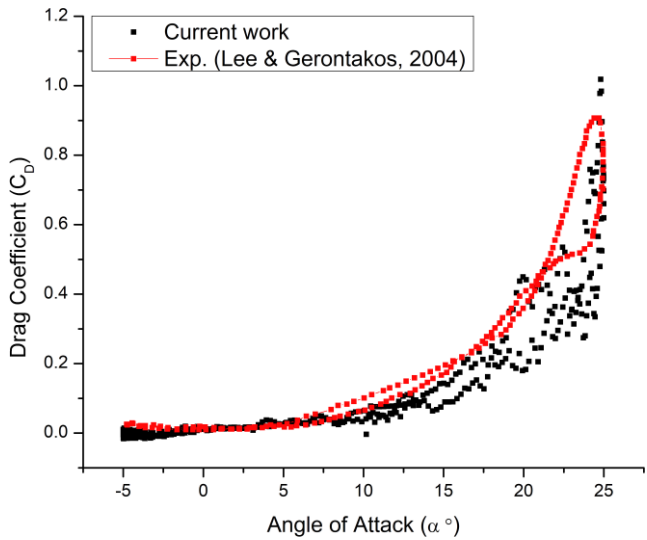

Figure 3: Drag coefficient hysteresis between experimental and simulation.

Results and Discussion

For all computations, the reduced frequency, $k = \pi fc/U_\infty = 0.3$ were set. In order to resolve adequate temporal resolution of fine scale structures, a very small non-dimensional time step was initiated. As a result of these parameters, the non-dimensional period of the motion is $T = 10.5$ where 350000-time steps are required to complete 1 pitching cycle. Due to limitations in computational time, the 3D simulations were running for only 1.5 cycles. This is a common practice for 3D LES simulations for oscillating airfoil where only 1 or 2 cycles were simulated [8], [24].

In order to investigate the effects of grid resolution in the spanwise direction, 2 different grid number were simulated in this study. Figure 4 shows the variation of lift and drag coefficient as a function of non-dimensional flow time (t/T) for N_Z=33 and N_Z=66. Note that symbols '↑' and '↓' refer to upstroke and downstroke motions, respectively. Generally, the drag and lift coefficients are increased during upstroke motion and reaches the peak value at the maximum pitching angle. However, this trend is not identical for drag coefficient where the peak value is observed beyond the maximum angle of attack (around $\alpha = 24° \downarrow$). After reaching the peak value, both drag and lift coefficient exhibit a sudden drop which is representing the dynamic stall. For the simulated operating conditions, a large difference peak value for coefficients between cycle-to-cycle at a high angle of attack during upstroke and downstroke motion is clearly observed. This phenomenon is as expected due to the dynamic stall phenomena such as large separation at trailing edge, effects of transition movement and turbulence [25], [26].

Figure 5 shows time and spanwise averaged pressure coefficients (C_P) for selected upstroke and downstroke pitching motions. The first LEV was detected at 20°↑. The size of the LEV increased as the angle of attack increased. This event led to the vortex shedding mechanism. At the maximum angle of attack 25°↑, the LEV was convected on nearly half of the suction side of the airfoil and at the same time, the DSV also appeared as shown in Figure 5. As a consequence, the airfoil lift dropped.

In the region of the downstroke phase, the vortex was shedding downstream. At 17°↓, the counter rotating vortex appeared at the trailing edge. This counter-rotating vortex also increased in size as the angle of attack decreased. This could be seen in pressure distribution where the suction pressure peaked at the trailing edge. Finally, this vortex merged with the first LEV and convected into the wake. At this angle of attack, the lift and drag continued to decrease.

The Q-criterion [27] is used to observe vortical phenomena in dynamic stall simulations. The unsteady flowfield for the upstroke and downstroke phases based on Q-criterion coloured by streamwise velocity are shown in Figure 6. Beginning from 15°↑, development of transitional flow field was observed (marked as 'a'). At 18°↑, a fine scale structure resulting from spanwise coherent structures from the transition region was formed. This observation was also discussed in detail in the work of [10]. The formation of the LEV was as shown at 21°↑. At the maximum angle of attack (25.0°↑), the LEV became larger and convected downstream. At this angle, the airfoil no longer produced lift. Besides, the formation of DSV also could be seen for the downstroke phase.

Overall, phenomena which occurred around the pitching airfoil was observed vto be similar to the N_z=33. Figure 7 shows the iso-surfaces of Q-criterion based on streamwise velocity for some selected angles of the pitching

motion. The hairpin-like vortices were captured during both upstroke and downstroke motions. As a result of vortices breaking down, finer and random well-developed turbulent structures [28] were observed downstream of the airfoil suction side. Additionally, Kobayashi et al. [29] elaborated that hairpin vortices were related to the forward and backwards scatter events. Hence, the non-equilibrium of the SGS model introduced in the OD model was useful in capturing these vortices. For pressure distribution curves, no apparent differences were observed for both grids (not shown here).

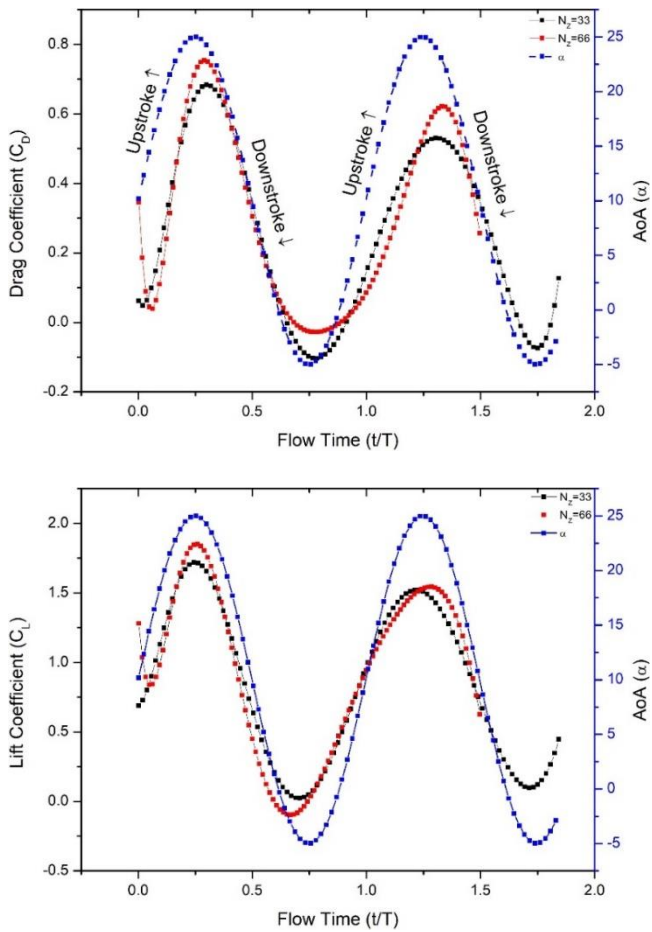

Figure 4: Coefficient of drag (C_D) and lift (C_L) versus non-dimensional flow time (t/T). The Angle-of-attack (AoA) is on the right axis.

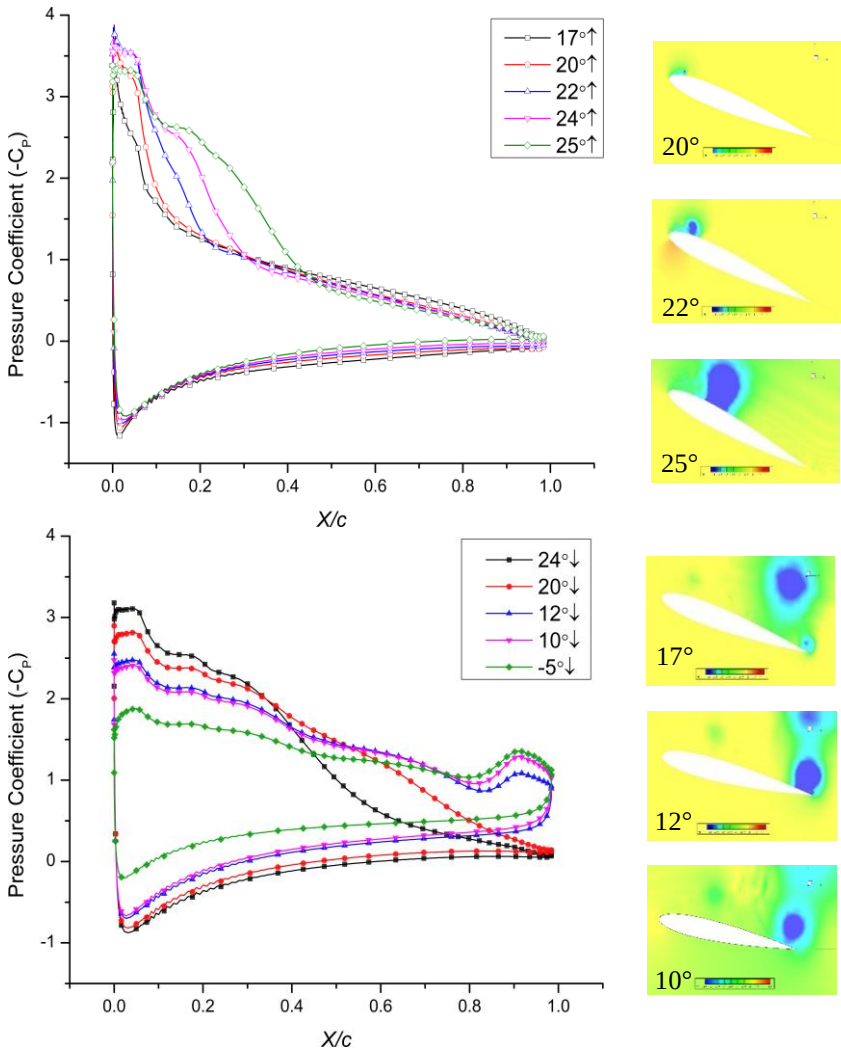

Figure 5: Time and Spanwise-Averaged Pressure Coefficient (C_P) for selected upstroke and downstroke angles (Grid N_z=33).

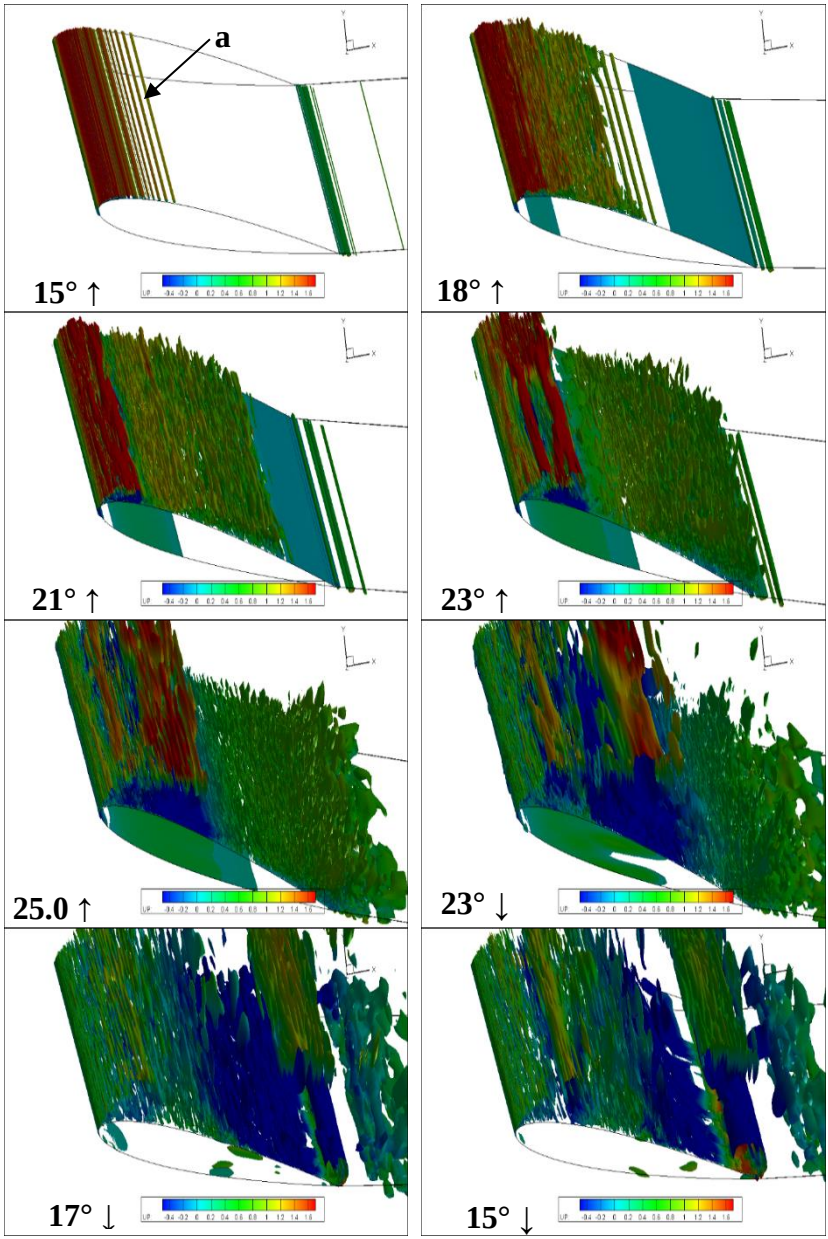

Figure 6: Iso-surfaces of Q-criterion colored by streamwise velocity for selected angles (Grid N_z=33).

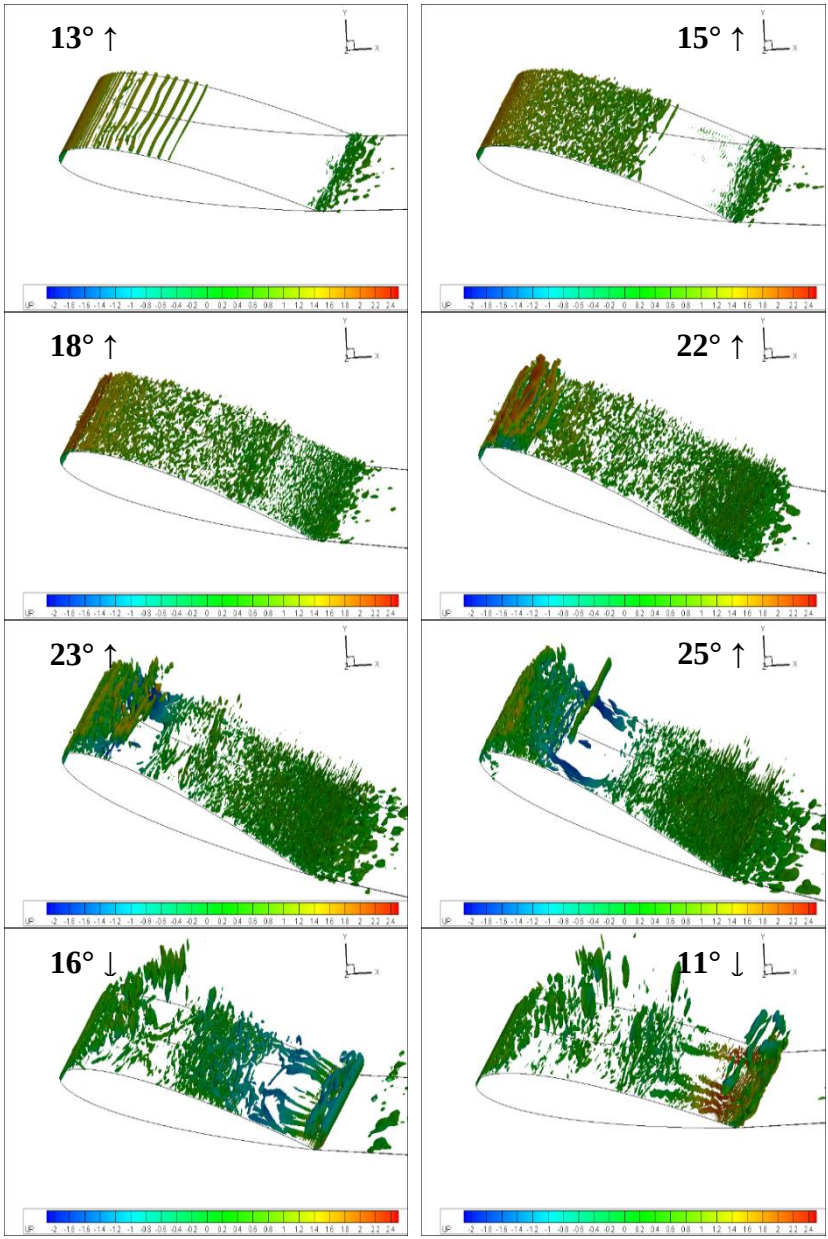

Figure 7: Iso-surfaces of Q-criterion colored by streamwise velocity for selected angles (Grid N_z=66).

Conclusion

LES over an oscillating NACA0012 airfoil were performed to evaluate the performance of a dynamic approach of a one-equation SGS model. Two different grids were used in this study to evaluate the resolution effects in the spanwise direction. It is observed that no significant differences can be seen in forces and pressure coefficients. However, increasing the number of spanwise direction to 66 led to an exciting finding where the hairpin vortices were captured for both upstroke and downstroke motions. On top of that, introducing the dynamic procedure in non-equilibrium SGS model is found useful in the leading edge transitional region. The laminar separation bubble, separation and reattachment were captured during the unsteady motion and can be seen in the pressure coefficient plots. The finding in this study could be more elaborated in terms of hysteresis forces if more cycles can be simulated. However, due to the limitations in computational capacity, only 1.5 cycles were simulated. Despite this, the findings of the present study could be served as a guideline to evaluate the effects of non-equilibrium SGS model with a variation of reduced frequency and grid resolution subjected to the moderate Reynolds number and deep dynamic stall problems.

Acknowledgements

The first author would like to acknowledge the Malaysia Government through Ministry of Higher Education (MoHE) and Universiti Teknologi MARA (UiTM) for financial support through its scholarship program (SLAB). The author is also grateful to Yasuaki Kaneko and Takeshi Omori for sharing their valuable knowledge and information about the simulations.

References

[1] G. Martinat, M. Braza, Y. Hoarau, and G. Harran, "Turbulence Modelling of the Flow Past a Pitching NACA0012 Airfoil at 10^5 and 10^6 Reynolds Numbers," *J. Fluids Struct.*, vol. 24, no. 8, pp 1294–1303, 2008.

[2] W. J. McCroskey, L. W. Carr, and K. W. McAlister, "Dynamic Stall Experiments on Oscillating Airfoils," *AIAA J.*, vol. 14, no. 1, pp 57–63, 2008.

[3] T. Lee and P. Gerontakos, "Investigation of Flow Over an Oscillating Airfoil," *J. Fluid Mech.*, vol. 512, pp 313–341, 2004.

[4] M. R. Visbal and S. I. Benton, "Exploration of High-Frequency Control of Dynamic Stall Using Large-Eddy Simulations," *AIAA J.*, vol. 56, no. 8, pp 2974–2991, 2018.

[5] M. R. Visbal and D. J. Garmann, "Analysis of Dynamic Stall on a Pitching Airfoil Using High-Fidelity Large-Eddy Simulations," *AIAA J.*, vol. 56,

no. 1, pp 46–63, 2017.
[6] K. Gharali and D. A. Johnson, "Dynamic Stall Simulation of a Pitching Airfoil under Unsteady Freestream Velocity," *J. Fluids Struct.*, vol. 42, pp 228–244, Oct. 2013.
[7] J. A. Ekaterinaris and F. R. Menter, "Computation of Oscillating Airfoil Flows with One- and Two-Equation Turbulence Models," *AIAA J.*, vol. 32, no. 12, pp 2359–2365, Dec. 1994.
[8] M. R. Visbal and D. J. Garmann, "Investigation of Spanwise End Effects on Dynamic Stall of a Pitching Wing Section," *J. Aircr.*, pp 1–13, 2019.
[9] S. I. Benton and M. R. Visbal, "Extending the Reynolds Number Range of High-frequency Control of Dynamic Stall," *AIAA J.*, vol. 57, no. 7, pp 2675–2681, 2019.
[10] M. R. Visbal, "Analysis of the Onset of Dynamic Stall using High-fidelity Large-Eddy Simulations," *52nd Aerosp. Sci. Meet.*, no. January, pp 1–25, 2014.
[11] M. Dindart and U. Kaynak, "Effect of Turbulence Modeling on Dynamic Stall of a NACA0012 Airfoil," in *30th Aerospace Sciences Meeting & Exhibit*, pp 1–14.
[12] J. Mukai, S. Enomoto, and T. Aoyama, "Large-Eddy Simulation of Natural Low-frequency Flow Oscillations on an Airfoil near Stall," *Collect. Tech. Pap. - 44th AIAA Aerosp. Sci. Meet.*, vol. 22, no. January, pp 17066–17075, 2006.
[13] J. H. Almutairi and I. M. AlQadi, "Large-Eddy Simulation of Natural Low-Frequency Oscillations of Separating–Reattaching Flow Near Stall Conditions," *AIAA J.*, vol. 51, no. 4, pp. 981–991, Apr. 2013.
[14] N. Guillaud, G. Balarac, and E. Goncalvès, "LES on a Pitching Airfoil: Analysis of the Lift Coefficient Unsteadiness," *Notes Numer. Fluid Mech. Multidiscip. Des.*, vol. 135, pp. 163–169, 2018.
[15] J. H. Almutairi, L. E. Jones, and N. D. Sandham, "Intermittent bursting of a laminar separation bubble on an airfoil," *AIAA J.*, vol. 48, no. 2, pp. 414–426, 2010.
[16] Y. Kim and Z. T. Xie, "Modelling the effect of freestream turbulence on dynamic stall of wind turbine blades," *Comput. Fluids*, vol. 129, pp. 53–66, 2016.
[17] H. Lu, C. J. Rutland, and L. M. Smith, "A posteriori tests of one-equation les modeling of rotating turbulence," *Int. J. Mod. Phys. C*, vol. 19, no. 12, pp. 1949–1964, 2008.
[18] M. Tsubokura, T. Kobayashi, N. Taniguchi, and T. Kogaki, "Subgrid scale modeling for turbulence in rotating reference frames," *J. Wind Eng. Ind. Aerodyn.*, vol. 81, no. 1–3, pp. 361–375, 1999.
[19] T. Kajishima and T. Nomachi, "One-Equation Subgrid Scale Model using Dynamic Procedure for the Energy Production," *J. Appl. Mech.*, vol. 73, no. 3, pp. 368–373, 2006.

[20] F. Mohamad and T. Kajishima, "Large eddy simulation using one-equation SGS model based on dynamic procedure for flows in laminar-transition region," *J. Adv. Res. Fluid Mech. Therm. Sci.*, vol. 60, no. 2, pp. 166–177, 2019.

[21] F. Geng, I. Kalkman, A. S. J. Suiker, and B. Blocken, "Sensitivity Analysis of Airfoil Aerodynamics during Pitching Motion at a Reynolds Number of 1.35×10 5," *J. Wind Eng. Ind. Aerodyn.*, vol. 183, pp. 315–332, Dec. 2018.

[22] S. Wang, D. B. Ingham, L. Ma, M. Pourkashanian, and Z. Tao, "Turbulence Modeling of Deep Dynamic Stall at relatively Low Reynolds Number," *J. Fluids Struct.*, vol. 33, pp. 191–209, 2012.

[23] X. Li, D. Grecov, Z. Guo, and Z. Hou, "Influence of Unsteady and Kinematic Parameters on Aerodynamic Characteristics of a Pitching Airfoil," *J. Aerosp. Eng.*, vol. 32, no. 1, pp 1–11, 2019.

[24] M. Sánchez-Rocha, M. Kirtaş, and S. Menon, "Zonal hybrid RANS-LES Method for Static and Oscillating Airfoils and Wings," *Collect. Tech. Pap. - 44th AIAA Aerosp. Sci. Meet.*, vol. 20, no. January, pp 15211–15231, 2006.

[25] Y. Shida, K. Kuhawahara, K. Ono, and H. Takami, "Computation of Dynamic Stall of a NACA-0012 Airfoil," *AIAA J.*, vol. 25, no. 3, pp 408–413, 1987.

[26] H. Liang, X. Wang, L. Zou, and Z. Zong, "Numerical study of two-dimensional heaving airfoils in ground effect," *J. Fluids Struct.*, vol. 48, pp 188–202, 2014.

[27] J. JEong and F. Hussain, "On the Identification of a Vortex," *J. Fluid Mech.*, vol. 285, no. February, pp 69–94, 1995.

[28] S. Kawai and K. Asada, "Wall-modeled Large-Eddy Simulation of High Reynolds Number Flow around an Airfoil near Stall Condition," *Comput. Fluids*, vol. 85, pp 105–113, 2013.

[29] H. Kobayashi, F. Ham, and X. Wu, "Application of a Local SGS Model based on Coherent Structures to Complex Geometries," *Int. J. Heat Fluid Flow*, vol. 29, no. 3, pp 640–653, 2008.

Evaluating the Gear Stress of Novel Reverse Rotation Bit Manual Screwdriver Design for Miniscrew Implants

Rizki Aldila Umas, Sugeng Supriadi, Yudan Whulanza, Andi Aditya Ahmad Fauzi Hasan*
Department of Mechanical Engineering, Faculty of Engineering, Universitas Indonesia, Kampus UI Depok 16424, Indonesia
**sugeng@eng.ui.ac.id*

Prasetyanugraheni Kreshanti
Cleft and Craniofacial Center Cipto Mangunkusumo Hospital – Plastic and Reconstructive Surgery Division, Department of Surgery, Faculty of Medicine, Universitas Indonesia, Indonesia

ABSTRACT

One of the problems faced by the screwdrivers used for craniomaxillofacial implant fixation is that the maximum torque required for implant removal is significantly higher than the maximum torque needed for inserting implants. Another problem is that the hand torque produced by a right-handed person is lower in the counterclockwise direction, which is the removal direction for miniscrews. The novel design presented here of a manual screwdriver equipped with an epicyclic gear will produce a reverse bit rotation and provide the mechanical advantage of higher torque output. In this study, simulations were conducted by varying the torque input within the range of 0-1000 Nmm with an applied load in each simulation to be adapted based on the epicyclic gear set. The materials used in this study are AISI 316L and Ti6Al4V. The maximum Von Mises stress value was observed in the sun gear from the second gear set at 522.59 MPa (AISI 316L) and 430.76 MPa (Ti6Al4V) for the maximum torque input, which was followed by the planetary and ring gear from the second gear set and then the planetary gear, ring gear, and sun gear from the first gear set. The total deformation also showed the difference between the two materials; the deformation when using AISI 316L as the material was lower than when using Ti6Al4V.

ISSN 1823-5514, eISSN 2550-164X
Received for review: 2020-12-01
Accepted for publication: 2020-12-19
Published: 2021-01-15

Keywords: *Surgical Screwdriver; Epicyclic Gear; Maxillofacial Implant*

Introduction

A screwdriver is the primary tool for the insertion and removal of miniscrew implants, which means that a surgeon's performance is highly dependent on them. One widely used screwdriver handle for miniscrew implants consists of two parts: the front and rear. The front part is rotatable and is usually rotated by the user's fingers (Figure 1), while the rear part fits into the palm of the user's hand, which is held fixed [1]. Some studies have reported making improvements in miniscrew surgical screwdrivers that include the ability to limit torque in miniscrew insertion in order to avoid a stripping of the bone caused by over torque [2] and a modification that adds an auxiliary positioning attachment in order to achieve a precise height for avoiding any tissue injuries [3].

However, the screwdriver design that is now widely used could be improved for even better performance to support surgeons. For example, there are some problems related to the osseointegration of the miniscrew and the hand's natural movement. One such problem is the higher torque needed for removing miniscrew implants. As widely used, reliable implants that provide temporary anchorage for orthodontics and craniomaxillofacial treatments [4], [5], miniscrew implants are usually made from titanium [5], [6], and in some cases need to removed once the treatment is finished (for temporary anchorage) or due to problems that occur after miniscrew implant placement. Even though there are biodegradable mini-implants, including miniscrews, due to their high pricing they are not much used in surgery [7]. A titanium miniscrew is manufactured as an untreated, smooth surface that will result in osseointegration or partial osseointegration. Studies [6], [8] show that the maximum removal torque of the miniscrews is significantly higher than the maximum insertion torque because of the osseointegration or partial integration of the miniscre.

Another problem that needs to be solved is the lower torque generated by the human hand due to the miniscrew removal motion and the screwdriver's geometry. The maximum torque produced by a right-handed person is lower in the counterclockwise direction [9], [10], which happens to be the motion for the removal of a miniscrew (Figure 1). Moreover, the maximum torque produced in two studies [9], [11] shows that even using the same motion, different torques were measured. One reason for this could be the difference in each circular object diameter. The smaller diameter of the circular object is subjected to a lower maximum torque that can be exceeded by hand [12]. As a medical device for inserting and removing miniscrews, surgical screwdrivers generally have a smaller diameter than the ones studied

(4.5 and 6.6 cm) [9], [11] which could result in a low maximum torque of a surgeon's hand due to their small diameter. Several studies found that the maximum value of torque generated by human fingers during screw insertion motion (clockwise direction) was 420 Nmm [13]–[16].

Figure 1: (a) The initial motion of a miniscrew removal, (b) the maximum counterclockwise motion for the fingers, and (c) returning to the position for the next motion in removing the miniscrew.

One solution for both rotation direction and torque needs is an epicyclic gear. The epicyclic gear could give the reversed bit rotation a mechanical advantage through its configuration. That mechanical advantage is determined by the gear ratio and its relation to torque; a higher gear ratio will produce a more significant output torque for the same input torque. Concerning the epicyclic gear itself, many configurations can produce different results based on its input, output, or stationary components [17], [18], its rotational speed, torque, and direction of the rotation. In this research, we will use two combinations; each of them has a different function but will create a reversed bit rotation and mechanical advantage at the same time. Therefore, the purpose of this study was to evaluate the stress in the epicyclic gear for a new manual screwdriver designed for the removal of miniscrew implants.

Methodology

Model and Design

The present study's screwdriver was designed using SolidWorks®. It has a round-shaped handle, which demonstrated the best ergonomics [2] when

tested by several Indonesian surgeons. In this design, a shaft will hold the ring gear in the second epicyclic gear set; it will automatically define the upper side of the screw because the shaft is immovable. There is no study yet about determining the size of the shaft that will not disturb the ergonomics of the screwdriver that could affect a surgeon's performance. The full design of the screwdriver is shown in Figure 2.

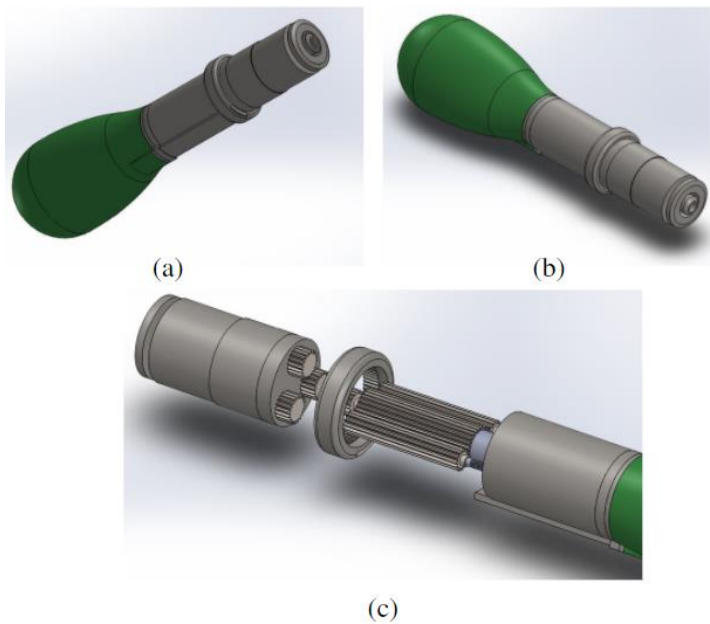

Figure 2: (a,b) overall screwdriver design and (c) epicyclic gear sets.

In this design, two sets of epicyclic gears are used, one for reversing the rotation of the bit and the other for gaining a mechanical advantage. The main reason the screwdriver needs two sets of epicyclic gears is because the first gear set (that reverses the rotation of the bit) will give this system lower torque output (based on the gear ratio, it will be lower than 1), which is not desirable in this design. Therefore, the second gear set is needed to give the mechanical advantage of higher torque output, which counteracts the undesirable effect of the first set. The arrangement of the epicyclic gears is shown in Figure 3. In the first epicyclic gear set, the planetary carrier (in this case, the handle of the screwdriver) is held stationary, so that the input of this system is in the ring gear and the output is in the sun gear. The first epicyclic gear set's sun gear is connected to the sun gear of the second epicyclic gear set, and, by holding the ring gear in this set (second gear set) stationary, the

planetary gear will rotate on its axis and revolve around the sun gear. That movement will cause the planetary carrier to become the output, transmitting the torque generated to the screwdriver's bit. The specifications of those two sets of epicyclic gears (all of them using the modified ISO standard in SolidWorks®) are shown in Table 1.

Table 1: Epicyclic gear set specification

Parts	Quantity	Module (mm)	Teeth	Pressure Angle (°)	Face Width (mm)
First Gear Set					
Sun Gear	1	0.25	28	20	24
Planetary Gear	2	0.25	15	20	24
Ring Gear	1	0.25	58	20	24
Second Gear Set					
Sun Gear	1	0.25	18	20	3
Planetary Gear	3	0.25	20	20	3
Ring Gear	1	0.25	58	20	3

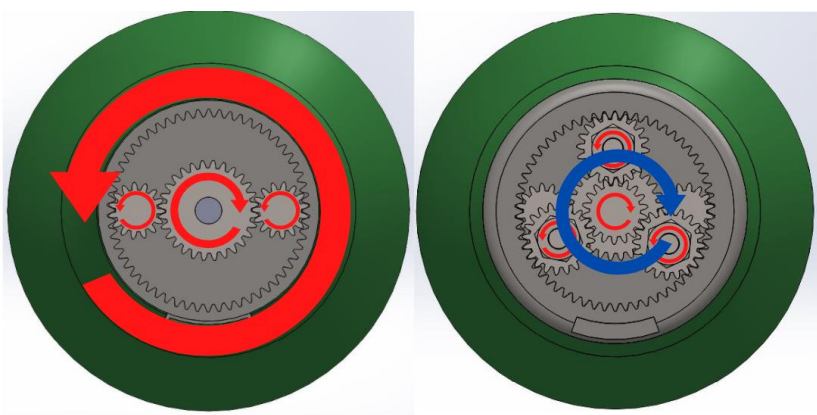

Figure 3: (a) First gear set's and (b) second gear set's movements. Both sun gears are designed to be in one shaft (see Figure 2).

The above specifications (Table 1) will create a mechanical advantage, which is one of the main developments of this screwdriver. The mechanical advantage from the epicyclic gear sets can be calculated using Equation (1),

with the number showing the position of each gear set and the letters representing the names of the components (S and R refer to the sun and ring gears):

$$\text{Gear Ratio} = \frac{\text{Torque Out}}{\text{Torque In}} = \left(\frac{N_{S1}}{N_{R1}}\right) \times \left(1 + \frac{N_{R2}}{N_{S2}}\right) \quad (1)$$

In Equation (1), we can find that the first half of the equation (the first gear set's R1 and S1) will produce a value less than one, which is the undesirable effect of the first gear set (the reverse function) arising from its lower output torque. The other half of the equation is the gear ratio of the second gear set, the higher gear ratio value of which can remove the undesirable effect of the first gear set and, according to the equation, will produce an output torque double the value of the input torque. This epicyclic gear arrangement will solve the need for higher torque in miniscrew removals by adding a mechanical advantage that will produce a torque output about twice the insertion torque.

Finite Element Analysis

This novel design was tested by simulation software (ANSYS®) to determine the stress distribution for each component. The main focus of this design test is the torque load inserted in the input ring gear (the ring gear in the first gear set) while holding the output (the carrier of the planetary gear in the second gear set) stationary. This will simulate the real-world conditions in which the screwdriver is used with a miniscrew strong enough to hold the load applied. These operating conditions were chosen for the simulation according to ISO 6336-1, which states that the most reliable known approach to the appraisal of overall system performance is testing a proposed new design [19].

In this simulation, AISI 316L and Ti6Al4V were used for the material. Both materials were chosen because they are widely used in biomedical applications, especially for surgical instruments, and because they are biocompatible. Both materials are considered light compared to the carbon steels commonly used in epicyclic gear [20], and both possess considerably high strength, which becomes crucial related to biomedical application designs in which a low failure rate is a primary consideration [21]. The mechanical properties of the material used are listed in Table 2.

Table 2: Mechanical properties of the material used in the simulation in SI

Properties	AISI 316 L	Ti6Al4V
Young Modulus (GPa)	193	119
Poisson's Ratio	0.25	0.37
Density	8000	4512
Ultimate Tensile Strength (MPa)	515	1200
Yield Strength (MPa)	205	862

The geometry for this simulation is simplified to shorten the simulation time needed to resolve this problem. The simplification pays attention to the minimum parts used for testing how they affect the results of the gear stress simulation. The torque in this simulation was designed to be varied from 0 to 1000 Nmm; this value was used considering that the removal torque value in several studies did not exceed 1000 Nmm [6], [22]. A perfect planetary gear (with no errors) will carry the same load in each planetary gear; however, manufacturing and assembly errors could create differences in each gear load [23]. Therefore, the simplification of the geometry used here will determine one of the planetary gears for each gear set with the load adjusted to the proportion between load and the number of planetary gear. For instance, the first planetary gear load is adjusted to up to 500 Nmm (ring gear) because we only use one planetary gear instead of two. The load for the second gear set must then be set up to at least 161 Nmm since the output torque from the first gear set is divided by 3 (160.9 Nmm).

Hex-dominant is used for model meshing [24], with refinement in specific areas defined as the contact area. Some bearings are involved in the design and will be represented by revolute joints. Two finite element analyses will be conducted for analyzing each gear. For the first gear set, the analysis was conducting by adding joint load (0-500 Nmm) in the ring gear and fixing the support in the sun gear (Figure 4). In this analysis, the model was meshed by 1,378,584 nodes and 930,563 elements (Figure 5), with the element in the gear tooth that will be in contact having a finer mesh than the whole structure to improve the accuracy of the simulation and to optimize the solving time by having a bigger mesh in the less affected areas. In the second gear set, the analysis was conducted by adding joint moment (0-161 Nmm) in the sun gear and fixing the support in the ring gear (Figure 6); fixed support in the ring gear was added to simulate the shaft that holds the second epicyclic ring gear, steadying it so that the planetary gear carrier could be the output. This analysis model was meshed by 332,831 nodes and 222,914 elements (Figure 7).

Figure 4: Parameters used in the first gear sets with A as fixed support and B as the area where the joint load is applied.

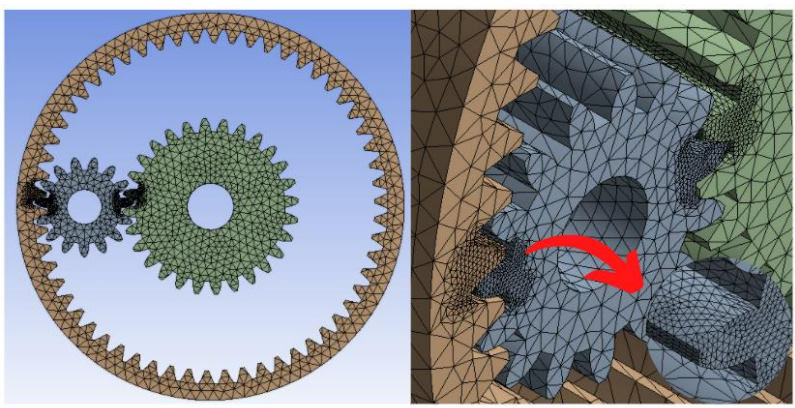

(a) (b)

Figure 5: (a) First gear set meshed and (b) refinement in the contact area.

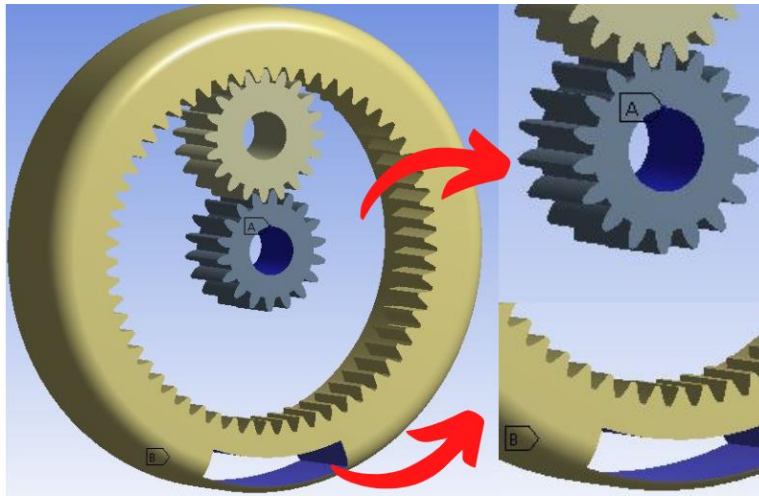

Figure 6: Parameters used in the second gear set with A being the joint load applied area and B as a fixed support.

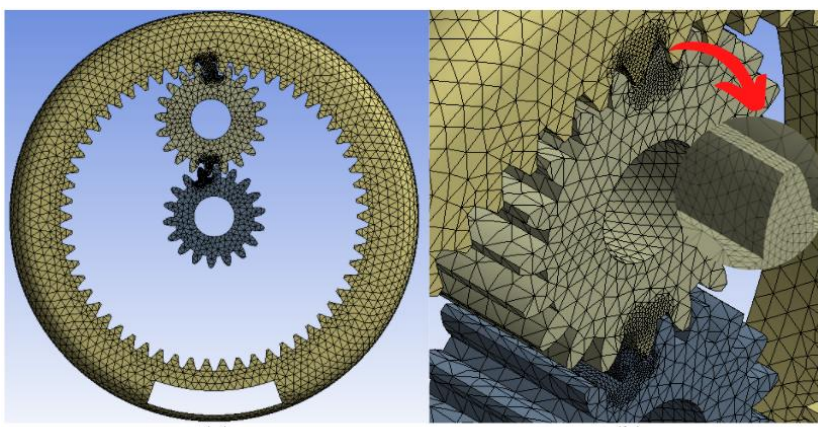

Figure 7: (a) The second gear set meshed and (b) refinement in its contact area.

Results and Discussion

The simulation results are shown in Tables 3 until Table 10; these tables list the maximum Von Mises stress values and total deformation of each part in each gear set. In this study, the overall torque load was designed to increase from 0-1000 Nmm at 200 Nmm increments, but this was adapted for each simulation setting. In other words, each load torque value represented two times its value for the first epicyclic gear sets and three times its value for the second epicyclic gear sets. (As results of the gear ratio of the first gear sets, the value transmitted would not be the same with the input load.) The results for the simulation model that used AISI 316L for its material in Tables 3 and 4 show the maximum Von Misses stress values for each component in each epicyclic gear set, while Tables 7 and 8 show the maximum total deformation in each epicyclic gear set. The maximum Von Mises stress value results for the model using Ti6Al4V are shown in Tables 5 and 6, while Tables 9 and 10 list the total deformation for each component in each epicyclic gear set.

The maximum Von Mises stress values increases linearly, subject to the increment of the load applied. In all of the simulations using different materials and gear sets, the highest maximum Von Misses stress happened in the second gear set with the sun gear, which comes in contact with the second planetary gears that transfer the load to be the screwdriver's output; here, the maximum Von Mises stress in AISI 316 L is higher than in Ti6Al4V. Since the yield strength of AISI 316 L is 205 MPa, it tends to be exceeded by the stress in the second gear set after the second load increment, which was 64.4 Nmm in the simulation with the second gear set (due to the adjustment mentioned before) or equal to 400 Nmm input torque if using designed geometry that has three planetary gears (see Figure 3).

Table 3: Maximum Von Mises stress values in the first epicyclic gear set using AISI 316L for the material

Torque (Nmm)	Maximum Von Mises Stress Value (MPa) (AISI 316L)		
	First Ring Gear	First Planetary Gears	First Sun Gear
500	65.946	103.71	53.741
400	52.768	86.63	45.095
300	39.513	69.394	36.342
200	26.293	52.025	27.453
100	13.162	31.363	14.975

Table 4: Maximum Von Mises stress values in second epicyclic gear set using AISI 316L for material

Torque (Nmm)	Maximum Von Mises Stress Value (MPa) (AISI 316L)		
	Second Ring Gear	Second Planetary Gears	Second Sun Gear
161	345.18	526.90	522.59
128.8	284.64	440.17	452.21
96.6	217.36	341.99	354.30
64.4	146.54	236.53	242.30
32.2	71.279	144.31	139.61

Table 5: Maximum Von Mises stress values in the first epicyclic gear set using Ti6Al4V for the material

Torque (Nmm)	Maximum Von Mises Stress Value (MPa) (Ti6Al4V)		
	First Ring Gear	First Planetary Gears	First Sun Gear
500	64.589	93.778	53.211
400	51.484	79.719	42.889
300	38.654	62.662	32.569
200	25.701	45.431	23.688
100	12.847	27.533	14.132

Table 6: Maximum Von Mises stress values in the second epicyclic gear set using Ti6Al4V for the material

Torque (Nmm)	Maximum Von Mises Stress Value (MPa) (Ti6Al4V)		
	Second Ring Gear	Second Planetary Gears	Second Sun Gear
161	291.53	415.46	430.76
128.8	246.07	372.81	362.36
96.6	201.75	310.75	292.74
64.4	139.11	221.33	217.95
32.2	70.143	124.55	116.65

Table 7: Maximum total deformation in the first epicyclic gear set using AISI 316L for the material

Torque (Nmm)	Maximum Total Deformation (mm) (AISI 316L)		
	First Ring Gear	First Planetary Gears	First Sun Gear
500	8.3481E-03	8.9776E-04	1.5404E-04
400	6.6852E-03	7.2361E-04	1.2295E-04
300	5.7862E-03	5.4773E-04	9.2204E-05
200	3.3409E-03	3.7140E-04	6.1868E-05
100	1.6749E-03	1.9125E-04	3,1188E-05

Table 8: Maximum total deformation in the second epicyclic gear set using AISI 316L for the material

Torque (Nmm)	Maximum Total Deformation (mm) (AISI 316L)		
	Second Ring Gear	Second Planetary Gears	Second Sun Gear
161	2.6871E-02	3.3386E-02	3.5439E-02
128.8	2.1571E-02	2.6859E-02	2.8552E-02
96.6	1.6231E-02	2.0261E-02	2.1580E-02
64.4	1.0863E-02	1.3617E-02	1.4547E-02
32,2	5.4467E-03	6.8665E-03	7.3664E-03

Table 9: Maximum total deformation in the first epicyclic gear set using Ti6Al4V for the material

Torque (Nmm)	Maximum Total Deformation (mm) (Ti6Al4V)		
	First Ring Gear	First Planetary Gears	First Sun Gear
500	1.2573E-02	1.3959E-03	2.5601E-04
400	1.0041E-02	1.1225E-03	2.0439E-04
300	7.5418E-03	8.5012E-04	1.5260E-04
200	5.0248E-03	5.7377E-04	1.0089E-04
100	2.5190E-03	2.9611E-04	5.0692E-05

Table 10: Maximum total deformation in the first epicyclic gear set using Ti6Al4V for the material

Torque (Nmm)	Maximum Total Deformation (mm) (Ti6Al4V)		
	Second Ring Gear	Second Planetary Gears	Second Sun Gear
161	4.2601E-02	5.2517E-02	5.5530E-02
128.8	3.4265E-02	4.2328E-02	4.4843E-02
96.6	2.5834E-02	3.2002E-02	3.3972E-02
64.4	1.7313E-02	2.1527E-02	2.2912E-02
32.2	8.7180E-03	1.0919E-02	1.1680E-02

In theory, there are some ways to decrease the maximum stress in the sun gear from the second epicyclic gear set. Increasing the number of planetary gear in this gear set might decrease the maximum Von Mises stress value since the total contact area will increase. Changing the gear tooth size or geometry might also decrease the Von Misses stress value but might also change the gear ratio (which would affect the mechanical advantage of the screwdriver) or increase the handle's size due to an increase of ring gear diameter that could affect the ergonomics of this design.

The stress and deformation distribution for both materials are similar (Figure 8) due to the geometry and condition of the simulations being the same. Both the above pictures were taken when the maximum load occurred and show no difference because the total deformations incurred are small (Tables 7-10). However, each gear component tends to have a large stress concentration in the contact area and the tooth root of the contacted tooth, as shown in Figure 8 and 9. A previous studies shows the same results in terms of stress distribution pattern [25], [26]. The gear tooth's root shows large stress because the contacted gear holds the force transmitted, just like a cantilever, with the root as the fixed base, and the contact area holds the most contact stress between the colliding gear components. Furthermore, the stress concentration also appears near the fixed support area at the ring gear from the second gear set (Figure 10). This demonstrates that the shaft might be objected to a certain amount of movement and requires the right materials and dimensions that would not or would less affect the screwdriver’s ergonomic factors that could affect a surgeon’s performance.

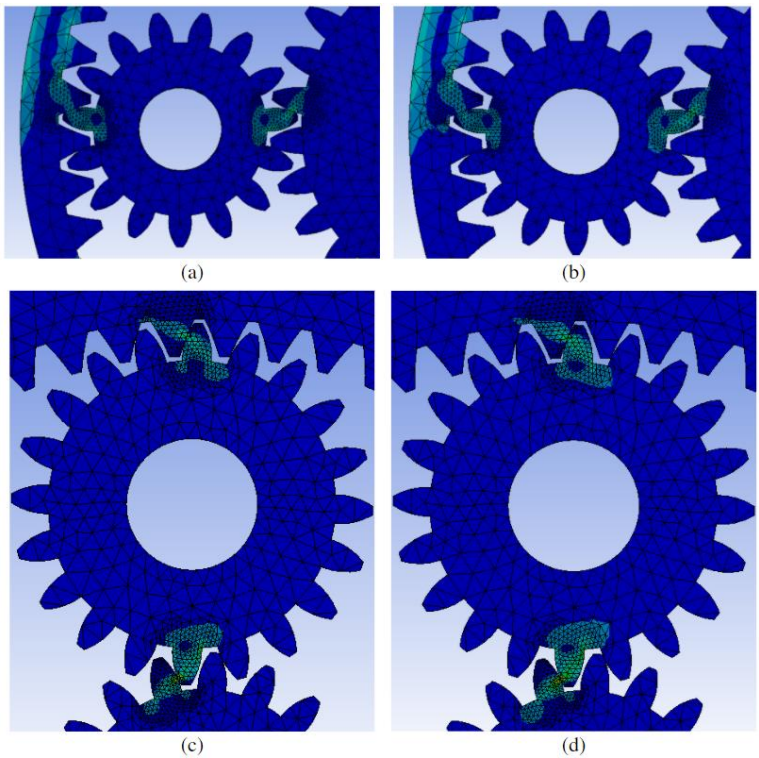

Figure 8: First epicyclic gear set using (a) AISI 316L and (b) Ti6Al4V; and second epicyclic gear set using (c) AISI 316L and (d) Ti6Al4V.

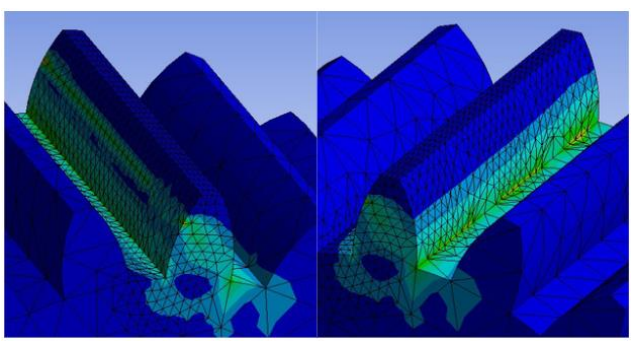

Figure 9: The planetary gear from the second epicyclic gear set shows the stress distribution.

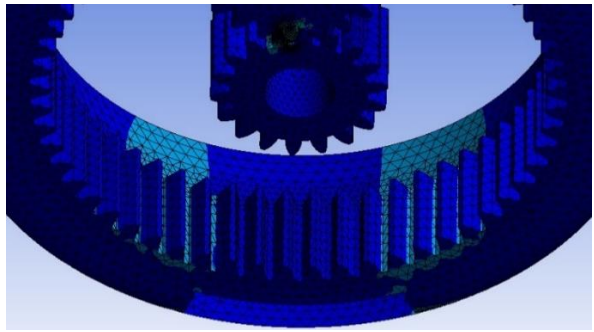

Figure 10: The built-up stress near the fixed support area at the ring gear from the second gear set.

Tables 7 to Table 10 show that the maximum total deformation is related to the stress experienced for each part and the material properties of the model. For instance, the maximum total deformation in the sun gear from the second planetary gear with the highest maximum Von Misses stress value tends to have higher total deformation. The maximum Von Misses stress value is also affected by the material assigned to the model; the maximum total deformation in Ti6Al4V is higher than in AISI 316L, but the maximum Von Misses stress value apparently shows the opposite because AISI 316L has a higher Young's modulus compared to Ti6Al4V, which would make AISI 316L stiffer. The highest maximum total deformation occurs in the sun gear from the second epicyclic gear set when the maximum torque is applied.

Conclusion

A novel design of a manual screwdriver that has reverse rotation and a mechanical advantage was successfully designed. This screwdriver will give about twice the torque in the output compared to the torque input. This simulation-based study shows that the torque input that simulates screwdriver usage will vary in Von Mises stress in each part of the epicyclic gear. In all torque inputs, the highest Von Mises stress always happened in the sun gear from the second epicyclic gear set, followed in order from high to low by the planetary and ring gears from the second gear set and then the planetary, ring, and sun gears from first gear set. The highest Von Misses stress value in each part, as expected, is found at the highest torque input, which represented 1000 Nmm but was adapted in each simulation setting. When AISI 316L was used for the material, the value of each part (from high to low) was 522.59 MPa, 526.90 MPa, 345.18 MPa, 103.71 MPa, 65.946 MPa, and 53.741 MPa.

When Ti6Al4V was used for the material, the value of each part was (from high to low) 430.76 MPa, 415.46 MPa, 291.53 MPa, 93.778 MPa, 64.589 MPa, and 53.221 MPa. The stress values and distribution of each part could be considered for further improvement of this novel design. The simulation's total deformation shows that the deformation that happened when using AISI 316L as the material is smaller than the total deformation when Ti6Al4V was used as the material. This study may need improvement in the screwdriver's design, along with related tests and simulations, to realize the final product.

Acknowledgement

This research work was funded by LPDP Ministry of Finance Republic of Indonesia under Grant Rispro Invitasi 2019 no. UI SK KEP-52/LPDP/2019.

References

[1] K. L. F. Leibinger, "Screwdriver, Particularly for Surgical Purposes," 4.763.548, 1988.
[2] S. Supriadi, R. N. Habibyanto, M. T. Ayman, and W. Muhamad, "Development of screwdriver for maxillofacial miniplate implant with torque-limiting capability," in *AIP Conference Proceedings*, vol. 2092, 2019.
[3] X. Liu, J. Shi, W. Ding, W. Xu, and X. Chen, "The effect of a new modified screwdriver in orthodontic," *Int. J. Clin. Exp. Med.*, vol. 12, no. 8, pp 9706-9711, 2019.
[4] F. D. Uzuner and B. Işık Aslan, "Miniscrew Applications in Orthodontics," in *Current Concepts in Dental Implantology*, 2015.
[5] M. S. M. Pires, L. C. Reinhardt, G. de Marco Antonello, and R. Torres do Couto, "Use of Orthodontic Mini-Implants for Maxillomandibular Fixation in Mandibular Fracture," *Craniomaxillofac. Trauma Reconstr.*, vol. 4, no. 4, pp 213–216, 2011.
[6] E. Y. Suzuki and B. Suzuki, "Placement and removal torque values of orthodontic miniscrew implants," *Am. J. Orthod. Dentofac. Orthop.*, vol. 139, no. 5, pp 669–678, 2011.
[7] S. Fadhilah, A. A. Agus, P. Kreshanti, H. D. S. Budiono, S. Supriadi, and Y. Whulanza, "Engineering economics of cranio-maxillofacial (CMF) degradable implant production in indonesia," in *AIP Conference Proceedings*, vol. 2227, 2020
[8] B. Vande Vannet, M. M. Sabzevar, H. Wehrbein, and K. Asscherickx, "Osseointegration of miniscrews: A histomorphometric evaluation," *Eur. J. Orthod.*, vol. 29, no. 5, pp 437–442, 2007.
[9] J. K. Shim, J. Huang, A. Hooke, M. Latsh, and V. Zatsiorsky, "Multi-

digit maximum voluntary torque production on a circular object," *Ergonomics*, vol. 50, no. 5, pp 660–675, 2007.
[10] J. K. Shim, M. L. Latash, and V. M. Zatsiorsky, "Finger coordination during moment production on a mechanically fixed object," *Exp. Brain Res.*, vol. 157, no. 4, pp 457–467, 2004.
[11] A. I. M. Voorbij and L. P. A. Steenbekkers, "The twisting force of aged consumers when opening a jar," *Appl. Ergon.*, vol. 33, no. 1, pp 105–109, 2002.
[12] Y. K. Kong and B. D. Lowe, "Evaluation of handle diameters and orientations in a maximum torque task," *Int. J. Ind. Ergon.*, vol. 35, no. 12, pp 1073–1084, 2005.
[13] M. Alikhasi, M. Kazemi, H. Jalali, S. Hashemzadeh, H. Dodangeh, and B. Yilmaz, "Clinician-generated torque on abutment screws using different hand screwdrivers," *Journal of Prosthetic Dentistry*, 2017, vol. 118, no. 4, pp 488–492.
[14] F. Parnia, J. Yazdani, P. Fakour, F. Mahboub, and S. M. Vahid Pakdel, "Comparison of the maximum hand-generated torque by professors and postgraduate dental students for tightening the abutment screws of dental implants," *J. Dent. Res. Dent. Clin. Dent. Prospects*, vol. 12, no. 3, pp 190–195, 2018.
[15] Y. Sameera and R. Rai, "Tightening torque of implant abutment using hand drivers against torque wrench and its effect on the internal surface of implant," *J. Indian Prosthodont. Soc.*, vol. 20, no. 2, pp 180, 2020.
[16] A. Kanawati, M. W. Richards, J. J. Becker, and N. E. Monaco, "Measurement of clinicians' ability to hand torque dental implant components.," *J. Oral Implantol.*, vol. 35, no. 4, pp. 185–188, 2009.
[17] I. Hüseyin Filiz, S. Olguner, and E. Evyapan, "A study on optimization of planetary gear trains," in *Acta Physica Polonica A*, 2017, vol. 132, no. 3, pp 728–733.
[18] Q. Zeng, S. Jiang, L. Wan, and X. Li, "Finite element modeling and analysis of planetary gear transmission based on transient meshing properties," *Int. J. Model. Simulation, Sci. Comput.*, vol. 6, no. 3, 2015.
[19] International Standard, *ISO 6336-1: Calculation of Load Capacity of Spur and Helical Gears – Part 1: Basic Principles, Introduction and General Influence Factors. 2nd edition*, 2006.
[20] D. Axinte, Y. Guo, Z. Liao, A. J. Shih, R. M'Saoubi, and N. Sugita, "Machining of biocompatible materials — Recent advances," *CIRP Ann.*, vol. 68, no. 2, pp 629–652, 2019.
[21] H. Delibaş, Ç. Uzay, and N. Geren, "Advanced Material Selection Technique For High Strength and Lightweight Spur Gear Design," *Eur. Mech. Sci.*, vol. 1, no. 4, pp 133–140, 2017.
[22] J. Y. Cha, T. M. Yoon, and C. J. Hwang, "Insertion and removal torques according to orthodontic mini-screw design," *Korean J. Orthod.*, vol. 38,

no. 1, pp 5–12, 2008.
[23] C. G. Cooley and R. G. Parker, “A review of planetary and epicyclic gear dynamics and vibrations research,” *Applied Mechanics Reviews*, vol. 66, no. 4, 2014.
[24] Y. Liu, Y. Zhao, M. Liu, and X. Sun, “Parameterized High-Precision Finite Element Modelling Method of 3D Helical Gears with Contact Zone Refinement,” *Shock Vib.*, vol. 2019, 2019.
[25] V. Karaveer, A. Mogrekar, T. Preman, and R. Joseph, “Modeling and Finite Element Analysis of Spur Gear,” *Int. J. Curr. Eng. Technol.*, 2013.
[26] M. P. Thu and N. L. Min, “Stress Analysis on Spur Gears Using ANSYS Workbench 16.0,” *Int. J. Sci. Eng. Appl.*, 2018.

Thin-walled Beam Bending Quartic Deplanation Analytical Function for Improved Experiment Matching

A Halim Kadarman[*], Nabilah Azinan, Junior Sarjit Singh Sidhu
School of Aerospace Engineering
Universiti Sains Malaysia, 14300 Nibong Tebal, Penang, Malaysia
[*]Email: ahalim@usm.my

Solehuddin Shuib
Faculty of Mechanical Engineering
Universiti Teknologi Mara, 40450 Shah Alam, Selangor, Malaysia

ABSTRACT

Ensuring the accuracy of an analytical solution is important in modeling real engineering structures. For determining the stress-deformation condition of a thin-walled beam structure in bending, inadequately, the simple beam formula can only provide uniform average stress-deformation distribution at specific cross-sectional elevations. The recently developed analytical solution for determining stress-deformation conditions with consideration of the shear lag effect of a prismatic thin-walled box beam subjected to transverse load causing bending using classical quadratic deplanation function did not provide an accurate but rather a good estimate when compared with finite element analysis results. In this paper, the objective of the study was to see if the accuracy can be improved. The same Vlasov's method was used. The method was developed using Calculus of Variations based on a Stress-form stationary condition complementary energy which included the shear lag effect. All calculations were computerized using the software MAPLE 18 which assisted in getting quick results (especially for preliminary design studies) for various geometries, material properties, and loading conditions. Several deplanation functions were introduced. Two variants of the quadratic functions, i.e. x^2y^3 and x^2y, and the quartic functions, i.e. x^4y^3 and x^4y were used to find the best match against empirical data and FEA (finite element analysis) results. The finding was that the quartic variant of the deplanation functions provided improved matching with experimental data as well as FEA results. Noteworthy to point

ISSN 1823-5514, eISSN 2550-164X
Received for review: 2020-08-28
Accepted for publication: 2020-12-11
Published: 2021-01-15

out that the characteristic of the functions with quartic-x or x^4 of having almost flat variation in the center part enhances matching with the experimental data. Moreover, the characteristic of the function with cubic-y or y^3 of having steeper slopes enhances matching with the FEM results at the edge.

Keywords: *Thin-walled beam bending, Deplanation function, Thickness-radius ratio, Shear lag, Analytical vs Experiment*

Introduction

Thin-walled box beams are widely used in engineering structures such as civil, mechanical, and aerospace for bridges, buildings, aircrafts, and rockets. The basic simple beam solution for determining the stress-deformation of beams in bending can only provide uniform average stress-deformation distribution at specific cross-sectional elevations which is inadequate for thin-walled beams that experience the shear lag effect. Hence, an analytical formula or calculation method which includes the shear lag effect is needed to provide a more reliable, and more accurate representative estimate of this stress-deformation condition.

The developed analytical solution in [1] based on Vlasov's method [2] for determining stress-deformation conditions with consideration of the shear lag effect of a prismatic thin-walled box beam subjected to transverse load causing bending using classical quadratic deplanation function did not provide an accurate but rather a good estimate when compared with finite element analysis results. In this paper, the objective of the study was to see if the accuracy can be further improved using the same method but only changing the deplanation/distortion functions. This Vlasov's method was developed using Calculus of Variations based on a Stress-form stationary condition complementary energy which included the shear lag effect. All calculations were computerized using the software MAPLE 18 [3] which assisted in getting quick results (especially for preliminary design studies) for various geometries, material properties, and loading conditions.

In this paper, several deplanation functions were introduced. Two variants of the quadratic functions, i.e. x^2y^3 and x^2y, and the quartic functions, i.e. x^4y^3 and x^4y were used to find the best match against empirical data and FEA (finite element analysis) results.

The finding was that the quartic variant of the deplanation functions provided improved matching with experimental data as well as FEA results. Noteworthy to point out that the characteristic of the functions with quartic-x or x^4 of having almost flat variation in the center part enhances matching with the experimental data. Furthermore, the characteristic of the function with cubic-y or y^3 of having steeper slopes enhances matching with the FEM results at the edge.

Literature background

Kadarman et al. [1] analytically developed a version of Vlasov's Stress-form using the variational method and found very close matching of the analytical Stress-form and recognized Displacement-form from [4]. Comparison with FEM showed that the Stress-form results were matching well at the high stress region and were slightly higher at the intermediate stress area.

In [5], using the variational method, both elastic and inelastic solutions were shown. Here, Lin and Zhao studied the effect of shear lag in steel box beams. The verification of the analytical method was done by experimental means of testing on steel box beams. Comparison of the proposed variation method with experimental data found that the model predicts quite well the steel box beams' plastic normal strain distribution and deflection.

In [6], using the variational principle, an analytical solution taking into account the shear lag was presented by Chen et al. Using the principle of superposition, the problem of loaded simply supported and cantilever beams were solved. The calculated normal stress was well predicted.

In this paper, an analytical method developed recently in [1] was verified further by comparison with experimental data from [5] – [8] and also by FEM. Flexural bending of a thin-walled box can cause Deplanation/Distortion due to the shear lag effect (Figure 1).

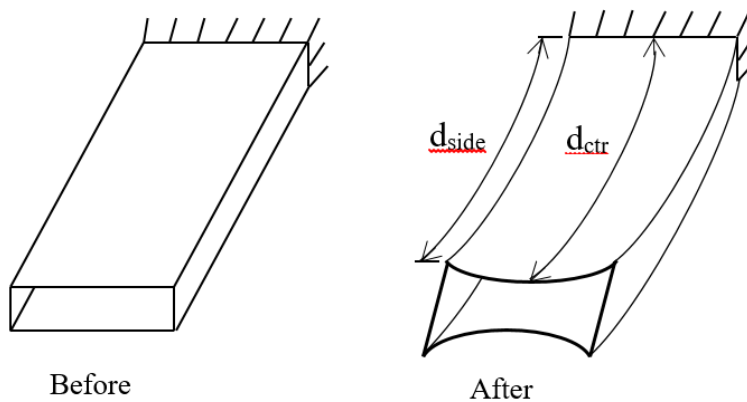

Figure 1: Box beam flexural bending causes contraction of d_{side} to differ from d_{ctr} [1].

Analytical Formulation

First Step – establishing stresses

The hollow doubly-symmetric prismatic thin-walled box beam in Figure 2 is clamped at one end and its section is centered at the origin of the x, y and, z axes. It is subjected to the transversal distributed load w_y acting through the elastic axis that causes shear $V_y = \int_0^z w_y(z)dz$ and moment $M_x = \int_0^z V_y(z)dz$. As in [1, 9] the analytical solution is derived based on these loads.

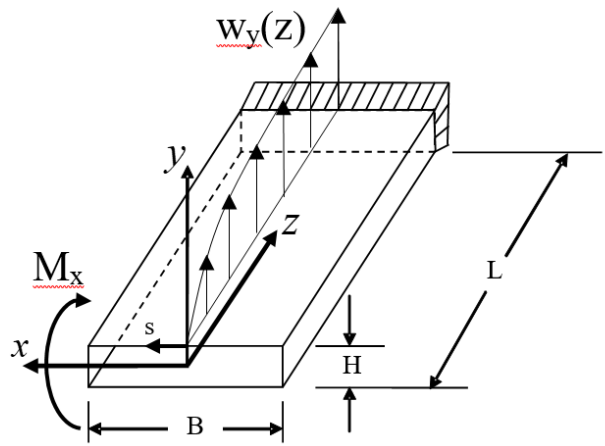

Figure 2: Hollow Box beam with distributed load w_y [1].

Using curvilinear coordinate s as in [10, 11], the equations of equilibrium similar to equations 3.90a and 3.90b in [12]:

$$\frac{\partial N_z}{\partial z} + \frac{\partial N_{zs}}{\partial s} = 0 \quad , \quad \frac{\partial N_{zs}}{\partial z} + \frac{\partial N_s}{\partial s} = 0 \tag{1}$$

From Equation (1), N_{zs} and N_s can be written in term of N_z,

$$N_{zs} = -\int \frac{\partial N_z}{\partial z} ds + q_0(z) \tag{2}$$

$$N_s = \iint \frac{\partial^2 N_z}{\partial z^2} ds^2 - \left[\int q_0'(z) ds\right] + n(z) \tag{3}$$

Let the longitudinal stress resultant, N_z be the combination of a simple beam solution and a term with the deplanation function $\overline{\varphi_4}(s)$ which shapes the stress resultant distribution due to distortion along the s-contour:

$$N_z = N_{z,SB} + X_4\varphi_4 \tag{4}$$

where $\quad N_{z,SB} = -\dfrac{M_x}{I_x} y h_i \quad$ (**S**imple **B**eam)

$$X_4(z) \equiv \text{deplanation intensity multiplier along z}$$

$$\varphi_4 = \overline{\varphi_4} + C_1 N_{z,SB} \quad , \quad \overline{\varphi_4} = x^2 y \text{ or } x^2y^3 \text{or } x^4 y \text{ or } x^4y^3$$

$$C_1 \equiv \text{ orthogonalization coefficient}$$

I_x= centroidal area moment of inertia. C_1 is determined by orthogonalization of functions [13] (also see Appendix) to ensure that the resulting distribution of stress resultants self-equilibrate (self-balance) in the section to preserve force equilibrium with the simple beam uniform stress level:

$$\oint N_{z,SB}\varphi_4 \, ds = 0$$

Now continue on with N_{zs}, insert Equation (4) into Equation (2):

$$N_{zs} = -\int (N'_{z,SB} + X'_4\varphi_4)\, ds + q_0(z) \tag{5}$$

Substitute $q_Q(s,z) = -\int N'_{z,SB}\, ds$ into Equation (5) and rearrange:

$$N_{zs} = q_Q(s,z) + q_0(z) - X'_4 \int \varphi_4 \, ds \tag{6}$$

The first two terms of Equation (6) are simple beam solutions. And:

$$q_Q(s,z) = \frac{V_y Q_x^{\Delta}}{I_x}$$

is familiarly known as the shear flow that varies with the first moment of area:

$$Q_x^{\Delta} = \int_0^s \bar{y} ds$$

while $q_0(z)$ is the constant shear flow. For the analytical solution of $q_0(z)$, the torsional moment equilibrium is used:

$$M_z = \oint N_{zs}\rho ds$$

There is no torsional moment and w_y is acting through the elastic axis, hence M_z is zero:

$$0 = \oint N_{zs}\rho ds \tag{7}$$

Insert Equation (6) into Equation (7):

$$0 = \oint \left\{ q_Q(s,z) + q_0(z) - X_4' \int \varphi_4 \, ds \right\} \rho ds$$

Take $q_0(z)$ out of the integral since it is independent of s and use $\omega = \oint \rho ds$:

$$q_0(z) = \frac{1}{\omega}\left[- \oint q_Q(s,z)\rho ds + X_4' \oint \left(\int \varphi_4 ds \right) \rho ds \right] \tag{8}$$

Insert Equation (8) into Equation (6) and let:

$$q_{Mz} = q_Q(s,z) - \frac{1}{\omega}\oint q_Q(s,z)\rho ds$$

and

$$b_4(s) = \int \varphi_4 ds - \frac{1}{\omega}\oint \left(\int \varphi_4 ds \right) \rho ds$$

Hence:

$$N_{zs} = q_{Mz} - X_4' b_4 \tag{9}$$

Second step – using variational calculus

Variational calculus is explained comprehensively in [14]. The analytical solution of $X_4(z)$ is obtained using the Variational Principle of the Least Work. After substituting the stresses into the Potential energy functional,

$$U = \int_0^L \Phi(X_4, X_4', z) dz$$

and minimization of this functional, a differential equation of displacement

compatibility is produced. Then after solving the differential equation and applying the boundary conditions the complete solution for N_z and N_{zs} can be obtained. In this case:

$$U = \int_0^L \left[\oint \left(\frac{N_z^2}{2Eh} + \frac{N_{zs}^2}{2Gh} + \frac{N_s^2}{2Eh} \right) ds \right] dz$$

.

N_s has relative negligible value as extensively discussed in [15], hence:

$$U = \frac{1}{2} \int_0^L \left[\oint \left(\frac{N_z^2}{Eh} + \frac{N_{zs}^2}{Gh} \right) ds \right] dz$$

Insert Equation (4) and Equation (9):

$$U = \frac{1}{2} \int_0^L \oint \left\{ C_{11} \left[N_{z,SB} + X_4 \varphi_4 \right]^2 + C_{33} [q_{Mz} - X_4' b_4]^2 \right\} ds dz$$

where $C_{11} = {}^1/_{Eh}$ and $C_{33} = {}^1/_{Gh}$. Let stress function,

$$\Phi = \frac{1}{2} \oint \left\{ C_{11} \left[N_{z,SB} + X_4 \varphi_4 \right]^2 + C_{33} [q_{Mz} - X_4' b_4]^2 \right\} ds$$

To minimize:

$$U = \int_0^L \Phi(X_4,\ X_4', z) dz$$

the Euler-Lagrange equation:

$$\frac{d}{dz} \frac{\partial \Phi}{\partial X_4'} - \frac{\partial \Phi}{\partial X_4} = 0$$

must be satisfied. Hence insert Φ and differentiate:

$$\frac{\partial \Phi}{\partial X_4'} \qquad \text{and} \qquad \frac{\partial \Phi}{\partial X_4}$$

and substitute to get:

$$\frac{d}{dz}\left\{\oint[-C_{33}(q_{Mz}-X_4'b_4)b_4]ds\right\}-\oint\left[C_{11}\left(N_{z,SB}+X_4\varphi_4\right)\varphi_4\right]ds=0$$

Continue to differentiate with respect to z,

$$\oint\left[-C_{33}\left(b_4q_{Mz}'-b_4^2X_4^{''}-2b_4b_4'X_4'+b_4'q_{Mz}\right)\right]ds$$
$$-\oint\left[C_{11}\left(N_{z,SB}+X_4(z)\varphi_4\right)\varphi_4\right]ds=0$$

And expanding:

$$\oint C_{33}b_4^2X_4^{''}ds+\oint C_{33}2b_4b_4'X_4'ds+\oint C_{11}X_4\varphi_4^2ds$$
$$=\oint C_{11}N_{z,SB}\varphi_4ds+\oint C_{33}b_4q_{Mz}'ds+\oint C_{33}b_4'q_{Mz}ds$$

As b_4 is independent of z, hence $b_4'=0$ and X_4 and $X_4^{''}$ are independent of s, so they can be taken out of the integrations:

$$X_4^{''}\oint C_{33}b_4^2ds-X_4\oint C_{11}\varphi_4^2ds=\oint C_{11}N_{z,SB}\varphi_4ds+\oint C_{33}b_4q_{Mz}'ds$$

And simplifying, produces a second order differential equation:

$$A_{11}X_4^{''}-A_{12}X_4=B_1+B_2$$

where

$$A_{11}=\oint C_{33}b_4^2ds \quad , \quad A_{12}=\oint C_{11}\varphi_4^2ds,$$

$$B_1=\oint C_{11}N_{z,SB}\varphi_4ds \quad , \quad B_2=\oint C_{33}b_4q_{Mz}'ds$$

Derived from calculus of variations, the natural boundary condition (condition of clamping) for determining constants of the solution at $z=L$:

$$\frac{\partial\Phi}{\partial X_4'}=0 \quad \rightarrow \quad \oint C_{33}\,q_{Mz}b_4ds-X_4'\oint C_{33}b_4^2ds=0 \qquad (10)$$

And at $z=0$, static equilibrium boundary condition:

$$\oint N_zyds=M_x=0$$

Finite Element Modeling

For the finite element modeling, 3-D solid elements were used instead of 2-D plate elements because of the need to compare with experimental data measured at the surface which 3-D solid elements can provide direct comparative values. The FEA are limited to linear static isotropic material meaning that plastic deformation beyond yielding was not considered. Quarter models were created and analyzed using the SOLIDWORKS software 2019 Education Edition [16] to represent the simply-supported structure with symmetry boundary constraints imposed at the longitudinal and center transverse planes and fixed vertical displacement at the bottom edge of the end of the transverse plane while 25% of the full vertical load were applied at the outside edge of the center transverse plane as shown in Figure 3.

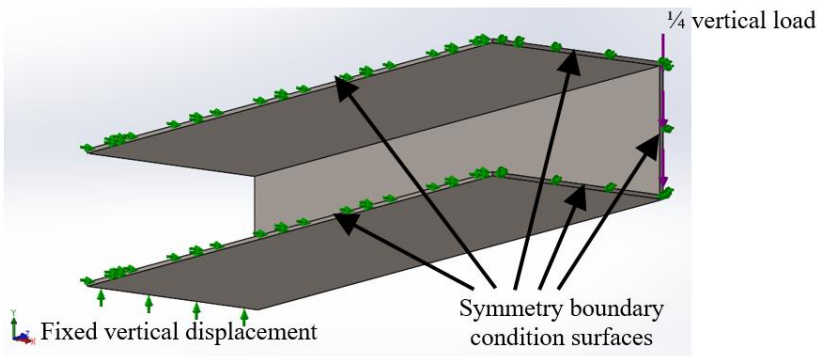

Figure 3: A sample of the Quarter FE Model (bottom view) showing how boundary conditions and load are imposed.

Comparison with Experimental Data and/or FEM

To evaluate the analytical Stress-form method developed, it was compared to existing experimental data by Ahmad stated in [5], [6], [8] and by Zhibin stated in [5], [6], [7] and newly acquired FEM results. Both Ahmad's and Zhibin's tests were conducted using simply-supported beams with measured strains at the mid-span, therefore these data were compared to the Stress-form method solutions at the fixed cantilever end to have a similar effect.

For the comparisons, the following two evaluation aspects were considered:

1. Geometry satisfying thin-walled definition. In Allen and Haisler [17]: thin-walled means a bar of circular cross- section to be one in which the

thickness t is less than or equal to 5 percent of the average radius, or $\frac{t}{r_{avg}} \leq 0.05$.

2. Matching experimental data and/or FEM results with solutions of the analytical Stress-form method using several Deplanation functions, $\overline{\varphi_4}$.

Table 1 summarized the comparisons that were done and the details are described subsequently.

Table 1: Summary of Comparisons

No.	Specimens	Comparison items	$\frac{t}{r_{avg}}$	Thin-walled?
1	300 x 100 x 3 mm	Experiment, FEM, x^4y^3, x^4y, x^2y^3 & x^2y	$\frac{3}{1/2\,(150+50)} = 0.03$	Yes
2	5 x 2 x 0.1875 in	Experiment, FEM, x^4y^3, x^4y, x^2y^3 & x^2y	$\frac{0.1875}{1/2\left(\frac{5}{2}+\frac{2}{2}\right)} = 0.107$	No
3	400 x 100 x 3 mm	FEM, x^4y^3, x^4y, x^2y^3 & x^2y	0.024	Yes
4	200 x 100 x 3 mm	FEM, x^4y^3, x^4y, x^2y^3 & x^2y	0.04	Yes

First comparison (Analytic, Data, and FEM)

The first experimental data for comparison comes originally from work done by Ahmad [5], [6], [7]. The box beam used in the experiment from Ahmad was a simply-supported beam that had a span length and cross-sectional dimensions of 1 m and 300 x 100 x 3 mm, respectively. A load of 6 kN was imposed at the mid-span as shown in Figure 4. Stresses were calculated from the strains measured at the mid-span [5]. The comparison result is shown in Figure 5.

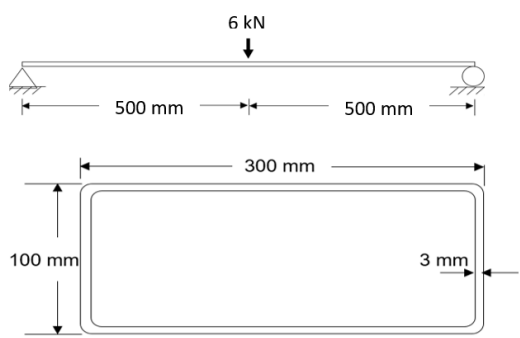

(a)

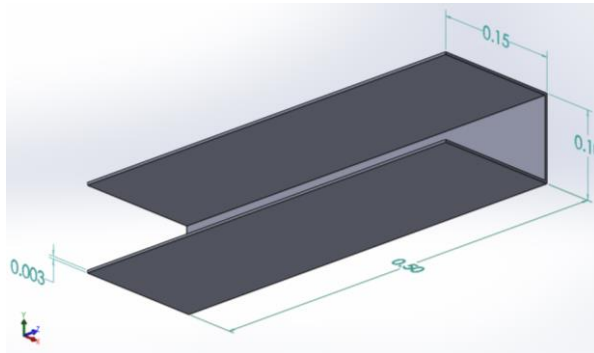

(b)

Figure 4: (a) Geometry of the Structure (b) Quarter FEM of the Structure with dimensions in meters.

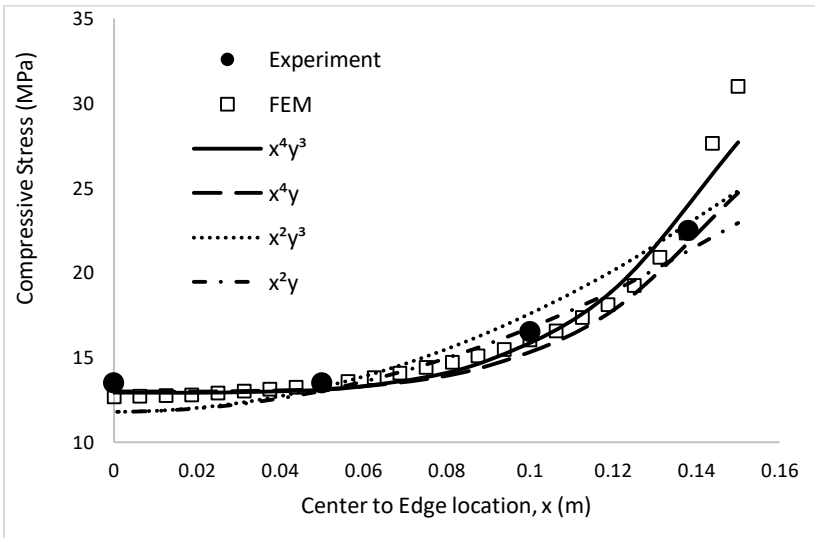

Figure 5: First Comparison of Experiment, Various Deplanation Functions, and FEM.

Second comparison (Analytic, Data, and FEM)

The second experimental data for comparison comes from a test carried out by Zhibin [5], [6]. The box beam used in the experiment by Zhibin [5], [6] was also a simply-supported beam which had a span length and cross-sectional dimensions of 21 inches (533 mm) and 5 x 2 x 3/16 inches (127 x 50.8 x 4.763

mm), respectively as shown in Figure 6. Again, at the mid-span, 45.43 kN (10.2 kips) load was imposed. And from the measured strains on the top flange's outer surface at mid-span, stresses were calculated. The comparison result is shown in Figure 7.

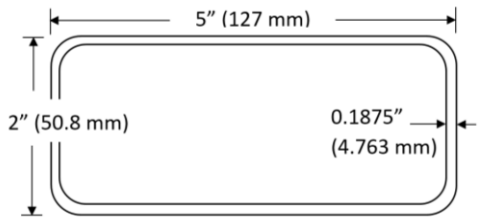

(a)

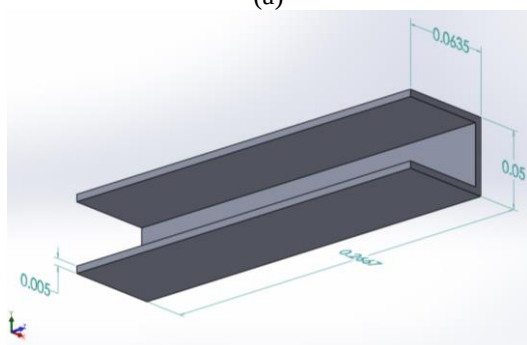

(b)

Figure 6: (a) Geometry of the Structure (b) Quarter FEM of the Structure with dimensions in meters.

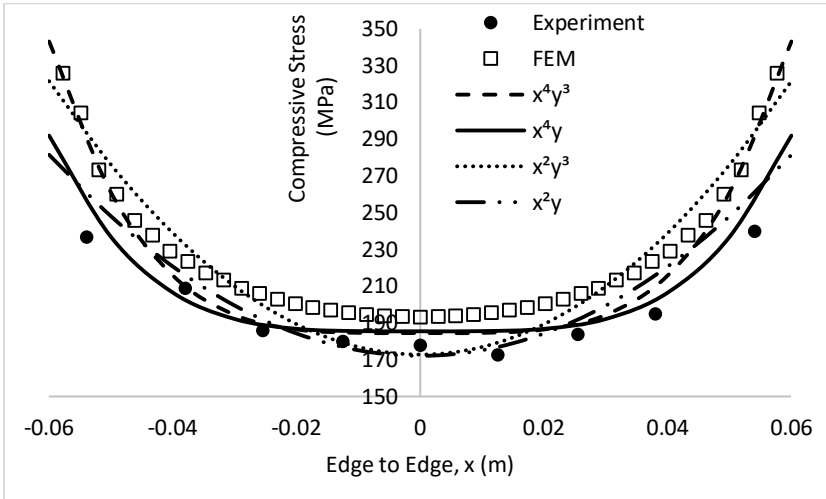

Figure 7: Second Comparison of Experiment, Various Deplanation Functions, and FEM.

Third and Fourth comparisons (Analytic and FEM only)

The third and fourth comparisons were with FEM only and also for a simply-supported beam that had the same span length and cross-sectional dimensions of 1 m and 400 x 100 x 3 mm and 200 x 100 x 3 mm, respectively. A load of 6 kN was imposed at the mid-span. The third and fourth comparison results are shown in Figures 8 and 9, respectively.

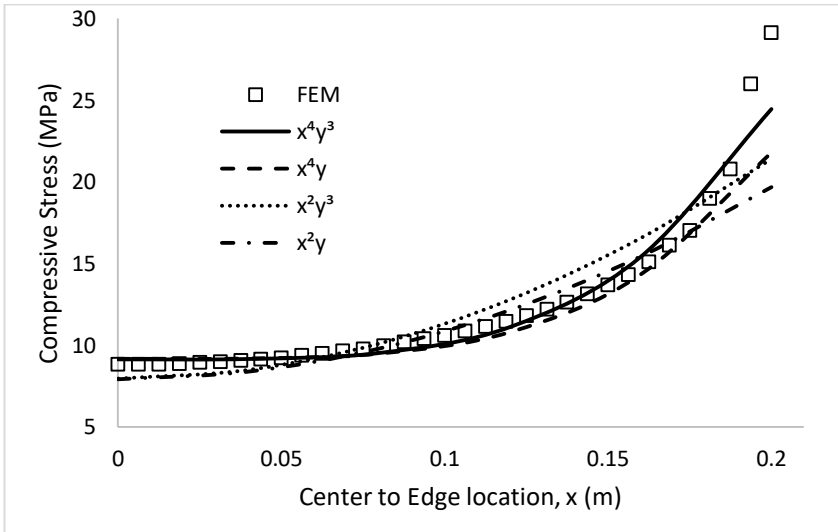

Figure 8: Third Comparison of Various Deplanation Functions, and FEM.

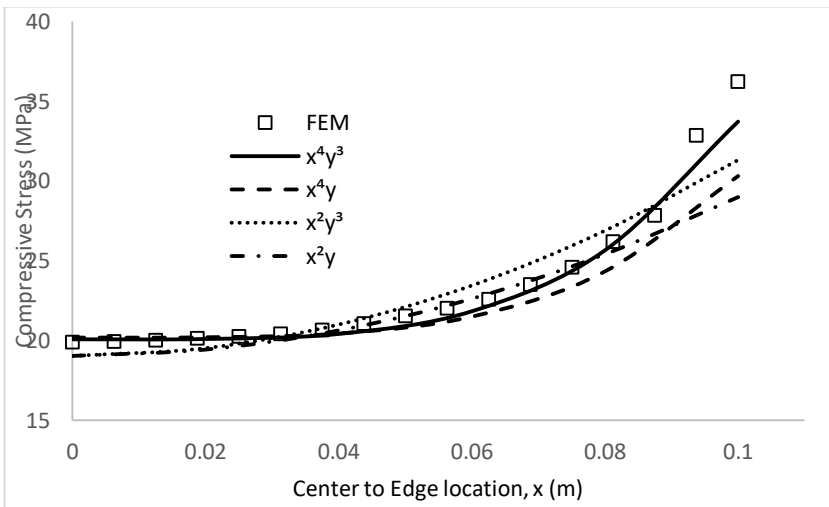

Figure 9: Fourth Comparison of Various Deplanation Functions, and FEM.

Discussion

The structure used in the first comparison had a small $\frac{t}{r_{avg}} \approx 0.030$ which satisfies the thin-walled structure definition. In comparing the analytical Stress-form Method's Deplanation functions with the experimental data, functions with quartic-x or x^4 provided the closest matches as opposed to quadratic-x or x^2, even though both of them slightly underestimated at most of the central part. However, the function $\overline{\varphi_4} = x^4y^3$, i.e. a combination of quartic-x and cubic-y function provides the best match combination of the experimental data curve as well as the FEM results near the edge part. It is interesting to note that the characteristic of the functions with quartic-x or x^4 of having almost flat variation in the center part enhances matching with the experimental data here. Moreover, the characteristic of the function with cubic-y or y^3 having steeper slopes enhances matching with the FEM results at the edge. Important to note that in contrast, the classical deplanation function was $\overline{\varphi_4} = x^2y$ as used in [1, 3].

The structure used in the second comparisons had a relatively large $\frac{t}{r_{avg}} \approx 0.107$ which also does not satisfy the thin-walled structure definition. In comparing the analytical Stress-form Method Deplanation functions with the experimental data, again functions with quartic-x or x^4 provided better matches as opposed to quadratic-x or x^2, even though in this case both of them slightly overestimated at some of the parts but also significantly at other parts especially with respect to the function $\overline{\varphi_4} = x^4y^3$. However, the function $\overline{\varphi_4} = x^4y$, i.e. a combination of quartic-x and linear-y function provides a better combined match for both the experimental data curve and FEM results.

Overall, the comparison of the second structure showed less satisfactory matching because it does not satisfy the thin-walled structure definition and probably the measured experimental data have significant errors. Figure 10 compares the differences of stresses from the FEM results between the outside and inside surfaces of both structures. Here it is observed that in the second structure, the difference of the stresses on the inside and the outside surfaces is significant in comparison to the first structure. As a result, the second structure cannot be considered a thin-walled structure.

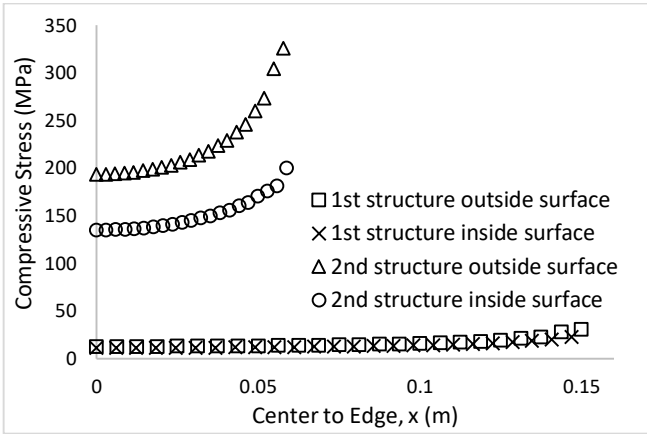

Figure 10: FEM results between outside and inside surfaces of both structure's flanges.

The structure used in the third and fourth comparisons had $\frac{t}{r_{avg}} \approx 0.024$ and $\frac{t}{r_{avg}} \approx 0.04$, respectively, which satisfy the thin-walled structure definition. No experimental data were available, however, as in the first comparison, the Deplanation function $\overline{\varphi_4} = x^4y^3$, i.e. a combination of quartic-x and cubic-y function provides the best match with FEM results.

Conclusion

Based on the comparative study done in this paper, the developed Stress-form analytical method for calculation of stresses discovered two significant findings. Primarily, the quartic variant deplanation functions were shown to produce improved matching to experimental results as compared to the classical quadratic one. Secondarily, only structures that conform to the definition of a thin-walled structure yield good results. Noteworthy to point out that the characteristic of the functions with quartic-x or x^4 of having almost flat variation in the center part enhances matching with the experimental data. Moreover, the characteristic of the function with cubic-y or y^3 having steeper slopes enhances matching with the FEM results at the edge.

Acknowledgments

Both Universiti Sains Malaysia (USM) Research University Grant RU814042 and USM Post-Graduate Incentive Grant funded this study.

References

[1] A. H. Kadarman, S. Shuib, A. H. Hassan, M. A. I. A. Zahrol, "Thin-walled Box Beam Bending Distortion Analytical Analysis", *Journal of Mechanical Engineering*, 14 (1). pp 1-17, 2017.

[2] V. Z.V lasov, *Thin-Walled Elastic Beams*, 2nd ed., State Publishing of Physics-Mathematical Literature, (in Russian), Moscow, 1959.

[3] MAPLE 18, Waterloo Maple Inc. (Maple Soft), 2018.

[4] I. F. Obraztsov, , L. A. Bulychev, V.V. Vasilev et al., "Mechanics of Building Flying Vehicles", Machine-building Publishing, (in Russian), Moscow, 1986.

[5] Zhibin Lin, Jian Zhao, "Least-work solutions of flange normal stresses in thin-walled flexural members with high-order polynomials", *Engineering Structures*, vol. 33, pp 2759-2760, 2011.

[6] Jun Chen, Shui-Long Shen, Zhen-Yu Yin, and Suksun Horpibulsuk, "Closed-form solution for shear lag with derived flange deformation function", *Journal of Constructional Steel Research*, vol. 102, pp 104-110, 2014.

[7] Zhibin Lin, Jian Zhao, "Modeling Inelastic Shear Lag in Steel Box Beams", Engineering Structures, vol. 41, pp 90-97, 2012.

[8] V. Kristek, H.R. Evan, M.K.M. Ahmad, "A shear lag analysis for composite box girders", *J Constr Steel Res*, vol. 16, no. 1, pp 16. 1990.

[9] A. A. Dudchenko, Building Mechanics of Composite Space Design, Educational text, Moscow Aviation Institute Publishing, (in Russian), Moscow, 1997.

[10] O. A. Bauchau, J. I. Craig, "Structural Analysis: With Applications to Aerospace Structures," Springer, Dordrecht Heidelberg London New York, pp 308, 2009.

[11] C. F. Kollbrunner, K. Basler, "Torsion in Structures: An Engineering Approach," Springer Science & Business Media, pp 3,123, 2013.

[12] E. Ventsel, and T. Krauthammer, "Thin Plates and Shells Theory, Analysis, and Applications," Marcel Dekker, Inc, New York, 2001.

[13] D. F. Griffiths, J. W. Dold, and D. J. Silvester, "Essential Partial Differential Equations: Analytical and Computational Aspects," Springer, Switzerland, 2015.

[14] F. Rindler, Calculus of Variations, Springer International Publishing AG, part of Springer Nature, 2018.

[15] P. Bertolinia, M.A. Eder, L. Taglialegne, P.S. Valvo, "Stresses in constant tapered beams with thin-walled rectangular and circular cross sections," Thin-Walled Structures, 2019.

[16] SOLIDWORKS 2019 Education Edition, Dassault Systemes, 2019.

[17] D. H. Allen & W. E. Haisler, "Introduction to Aerospace Structural Analysis", John Wiley & Sons, pp 190, 1985.

Nomenclatures

E, G	= modulus of elasticity and rigidity of thin walled panel, respectively
μ	= poisson ratio
x, y, z	= dimensional coordinates with respect to width, height and length of the thin panel beam
s	= curvilinear coordinates with respect to the contour of the thin panel
w_y	= distributed load in y-direction
V_y	= transversal shear force in the y-direction
M_x	= flexural bending about axis x
M_z	= torsional twisting about axis z
N_z, N_s, N_{zs}	= stress resultants in thin panel, force per unit length
r	= r-th panel
h_r	= thickness of the panel of the corresponding r-th panel
t	= thickness of the uniform thickness box beam
r_{avg}	= average radius
l_r	= length along the contour of the r-th panel
ρ	= moment-arm of the shear flow q about axis z
ω	= double of area of the analyzed contour
$\overline{\varphi_4}$	= deplanation function

Appendix

Self-equilibrium coefficient is the same as the coefficient of orthogonalization. Here, orthogonal means: Any two nontrivial functions u(x) and v(x) are said to be orthogonal if

$$<u,v> = \int u \cdot v \, dx = 0$$

The special characteristic of this concept is described in [4] whereby using the orthogonalization process the function $\overline{\varphi_3}(s)$ in Figure A1.1 can be balanced or self-equilibrium to be $\varphi_3(s)$ as in Figure A1.2 where essentially the area above and below the horizontal axis is the same and if integration of $\varphi_3(s)$ is taken, the result will be zero.

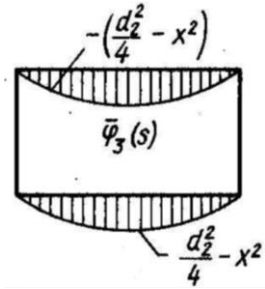

Figure A1: Deplanation function, $\overline{\varphi_3}$(s) [4]

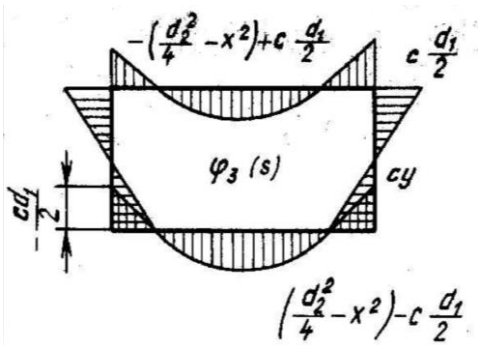

Figure A2: Balanced or self-equilibrium, φ_3(s) [4]

Free Vibration Analysis of Laminated CNTRC Plates using the pb2-Ritz Method

Dang Xuan Hung, Tran Minh Tu, Tran Dai Hao*
National University of Civil Engineering, 55 Giai Phong Road, Hanoi, VN
**tutm@nuce.edu.vn*

ABSTRACT

This paper presents the free vibration analysis of laminated functionally graded carbon nanotube reinforced composite (FG-CNTRC) plates. The CNTRC layer consists of single-walled carbon nanotubes (SWCNTs) as reinforcement and polymer as a matrix. The material properties are determined according to the extended rule of mixture. Four different patterns of SWCNTs distribution across the thickness of individual layers are considered. Based on the first-order shear deformation theory (FSDT), the equations of motion are derived and then solved by employing the pb2-Ritz method. The accuracy of the present approach is verified by comparing the obtained results with those available in the literature and commercial ANSYS software. The significant influences of CNT volume fractions, CNT distribution patterns, plate aspect ratio, plate width-to-thickness ratio, and boundary conditions on the non-dimensional fundamental frequency of symmetric and anti-symmetric laminated FG-CNTR plates has been proven through the numerical examples. Furthermore, the influence of lamination schemes, CNT fiber orientation and the number of layers is also investigated.

Keywords: *Laminated carbon nanotube-reinforced composite; Free vibration analysis; First-order shear deformation theory; pb2-Ritz method.*

Introduction

Since they were invented in 1991 by Iijima [1], carbon nanotubes (CNTs) have been increasingly used in many modern industries due to their exceptional mechanical, thermal and electrical properties. Therefore, the CNTs are used as a new type of reinforcement of polymer composite that has the potential to replace traditional reinforcement materials for structural components. With the

ISSN 1823-5514, eISSN 2550-164X
Received for review: 2020-08-24
Accepted for publication: 2021-01-06
Published: 2021-01-15

idea of functionally graded (FG) materials, CNTs have been distributed continuously through the matrix along the certain direction of composite structures. Functionally graded carbon nanotube-reinforced composites (FG-CNTRCs) can be applied as structural members such as beam, plate or shell in many engineering branches such as mechanical, aeronautical, civil, and marine industries. In order to optimize the design of CNTRC's structures, a thorough understanding of their mechanical behavior is required. Thus, the study on vibrational characteristics of these structures always attracts the attention of design engineers.

The mechanical behavior of single-layer FG and FG-CNTRC structures has been studied by many researchers. Based on first-order shear deformation theory (FSDT), Bidgoli et al. presented a three-dimensional thermo-elastic analysis [2], two-dimensional stress and strain behavior [3] of a rotating FG cylindrical shell subjected to inner and outer pressures; Zhu et al. [4] investigated the static and free vibration characteristics of FG-CNTRC plates by the FEM. Using Ritz method, Shahrbabaki and Alibeigloo [5] analyzed the free vibration of FG-CNTRC plates with various boundary conditions. Nami and Janghorban [6] studied the free vibration of FG-CNTRC plates using the differential quadrature method (DQM) and the theory of elasticity. Adopting the generalized DQM and Galerkin's technique, the forced vibration of FG-CNTRC plates based on the FSDT was analyzed by Ansari et al. [7]. Selim et al. [8] adopted the element-free kp-Ritz method to study the free vibration behavior of FG-CNTRC plates including thermal effect based on Reddy's higher-order shear theory (HSDT). Zhang [9] employed the element-free IMLS-Ritz method and FSDT to analyze the vibrational characteristics of FG-CNTRC triangular plates. Using the same method, Zhang et al. [10-12] presented the vibration analysis of FG-CNTRC thick and moderately thick plates using the FSDT and HSDT. Using DQM, the free vibration and static behavior of FG-CNTRC plate was studied by Alibeigloo and Emtehani [13]. Using HSDT and the state-space Levy solution, Zhang et al. [14] investigated the vibration response of FG-CNTRC plates subjected to in-plane loads. Using a variational differential quadrature approach, Ansari et al. [15] analyzed the free vibration of arbitrary shaped thick FG-CNTRC plates based on the HSDT.

The Ritz method, an effective tool to solve a system of differential equations, was applied by Kiani [16] to study the free vibration of FG-CNTRC skew plates plates. Wang et al. [17] presented Kantorovich-Galerkin method for free vibration and buckling analysis of FG-CNTRC thin plates with the Kirchhoff plate theory. Duc et al. [18] discussed the bending and free vibration of FG-CNTRC rectangular plates resting on Winkler-Pasternak elastic foundations using the FSDT. The cell-based smoothed discrete shear gap method (CS-DSG3) for the bending and free vibration analyses of FG-CNTRC rectangular plates is proposed by Tam et al.[19]. Using the element-

free kp-Ritz method, the free vibration analysis of laminated FG-CNTRC plates were studied by Lei et al. [20] based on the FSDT.

As is well-known, multi-layer composite structures are more commonly used than single-layer composite structures. The advantage of these structures is the motivation for scientists to understand thoroughly the mechanical behavior of laminated FG-CNTRC beams, plates and shells, whose bearing capacity depends on many parameters such as CNT configurations, CNT orientations, and number of layers. However, so far there have not been many studies on this topic; only a few studies have been introduced. Malekzadeh and Zarei [21] predicted natural frequencies of quadrilateral multi-layered FG-CNTRC plates using the DQM and the FSDT. Free vibrational behaviors of FG-CNTRC and laminated FG-CNTRC plates under different boundary conditions based on Reissner's mixed variational theorem using finite prism methods was analyzed by Wu and Li [22]. Malekzadeh and Heydarpour [23] employed the layerwise-DQM to study static and free vibration analysis of laminated FG-CNTRC plates. Based on a simple four-variable FSDT, Huang et al. [24] used the Navier solution to solve bending and free vibration problems of anti-symmetrically laminated FG-CNTRC plates. Lei et al. [25] investigated static behaviors of laminated FG-CNTR plates by the element-free kp-Ritz method.

An above-mentioned review shows that there are very few researches on the vibrational characteristics of CNTRC multi-layered composite plates using a Rayleigh-Ritz procedure that does not require topological discretization. For the Rayleigh-Ritz method, there is difficulty in choosing a suitable Ritz displacement function for plates with arbitrary supporting edges such that it can be easily automated. The pb2-Ritz function consists of the products of the two-dimensional polynomial functions and the basic boundary functions. As a result, this method can be easily automated and requires less computer memory space due to the reduction of unknowns.

In this paper, the pb-2 Rayleigh-Ritz method is applied to find a solution for the free vibration problem of laminated FG-CNTRC plates under various boundary conditions for the first time. The convergence test is conducted to illustrate the accuracy of the present approach. In addition, the effects of volume fraction of CNTs, different CNT distributions, lamination schemes, geometric parameters of the plate, and boundary conditions on the natural frequency parameters are investigated.

Laminated FG-CNTRC plates

In this article, a multi-layered rectangular plate of length *a*, width *b* and total thickness *h* is considered. The plate composed of the FG-CNTRCs layers, which are perfectly bonded (Figure 1). It is assumed that the individual layers are made of a mixture of SWCNTs (single-walled CNTs) and an isotropic matrix. The Cartesian coordinate system, four patterns of CNT distribution

along the thickness of the layer are also illustrated in Figure 1. The conventional single-walled CNT (SWCNT) distributions are assumed to be graded along the thickness direction and represented by four types of distribution: the uniform distribution (UD), and other three functionally graded distributions are denoted as FG-V, FG-X and FG-O respectively.

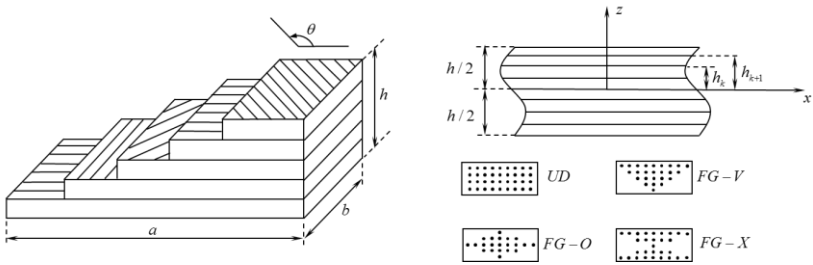

Figure 1: Geometry and configuration of laminated FG-CNTRC plate with different types of CNT distributions through layer's thickness.

The CNT volume fractions for each FG-CNTRC layer can be determined according to the types of CNT's distributions as [26]:

$$V_{CNT} = V_{CNT}^{*} \quad (\text{UD}); \; V_{CNT}(z) = \left(1 - \frac{2|z|}{h}\right) V_{CNT}^{*} \quad (\text{FG-O})$$

$$V_{CNT}(z) = \left(1 + \frac{2z}{h}\right) V_{CNT}^{*} \; (\text{FG-V}); \; V_{CNT}(z) = \frac{4|z|}{h} V_{CNT}^{*} \quad (\text{FG-X}) \tag{1}$$

with,

$$V_{CNT}^{*} = \frac{w_{CNT}}{w_{CNT} + \left(\rho^{CNT} / \rho^{m}\right) - \left(\rho^{CNT} / \rho^{m}\right) w_{CNT}} \tag{2}$$

in which ρ^{CNT} and ρ^{m} are the densities of the CNTs and the matrix respectively; w_{CNT} is the mass fraction of the CNT.

The effective CNTs properties can be approximated using the Eshelby–Mori–Tanaka scheme [27] or the extended rule of mixture [28]. In the present research, the extended rule of mixtures is chosen for simplicity, and effective Young's modulus, shear modulus, Poisson's ratio and density of CNTRC layers can be expressed as:

$$E_{11} = \eta_1 V_{CNT} E_{11}^{CNT} + V_m E^m;\ \frac{\eta_2}{E_{22}} = \frac{V_{CNT}}{E_{22}^{CNT}} + \frac{V_m}{E^m};\ \frac{\eta_3}{G_{12}} = \frac{V_{CNT}}{G_{12}^{CNT}} + \frac{V_m}{G^m}; \qquad (3)$$
$$\nu_{12} = V_{CNT}^{*} \nu_{12}^{CNT} + V_m \nu^m;\quad \rho = V_{CNT}\rho^{CNT} + V_m \rho^m$$

where $E_{11}^{CNT}, E_{22}^{CNT}$ and G_{12}^{CNT} are the Young's and shear moduli of single-walled carbon nanotubes (SWCNTs) in the principal material coordinate, respectively; E^m and G^m are the corresponding properties of the isotropic matrix; η_1, η_2, and η_3 are the CNT efficiency parameters; V_{CNT} and V_m are the volume fractions of the CNTs and polymer matrix, respectively. ν^m, ρ^m are the Poisson's ratio, the density of the CNT and the polymer matrix, respectively.

Theoretical formulation

First-order shear deformation theory (FSDT)

The in-plane displacement components and the transverse displacement component according to the FSDT can be assumed as [29]:

$$\begin{aligned} \bar{u} &= u(x,y) + z\theta_x(x,y) \\ \bar{v} &= v(x,y) + z\theta_y(x,y) \\ \bar{w} &= w(x,y) \end{aligned} \qquad (4)$$

in which u, v, w are in-plane and the transverse displacements of a point on the mid-plane following the (x, y, z) directions, respectively; θ_x, θ_y are the rotations of the transverse normal about the y- and x-axes, respectively.

The nonzero strains associated with the displacement field (5) are given as:

$$\bar{\boldsymbol{\varepsilon}} = \begin{Bmatrix} \bar{\varepsilon}_{xx} \\ \bar{\varepsilon}_{yy} \\ \bar{\gamma}_{xy} \end{Bmatrix} = \boldsymbol{\varepsilon} + z\boldsymbol{\kappa};\ \begin{Bmatrix} \gamma_{yz} \\ \gamma_{xz} \end{Bmatrix} = \boldsymbol{\gamma} \qquad (5)$$

where,

$$\boldsymbol{\varepsilon} = \begin{Bmatrix} \partial u/\partial x \\ \partial v/\partial y \\ \partial u/\partial y + \partial v/\partial x \end{Bmatrix};\ \boldsymbol{\kappa} = \begin{Bmatrix} \partial \theta_x/\partial x \\ \partial \theta_y/\partial y \\ \partial \theta_x/\partial y + \partial \theta_y/\partial x \end{Bmatrix};\ \boldsymbol{\gamma} = \begin{Bmatrix} \dfrac{\partial w}{\partial y} + \theta_y \\ \dfrac{\partial w}{\partial x} + \theta_x \end{Bmatrix} \qquad (6)$$

The stress-strain relations of the k^{th} - CNTRC layer are given as:

$$\begin{Bmatrix} \sigma_{xx} \\ \sigma_{yy} \\ \sigma_{xy} \\ \sigma_{yz} \\ \sigma_{xz} \end{Bmatrix}^{(k)} = \begin{bmatrix} \tilde{Q}_{11} & \tilde{Q}_{12} & \tilde{Q}_{16} & 0 & 0 \\ \tilde{Q}_{12} & \tilde{Q}_{22} & \tilde{Q}_{26} & 0 & 0 \\ \tilde{Q}_{16} & \tilde{Q}_{26} & \tilde{Q}_{66} & 0 & 0 \\ 0 & 0 & 0 & \tilde{Q}_{44} & \tilde{Q}_{45} \\ 0 & 0 & 0 & \tilde{Q}_{45} & \tilde{Q}_{55} \end{bmatrix}^{(k)} \begin{Bmatrix} \overline{\varepsilon}_{xx} \\ \overline{\varepsilon}_{yy} \\ \overline{\gamma}_{xy} \\ \gamma_{yz} \\ \gamma_{xz} \end{Bmatrix}^{(k)} \tag{7}$$

with $\tilde{Q}_{ij}$ are engineering constants of the transformed stiffness matrix for the k^{th} layer, and are defined by:

$$\left[\tilde{Q}\right]_k = \left[T\right]^{-1}\left[Q\right]_k\left[T\right]^{-T} \tag{8}$$

in which θ is the CNT angle of lamination, and the transformation matrix [T] related to the principal materials coordinates and the structural coordinates are defined in [29].

The engineering constants Q_{ij} of the stiffness matrix $\left[Q\right]_k$ for the k^{th} layer are given as follow:

$$\begin{aligned} &Q_{11} = \frac{E_{11}}{1-\nu_{12}\nu_{21}};\ \ Q_{12} = \frac{\nu_{12}E_{22}}{1-\nu_{12}\nu_{21}};\ \ Q_{22} = \frac{E_{22}}{1-\nu_{12}\nu_{21}}; \\ &Q_{44} = G_{23};\ \ Q_{55} = G_{13};\ \ Q_{66} = G_{12}; \end{aligned} \tag{9}$$

in which the effective Young's moduli, shear moduli in the principal material coordinate and Poisson's ratios of the CNTRC materials, respectively are determined from Eqs. (2), (3).

The strain energy of laminated FG-CNTRC plates is given as:

$$U = \frac{1}{2}\int_A \tilde{\boldsymbol{\varepsilon}}^T \boldsymbol{S}\tilde{\boldsymbol{\varepsilon}}dA; \tag{10}$$

in which:

$$\tilde{\boldsymbol{\varepsilon}} = \begin{Bmatrix} \boldsymbol{\varepsilon} \\ \boldsymbol{\kappa} \\ \boldsymbol{\gamma} \end{Bmatrix}; \boldsymbol{S} = \begin{bmatrix} A & B & 0 \\ B & D & 0 \\ 0 & 0 & \overline{A} \end{bmatrix} \tag{11}$$

The stiffness coefficients of laminated FG-CNTRC are defined as:

$$\begin{aligned}(A_{ij}, B_{ij}, D_{ij}) &= \sum_{k=1}^{N} \int_{h_k}^{h_{k+1}} \overline{Q}_{ij}^{k}(1, z, z^2)dz \qquad (i, j = 1,2,6)\\ \overline{A}_{ij} &= f\sum_{k=1}^{N} \int_{h_k}^{h_{k+1}} \overline{Q}_{ij}^{k}dz \qquad (i, j = 4,5)\end{aligned} \tag{12}$$

where f is the transverse shear correction factor; h_k, h_{k+1} are the coordinates from the mid-plane of the plate to the top and bottom surface of the k^{th} layer; N is the total number of layers.

The kinetic energy of laminated FG-CNTRC plates is given as:

$$K = \frac{1}{2}\int_{A}\int_{-h/2}^{h/2} \rho(z)(\dot{\bar{u}}^2 + \dot{\bar{v}}^2 + \dot{\bar{w}}^2)dzdA \tag{13}$$

where $\rho(z)$ is the mass density and $(\dot{\bar{u}},\ \dot{\bar{v}},\ \dot{\bar{w}})$ are the velocity components along with the (x, y, z) directions, respectively. The total energy function of laminated FG-CNTRC plates for free vibration analysis is expressed as:

$$\Pi = U - K \tag{14}$$

Pb2- Ritz method based on the FSDT plate theory

Adopting the FSDT in conjunction with geometric boundary conditions of Mindlin plate, the displacement components are represented as follow:

$$\begin{aligned}u(x,y) &= \sum_{i=1}^{m}\sum_{j=1}^{n} U_{ij}^{mn} f_{ij}(x,y)\psi^{u}(x,y)e^{i\omega t}\\ v(x,y) &= \sum_{i=1}^{m}\sum_{j=1}^{n} V_{ij}^{mn} f_{ij}(x,y)\psi^{v}(x,y)e^{i\omega t}\\ w(x,y) &= \sum_{i=1}^{m}\sum_{j=1}^{n} W_{ij}^{mn} f_{ij}(x,y)\psi^{w}(x,y)e^{i\omega t}\\ \theta_x(x,y) &= \sum_{i=1}^{m}\sum_{j=1}^{n} \theta_{ij}^{xmn} f_{ij}(x,y)\psi^{\theta_x}(x,y)e^{i\omega t}\\ \theta_y(x,y) &= \sum_{i=1}^{m}\sum_{j=1}^{n} \theta_{ij}^{ymn} f_{ij}(x,y)\psi^{\theta_y}(x,y)e^{i\omega wt}\end{aligned} \tag{15}$$

where $i=\sqrt{-1}$ and ω is the natural frequency; *m* and *n* are degrees of the mathematically complete two-dimensional polynomial space; $U_{ij}^{mn}, V_{ij}^{mn}, W_{ij}^{mn}, \theta_{ij}^{xmn}, \theta_{ij}^{ymn}$ are the unknown coefficients to be determined; the complete set of two-dimensional polynomials $f_{ij}(x,y)$ can be expressed as: $X^{i-1}Y^{j-1}$ $(i=1,2,3,...m;\ j=1,2,3,...n)$; $\psi^{\alpha}(x,y)$, $\left(\alpha=u,v,w,\theta_x,\theta_y\right)$ are the functions that satisfy the geometric boundary conditions (BCs) and are expressed as:

$$\psi^{\alpha}(x,y)=\prod_{k=1}^{n_e}\left[\Gamma_k(x,y)\right]^{\Omega_k} \tag{16}$$

with n_e is the number of supporting edges; Γ_k is the equation of the k^{th} supporting edge (Figure 2); Ω_k are the representative parameters of the BCs and are given in Table 1. In this study, four types of BCs are considered: clamped edge (C), simply supported edge (S) and free edge (F).

Table 1: Representative parameters of various boundary conditions

	Ω_k		
α	F	S	C
u, v, w	0	1	1
θ_x, θ_y	0	0	1

Through substituting Equation (15) into Equation (14) and applying the Ritz procedure to the total energy functional, the eigenvalue problem is obtained as:

$$\left(\tilde{\boldsymbol{K}}-\omega^2\tilde{\boldsymbol{M}}\right)\{\boldsymbol{X}\}=0 \tag{17}$$

where $\tilde{\boldsymbol{K}}$ is the stiffness matrix and $\tilde{\boldsymbol{M}}$ is the mass matrix. $\boldsymbol{X}$ is the unknown displacement coefficients $\left(U_{ij}^{mn}, V_{ij}^{mn}, W_{ij}^{mn}, \theta_{ij}^{xmn}, \theta_{ij}^{ymn}\right)$. The eigenvalue problem (17) is solved by using the standard eigenvalue algorithm provided in a Matlab's code.

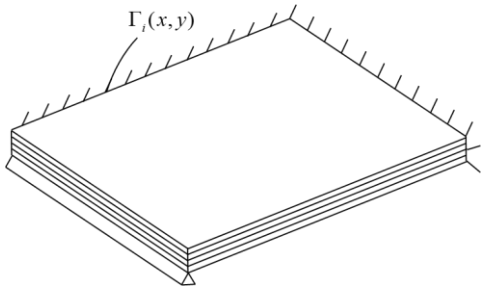

Figure 2: A rectangular laminated FG-CNTRC plate

Numerical Results and Discussions

In this section, after conducting convergence and accuracy of the solutions of the proposed method, the parametric studies will be performed to explore the effects of CNT volume fractions, length-to-width ratio, width-to-thickness ratio, CNT distribution pattern, fiber orientation, number of layers and boundary conditions on the natural frequencies of multi-layered FG-CNTRC plates.

Laminated FG-CNTR plates, whose each layer is made of poly{(m-phenylenevinylene)-co-[(2,5-dioctoxy-p-phenylene) vinylene] (PmPV) as matrix, with CNTs as fibers are considered. PmPV is an isotropic material with $\nu_m = 0.34$; $\alpha^m = 45\times10^{-6}K$; $E^m = 2.1$ GPa; $\rho^m = 1.15$ g/cm^3. The (10,10) single-walled carbon nanotubes (SWCNTs) are chosen as reinforcements, whose material properties are: $E_{11}^{CNT} = 5.6466$ TPa; $E_{22}^{CNT} = 7.0800$ TPa; $G_{12}^{CNT} = 1.9455$ TPa; $\rho^{CNT} = 1.4$ g/cm^3 [30]. The CNT efficiency parameters $\eta_j\,(j = 1,2,3)$, which are taken from Shen [30], are given in Table 2. In addition, the shear moduli are assumed as: $G_{13} = G_{12} = G_{23}$. These material properties will be used to perform the bellow numerical results.

Table 2: CNT efficiency parameters for three different value of volume fractions

V_{CNT}^*	η_1	η_2	η_3
0.11	0.149	0.934	0.934
0.14	0.150	0.941	0.941
0.17	0.149	1.381	1.381

Each edge of the plate is assumed to be simply supported (S); fully clamped (C); or free (F). Four CNT distribution patterns along the thickness

of each layer such as UD, FG-O, FG-V and FG-X are considered. For convenience, the non-dimensional natural frequency is defined as [4]:

$$\bar{\omega}_{mn} = \omega_{mn} \frac{b^2 \sqrt{\rho^m / E^m}}{h} \tag{18}$$

where $\bar{\omega}_{mn}$ is the natural frequency of the laminated FG-CNTRC plate.

Convergence study

To obtain a reasonable accuracy, the first three non-dimensional frequencies are calculated with increasing the polynomial terms (*m*, *n*). Table 3 presents the convergence of the non-dimensional frequency of square anti-symmetric cross-ply $[0^0/90^0]_5$ laminated UD-CNTRC plates under various types of BCs.

As can be observed, the increasing number of polynomial terms improves the accuracy of results which converge at $m = n = 7$.

Table 3: Convergence study of the first three non-dimensional frequency for antisymmetric cross-ply $[0^0/90^0]_5$ square laminated UD-CNTRC plates $(a/h = 10)$

Mode		polynomial terms ($m \times n$)						
		1×1	2×2	3×3	4×4	5×5	6×6	7×7
SSSS	1	19.874	18.069	16.347	15.381	15.344	15.337	15.335
	2	45.315	39.042	34.974	33.389	31.640	31.545	31.537
	3	45.315	39.042	34.974	33.389	31.640	31.545	31.537
CCCC	1	23.549	22.511	21.714	21.705	21.703	21.703	21.703
	2	40.492	38.057	36.314	34.922	34.885	34.869	34.869
	3	40.492	38.057	36.314	34.922	34.885	34.869	34.869
CSCS	1	20.365	19.917	19.198	18.779	18.772	18.771	18.770
	2	38.694	36.768	34.913	33.244	33.196	33.179	33.176
	3	43.125	40.139	36.005	35.043	33.356	33.331	33.299
CFCF	1	16.458	15.908	15.338	15.331	15.329	15.329	15.329
	2	16.884	16.003	15.458	15.450	15.449	15.447	15.447
	3	20.468	19.522	19.389	19.305	19.304	19.206	19.206
SSFF	1	11.877	11.471	11.441	10.718	10.718	10.716	10.716
	2	14.326	13.958	11.782	11.126	11.067	11.059	11.049
	3	20.014	19.522	19.390	19.304	19.304	19.205	19.205

Validation studies

The first validation study is performed for SSSS and CCCC square single-layer UD-CNTRC plates. Table 4 presents the first six non-dimensional frequencies in comparison with those obtained by Zhu et a. [4] using the finite element method. It can be seen that the good agreement exists between the results of the present approach and the results given by Zhu et al. with maximal discrepancy is only 1.73% for the third frequency of SSSS FG-CNTR plate.

Table 5 and Table 6 show a further comparison for laminated UD-CNTR square plates under various boundary condition with input data: $b/a=1;\ b/h=10;\ V_{CNT}^{*}=0.11$. First six non-dimensional frequencies for laminated UD-CNTR antisymmetric cross-ply $[0^0/90^0]_5$ are presented in Table 5, and for laminated UD-CNTR antisymmetric angle-ply $[45^0/-45^0]_5$ are tabulated in Table 6. The present results are compared with those obtained by using the commercial software ANSYS. The element "SHELL-181" is selected to obtain the natural frequencies. The very good agreement is found with the small discrepancy between the results.

Table 4: The non-dimensional frequency of square single-layer UD-CNTRC plates $\left(V_{CNT}^{*}=0.11; a/h=50\right)$

Mode	SSSS			CCCC		
	Present	Zhu [4]	Error %	Present	Zhu [4]	Error %
1	19.216	19.223	0.03%	40.072	39.730	0.86%
2	23.314	23.408	0.4%	44.082	43.876	0.47%
3	34.078	34.669	1.73%	54.207	54.768	1.03%
4	53.609	54.043	0.81%	75.179	74.448	0.97%
5	70.906	70.811	0.13%	99.619	98.291	1.33%
6	72.996	72.900	0.13%	101.926	100.537	1.36%

Table 5: The non-dimensional frequency of square laminated antisymmetric cross-ply $[0^0/90^0]_5$ UD-CNTRC plates with different boundary conditions ($V^*_{CNT} = 0.11; a/h = 10$)

	Mode	1	2	3	4	5	6
	Present	15.335	31.537	31.537	41.928	50.026	50.029
SSSS	Ansys	15.220	31.135	31.135	41.358	49.119	49.119
	Error %	0.75%	1.27%	1.27%	1.36%	1.81	1.82
	Present	21.703	34.323	34.323	43.642	50.895	50.923
CCCC	Ansys	21.387	34.323	34.323	43.642	50.895	50.923
	Error %	1.45%	1.56%	1.56%	1.59%	1.64%	1.65%
	Present	18.770	33.176	33.299	43.147	50.659	51.147
CSCS	Ansys	18.541	32.678	32.845	42.509	49.835	50.207
	Error %	1.22%	1.50%	1.36%	1.48%	1.63%	1.84%
	Present	15.329	15.447	19.206	27.726	31.262	31.464
CFCF	Ansys	15.107	15.223	19.131	27.445	30.766	30.967
	Error %	1.45%	1.45%	0.39%	1.01%	1.59%	1.58%
	Present	10.716	11.049	19.205	25.653	29.485	29.709
SSFF	Ansys	10.640	10.963	19.095	25.441	29.094	29.310
	Error %	0.71%	0.79%	0.57%	0.83%	1.33%	1.34%

Table 6: The non-dimensional frequency of square laminated antisymmetric angle-ply $[45^0/-45^0]_5$ UD-CNTRC plates with different boundary conditions ($V^*_{CNT} = 0.11; a/h = 10$)

	Mode	1	2	3	4	5	6
	Present	16.258	31.347	31.347	43.310	48.645	48.901
SSSS	Ansys	16.058	30.835	30.835	42.474	47.729	47.970
	Error %	1.23%	1.63%	1.63%	1.93%	1.88%	1.90%
	Present	21.013	34.590	34.590	46.219	50.228	50.841
CCCC	Ansys	20.634	33.902	33.902	45.227	49.193	49.784
	Error %	1.80%	1.99%	1.99%	2.15%	2.06%	2.08%
	Present	18.751	32.027	33.848	44.698	48.954	50.273
CSCS	Ansys	18.414	31.451	33.174	43.746	48.012	49.235
	Error %	1.79%	1.80%	1.99%	2.13%	1.92%	2.06%
	Present	12.940	17.284	27.733	28.291	32.332	43.922
CFCF	Ansys	12.723	17.016	27.214	27.847	31.721	43.056
	Error %	1.68%	1.55%	1.87%	1.57%	1.89%	1.97%
	Present	5.526	11.279	21.567	25.303	25.463	39.525
SSFF	Ansys	5.467	11.088	21.280	24.904	25.033	38.744
	Error %	1.07%	1.70%	1.33%	1.57%	1.69%	1.98%

Parametric studies

After verifying the proposed method and Matlab's code, the non-dimensional frequency for laminated FG-CNTRC plates is analyzed in detail. The effects of CNT volume fractions, CNT distribution type, CNT fiber orientation, number of layers, length-to-width ratio, width-to-thickness ratio, and boundary conditions on the non-dimensional fundamental frequencies of FG-CNTRC plates are investigated.

The non-dimensional fundamental frequencies of SSSS anti-symmetric cross-ply $[0^0/90^0]_2$, symmetric cross-ply $[0^0/90^0]_s$, anti-symmetric angle-ply $[45^0/-45^0]_2$, and symmetric angle-ply $[45^0/-45^0]_S$ laminated UD-CNTRC plates with various values of *a/h* ratio and CNT volume fraction are tabulated in Table 7. The geometric parameters of the plate are $a/h = 5; 10; 20; 30; 40$ and 50, and $b/a = 2$.

Table 7: The non-dimensional frequency of SSSS cross-ply and angle-ply laminated UD-CNTRC plates with various values of *a/h* ratio and volume fraction of CNT

	V^*_{CNT}	a/h					
		5	10	20	30	40	50
$[0^0/90^0]_2$	0.11	7.860	11.142	12.971	13.429	13.601	13.684
	0.14	8.255	12.054	14.352	14.953	15.183	15.294
	0.17	9.533	13.794	16.002	16.550	16.756	16.855
$[0^0/90^0]_s$	0.11	6.452	7.910	8.487	8.613	8.658	8.680
	0.14	6.889	8.644	9.373	9.534	9.592	9.620
	0.17	8.005	9.777	10.475	10.625	10.680	10.706
$[45^0/-45^0]_2$	0.11	7.689	10.762	12.807	13.518	13.864	14.065
	0.14	8.100	11.637	14.105	14.984	15.416	15.667
	0.17	8.811	13.325	15.811	16.672	17.091	17.334
$[45^0/-45^0]_s$	0.11	7.198	10.180	12.152	12.784	13.078	13.246
	0.14	7.572	10.971	13.367	14.158	14.527	14.737
	0.17	8.953	12.611	15.005	15.770	16.125	16.329

Figure 3 illustrates the effect of CNT volume fraction and *a/h* ratios on non-dimensional fundamental frequencies. For both cross-ply and angle-ply CNT lamination scheme, it can be observed that enrichment of the polymeric matrix with more carbon nanotube results in higher frequencies of the plate. The non-dimensional fundamental frequency increases with increasing value of width-to-thickness ratios; with increasing *a/h* ratio (thinner plates), the gap between symmetric and anti-symmetric cross-ply lamination becomes bigger. It means the influence of volume fraction of CNT on non-dimensional

fundamental frequencies on thin plates is more considerable than that of thick plates. Furthermore, the non-dimensional natural frequencies of anti-symmetric lamination are higher than those of symmetric lamination for UD configuration of CNT distribution of CNTRC plates.

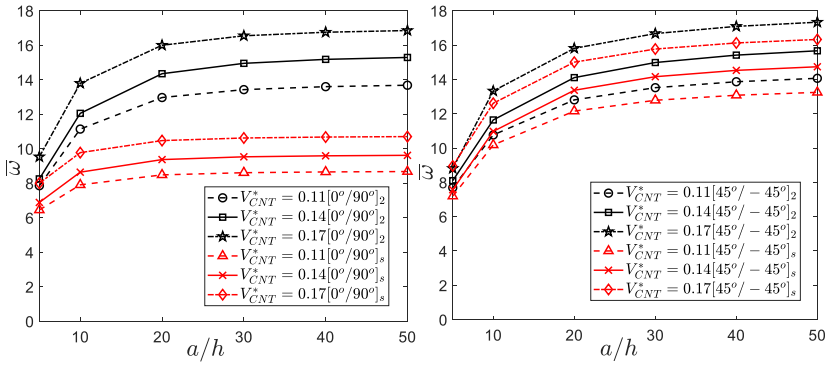

Figure 3: The change of the non-dimensional fundamental frequency of cross-ply and angle-ply laminated UD-CNTRC plates against a/h ratio with different CNT volume fractions

Table 8 presents non-dimensional fundamental frequencies of SSSS anti-symmetric cross-ply $[0^0/90^0]_2$, symmetric cross-ply $[0^0/90^0]_s$, anti-symmetric angle-ply $[45^0/-45^0]_2$, and symmetric angle-ply $[45^0/-45^0]_S$ laminated FG-CNTRC plates with various values of *a/h* ratios, and four different types of SWCNT distribution. The input data are $a/h = 5; 10; 20; 30; 40$ and 50, and $V^*_{CNT} = 0.11$.

Figure 4 depicts the influence of *a/h* ratios and configuration type of SWCNTs on non-dimensional fundamental frequencies. A similar observation can be found from Figure 4: the non-dimensional fundamental frequency increases as *a/h* ratio increases for all types of FG-CNTRC plates. For both cross-ply and angle-ply CNT lamination scheme, it is clearly seen that the FG-O CNTR plates own the lowest non-dimensional frequency and the FG-X CNTR plates own the highest non-dimensional frequency. Thus, to achieve the greater stiffness, the CNTs distributions close to the top and bottom surface of the plate are more efficient than those distributed near the mid-surface. Furthermore, we realize that the fundamental frequencies of the UD type are higher than the FG-V type for both symmetric and antisymmetric laminated FG-CNTR plates.

Table 9 presents the influence of the number of laminae on the non-dimensional fundamental frequency of SSSS anti-symmetric cross-ply and angle-ply UD-CNTRD plates. It is obvious that with a constant thickness, the increase in the number of laminae increases the stiffness of the plate resulting in an increased non-dimensional fundamental frequency of both anti-symmetric cross-ply and angle-ply UD-CNTRD plates.

The effects of angle of CNT orientation on non-dimensional fundamental frequencies of four-edge simply supported antisymmetric angle-ply $[\theta^0/-\theta^0]_2$ and symmetric angle-ply $[\theta^0/-\theta^0]_s$ laminated UD-CNTRC are depicted in Figure 5. The plate with $b/a=2; a/h=10$ and $V^*_{CNT}=0.11$ is investigated. It is seen that the curves are symmetric to the line of $\theta=45^0$ and it corresponds to the maximal values of non-dimensional natural frequencies for both lamination schemes.

Table 8: The non-dimensional fundamental frequency of SSSS cross-ply and angle-ply FG-CNTRC plates with various values of *a/h* ratio and four types of SWCNT distribution (UD, FG-O, FG-V, FG-X) ($V^*_{CNT}=0.11$)

		a / *h*					
		5	10	20	30	40	50
$[0^0/90^0]_2$	UD	7.860	11.142	12.971	13.429	13.601	13.684
	FG-V	7.851	11.091	12.953	13.380	13.573	13.565
	FG-O	7.832	11.039	12.801	13.238	13.402	13.481
	FG-X	7.915	11.264	13.150	13.625	13.804	13.890
$[0^0/90^0]_s$	UD	6.452	7.910	8.487	8.613	8.658	8.680
	FG-V	6.441	7.883	8.453	8.577	8.622	8.643
	FG-O	6.295	7.644	8.173	8.287	8.329	8.348
	FG-X	6.610	8.173	8.799	8.935	8.985	9.008
$[45^0/-45^0]_2$	UD	7.689	10.762	12.807	13.518	13.864	14.065
	FG-V	7.683	10.732	12.752	13.451	13.790	13.986
	FG-O	7.655	10.661	12.642	13.326	13.658	13.851
	FG-X	7.746	10.882	12.984	13.718	14.076	14.284
$[45^0/-45^0]_s$	UD	7.198	10.180	12.152	12.784	13.078	13.246
	FG-V	7.191	10.144	12.076	12.690	12.975	13.137
	FG-O	7.121	10.029	11.920	12.516	12.793	12.945
	FG-X	7.292	10.343	12.387	13.049	13.361	13.541

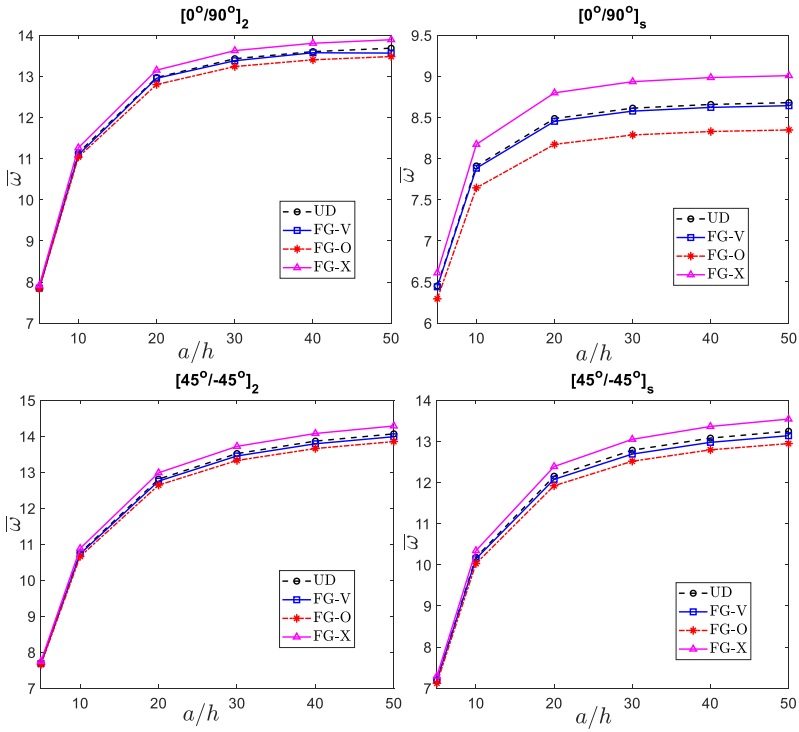

Figure 4: The variation of the non-dimensional fundamental frequency of cross-ply and angle-ply laminated FG-CNTRC plates versus a/h ratio with four types of SWCNT distributions (UD, FG-O, FG-V, FG-X).

Table 9: The non-dimensional fundamental frequency for SSSS antisymmetric cross-ply $[0^0/90^0]_n$ and antisymmetric angle-ply $[45^0/-45^0]_n$ laminated UD -CNTRC plates with different number of lamina

	Number of laminae				
	2	4	6	8	10
$[0^0/90^0]_n$	10.054	11.142	11.224	11.249	11.260
$[45^0/-45^0]_n$	9.232	10.762	10.893	10.934	10.952

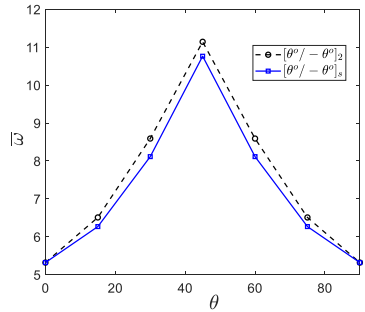

Figure 5: Effects of fiber orientation on the non-dimensional fundamental frequency for SSSS laminated UD-CNTRC plates ($V^*_{CNT} = 0.11$).

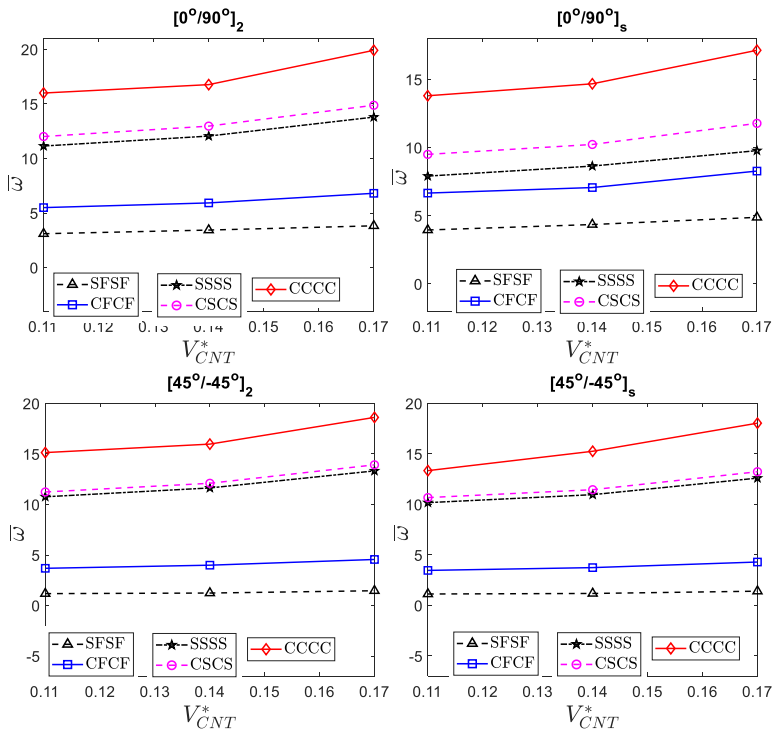

Figure 6: Effects of various BCs on non-dimensional fundamental frequency of laminated UD-CNTRC plates (b/a = 2; a/h = 10; $V^*_{CNT} = 0.11$).

Conclusion

Using the pb2 Rayleigh-Ritz method and based on the FSDT, the free vibration characteristics of FG-CNTRC plates are investigated in this paper. The FG-CNTRC plate is composed of multi-layers that are perfectly bonded. In each layer, four patterns of SWCNTs arrangements including uniform or functionally graded distribution through the thickness are considered. The modified rule of the mixture is used to estimate the effective material properties of the CNTRC. A Matlab's code has been developed and used to validate the present solution against published results. Numerical examples show the significant effects of volume fraction of CNTs, distribution patterns of CNT, thickness to width ratio (*a/h*), aspect ratio (*a/b*), numbers of layers, and boundary conditions on the natural frequencies of FG-CNTRC laminated plates.

Acknowledgement

This research is funded by the National University of Civil Engineering (NUCE) under grant number 23-2020/KHXD-TĐ.

References

[1] S. Iijima, "Helical microtubules of graphitic carbon," *Nature*, vol. 354, pp 56-58, 1991.

[2] M. O. Bidgoli, A. Loghman, and M. Arefi, "Three-Dimensional Thermo-Elastic Analysis of a Rotating Cylindrical Functionally Graded Shell Subjected to Mechanical and Thermal Loads Based on the FSDT Formulation," *Journal of Applied Mechanics and Technical Physics*, vol. 60, pp 899-907, 2019.

[3] M. Omidi Bidgoli, A. Loghman, and M. Arefi, "The Effect of Grading Index on Two-dimensional Stress and Strain Distribution of FG Rotating Cylinder Resting on a Friction Bed Under Thermomechanical Loading," *Journal of Stress Analysis*, vol. 3, pp 75-82, 2019.

[4] P. Zhu, Z. Lei, and K. M. Liew, "Static and free vibration analyses of carbon nanotube-reinforced composite plates using finite element method with first order shear deformation plate theory," *Composite Structures*, vol. 94, pp 1450-1460, 2012.

[5] E. A. Shahrbabaki and A. Alibeigloo, "Three-dimensional free vibration of carbon nanotube-reinforced composite plates with various boundary conditions using Ritz method," *Composite Structures*, vol. 111, pp 362-370, 2014.

[6] M. R. Nami and M. Janghorban, "Free vibration of thick functionally graded carbon nanotube-reinforced rectangular composite plates based on

three-dimensional elasticity theory via differential quadrature method," *Advanced Composite Materials,* vol. 24, pp 439-450, 2015.

[7] R. Ansari, E. Hasrati, M. F. Shojaei, R. Gholami, and A. Shahabodini, "Forced vibration analysis of functionally graded carbon nanotube-reinforced composite plates using a numerical strategy," *Physica E: Low-dimensional Systems and Nanostructures,* vol. 69, pp 294-305, 2015.

[8] B. Selim, L. Zhang, and K. M. Liew, "Vibration analysis of CNT reinforced functionally graded composite plates in a thermal environment based on Reddy's higher-order shear deformation theory," *Composite structures,* vol. 156, pp 276-290, 2016.

[9] L. Zhang, Z. Lei, and K. M. Liew, "Free vibration analysis of functionally graded carbon nanotube-reinforced composite triangular plates using the FSDT and element-free IMLS-Ritz method," *Composite Structures,* vol. 120, pp 189-199, 2015.

[10] L. Zhang, W. Cui, and K. M. Liew, "Vibration analysis of functionally graded carbon nanotube reinforced composite thick plates with elastically restrained edges," *International Journal of Mechanical Sciences,* vol. 103, pp 9-21, 2015.

[11] L. Zhang, Z. Lei, and K. M. Liew, "Vibration characteristic of moderately thick functionally graded carbon nanotube reinforced composite skew plates," *Composite Structures,* vol. 122, pp 172-183, 2015.

[12] L. Zhang and B. Selim, "Vibration analysis of CNT-reinforced thick laminated composite plates based on Reddy's higher-order shear deformation theory," *Composite Structures,* vol. 160, pp 689-705, 2017.

[13] A. Alibeigloo and A. Emtehani, "Static and free vibration analyses of carbon nanotube-reinforced composite plate using differential quadrature method," *Meccanica,* vol. 50, pp 61-76, 2015.

[14] L. Zhang, Z. Song, and K. M. Liew, "State-space Levy method for vibration analysis of FG-CNT composite plates subjected to in-plane loads based on higher-order shear deformation theory," *Composite Structures,* vol. 134, pp 989-1003, 2015.

[15] R. Ansari, J. Torabi, and R. Hassani, "A comprehensive study on the free vibration of arbitrary shaped thick functionally graded CNT-reinforced composite plates," *Engineering Structures,* vol. 181, pp 653-669, 2019.

[16] Y. Kiani, "Free vibration of FG-CNT reinforced composite skew plates," *Aerospace Science and Technology,* vol. 58, pp 178-188, 2016.

[17] M. Wang, Z. M. Li, and P. Qiao, "Semi-analytical solutions to buckling and free vibration analysis of carbon nanotube-reinforced composite thin plates," *Composite Structures,* vol. 144, pp 33-43, 2016.

[18] N. D. Duc, J. Lee, T. Nguyen Thoi, and P. T. Thang, "Static response and free vibration of functionally graded carbon nanotube-reinforced composite rectangular plates resting on Winkler–Pasternak elastic

foundations," *Aerospace Science and Technology,* vol. 68, pp 391-402, 2017.
[19] T. Truong Thi, T. Vo Duy, V. Ho Huu, and T. Nguyen Thoi, "Static and free vibration analyses of functionally graded carbon nanotube reinforced composite plates using CS-DSG3," *International Journal of Computational Methods,* vol. 17, pp 1850133, 2020.
[20] Z. Lei, L. Zhang, and K. M. Liew, "Free vibration analysis of laminated FG-CNT reinforced composite rectangular plates using the kp-Ritz method," *Composite Structures,* vol. 127, pp 245-259, 2015.
[21] P. Malekzadeh and A. Zarei, "Free vibration of quadrilateral laminated plates with carbon nanotube reinforced composite layers," *Thin-Walled Structures,* vol. 82, pp 221-232, 2014.
[22] C. P. Wu and H. Y. Li, "Three-dimensional free vibration analysis of functionally graded carbon nanotube-reinforced composite plates with various boundary conditions," *Journal of Vibration and Control,* vol. 22, pp 89-107, 2016.
[23] P. Malekzadeh and Y. Heydarpour, "Mixed Navier-layerwise differential quadrature three-dimensional static and free vibration analysis of functionally graded carbon nanotube reinforced composite laminated plates," *Meccanica,* vol. 50, pp 143-167, 2015.
[24] B. Huang, Y. Guo, J. Wang, J. Du, Z. Qian, T. Ma, *et al.*, "Bending and free vibration analyses of antisymmetrically laminated carbon nanotube-reinforced functionally graded plates," *Journal of Composite Materials,* vol. 51, pp 3111-3125, 2017.
[25] Z. Lei, L. Zhang, and K. M. Liew, "Analysis of laminated CNT reinforced functionally graded plates using the element-free kp-Ritz method," *Composites Part B: Engineering,* vol. 84, pp 211-221, 2016.
[26] H. S. Shen, "Nonlinear bending of functionally graded carbon nanotube-reinforced composite plates in thermal environments," *Composite Structures,* vol. 91, pp 9-19, 2009.
[27] J. Wang and R. Pyrz, "Prediction of the overall moduli of layered silicate-reinforced nanocomposites—part I: basic theory and formulas," *Composites Science and Technology,* vol. 64, pp 925-934, 2004.
[28] J. Fidelus, E. Wiesel, F. Gojny, K. Schulte, and H. Wagner, "Thermo-mechanical properties of randomly oriented carbon/epoxy nanocomposites," *Composites Part A: Applied Science and Manufacturing,* vol. 36, pp 1555-1561, 2005.
[29] J. N. Reddy, *Mechanics of laminated composite plates and shells: theory and analysis*: CRC press, 2004.
[30] H. S. Shen, "Nonlinear bending of functionally graded carbon nanotube-reinforced composite plates in thermal environments," *Composite Structures,* vol. 91, pp 9-19, 2009.